Vapor-Deposited Chromium Coatings on Silicon Carbide Fuel Cladding: Multi-Scale Investigation of Structure and Performance

By

Kyle Matthew Quillin

A dissertation submitted in partial fulfillment of
the requirements for the degree of

Doctor of Philosophy
(Materials Science and Engineering)

at the

UNIVERSITY OF WISCONSIN-MADISON

2024

Date of final oral examination: 02/27/2024

The dissertation is approved by the following members of the Final Oral Committee:

Kumar Sridharan, Professor, Materials Science and Engineering and Nuclear Engineering and Engineering Physics

Frank Pfefferkorn, Professor, Mechanical Engineering

Xudong Wang, Professor, Materials Science and Engineering

Yongfeng Zhang, Assistant Professor, Nuclear Engineering and Engineering Physics

Hwasung Yeom, Assistant Professor, Division of Advanced Nuclear Engineering, Pohang University of Science and Technology

David Frazer, Staff Engineer, Nuclear Technology and Materials, General Atomics

Abstract

The development of advanced cladding and fuel materials is central to enhancing the safety and accident tolerance of light water reactors (LWRs). Silicon carbide fiber-reinforced silicon carbide matrix composites (SiC-SiC_f), on account of their superior high temperature strength and steam oxidation resistance, as well as acceptable irradiation damage resistance and neutronic characteristics, are being considered as potential accident tolerant fuel cladding materials for LWRs. However, the hydrothermal corrosion of SiC at normal reactor operating conditions presents a challenge toward its implementation. Protective corrosion-resistant coatings deposited on the outer surface of the SiC cladding offer a potential solution to addressing this challenge.

For a coating material to serve as a corrosion barrier, it must effectively passivate when in contact with high temperature water. To this end, the coating should also possess a combination of mechanical characteristics including good adhesion to the substrate, a compressive residual stress state, and ductility to maintain its mechanical integrity during in-reactor service. The coating will be required to withstand the harsh environment inside the reactor core and be compatible with the underlying SiC at elevated temperature and under irradiation. Cr was selected as the coating material for investigation in this research as it has the potential to address these requirements, if a more fundamental understanding of the deposition processes, structure, properties, and performance can be achieved.

A variety of magnetron sputtering technologies were used to deposit Cr films 5–10 μm in thickness on SiC substrates to understand the effects of process parameters on the structure of the films and their interface with the substrate, as well as their performance in harsh environments. Six types of sputtering processes were investigated, including (i) standard direct current magnetron sputtering (S-DCMS), (ii) pulsed DCMS (P-DCMS), (iii) ion-assisted DCMS (I-DCMS), and (iv)

pulsed ion-assisted DCMS (PI-DCMS), (v) high-power impulse magnetron sputtering (HiPIMS), and (vi) bipolar HiPIMS (B-HiPIMS). The DCMS processes are characterized by low power densities, minimal atomic mobility during film growth, and negligible ionization of the sputtered flux prior to impingement on substrate surface. HiPIMS processes (both conventional and B-HiPIMS) involve much higher power densities and ionization levels, and consequently impart greater surface atomic mobilities than the DCMS processes.

The research employs multi-scale materials characterization and testing approaches in harsh conditions to understand multiple scientific phenomena and themes that fundamentally govern the relationships between the deposition process and coating structure and properties with respect to the important performance considerations necessary for a materials system inside a reactor core. The first topic is understanding how energetics of deposition manifest in the coatings' structure, residual stress state, and mechanical behavior. The second relates to ion irradiation effects, from low energy (on the order of eV) during deposition (film evolution and growth) to high energy (on the order of MeV) ion beam irradiation experiments (to induce radiation damage) that provide insights into morphological evolution and compositional redistribution in the coating and coating-substrate interface in different energy regimes. The third theme involves elucidating interfacial phenomena including deposition-induced atomic mixing, coating-substrate interdiffusion and chemical interaction at elevated temperatures, interfacial evolution under irradiation, and mechanical behavior at the interface. Lastly, aspects specifically related to the Cr-SiC materials system, such as corrosion, phase equilibria, and amorphization under high energy irradiation are elucidated.

Transmission electron microscopy (TEM) was used to characterize the structural features of the coatings at a nanoscale, including porosity, and grain size and orientation. Regardless of the

specific process variant used, DCMS coatings exhibited fibrous grains separated by nanoscale porosity. The additional energetic ion bombardment in the two types of HiPIMS deposition processes and associated enhanced mobility resulted in coatings with fully dense microstructures and smoother surfaces. However, the morphology and grain size in the conventional HiPIMS and B-HiPIMS coatings were quite different and found to be dependent on substrate temperature and different characteristics of the ionized sputtered flux. High-resolution TEM (HRTEM) imaging of the interface revealed that a Cr-SiC mixed region about 2 nm in thickness formed at the coating-substrate interface for B-HiPIMS but was not evident for the DCMS coating. The observation of the mixed interfacial region in the B-HiPIMS coating was supported by a dynamic Monte Carlo simulation of interfacial composition evolution during the early stages of deposition. Using spatially resolved electron energy loss spectroscopy (EELS), it was determined that the mixed region formed on the Cr-rich side of the interface and contained a significant amount of carbon. Analysis of the fine structure of core-loss ionization edges supported with statistical compositional profiling of the interface revealed that Cr-C bonds are present in the mixed region, and the width of the B-HiPIMS is wider on average than DCMS. This mixed layer contributes to enhanced coating-substrate adhesion in the HiPIMS coatings.

Both ambient and *in situ* high temperature x-ray diffraction techniques were used to measure the residual stress state in the coatings and study stress evolution during thermal exposure. All DCMS coatings exhibited tensile residual stress induced by both thermal and deposition-induced conditions. HiPIMS and B-HiPIMS coatings exhibited compressive residual stresses which is attributed to the increased surface mobility of atoms and atomic peening effects during the respective deposition processes. The compressive residual stress of these HiPIMS coatings is deemed beneficial as it will make the coatings more effective in withstanding tensile stresses

generated by swelling of the SiC cladding under irradiation. Over time at 300 °C, the compressive stress was gradually relieved. At 700 °C, grain growth in the B-HiPIMS coating resulted in a transition from compressive to tensile stress. The deposition-induced mixing layer present at the B-HiPIMS interface facilitated the formation of a continuous interdiffusion layer composed of Cr-C and Cr-Si phases, consistent with thermodynamic predictions.

The influence of microstructure on the mechanical properties and deformation behavior of the coatings was evaluated using nanoindentation coupled with post-test TEM and atomic force microscopy (AFM). The hardness of the coatings ranged between 4–10 GPa. On account of its coarse columnar grain structure, the B-HiPIMS coating exhibited the lowest hardness and greatest material pile-up around the edges of the indenter. The pile-up phenomenon was investigated further via AFM and cross-sectional TEM imaging, where it was observed that the columnar grains deform in a coherent, wave-like manner allowing for ductile deformation, a desirable characteristic for cladding application. In contrast, for multiple DCMS coatings, cracks initiated at indent corners due to the presence of intercolumnar porosity and poor intergranular cohesion, and the columns were observed to buckle underneath the center of the indent.

Hydrothermal corrosion testing was conducted in two environments: a static deionized water autoclave (360 °C, 18.6 MPa, 720 hours) and a continuously refreshing flow loop (330 °C, 13.1 MPa, 2160 hours) with dissolved hydrogen added to simulate pressurized water reactor conditions. For the coatings that remained fully adhered after the tests, namely S-DCMS, HiPIMS, B-HiPIMS, a protective Cr_2O_3 layer formed on the surface, and the coatings successfully prevented corrosion of the underlying SiC. Oxide formation was also observed along the porous intercolumnar regions below the surface of the S-DCMS coating. Through further characterization of the oxide layers, it was found that the morphology and composition of the oxide is altered depending on the corrosion

test conditions. In the static autoclave, the corrosion layer formed as a uniform film on the surface, while the layer formed in the flow loop tended to be more heterogeneous with greater variations in thickness and morphology, likely an effect of the coolant flow. Using X-ray photoelectron spectroscopy (XPS) to analyze the near-surface chemical state of the corrosion product layer, it was determined that introduction of hydrogen in water promoted Cr-oxide phase while evidence of Cr-hydroxide phase was observed in corrosion product layer in tests performed in the absence of hydrogen in the water. This finding was consistent between different Cr coating types tested in the same corrosion environment.

A B-HiPIMS coating sample was irradiated using 80 MeV Xe^{26+} ions to study the effects of radiation damage on the Cr coating structure and Cr-SiC interface. After irradiation, the presence of numerous linear arrays of defects, likely dislocation loops, were observed within the columnar structure of the coating, which resulted in a slight increase in coating hardness. Detailed TEM examination in conjunction with compositional analysis showed that at the interface, a 20 nm-thick, Cr-rich amorphous layer had formed during irradiation. These examinations, supported by atomistic and CALPHAD modeling, showed that the combination of intrinsic radiation damage in Cr and ion beam mixing of Si and C across the interface eventually lead to the destabilization of the crystalline Cr-Si-C mixture. Irradiation-induced embrittlement was observed in *in situ* microcantilever bending experiments, likely driven by radiation damage in both Cr and SiC.

Acknowledgments

I would like to begin by expressing my sincere thanks to my advisor, Professor Kumar Sridharan. First, for taking me on as an undergrad the summer of my freshman year when I hadn't taken a single materials science class yet and introducing me to the world of nuclear materials, surface engineering, and thin films. Secondly, for his continued support throughout my graduate studies, willingness to talk at any time of day, and starting me out on a great path to begin my career. I am safe in knowing his support will continue even after I've graduated.

I am extremely grateful to have had the opportunity to work with two excellent scientists throughout, Dr. Hwasung Yeom and Dr. K. N. Sasidhar. Sung's guidance and encouragement during my first years in graduate school were extremely valuable to my growth as a researcher. I knew I could rely on him for technical discussions or solving purchasing issues, and there were plenty of both. Many thanks are due to Sasidhar as well for helping push my work to the finish line. I will always appreciate his willingness to assist with all aspects of research and for re-teaching me the basics of thermodynamics. The work of these staff members is truly crucial to the success of the research group.

I would also like to thank the many researchers I got to know during my time at Idaho National Laboratory for facilitating many aspects of my work, starting with Dr. David Frazer. I will always be grateful for his mentorship and friendship while I was at INL. Thank you to Dr. Kaustubh Bawane for his assistance with EELS measurements, Dr. Xiaofei Pu for her help with XRD, Dr. Lingfeng He for his support on the TEM, and Dr. Fei Teng for his assistance with micromechanical testing. At Argonne National Laboratory, Dr. Laura Jamison and Dr. Peter Mouche were very helpful in assisting with the irradiation experiment. Thank you also to Dr. Andrew Hoffman and Dr. Rajnikant Umretiya and GE Research for conducting flow loop tests.

I have been assisted by multiple undergraduate students over the years including Evan Willing, Xinwu Liu, and Laura Stern – thank you for all your help. I would like to specifically acknowledge my fellow grad student Tyler Dabney as we've traveled down similar paths together. I am lucky to have had someone to continuously discuss things and commiserate over instruments breaking down. I must also thank JP Lacy for being an excellent conference hotel roommate. I would also like to acknowledge the staff at the NIAC, primarily Dr. Julie Morasch and Dr. Alex Kvit, for keeping the characterization facilities up and running. Also thank you to Dr. Izabela Szlufarska and Dr. Waqas Qureshi for their help with DFT calculations.

Financially, this work has been supported by a grant from the NEUP, and I was personally supported by a Graduate Fellowship through the University Nuclear Leadership Program. This fellowship provided me with extremely valuable opportunities to travel to INL and research topics that interested me. I also would like to acknowledge Dr. Mike McFarland at Acree Technologies and Stan Amyotte and Dr. Paola Russo at Angstrom Engineering for their work on coating deposition.

I would like to end by recognizing my friends and family who have been there every step of the way. Many thanks to my friends in Madison: Casey, Ean, and Jeff for tolerating me as I spent nearly a decade as a college student. To my parents, Dan and Cathy for their continuous love, encouragement, and patience. And lastly to my girlfriend Haley for developing the ability to explain to other people what I've been working on all these years, and more importantly for her unconditional companionship.

Table of Contents

List of Figures

List of Tables

Abbreviations

ADF – annular dark field

AFM – atomic force microscopy

ATF – accident tolerant fuels

BCC – body-centered cubic

BF – bright field

B-HiPIMS – bipolar high power impulse magnetron sputtering

BWR – boiling water reactor

CVD – chemical vapor deposition

CVI – chemical vapor infiltration

DCMS – direct current magnetron sputtering

DF – dark field

EDS – energy dispersive X-ray spectroscopy

EELS – electron energy loss spectroscopy

FIB – focused ion beam

FCC – face-centered cubic

HAADF – high-angle annular dark field

HCP – hexagonal close-packed

HiPIMS – high power impulse magnetron sputtering

HRTEM – high-resolution transmission electron microscopy

I-DCMS – ion-assisted direct current magnetron sputtering

LWR – light water reactor

P-DCMS – pulsed direct current magnetron sputtering

PI-DCMS – pulsed ion-assisted direct current magnetron sputtering

PFIB – plasma focused ion beam

PVD – physical vapor deposition

PWR – pressurized water reactor

S-DCMS – standard direct current magnetron sputtering

SEM – scanning electron microscopy

STEM – scanning transmission electron microscopy

TEM – transmission electron microscopy

XPS – X-ray photoelectron spectroscopy

XRD – X-ray diffraction

1. Introduction

1.1 Motivation

The Fukushima Daiichi nuclear accident of 2011 brought to light the need for better-performing light water reactor (LWR) fuel materials in beyond design-basis accident conditions [1]. In response, the United States Department of Energy initiated the Accident Tolerant Fuel (ATF) program in 2012 as a large-scale research effort to develop materials with enhanced safety performance [2]. A principal component of ATF research is the investigation of materials with significantly improved oxidation resistance compared to currently-used Zr-alloy fuel cladding, which rapidly degrades in the high temperature steam environment generated during a severe accident [3]. One material under consideration for accident tolerant fuel cladding in future LWRs is SiC-SiC_f composite (subscript *f* indicating fiber) on account of its excellent high temperature strength and oxidation resistance of SiC [1].

While SiC offers notable performance advantages over Zr-alloys in accident conditions, at normal reactor operating conditions, SiC is prone to hydrothermal corrosion via reaction with the high temperature water coolant in the reactor [4]. This can lead to dimensional changes of the cladding tubes, contamination of the reactor coolant, and buildup of SiO_2 in cooler sections of the reactor system [4]. Figure 1.1a illustrates the mass and thickness loss of SiC exposed in different LWR water chemistries. The corrosion kinetics are strongly dependent on the water chemistry, which varies between pressurized (PWR) and boiling water reactor (BWR) designs and can also be altered by radiolysis inside the reactor core. While corrosion can be controlled by adjusting water chemistry, it is unrealistic to rely on this method alone to control corrosion of SiC. Figure 1.1b shows the buildup of SiO_2 in cooler sections of a flow loop (used to simulate coolant flow in a reactor) where the solubility of SiO_2 in water is relatively low.

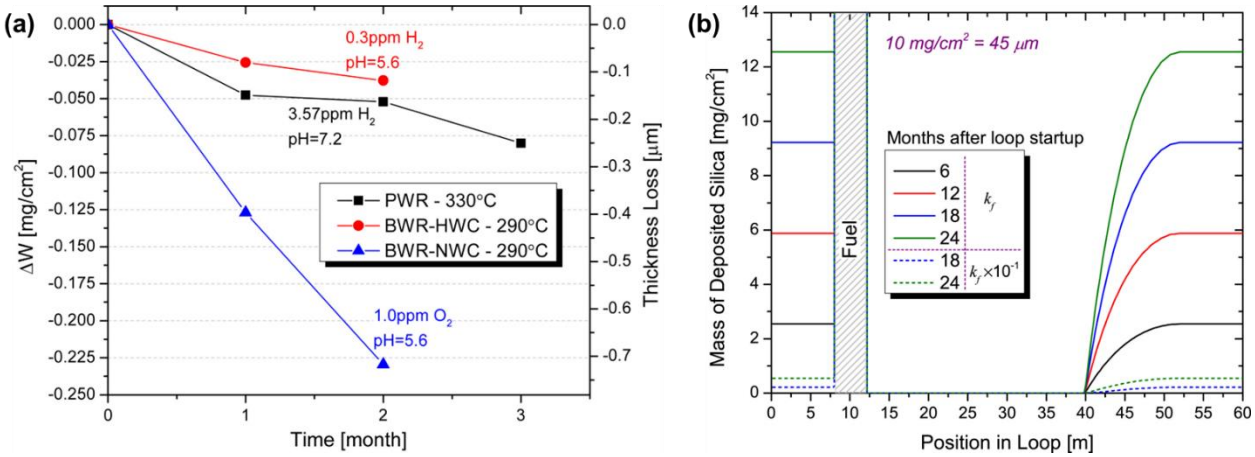

Figure 1.1: (a) Mass loss and thickness loss of monolithic SiC in different LWR water chemistries [4]; (b) Buildup of SiO_2 after a certain time periods with different corrosion rates in a simulated loop [4].

One approach to mitigate the hydrothermal corrosion of SiC during reactor operation is the deposition of a thin, corrosion-resistant coating on the outer surface of the SiC cladding [5]. To function as an effective protective layer against corrosion in the aqueous reactor coolant, the coating must also have suitable mechanical behavior that minimizes cracking or delamination as the cladding experiences geometric changes under irradiation and elevated temperature exposure. Researchers at Oak Ridge National Laboratory (ORNL) have investigated a variety of metallic and ceramic coating materials on SiC deposited using electroplating, thermal spray, and physical vapor deposition techniques [5–14]. From this body of work, Cr coatings produced with physical vapor deposition have emerged as among the lead candidate material/method for SiC cladding for the LWR application. However, this work underscores the need for better understanding of the effects of the wide physical vapor deposition parameter space on all aspects of film properties (e.g., structure, residual stress, mechanical behavior), the performance of Cr coatings in reactor-relevant environments (e.g., hydrothermal corrosion, irradiation, elevated temperatures), and the interaction between Cr and SiC in these extreme environments.

1.2 Research goals and scope

The goal of this research is to develop a fundamental understanding across multiple length scales of the interrelationship between deposition processes, coating growth mechanisms and structural characteristics, interfacial evolution, mechanical behavior including residual stress evolution, and the resulting performance in environments involving corrosion and irradiation. This research addresses the following scientific and engineering aspects of coating development:

- Effects of energetic magnetron sputter deposition on coating micro/nanostructure, nanoscale interfacial mixing, and residual stress
- Relationships between coating structure, mechanical properties, and deformation behavior
- Residual stress evolution and coating-substrate chemical interaction at elevated temperatures
- Understanding the hydrothermal corrosion response of coatings and its efficacy in mitigating corrosion of SiC
- Effects of irradiation on structural and compositional evolution at the interface, defect formation within the coatings, and the subsequent effects on mechanical behavior

2. Literature Review

2.1 Nuclear energy and materials challenges

2.1.1 Overview of nuclear reactors

Nuclear power is a crucial source of carbon-free, baseload energy worldwide. On account of its significantly higher energy density compared to other sources of energy [15], the importance of nuclear energy is growing as reliance on fossil fuels continues to shrink further into the 21st century. The majority of commercial reactors in the United States use water as the coolant and neutron moderator and are classified as either PWRs or BWRs [15]. Figure 2.1 shows a schematic diagram of a PWR and the materials used for its many components.

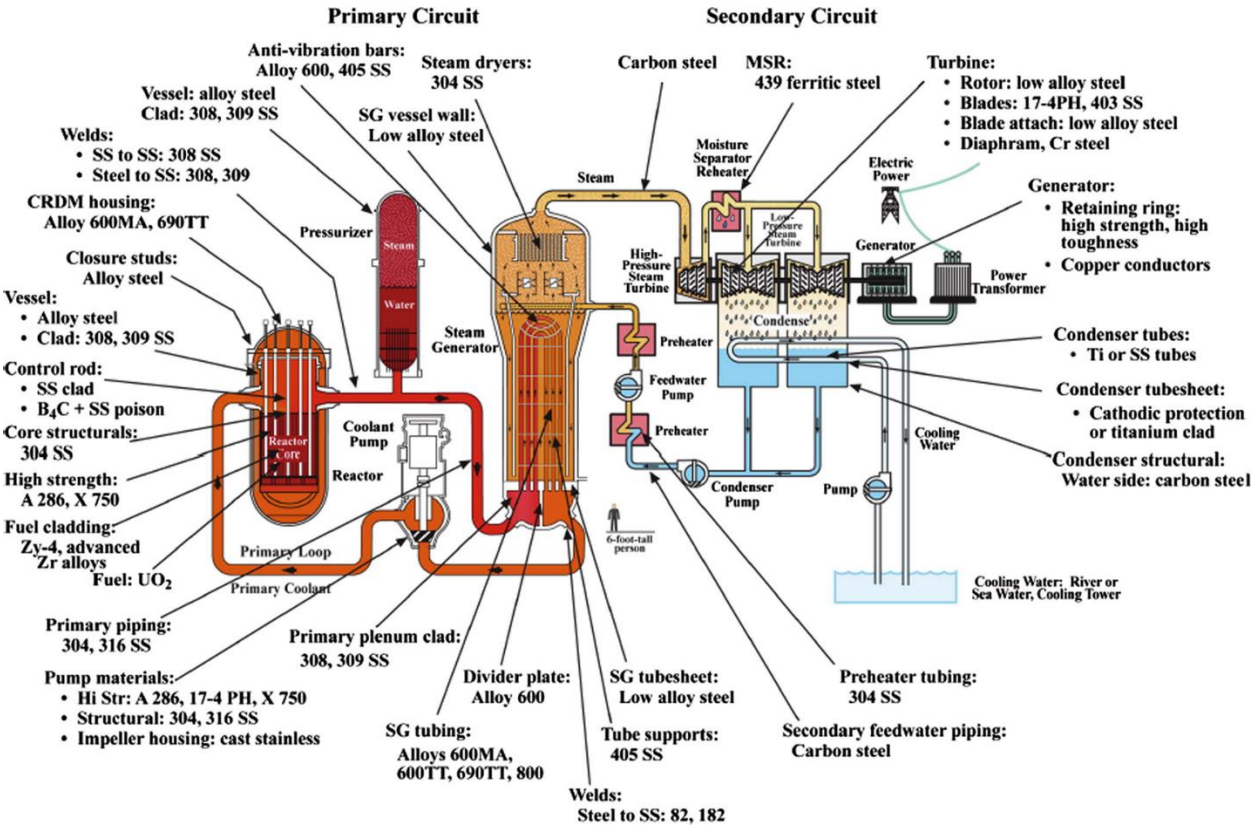

Figure 2.1: Schematic of a PWR and the materials used for reactor components [15].

The energy produced by a nuclear reactor originates from the continuous atomic fission reactions taking place inside the reactor core. LWRs are fueled by millions of UO_2 pellets about 1

cm in diameter and 2 cm in length (Figure 2.2a). The pellets are housed in long, slender tubes referred to as fuel cladding that are fabricated with Zr-alloys (on account of the relatively high neutron transparency of the Zr) which in turn is surrounded by the water coolant which transfers the fission heat generated from the fuel within the cladding to the secondary side of the reactor. The cladding is the most important structural member of a reactor as it protects the fuel from exposure to the coolant and prevents the escape of radioactive fission products [15]. The cladding tubes are only about 1 cm in diameter and less than 1 mm in wall thickness, but 3–4 m in length. Cladding tubes are bundled together in the form of fuel assemblies (Figure 2.2b), and hundreds of assemblies are typically present in a reactor core during operation.

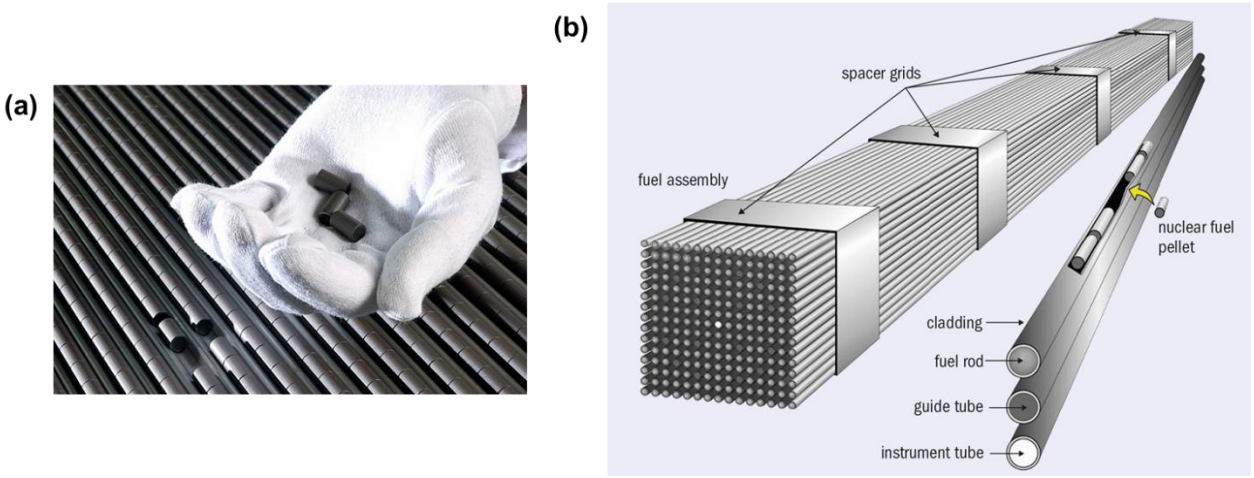

Figure 2.2: (a) Photograph of UO_2 fuel pellets [16]; (b) Illustration of the fuel cladding and a fuel assembly [17].

2.1.2 Effects of reactor environment on materials

The environment inside a reactor core is extremely harsh; elevated temperatures, mechanical stress, corrosion, and irradiation can all contribute to the degradation of core materials [15]. The temperature inside the core of LWRs is approximately 300 °C. While this temperature is still low relative to the melting point of structural alloys, the elevated operating temperature can induce thermal stresses, accelerate corrosion reactions, and facilitate creep deformation of materials

during prolonged exposure [15]. Corrosion of reactor materials primarily occurs through exposure of components to the high temperature water coolant. Consequences of corrosion include the buildup of CRUD on the Zr-alloy cladding, stress corrosion cracking of other structural alloys, and coolant contamination [15].

Most of the above materials degradation processes are accelerated or exacerbated by radiation damage [15]. The structure and compositional makeup of a material can be altered by the continuous bombardment of energetic neutrons that are present in a reactor core. As a neutron passes through a material, it generates a cascade of atomic collisions resulting in displacement of atoms from their lattice site and the formation of interstitial and vacancy point defects [18]. These defects tend to cluster in the form of dislocation loops or voids. Some of the most significant consequences of defect formation include hardening, mechanical embrittlement, and swelling (i.e., macroscopic increase in volume) [18]. Numerous other physical and environmental effects are possible, such as phase changes or precipitation of secondary phases, radiation-induced segregation, and irradiation-assisted stress corrosion cracking [18]. For most irradiation-induced processes, the exact effects on a material often depend on the irradiating particle type (neutrons, electrons, ions), irradiation temperature, and the radiation dose (number of particles impinging per unit area of a material) [18].

Along with the aforementioned consequences of radiation damage, interfaces between materials may also experience irradiation-driven transfer of atoms across the interface, a phenomenon termed “ion beam mixing” [19]. Due to the stochastic nature of atomic collisions and extremely rapid quenching time of the collision cascade caused by energetic particle irradiation, ion beam mixing can result in the formation of non-equilibrium composition states, such as highly supersaturated solid solutions, metastable secondary phases, and amorphous regions [19,20]. The

behavior of irradiation-induced interfacial mixing is strongly dependent on what elements are present on either side of the interface, their thermodynamic affinity for one another, and the irradiation parameters [21].

2.2 Accident tolerant fuels

While the confluence of many factors inside a reactor core makes for a harsh environment for materials, the conditions arising during a severe loss of coolant accident can in many respects be far more severe. At the Fukushima reactor plant, for example, the earthquake and subsequent tsunami eliminated all ability to circulate coolant through reactor core, causing the core temperature to rise above 1000 °C. The liquid water coolant boiled off into steam, which then reacted with the Zr-alloy cladding,

$$\mathrm{Zr_{(s)}} + 2\mathrm{H_2O_{(g)}} \rightarrow \mathrm{ZrO_{2(s)}} + 2\mathrm{H_{2(g)}} \qquad \text{(Eq. 2.1).}$$

The high-temperature oxidation of the cladding led to loss of mechanical integrity and ballooning and burst of cladding tubes [15]. The reaction also produces massive amounts of heat due to the exothermic nature of the reaction as well as hydrogen gas, resulting in an explosion that destroyed reactor containment structures and released radioactive material into the environment [1].

Accident tolerant fuel (ATF) cladding concepts aim to improve the performance of the cladding in high temperature steam environments by implementing oxidation-resistant fuel cladding materials [1]. Both short-term and long-term ATF cladding concepts are currently under investigation [3,22]. Short-term solutions involve depositing coatings of an oxidation-resistant material on the outer surface of the Zr-alloy cladding. A wide range of coating materials have been studied for this purpose including MAX phases [23], intermetallics [24], FeCrAl alloys [25], and pure metallic coatings [26,27]. Pure Cr coatings deposited by either cold spray [26] or physical

vapor deposition [27] have emerged as promising candidates for this application based on their slow oxidation kinetics relative to uncoated Zr-alloy cladding [28].

Long-term ATF solutions involve the complete replacement of Zr-alloys with a more oxidation-resistant material. Two options are monolithic FeCrAl alloys [29] and SiC-SiC_f composites [30]. FeCrAl alloys are able to form protective chromia layer at normal reactor temperatures and protective alumina layer at the high temperatures associated with accident conditions making them attractive candidates for ATF cladding [22]. The next section provides an overview of the advantages and concerns associated with SiC-SiC_f as cladding material.

2.3 SiC-SiC_f fuel cladding

SiC-SiC_f composites consist of a SiC matrix reinforced with SiC fibers. This material is unique among ATF concepts in that it is a ceramic material rather than metallic. While there are many possible manufacturing routes to produce monolithic SiC, for nuclear applications, a chemical vapor deposition (CVD) process with silicon and carbon-based gaseous precursors has been the preferred approach [31]. To form the composite, SiC fibers are braided in a certain geometry, and a chemical vapor infiltration (CVI, a type of CVD) process is used to form the SiC matrix by sealing gaps between the fibers [32]. A thin pyrolytic carbon interlayer is often used to improve bonding between the matrix and the fibers [33]. SiC cladding designs incorporate both monolithic CVD SiC and the SiC-SiC_f composite. Duplex designs use a composite inner layer and monolithic outer layer to avoid exposure of the fiber-matrix interface from exposure to the coolant, while triplex designs add an inner monolithic layer to improve gas tightness to prevent fission product release [32,34]. The use of SiC-SiC_f composite enhances the mechanical performance of the cladding and provides pseudo-ductility to what is normally an brittle ceramic [32]. The triplex SiC cladding design and SiC-SiC_f composite structure are shown in Figure 2.3.

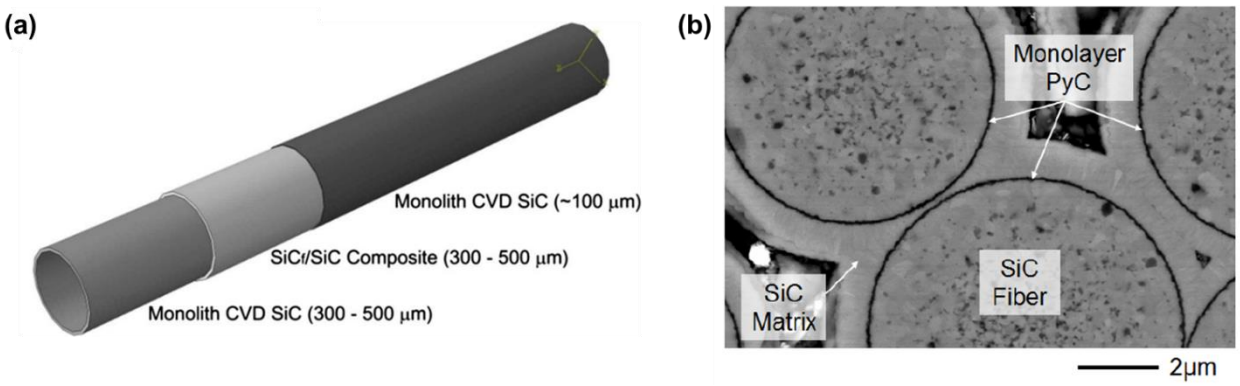

Figure 2.3: (a) Triplex SiC cladding design [34]; (b) Structure of SiC-SiC_f composite [33].

SiC offers numerous performance benefits over Zr-alloys in high temperature steam environments. First, SiC-SiC_f composites are able to maintain their strength and creep resistance, even at high temperatures, significantly lowering the risk of mechanical failure of the cladding during an accident [35]. Figure 2.4a shows the tensile strength of SiC fibers as a function of temperature. Second, SiC relies on the formation of an SiO_2 layer for protection in oxidative steam environments, while Zr-alloys rely on the formation of a ZrO_2 layer on the surface to prevent further corrosion. Based on the thermodynamic stability and kinetics of oxide growth rate, as illustrated in Figure 2.4b, the oxidation of SiC in steam is orders of magnitude slower than Zr. Whereas Zr-alloy cladding can be fully consumed and lose all mechanical strength via oxidation within a matter of hours, SiC can greatly extended the response time prior to cladding failure [36]. SiC also provides benefits at normal reactor operating conditions, including a lower neutron absorption cross section than Zr and irradiation-induced swelling that saturates at low damage levels [33,37].

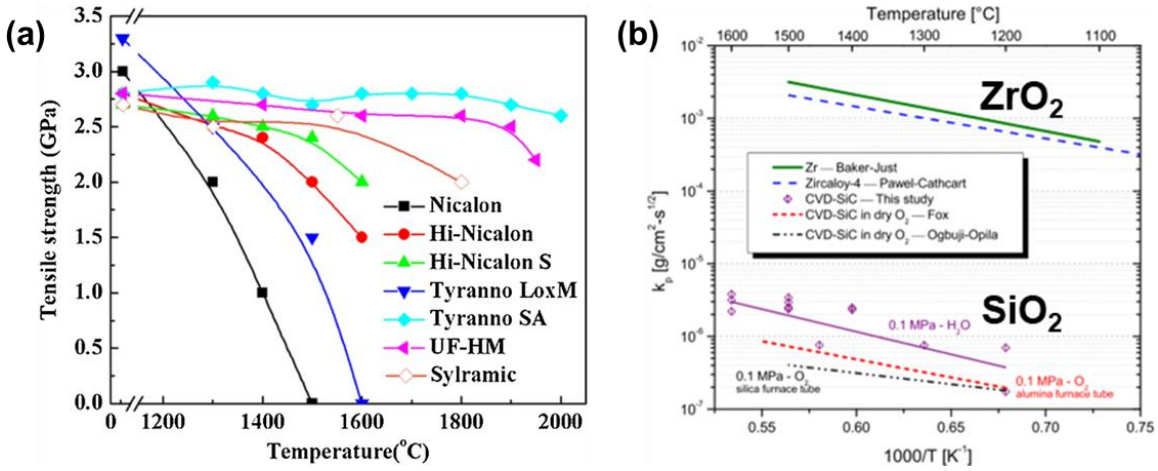

Figure 2.4: (a) Tensile strength vs. temperature for different SiC fiber types [35]; (b) Parabolic oxidation rate constants in high temperature steam of SiO_2 and ZrO_2 [36].

As introduced previously, the hydrothermal corrosion of SiC at normal reactor operating conditions is one technical challenge that must be addressed for SiC to serve as an effective fuel cladding material. The corrosion behavior of SiC in different water chemistries has been studied extensively [4,38–40]. Work from Terrani et al. has shown that it is always thermodynamically favorable for SiC to react with water molecules to form SiO_2 via one of two major pathways (although many others have been identified) depending on the oxygen activity [4],

$$SiC_{(s)} + 2H_2O_{(aq)} \rightarrow SiO_{2\,(s)} + CH_{4(g)} \text{ (low oxygen activity)} \quad \text{(Eq. 2.2)}$$

$$SiC_{(s)} + 4H_2O_{(aq)} \rightarrow SiO_{2\,(s)} + 4H_{2(g)} + CO_{2(g)} \text{ (high oxygen activity)} \quad \text{(Eq. 2.3).}$$

Once SiO_2 has formed, it also subsequently reacts with the water coolant to form aqueous silicic acid [4],

$$SiO_{2(s)} + 2H_2O_{(aq)} \rightarrow Si(OH)_{4(aq)} \quad \text{(Eq. 2.4).}$$

As indicated, this compound is soluble in water, meaning that its formation provides a reaction pathway for SiC to readily dissolve into the water coolant as a result of corrosion reactions. It is well known that environments with high amounts of dissolved oxygen, such as certain BWR conditions, accelerate the rate of corrosion and degree of grain boundary attack in SiC [40].

Aside from hydrothermal corrosion, other challenges related to the implementation of SiC as a fuel cladding material are hermeticity and joining [41]. Although the extent of swelling of SiC under irradiation is low, it has been shown that microcracking can occur within the SiC-SiC_f composite at small strains [42], which provides pathways for escape of fission gas. The sealing of gas-tight end caps on SiC is also an issue because the conventional welding methods are not applicable due to the high decomposition temperature of SiC [30]. Many different diffusion bonding and sintering processes are under investigation to find an effective joining method [43].

2.4 Magnetron sputtering

2.4.1 Coating processes and effect of deposition method on film structure

Magnetron sputtering is one technique within the larger family of physical vapor deposition (PVD) methods to deposit a thin coating onto a substrate. Other common PVD methods include evaporation and cathodic arc deposition. All PVD processes are vacuum-based and use some physical process to vaporize atoms from a solid source (referred to as the target, composed of the desired coating material) that then condense on the substrate to form the film. A schematic of the sputter deposition process is shown in Figure 2.5. In the sputter deposition process, a working gas, typically argon, forms a plasma via the application of a strong voltage between the target and substrate. The ionized gas atoms collide with and transfer their energy to the surface of negatively charged sputter target. From these collisions, atoms are ejected from the target surface into the vapor phase. The vaporized atoms then travel toward the substrate and condense on the surface to form the coating.

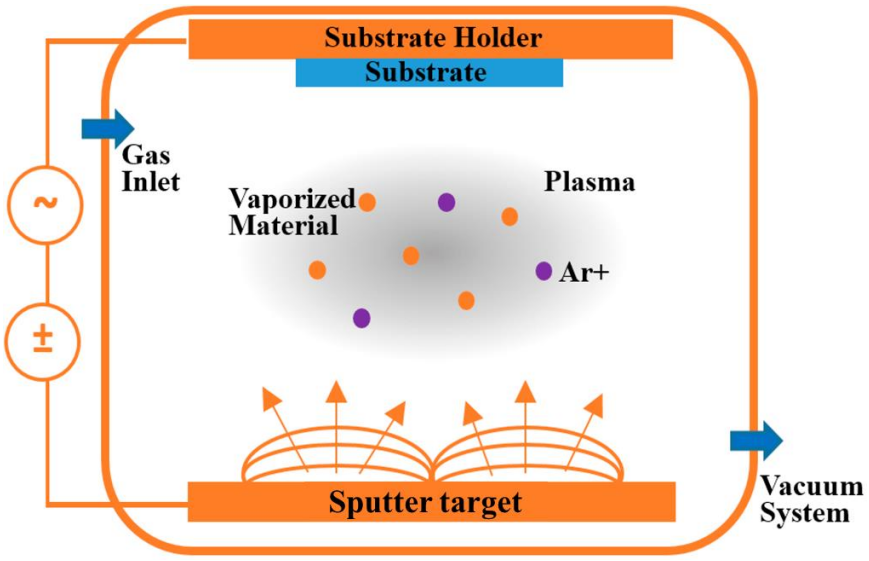

Figure 2.5: Schematic illustration of the magnetron sputter deposition process, modified from [44].

Sputter-deposited coatings have been used for decades in industry for applications including wear protection, electronics and optics, energy, and aerospace [44]. The process is very flexible in terms of the types of materials that can be deposited. Alloyed films can be deposited either via a single sputter target of the desired composition or via a co-sputtering process where multiple sputter targets of different elements are simultaneously active. The deposition rate of different elements can be scaled by controlling the voltage applied to each target. This also opens the door for the efficient fabrication of compositionally graded and multi-layer coatings. Insulating materials can be deposited via radio frequency (RF) sputtering where an alternating voltage is applied to the non-conducting sputter target to avoid charge buildup. Another option is reactive sputtering where a metallic target is used in conjunction with the introduction of a secondary reactive gas, such as oxygen, nitrogen, or methane into the chamber, to produce oxide, nitride, or carbide coatings, respectively. Overall, magnetron sputtering can produce coatings of a wide range of materials with high uniformity and good adhesion with precise control of film microstructure and composition through the coating thickness [44]. The deposition rates of magnetron sputtering

processes are on the order of tens of nanometers per minutes (equivalent to a few microns per hour) [45].

Another important aspect of the deposition process is the substrate pre-treatment. Standard industrial practice often involves mechanical preparation of substrates via a grinding or polishing process followed by a *in situ* cleaning process inside the vacuum chamber immediately prior to deposition [46]. These processes are critical to film adhesion as they remove the few monolayers of adsorbed hydrocarbons or native oxide films. The *in situ* pre-treatment processes are especially useful, as they can be incorporated directly into the coating deposition procedure within the vacuum chamber under the general conditions required for the deposition of the film itself [46]. One common *in situ* treatment is plasma cleaning. The process shares many similarities to the RF sputtering process. An alternating bias is applied to the substrates, and the bombardment of ionized gas atoms can remove undesirable surface contaminants. An ion milling treatment also achieves similar results, but rather than using the process gas as the source of ions, an auxiliary source attached to the deposition chamber bombards the substrates with ions [46].

Direct current magnetron sputtering (DCMS) is the most common industrial sputter deposition process. In standard direct current magnetron sputtering (S-DCMS), a constant negative voltage is applied to the sputter target to attract the positively charged argon ions. The power density is normally on the order of a few W/cm^2 [47]. Because of the relatively low power density, little ionization of the sputtered atoms occurs, and uncharged, neutral atoms mainly comprise the sputtered flux. The fraction of ionized atoms is typically less than 5% [47]. In traditional sputter deposition, the three major process parameters are argon pressure, substrate temperature, and target power. Depending on the combination of these parameters, different coating microstructures can be obtained.

Thornton developed what is called a structure zone diagram to show the different types of microstructural features that can be achieved via sputter deposition [48]. The Thornton diagram is shown in Figure 2.6. The two axes are T/T_m (or "homologous temperature"), which is the ratio of the substrate temperature to the melting point of the coating material, and argon pressure. Substrates are often heated during deposition to improve film properties, and using the homologous temperature allows for comparison between film materials of different melting points. The degree of mobility possessed by atoms arriving at the film surface (often termed adatoms) is strongly influenced by the substrate temperature [49]. Because the growth of sputtered films occurs almost in a layer-by-layer manner, the coatings tend to grow in a columnar or bamboo-like fashion.

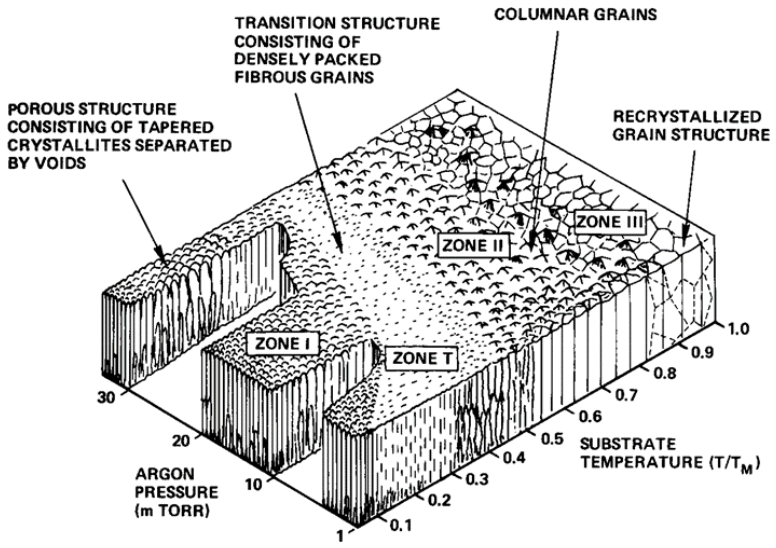

Figure 2.6: Thornton's structure zone diagram for coatings produced by direct current magnetron sputtering [48].

At low T/T_m values, adatom mobility is quite low, and the resulting film structure is typically comprised of fine, fibrous grains separated by nanoscale porosity (Zone 1). As T/T_m is increased, adatoms gain more mobility and can diffuse on the film surface or along grain boundaries, densifying the coating microstructure (Zone T). At T/T_m values > 0.5, coarsening of the columnar grains can occur, and at the highest temperatures, recrystallization into equiaxed grains is possible

(Zones 2 and 3). The effect of deposition pressure is generally less drastic. Film density is often higher at lower argon pressures because sputtered atoms can travel through the plasma with fewer collisions with gas atoms and can arrive and condense on the surface with greater energy. Higher gas pressures reduce the mean free path of atoms and create more scattering events between atoms which tends to decrease film density [49].

It is not a necessity to keep the sputter target voltage constant during deposition. Certain power supplies can apply voltage pulses to the sputter target and also reverse the target polarity from negative to positive. One such example is asymmetric bipolar pulsed direct current magnetron sputtering, or more simply, pulsed direct current magnetron sputtering (P-DCMS). The term "asymmetric" implies that the positive pulse is not of the same magnitude as the normal negative operating voltage, while "bipolar" implies that the polarity is reversed during the pulses. This type of process was originally developed to improve deposition of insulating compounds [50]. The pulses are typically operated in the mid-frequency range (10-250 kHz) [50]. The duty cycle of the process (the fraction of the time that sputtering is actually occurring) is commonly 80-90% [50]. The P-DCMS process has been shown to induce slightly more ionization compared to the S-DCMS process, which provides the atoms additional mobility once they arrive at the substrate surface [51].

Another modification to the DCMS process is the implementation of ion beam-assisted techniques (I-DCMS). In this deposition technique, the target voltage characteristics are the same as the S-DCMS process. To promote densification of the growing film, an ion beam is directed at the substrate during deposition to induce atomic peening and mixing effects [50]. The ion beam consists normally of an inert gas, such as argon. The I-DCMS process has been shown to increase density and tribological performance of coating materials [52]. It is also possible to incorporate

the pulsed and ion-assisted techniques into one single pulsed ion-assisted direct current magnetron sputtering (PI-DCMS) process. Figure 2.7 provides illustrations of the target voltage characteristics for the four aforementioned DCMS processes.

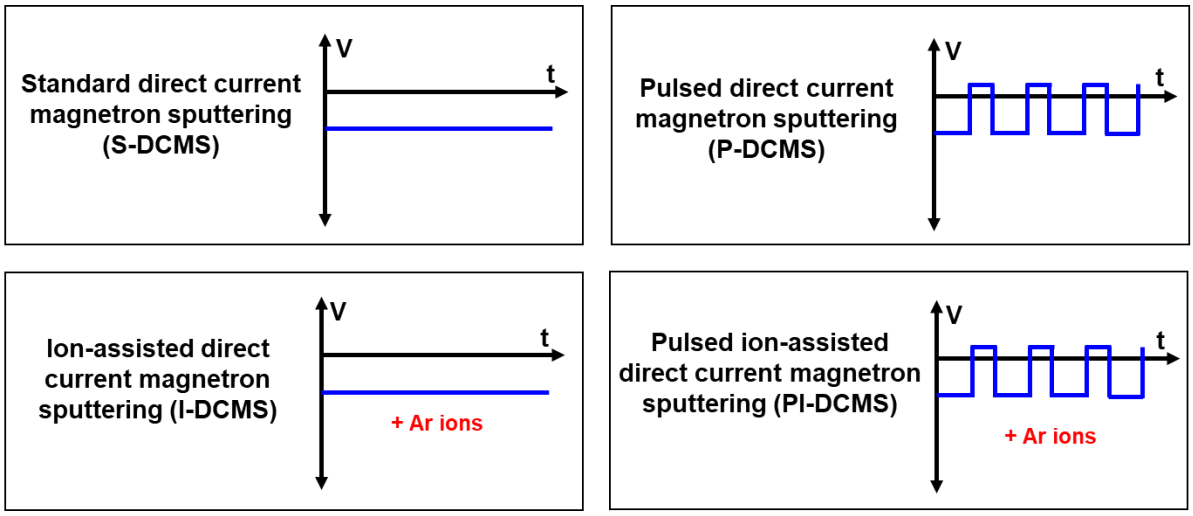

Figure 2.7: Qualitative plots of sputter target voltage vs. time to illustrate the concept underlying four different DCMS processes.

High-power impulse magnetron sputtering (HiPIMS) is a relatively recent advancement in sputter deposition technology [53]. In this process, very short high-power pulses are applied to the sputter target. The pulse frequency is typically between 50–5000 Hz and resulting duty cycles are only 1–3% [50]. The peak power densities reach values on the order of kW/cm^2 [47]. These high-power pulses induce much greater ionization fractions compared to DCMS processes. Ionization fractions upwards of 70% have been measured for certain materials [45]. To accelerate the ions produced during a HiPIMS pulse toward the substrate, a negative bias is usually applied to the substrates [47]. The energy of these ions is in the range of tens to a few hundred eV, which can lead to ballistic collisions between incident and surface atoms and provides them with greater mobility as they arrive at the substrate [54]. More recently, a modified HiPIMS process called bipolar HiPIMS has been developed [55]. This technique features a positive reverse pulse following each negative HiPIMS pulse, similar to the positive pulses used in the P-DCMS process.

Because a significant fraction of the sputtered atoms is ionized, the positive pulse applied to the sputter target accelerates the ions away from the target and toward the substrate. The B-HiPIMS process was developed as an alternative to HiPIMS deposition to be used for substrates that could not be biased due to their properties or geometry and with the possibility of using the so-called "positive kick" to increase ion energy even further beyond HiPIMS [56]. Figure 2.8 shows the target voltage cycle characteristics for the HiPIMS and B-HiPIMS processes.

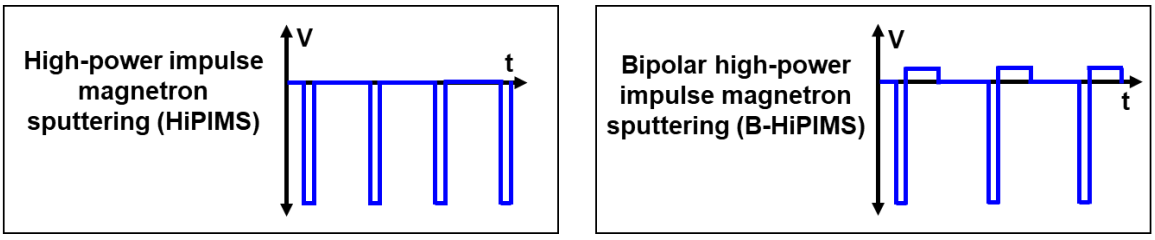

Figure 2.8: Qualitative plots of sputter target voltage vs. time for the two different HiPIMS processes.

The effects of ion bombardment on film structure are not accounted for in the traditional structure zone model developed by Thornton. Anders has developed a modified structure zone diagram that replaces the traditional pressure and temperature axes with axes that represent the effective energy and temperature [57]. This modified diagram is shown in Figure 2.9. The effective energy axis (E^*) is plotted on a logarithmic scale and accounts for the effects of kinetic energy (or momentum) transfer to the film by bombarding ions which can generate atomic collision cascades and localized thermal spikes [57]. The effective temperature axis (T^*) accounts for the substrate temperature plus the potential energy of ionized atoms arriving at the film surface and can essentially be viewed as a representation of atomic mobility. The structure zone diagram from Anders displays many regimes similar to the original model from Thornton, but additionally highlights the effects of energetic ions on residual stress. At low energies and temperatures, the film is under a tensile residual stress while exhibiting a porous microstructure. As the effective temperature and energy increase, the film becomes denser while also converting to a more

compressive residual stress state. The mechanisms of residual stress formation are discussed in the next section. This model also illustrates the effects of momentum transfer and atomic mobility on the film structure. If the momentum transferred to the growing film by bombarding ions is large (i.e., high E^*, low T^*), the nucleation of new grains dominates film growth, resulting in a fine-grained structure. If momentum transfer is minimal, but atomic mobility is high (i.e., low E^*, low T^*), growth of existing grains is promoted, resulting in a coarser grain size.

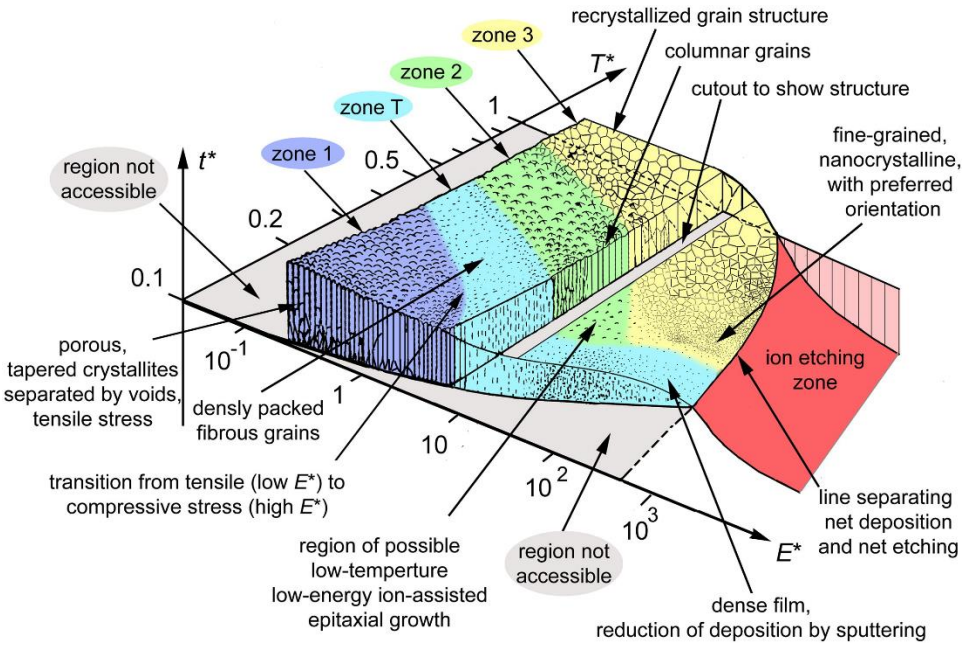

Figure 2.9: Modified structure zone diagram from Anders with effective temperature and energy axes accounting for the effects of energetic ions during film growth [57].

HiPIMS processes have been applied to produce a wide variety of metallic and ceramic coatings [45,47,54,58–60]. Almost every comparative study of films produced with DCMS and HiPIMS processes reports that the energetic HiPIMS deposition promotes densification of the film structure and a decrease in surface roughness. HiPIMS has also been reported to improve film adhesion by promoting atomic-scale interactions between the coating and substrate [47]. In other cases, HiPIMS has been used to produce dense films on substrates with complex features, such as narrow trenches, and to improve the electronic and optical properties of coating materials [60].

While HiPIMS processes produce high quality films, they also tend to suffer from slower deposition rates compared to DCMS processes by at least 20% [45]. This is in part due to the low duty cycle of HiPIMS pulses (i.e., the target is only active for a small fraction of the time), the back-attraction of metallic ions to the target, and the increased film density producing a lower effective film thickness [47]. Additionally, all PVD techniques are line-of-sight processes, making it more challenging to deposit uniform coatings on complex substrates.

2.4.2 Formation and measurement of residual stress in sputtered coatings

Residual stress is the stress left within a material in the absence of an external load after processing, such as heat treatment, welding, or coating deposition, has been completed. Residual stress is a crucial aspect of thin film deposition, as it can influence the mechanical properties, adhesion and durability of a coating [61]. In relation to coatings, residual stresses are typically thought of in the in-plane directions. Stress can be generated by both thermal (σ_{th}) and deposition-related (σ_{dep}) sources. There are also other microstructural sources (σ_{other}) of stress, such as voids or entrapped gases. The total stress state (σ_{tot}) is simply the sum of various stress contributions [61],

$$\sigma_{tot} = \sigma_{dep} + \sigma_{th} + \sigma_{other} \quad \text{(Eq. 2.5).}$$

Thermal stresses arise from dimensional changes of the coating and substrate during heating and cooling. The governing materials property is the coefficient of thermal expansion (α), which describes how the size of the materials changes with a change in temperature. The magnitude of thermal stress also depends on the elastic modulus (E_f) and Poisson's ratio (ν_f) of the film material. Thermal stresses most often arise during cooling after a elevated-temperature deposition process and can be calculated by,

$$\sigma_{th} = \frac{E_f}{(1-\nu_f)}(\alpha_f - \alpha_s)(T_d - T_0) \quad \text{(Eq. 2.6)}$$

where α_f and α_s are the coefficients of thermal expansion for the film and substrate, T_d is the deposition temperature, and T_0 is the reference temperature, usually 20 °C [61]. One should note that the thermal stress depends on the properties of the substrate and the deposition temperature, so if the same film is deposited on a different substrate material or at a different temperature, the magnitude of thermal stress will change. If the coefficient of thermal expansion of the film is greater than the substrate, σ_{th} will be > 0, indicating a tensile stress. In the opposite case, σ_{th} will be < 0, indicating a compressive stress.

Deposition-induced stresses arise from atomic processes occurring during film growth and can also be tensile or compressive in nature [61]. In coatings produced with DCMS processes, the deposition-induced stress tends to be tensile in nature. Researchers have associated this tensile stress with the coalescence of crystallites during film [62]. Because adatom mobility is low during DCMS deposition, small gaps tend to exist between growing crystallites, resulting in the incorporation of additional surface energy in the growing film. To reduce the surface free energy, it is favorable for the crystallites to coalesce to form grain boundaries. However, for this to occur, the crystals must stretch to close the gaps between crystallites, thus creating a tensile stress [62]. This process is illustrated in Figure 2.10a.

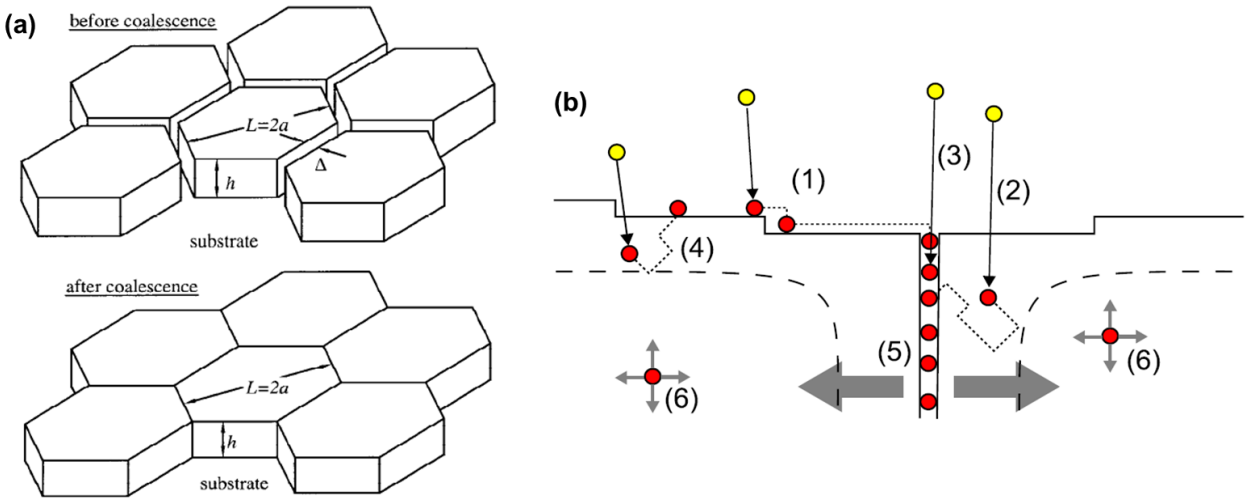

Figure 2.10: (a) Illustration of crystallite coalescence mechanism for tensile residual stress generation, primarily in DCMS coatings [62]; (b) Illustration of ion bombardment and grain boundary diffusion processes producing compressive residual stress primarily in HiPIMS coatings [63].

The effects of energetic HiPIMS deposition on residual stress have also been studied [63–66]. The two important differences from DCMS processes are the presence of more mobile adatoms and the momentum transfer of impinging ions to the surface layers of the growing film. During deposition, the surface of the film contains a supersaturation of adatoms, creating an excess chemical potential [66]. Because the adatoms are mobile, they can diffuse to areas of lower chemical potential, such as grain boundaries. This process is illustrated by position (1) in Figure 2.10b. The incorporation of these atoms into grain boundaries produces a force for the coating to expand to accommodate the extra volume. However, the coating is dimensionally constrained by the substrate and unable to expand, thus giving rise to compressive stress. Excess atoms can also be incorporated into the film via ion bombardment where impinging ions either are implanted directly into the coating or creating collision cascade resulting in the incorporation of surface atoms [63].

With a reasonable understanding of the mechanisms involved in residual stress generation in thin films, it is possible to identify the relationship between stress and incident ion energy. Figure

2.11 qualitatively shows how residual stress changes as a function of incident ion energy during deposition [64]. At low energy, adatoms have little mobility and there is minimal kinetic energy transferred to the film by the sputtered flux, and the residual stress is tensile due to the coalescence of crystallites. As ion energy increases, adatoms become more mobile and ballistic effects become more significant, and the stress transitions from tensile to compressive as excess atoms become incorporated into the film. However, above a certain energy threshold, the compressive effects start to get reduced as the thermal spikes generated by ion bombardment become large and promote stress relief [64].

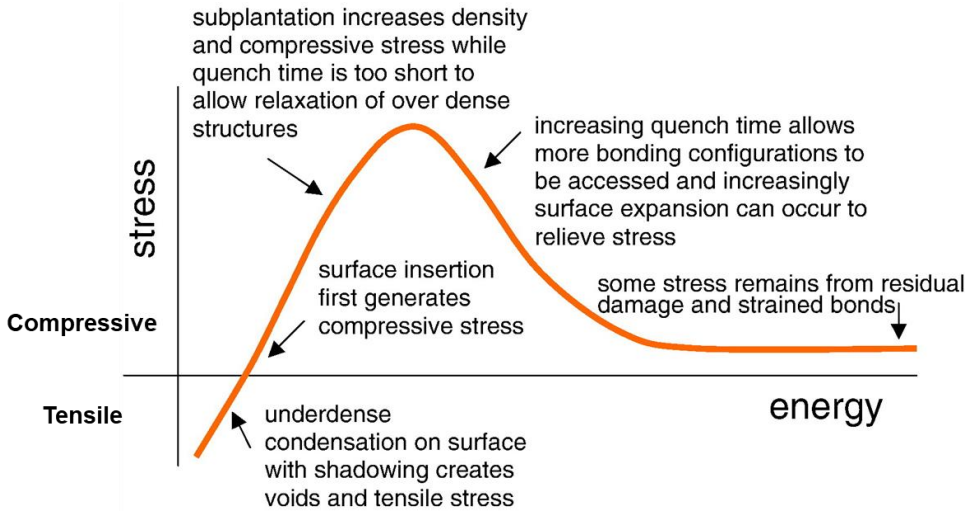

Figure 2.11: Qualitative plot describing the relationship between residual stress and incident ion energy during deposition, modified from [64].

The importance of residual stress on coating behavior has also led to the development of many techniques to measure stress. The earliest methods to determine residual stress of a film is the wafer curvature method which relates the deformation of the substrate to the film stress [61]. This technique is quite easy to perform but does not provide a full picture of the stress state and requires a specific substrate geometry. X-ray diffraction-based techniques are another extremely common stress measurement method, especially for thin films research. The analysis can be performed on a laboratory-scale diffractometer and involves manipulation of various goniometer axes to collect

data that can be processed to analyze the stress state [67]. The simplest diffraction method is called the $\sin^2\psi$ technique and assumes the stress is equally biaxial and the coating is randomly oriented [61]. Increasing levels of complexity can be added to account for stress states that vary through the coating thickness or coatings with a preferred orientation [67]. More sophisticated diffraction-based analysis of stress can be performed inside a synchrotron x-ray source which offers excellent spatial resolution for mapping of the residual stress [61]. Finally, focused ion beam (FIB) milling combined with digital image correlation (DIC) that involve a serial process of milling and image analysis have emerged as a way to probe stress gradients at the microscale [61].

2.5 Prior work on coated-SiC fuel cladding

The earliest development of coatings for SiC-SiC_f fuel cladding took place at Oak Ridge National Laboratory. A range of deposition processes and coating materials were investigated in the initial stages of this research [6]. A Zr coating was deposited using a thermal spray process but did not perform well in corrosion tests due to poor adhesion and the presence of impurity phases. An electroplating process was used to produce a chromium coating. However, the deposition of an interlayer was necessary to improve the conductivity of Cr and cracking occurred in the Cr deposits to due to large stresses generated during the coating process [7].

Metal-nitride and Cr coatings were deposited using cathodic arc PVD. Most of the coatings were initially well-adhered, although further characterization revealed that the coatings contained macroparticle defects, gaseous impurities, and tensile residual stresses, all of which are typical of cathodic arc coatings. Consequently, the coatings did not exhibit the desired performance in corrosion and irradiation experiments [9,11,13,14]. HiPIMS deposition of Cr was adopted to produce a coating with stronger adhesion and a compressive residual stress state [11]. However, a decrease in coating ductility was reported along with these other more desirable properties. To

combat this, the researchers deposited a dual-layer Cr coating using HiPIMS for the inner layer and cathodic arc deposition for the outer to produce a film with strong interfacial adhesion but a more compliant outer layer [11]. Lastly, it should also be noted that a limited number of helium leak tests were performed using the earlier generations of coatings, and results of these tests showed that the coatings may also be able to serve as a hermetic barrier to prevent the escape of fission gas from the cladding along with providing corrosion protection [6].

3. Experimental Methods

This section provides a basic overview of the experimental methods and characterization techniques used in this research. Specific details of these methods, including their application, analysis, and interpretation of data are presented in association with the sections discussing the results obtained from the application of these methods.

3.1 Substrate material

Most SiC-SiC_f cladding designs feature a monolithic CVD SiC outer layer to protect the underlying composite architecture from direct exposure to the water coolant [41]. For this reason, CVD SiC coupons were used as the substrate material for this study as it offers a realistic representation of the outer surface of the SiC-SiC_f cladding. The procured monolithic, high-resistivity, CVD SiC coupons with dimensions of 20 mm × 20 mm × 1 mm were manufactured by PremaTech Advanced Ceramics (MA, USA). The CVD SiC coupons possessed a cubic (zinc blende) crystal structure, also referred to as 3C-SiC or β-SiC [37]. The nominal purity of the material was >99.9995%. These uncoated coupons were used as control samples in autoclave testing and as substrates for coating processes. Prior to coating deposition, the SiC coupons were polished with a 15 µm diamond-embedded nickel disc resulting in a surface roughness (R_a) of about 150 nm and then cleaned ultrasonically with acetone and ethanol prior to coating deposition. The surface of the CVD SiC after the preparation process is shown in Figure 3.1.

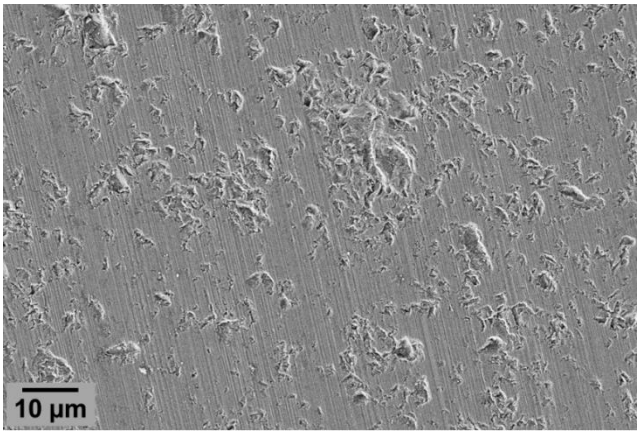

Figure 3.1: Plan-view SEM micrograph of the CVD SiC substrate after polishing.

X-ray photoelectron spectroscopy (XPS) depth profiling of the SiC substrate material was performed to understand the near-surface composition of the substrate that the coating material will encounter during the initial stages of deposition. A SiC coupon was prepared using the same procedure as was used to prepare samples prior to deposition. Depth profiling was conducted by sputtering the region to be analyzed with 2 keV Ar^+ ions in time steps of 10 seconds. In between each sputtering step, high resolution scans of the Si (~ 102 eV), C (~ 284 eV), and O (~ 533 eV) peaks were conducted. A total of 100 sputtering steps were performed. Select XPS spectra collected during depth profiling are shown in Figure 3.2.

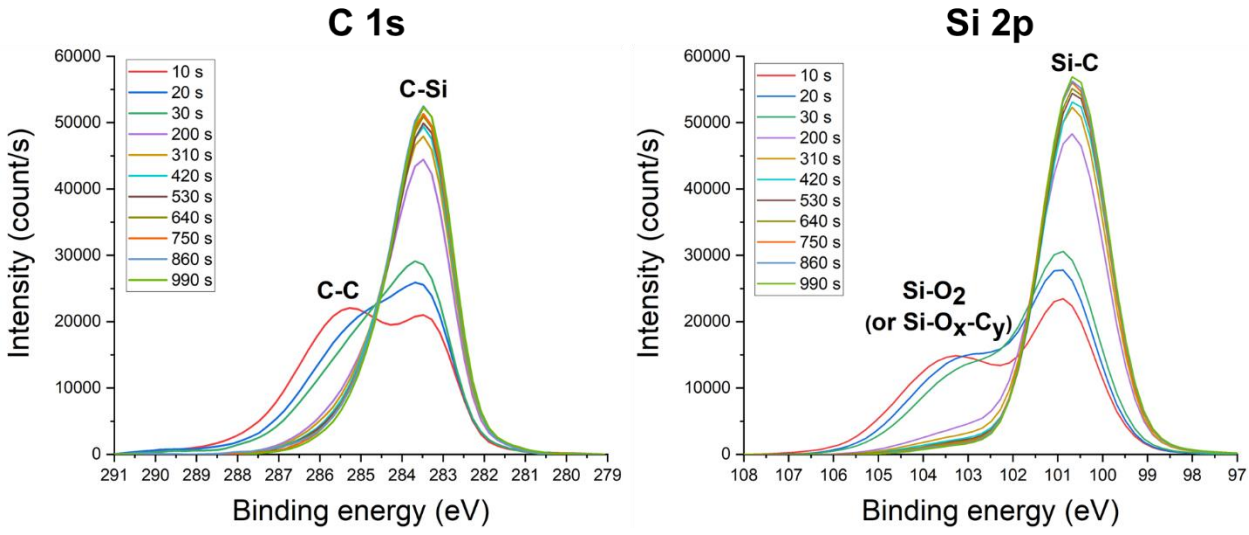

Figure 3.2: Scans of the C 1s and Si 2p peaks collected at different sputtering times during XPS depth profiling.

The XPS peaks were identified and deconvoluted using tabulated binding energy values [68] and previous XPS studies of SiC [69–71]. The initial scan taken before any etching of the surface was not included in Figure 3.2 due to the presence of adventitious carbon on the sample surface. This is a well-known occurrence in XPS, and the hydrocarbon layer was removed after 10 seconds of sputtering. In the early stages of depth profiling, peaks of equal intensity corresponding to C-C (graphite) and C-Si were observed. As sputtering progressed, the C-C peak diminished while the intensity of the C-Si peak increased. However, even at the final etching stage (990 seconds), some asymmetry was still present in the C 1s peak, suggesting that there is still some remaining C-C bonding in the material. In perfectly stoichiometric 3C-SiC, one C atom should be bonded to four Si atoms and vice-versa which would produce only a C-Si bonding peak. The presence of the minor C-C peak contributing to the C 1s spectra may indicate that there is a minor excess of C within the SiC. Free carbon within SiC has previously been reported depending on the CVD parameters and gaseous precursors used [72], and it is also a possibility that the enrichment of C tends to be most pronounced near the edges of the bulk materials, which is the region probed by XPS.

The most notable feature of the Si 2p spectra shown in Figure 3.2 is the presence of a peak corresponding to Si-O_2 or Si-O_x-C_y bonds. This peak can be attributed to the presence of a native oxide layer on the surface of the SiC coupon. The intensity of the peak rapidly diminished upon ion etching, and the peak completely disappeared after about 600 s of etching. The sputtering rate of SiO_2 with 2 keV Ar^+ ion has been reported to be about 2 nm/min [73], so the native oxide layer thickness is estimated as approximately 20 nm. Prior to deposition, the substrates were cleaned using either *in situ* plasma cleaning or ion milling inside the deposition vacuum chamber. Coating deposition was conducted immediately following the *in situ* cleaning without re-exposing the

substrates to atmospheric conditions. It is expected that much of the native oxide on the SiC substrates was removed during these cleaning processes.

3.2 Microstructural characterization and compositional analysis

Zeiss Gemini 450 and Zeiss LEO 1530 scanning electron microscopes (SEM) equipped with energy dispersive spectroscopy detectors (EDS) were used for general microstructural characterization of coatings, imaging of samples after mechanical testing (e.g., nanoindentation, scratch testing, microcantilever bending), and general compositional analysis of as-deposited coatings and corrosion-tested samples. A Bruker Icon atomic force microscope (AFM) in tapping mode was used for measurement of coating surface roughness and analysis of nanoindentation pile-up features. A Thermo Scientific K-Alpha x-ray photoelectron spectrometer (XPS) was used for analysis of near-surface composition and chemical bonding states. A spot size of 400 μm was used for all XPS scans. Full spectrum survey scans were collected using a pass energy of 200 eV. Higher resolution elemental peak scans were collected using a pass energy of 50 eV. XPS depth profiling was performed by repeatedly sputtering the surface with 2 keV Ar^+ followed by XPS data collection to gradually probe deeper into the sample.

Cross-sectional microstructural characterization was conducted using focused ion beam milling (FIB) on Zeiss Auriga and FEI Helios G4 dual-beam FIB-SEM instruments. The Auriga instrument uses a liquid metal ion source to produce Ga^+ ions for milling, while the Helios instrument is a plasma FIB operating with Xe^+ ions allowing for much higher milling currents. The typical incident ion energy on both instruments is 30 keV. Cross-sectional trenches were fabricated by tilting the specimen parallel to the ion beam column and removing material by milling with successively lower beam currents. This technique allows for examination of the coating microstructure, density, thickness, and bonding. FIB milling was also used to fabricate

microcantilevers for small-scale in situ mechanical testing. More details on this experiment are provided in Section 8.3.2.

3.3 Transmission electron microscopy

All steps necessary to fabricate thin foils for transmission electron microscopy (TEM) were performed on the (P)FIB instruments. Typically, the initial steps of TEM lamella preparation were conducted on Helios PFIB because it allows for faster milling rates. First, the MultiChem system was used to deposit a protective 3 µm thick carbon cap on top of the region of interest at an ion voltage and current of 12 kV and 100 pA. In the case of corrosion-tested or irradiated samples where protection of the near-surface region is crucial, the C cap deposition was preceded by deposition of a thin Pt layer using the electron beam at 5 kV and 6.4 nA. With the sample surface normal to the ion beam (52° sample tilt), rough ion milling steps at progressively lower currents of 60 nA, 15 nA, and 4 nA were used to remove enough material to allow for extraction of the lamella from the bulk sample. When the lamella thickness was approximately 2 µm, the sample was tilted back to 0° to undercut the lamella. A current of 4 nA was used to detach the sides and bottom of the lamella from the bulk sample. Using the EasyLift micromanipulator, the lamella was lifted out from the bulk sample and attached to a Cu grid using Pt welding for the final thinning steps. An image of a lamella welded to a Cu grid prior to thinning is shown in Figure 3.3a. The Cu grid was transferred to Zeiss Auriga FIB due to its better milling quality at lower currents. For thinning, the sample was tilted away from the ion beam by 1-2° to allow for more even milling. The thinning steps were performed with milling currents of 2 nA, 600 pA, 300 pA, and 140 pA at an accelerating voltage of 30 kV. The final cleaning step was conducted at 5 kV and 100 pA to make the sample electron transparent and remove surface damage that may have occurred during the higher energy milling steps. The transparency of the sample was monitored with the SE2

electron detector. The foil was deemed thin enough for TEM when the Cr layer became transparent when imaging with the electron beam at an accelerating voltage between 7–10 kV. SEM images of a representative TEM foil are shown in Figure 3.3b and Figure 3.3c.

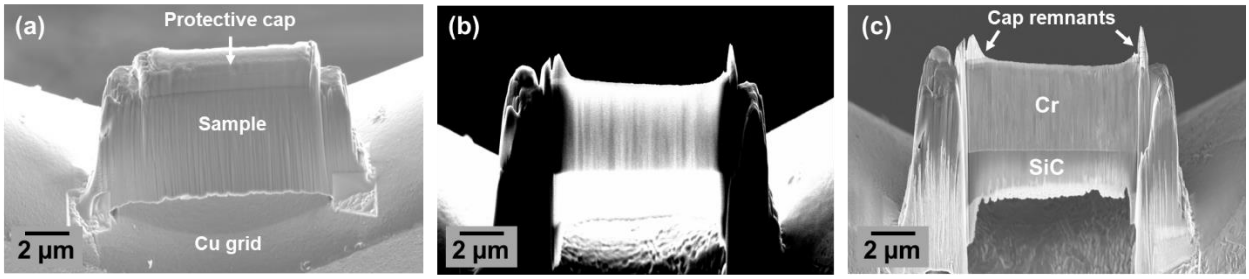

Figure 3.3: (a) TEM lamella lift-out from a PVD Cr-coated SiC attached to Cu grid; (b) Lamella showing electron transparency in the SE2 detector after thinning; (c) SEM image of the same lamella captures using the in-lens detector.

A FEI Tecnai TF30 field-emission TEM was used for conventional bright field (BF) and dark field (DF) TEM imaging using an accelerating voltage of 300 kV. High-resolution TEM (HRTEM) imaging was also performed to characterize nanoscale features, such as interfacial structures and oxide layers. Electron diffraction patterns were collected using both select area electron diffraction (SAED) and convergent beam electron diffraction (CBED) methods. The TEM-based ASTAR nanoscale orientation mapping system manufactured by NanoMegas (Brussels, Belgium) was used to collect orientation maps and generate pole figures for select coatings. The system operates by collecting electron diffraction patterns from a precessed nanobeam (i.e., a narrow, parallel electron beam) in a grid of predefined points within a region of interest and then indexes the patterns with respect to user-input crystal structures to determine the crystal orientation at each point [74]. A spatially resolved orientation map of the region of interest can then be constructed. A precession angle of 0.3° and step size of ~5 nm was used for all ASTAR measurements.

A FEI Titan 80-200 probe-corrected scanning TEM (STEM) was used for additional imaging and compositional analysis of samples. STEM images were collected in bright field (best

diffraction contrast) and high angle annular dark field (HAADF, best Z contrast) imaging modes. Compositional analysis was also conducted using STEM-EDS to collect quantitative chemical information at specific points or in line profiles across a region of interest. For EDS measurements, the sample was tilted by about 15° in the column toward the EDS detector to improve data acquisition. A dwell time of 10 seconds was used for point and line scans to collect enough signal to allow for analysis of the spectra.

3.4 X-ray diffraction and residual stress measurements

A Malvern Panalytical Empyrean diffractometer was used for x-ray diffraction (XRD) analysis of samples. The instrument is equipped with a Cu Kα source ($\lambda = 1.5406$ Å), parallel beam optics, and scanning line detector. 2θ patterns were collected in the range of 30–120° with a step size of 0.04°. After data collection, the background and Kα2 contribution were subtracted from the data. XRD patterns were collected from as-deposited samples to analyze texturing and qualitatively evaluate residual stresses and for phase analysis of samples after corrosion or high-temperature testing.

Residual stress measurements of coatings were performed using the $\sin^2\psi$ technique. This method is commonly used for stress analysis in thin films [67]. The residual stress is calculated by assuming a biaxial, elastic plane stress condition in the coating, meaning there is assumed to be no stress gradient through the coating thickness. One (*hkl*) diffraction peak is selected for analysis and is scanned at a range of ψ tilt angles. The angle ψ represents the off-axis tilt angle between the scattering vector (vector bisecting the angle between the x-ray source and detector) and the vector normal to the sample surface. By changing the ψ tilt angle, a different set of (*hkl*) planes is probed. Each set of (*hkl*) planes also possesses an interplanar d-spacing that has been altered to some degree by the presence of residual stress. The stress can be calculated by analyzing the linear relationship

between d-spacing and the tilt angle as a function of $\sin^2\psi$ [75]. The relationship connecting the residual stress, d-spacing, and ψ angle is:

$$\sigma = \left(\frac{E}{1+\nu}\right)\frac{1}{d_0}\left(\frac{\partial d_\psi}{\partial \sin^2\psi}\right) \quad \text{(Eq. 3.1)}$$

where E is the elastic modulus, ν is Poisson's ratio, d_0 is the stress-free interplanar spacing (determined from the intercept of the linear fitting), and $\partial d_\psi/\partial \sin^2\psi$ is the slope of the linear fit.

The (211) bcc Cr diffraction peak at $2\theta = 81.7°$ was selected for residual stress analysis. While a high-angle diffraction peak ($2\theta > 100°$) is preferred as it is more sensitive to d-spacing changes, it can be challenging to collect enough diffracted intensity from high-angle peaks to allow for reliable peak fitting, especially when a preferred orientation is present within the sample. The Cr (211) peak was scanned across a 4° range centered at 81.7° with a step size of 0.04°. The (211) peak was scanned at a series of eight different ψ tilt angles evenly spaced on a $\sin^2\psi$ scale between 0–0.35. Similar to the full range XRD scans, the background and Kα2 contribution were removed from the data prior to analysis. A commercial data analysis software (Origin) was used to fit a pseudo-Voigt function to the experimental peaks. The elastic modulus value used for the stress calculation was determined via nanoindentation for each sample [76], and a Poisson's ratio of 0.21 was used for Cr [77].

3.5 Mechanical test methods

The mechanical testing techniques applied in this work span multiple length scales including macroscale scratch testing, nanoindentation, and *in situ* microcantilever bending. Description of experimental details for these methods are provided in the corresponding chapters. A Bruker TI-950 Triboindenter was used to conduct nanoindentation testing of the coating materials. A diamond Berkovich probe was used for indentation testing. A polycarbonate sample was used to align the indenter probe under the optical microscope attached to the instrument. The indenter area

function was calibrated with a fused quartz standard sample. The instrument was equipped with low load, high load, and lateral force transducers. Typical indents were performed in load-controlled mode with a constant loading rate load function in quasistatic mode. The hardness and elastic modulus were determined using the Oliver-Pharr method [78]. In some cases, the continuous stiffness measurement (CSM) technique [79] was used for hardness depth profiling and to minimize the effects of thermal drift during indentation creep tests. More details on the nanoindentation measurements, calculations, and characterization are given in the relevant sections.

3.6 Simulation of radiation damage and ion beam mixing

The Stopping and Range of Ions in Matter (SRIM) 2013 software package was used to simulate the effect of radiation damage on the Cr/SiC coating-substrate system and determine the depth of implantation for incident energetic ions [80]. The average number of displacements per atom (dpa) caused by irradiation was calculated using the procedure developed by Stoller et al. and the phonon.txt output file from SRIM and [81]. Threshold displacement energies of 40 eV, 35 eV, and 21 eV were used for Cr, Si, and C, respectively [82,83]. The SRIM interface was used to create a Cr/SiC two-layer system when necessary. SRIM uses the binary collision approximation [84] to model collision cascades and assumes the target material is amorphous and at a temperature of 0 K.

Version 6.10 of the SDTrimSP software package [85], implemented with the help of the graphical user interface developed by Szabo et al. [86], was used to simulate the atomic mixing generated between Cr and SiC. The program was employed to model atomic mixing under low energy irradiation, such as during coating deposition, and high energy ion irradiation. SDTrimSP operates using the same underlying physics and assumption as SRIM [85]. However, the use of

SDTrimSP rather than SRIM was preferred for ion beam mixing simulations due to the capability of SDTrimSP to run dynamic simulations which take into account continual changes in target material composition throughout the course of the simulation rather than the static target composition employed in SRIM [87]. SDTrimSP monitors the extent of atomic displacement generated by a user-input number of incident ions, and then updates the target composition for the next round of incident ions, allowing the dynamic simulation of ion mixing. The KrC interaction potential [88] and Ziegler-Biersack [89] inelastic loss model were used for all atoms and collisions in the simulations. For both SRIM and SDTrimSP simulations, whenever SiC was used as a target material, the atomic densities of Si and C were set to match that of the SiC compound rather than an equiatomic mixture of elemental Si and elemental C.

4. Understanding Deposition Mechanisms in Magnetron Sputtered Coatings

This chapter features direct content from the following journal articles first-authored by the PhD candidate:

K. Quillin, H. Yeom, T. Dabney, E. Willing, K. Sridharan, "Microstructural and nanomechanical studies of PVD Cr coatings on SiC for LWR fuel cladding applications," *Surface and Coatings Technology* 441 (2022) 128577.

K. Quillin et al., "Effects of energetic deposition on the nanoscale interfacial features of magnetron sputtered Cr coatings on SiC," *Journal of Applied Physics* (2024), in preparation.

4.1 Selection of coating materials and deposition processes

Multiple criteria were considered during the coating material selection process. First, the material must form a thin protective surface oxide layer in high temperature water in order to provide the necessary hydrothermal corrosion resistance. In other words, the material should have a large passivating region in the Pourbaix diagram and exhibit slow logarithmic growth kinetics. The formation of a passivating oxide on the coating surface ensures that the coating can remain protective for the underlying SiC cladding. Some metals and alloys known to form stable oxides in high temperature water include stainless steels, Ni superalloys, Cr, and Zr [15]. From a mechanical stability standpoint, it is desirable for the coating material to have a similar coefficient of thermal expansion to that of SiC (~ 4.0×10^{-6}/K) [31] to minimize thermal stress that is generated during elevated temperature exposure [90] in order to maintain mechanical integrity of the coating. Additionally, the ability to deform in a ductile manner is also desirable. Under irradiation, SiC swells via the formation and clustering of point defects [37]. The swelling of the SiC cladding tube will impart a tensile stress on a coating present on its outer surface. Therefore, the coating must be able to deform plastically without cracking that could lead to catastrophic

failure and delamination of the coating. This criterion likely precludes most ceramic coating materials which tend to fail in a brittle manner [9].

With the above points in mind, pure Cr was selected as the primary coating material for investigation. During initial screening studies, deposition of other coating materials (e.g., CrN, Cr-carbides, Zr, Y) was also investigated, but Cr was identified as the most promising candidate. The investigation of other these other coating materials is described in Appendix A. It is well known that Cr forms Cr_2O_3, a very stable passivating oxide, in most oxidative environments [13]. The coefficient of thermal expansion of Cr is about 6.0×10^{-6}/K [91], closer to that of SiC than many other metals. Also, as a metal, Cr has some ability to deform plastically in contrast with for example, Cr-based ceramics, such as CrN, Cr-carbides, and Cr-oxides. Lastly, Cr has been studied extensively for use as accident tolerant, oxidation resistant coating material for existing Zr-alloy fuel cladding and has performed quite well from standpoints of both corrosion and mechanical behavior [92,93].

In addition to the coating material, selection of the deposition process is also crucial. The deposition process must be able to produce a coating with a uniform thickness and homogenous microstructure. Additionally, the deposition process must be able to produce a coating that adheres to SiC substrate material (a relatively uncommon substrate for PVD coatings) and must be capable of depositing on cylindrical substrates for eventual deposition on cladding tubes in a cost-effective manner. Many deposition processes were initially investigated, including cold spray deposition, magnetron sputtering, cathodic arc vapor deposition, and a chromizing surface treatment. More details on the coatings produced with these processes are described in Appendix A. Magnetron sputtering emerged as the most promising deposition technique. Magnetron sputtering offers the

ability to tailor coating microstructure by varying many process parameters, produces uniform coatings with minimal defects, and has the potential to deposit films that are adherent to SiC.

4.2 First generation of magnetron sputtered Cr coatings

4.2.1 Coating deposition parameters

Sputtered coatings were deposited on one side of the CVD SiC substrates in collaboration with commercial coating Vendor I. Supplier names have been excluded from this document to protect intellectual property and remain neutral with respect to the performance of different coatings and deposition processes. Pure Cr coatings were produced with a conventional DCMS process and with an advanced HiPIMS process. Prior to deposition, an *in situ* plasma cleaning process was performed to remove organic surface contaminants and any native oxide layer present on the SiC substrates. The DCMS deposition was conducted with an argon pressure of 0.3 Pa. The substrates were biased to -100 V and heated to 120 °C. The power density for the DCMS process was 11.6 W/cm^2. The HiPIMS deposition was performed at an argon pressure of 0.5 Pa. The substrates were biased to -20 V, and the deposition process was conducted at room temperature. The peak HiPIMS power density was 605 W/cm^2 with a duty cycle of 1.8% and pulse frequency of 95 Hz.

4.2.2 Structural analysis of coatings

Figure 4.1 presents results of characterization of the as-deposited DCMS Cr and HiPIMS Cr coatings. The surface of the DCMS coating was matte in appearance (Figure 4.1a). The surface morphology of the DCMS Cr coating is shown in Figure 4.1b. The coating is comprised of fine, pyramidal grains which are typical of the DCMS process. The fibrous growth structure of the film, which typically occurs during deposition under conditions of low homologous temperature and limited adatom surface mobility, can be observed in the FIB-milled cross section in Figure 4.1c. In addition, there is inherent surface roughness caused by the magnetron sputter process, and the

microstructure does not appear to be fully dense. The thickness of the S-DCMS coating was measured to be about 5 µm.

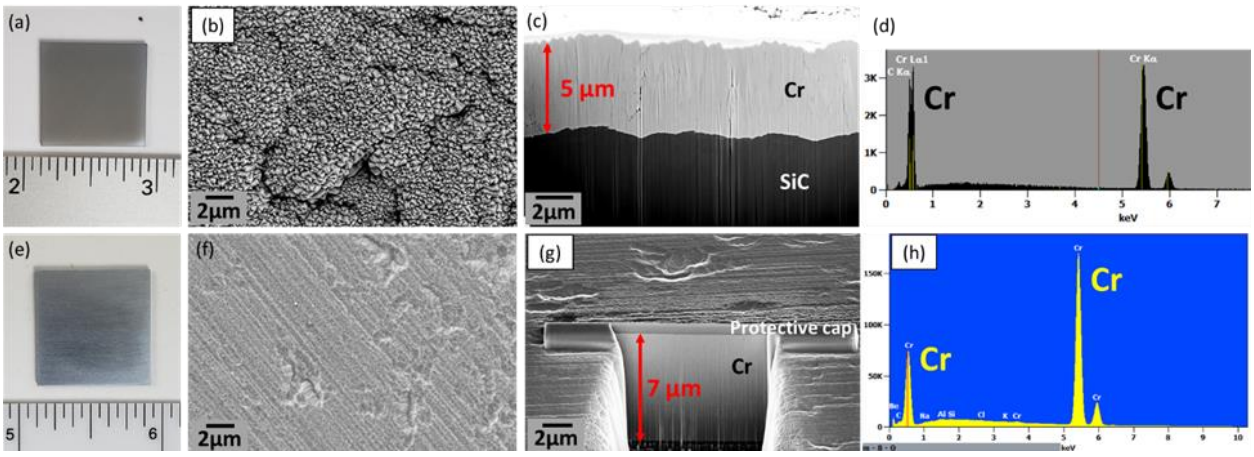

Figure 4.1: Photographs, plan-view surface SEM micrographs, cross-sectional trenches prepared with FIB milling, and EDS spectra for: (a-d) as-deposited S-DCMS Cr showing rough surface and columnar microstructure; (e-h) as-deposited HiPIMS Cr showing the smooth surface and densified microstructure.

Visual inspection of the HiPIMS Cr coating shown in Figure 4.1e revealed a smoother and more reflective surface appearance. This was corroborated by SEM imaging of the surface (Figure 4.1f). The smooth surface morphology is a result of the high-energy ion bombardment during deposition caused by the high-power pulses in the HiPIMS process. The FIB-milled cross-sectional image of HiPIMS Cr coating in Figure 4.1g shows a denser and more structurally homogeneous coating. The coating is slightly thicker than the S-DCMS coating, and approximately 7 µm in thickness. The elemental purity of both types of Cr coatings were confirmed via the EDS spectra shown in Figure 4.1d and h.

STEM imaging of the coatings provides a high-resolution view of the differing microstructures. The columnar microstructure of the DCMS Cr coating is clearly evident in Figure 4.2a. In Figure 4.2b, high-magnification STEM imaging confirms the presence of porous intercolumnar regions. The grain structure of the HiPIMS coating is also columnar but is completely dense with no porous intercolumnar defects (Figure 4.2c). In addition, the columnar

microstructure of the DCMS coating shows some directionality of the columns which are likely oriented towards the direction of the oncoming sputtered flux, while the HiPIMS structure is more coherently arranged perpendicular to the substrate [54]. Based on the traditional structure zone models, these coatings lie in Zone 1 where adatom mobility is low and an abundance of nucleation sites leads to the growth of vertical columnar structures [94]. However, these structure models do not account for increased ion energies encountered in the HiPIMS process. An updated structure zone model from Anders [57] would place the HiPIMS coating in Zone T by accounting for the densification caused by the increased ion energies and also allows one to predict the compressive stress state of the coating, which is addressed in the next section.

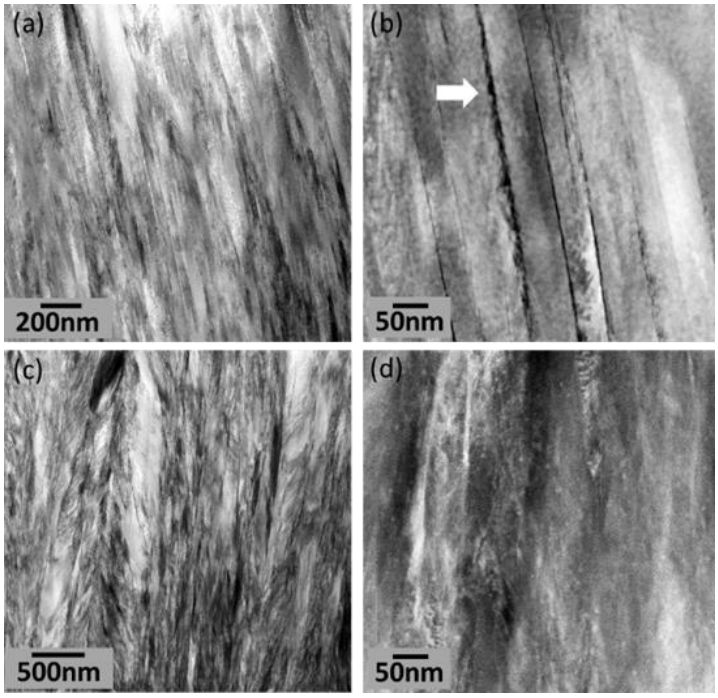

Figure 4.2: (a) Low magnification BF-STEM image and (b) high magnification HAADF-STEM image of the DCMS Cr coating indicating the presence of columnar grains with nanoscale intercolumnar channels; (c) Low magnification BF-STEM image and (d) high magnification HAADF-STEM image of the HiPIMS Cr coating showing the absence of intercolumnar channels.

4.2.3 X-ray diffraction analysis of texture and residual stress

The XRD patterns shown in Figure 4.3 confirmed the pure Cr bcc phase for the coatings. The diffraction pattern from an annealed bulk Cr sample is included as a reference for peak locations and relative intensities. The DCMS coating diffraction pattern shows additional peaks corresponding to the SiC substrate due to the slightly lower thickness and density of the coating allowing X-rays to penetrate through the entire coating thickness. Due to the low atomic mobility inherent to DCMS deposition, the resulting coating does not show a strong preferred orientation because deposited atoms lack the energy required for reconfiguration to a preferred orientation. Also, the substrate heating temperature for the DCMS deposition (120 °C) was low relative to the melting point of Cr (1900 °C), which further limits the mobility of adatoms. The HiPIMS Cr coating exhibited a (110) preferred orientation. As has been previously reported, the (110) orientation is favored due to the surface energy minimization of the closest-packed (110) plane in the bcc structure [95]. The ionization of sputtered atoms produced during HiPIMS deposition provides atoms with enough mobility to grow in an energetically favorable orientation [96].

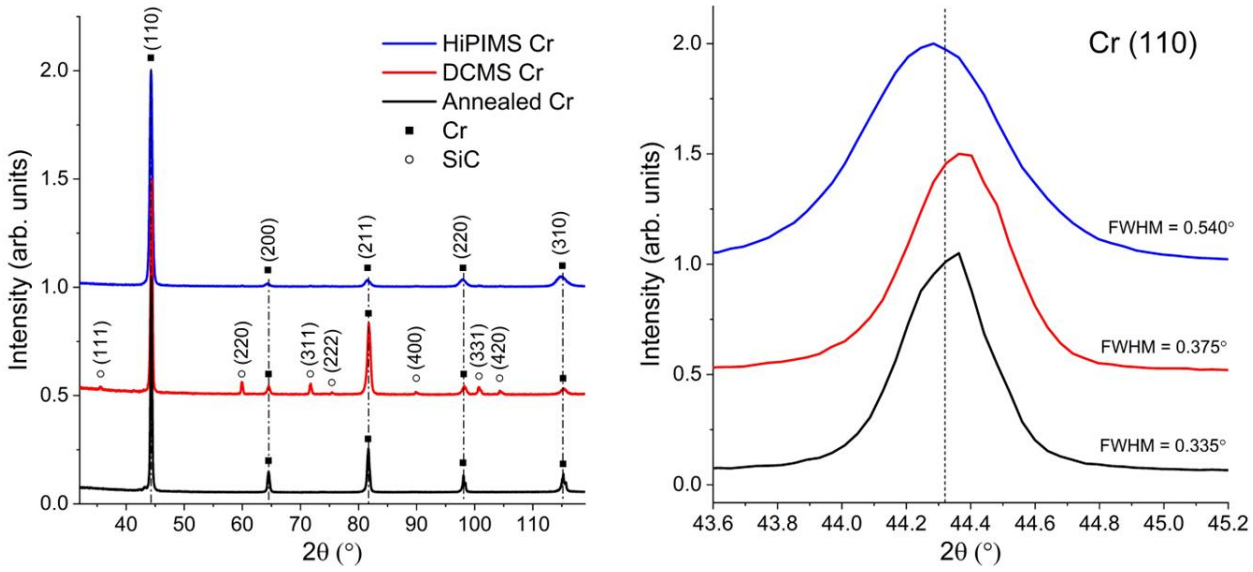

Figure 4.3: XRD patterns of annealed bulk Cr, and DCMS and HiPIMS coatings and enlarged view of the (110) peaks with measured FWHM values.

Analysis of peak shifting provides insight on the stress state of the coatings, assuming that the residual stress is uniform throughout the coating. Closer examination of the (110) peak of the diffraction patterns indicates a peak shift to a lower angle for the HiPIMS coating compared to that of the stress-relieved annealed sample. Other studies also reported a similar result [58,97]. The peak shift to a lower angle can be explained by the compressive stress induced by the HiPIMS process causing the out-of-plane lattice parameter to increase, which is manifested by a peak shift to a lower angle. On the other hand, a very slight shift to a higher angle was observed for the DCMS peak, indicating the coating is under a tensile stress, which is expected for conventionally sputtered Cr coatings deposited with argon pressures ranging from 0.4-1.3 Pa at low substrate temperatures [98]. These stresses were quantified by applying the $\sin^2\psi$ technique. A residual stress of 200 MPa (tensile) and -1050 MPa (compressive) were measured in the DCMS and HiPIMS coatings, respectively.

4.3 Second generation of magnetron sputtered Cr coatings

4.3.1 Coating deposition parameters

Based on the characterization and performance of the DCMS Cr and HiPIMS Cr coatings produced by Vendor I, a second generation of Cr coatings were deposited on CVD SiC in collaboration with commercial coating Vendor II to expand the scope of investigated deposition processes and parameters. Supplier names have been excluded from this document to protect intellectual property and remain neutral with respect to the performance of different coatings and deposition processes. Six different magnetron sputtering processes were used to deposit Cr coatings on one major face of the SiC substrates. The base pressure was 2.7×10^{-4} Pa for all deposition processes. Prior to deposition, substrates were cleaned *in situ* via ion milling with argon ions at 200 eV and a current of 2 A for five minutes to remove surface contaminants. The diameter

of the magnetron was 50 mm, and the target-to-substrate distance was 127 mm. During coating deposition, substrates were heated to 250 °C and continuously rotated. The substrates were actively grounded for all deposition processes.

Four types of DCMS Cr coatings were deposited: (i) standard DCMS, (ii) pulsed DCMS, (iii) ion-assisted DCMS, and (iv) pulsed ion-assisted DCMS. A Trumpf Huttinger TruPlasma DC 4002 power supply was used to control the voltage applied to the sputter target for all DCMS processes. The pulsed DCMS method used in this work was an asymmetric bipolar pulsed process where polarity of the sputter target was reversed from negative to positive during the pulses, but the magnitude of the reverse pulse voltage was not equal to the negative operating voltage. During ion-assisted deposition, the substrates were continuously bombarded with 100 eV argon ions generated by a Kaufman & Robinson Inc. eH400 ion source, while the target voltage characteristics were identical to the parameters used for standard DCMS deposition. The pulsed ion-assisted deposition method simultaneously incorporated the pulsed target voltage and ion bombardment of the substrate to obtain the synergistic effects of the pulsed and ion-assisted processes. The power density for all DCMS processes was 12.4 W/cm^2. The relevant parameters for these depositions are summarized in Table 4.1 along with the resulting coating thickness and surface roughness.

Table 4.1: Deposition parameters for DCMS processes and resultant coating thickness and surface roughness.

Process	ID	Working pressure (Pa)	Pulse frequency (kHz)	Reverse voltage (V)	Reverse pulse width (µs)	Ion discharge voltage (V)	Ion discharge current (A)	Deposition rate (µm/h)	Coating thickness (µm)	Ra (nm)
Standard DCMS	S-DCMS	0.40	–	–	–	–	–	3.24	5.6	108
Pulsed DCMS	P-DCMS	0.40	50	80	3	–	–	3.07	5.3	31
Ion-assisted DCMS	I-DCMS	0.13	–	–	–	100	0.5	2.73	4.7	58
Pulsed ion-assisted DCMS	PI-DCMS	0.13	50	80	3	100	3.5	3.23	7.0	39

Cr coatings were also deposited on SiC substrates using HiPIMS and bipolar HiPIMS processes, and the deposition parameters are summarized in Table 4.2. To differentiate this HiPIMS coating from the HiPIMS coating produced by Vendor I, the HiPIMS coating from Vendor II is identified as HiPIMS(II) in the text and figures. A Magna-Power SL1000-6/208 power supply was used to control the voltage pulses in the HiPIMS processes. It is noted that a slightly higher working pressure was required for HiPIMS processes to maintain stability of the plasma. The average power density during deposition was identical to the DCMS power density (12.4 W/cm^2). The duty cycle of the negative HiPIMS pulses was 1.3%. During bipolar HiPIMS deposition, the positive pulses were delayed from the negative pulses by 15 µs.

Table 4.2: Deposition parameters for HiPIMS processes and resultant thickness and surface roughness.

Process	ID	Working pressure (Pa)	Pulse frequency (Hz)	Peak voltage (V)	Peak current (A)	Pulse width (µs)	Reverse voltage (V)	Reverse pulse width (µs)	Deposition rate (µm/h)	Coating thickness (µm)	Ra (nm)
HiPIMS	HiPIMS(II)	0.93	150	1000	55	85	--	--	0.80	6.2	76
Bipolar HiPIMS	B-HiPIMS	0.93	150	1000	50	85	150	2000	0.50	4.3	44

4.3.2 Micro- and nano-structural features of coatings

Plan-view and cross-sectional SEM images of the four types of DCMS Cr coatings are shown in Figure 4.4. All coatings exhibited columnar growth typical of sputter deposition processes, but different grain morphologies depending on the process used to deposit the coating. Cross-sectional BF TEM images taken from the central region of each coating are presented in Figure 4.5 and show the relative grain size and porosity content for each type of coating. In the TEM images, the porosity appears as bright narrow streaks running parallel to the growth direction and is indicated by white arrows. The S-DCMS coating showed a typical DCMS surface morphology consisting of fine, fibrous growth features separated by narrow regions of intercolumnar porosity and a rougher surface compared to the other DCMS coatings. In the P-DCMS coating, the columnar

grains become more elongated and coarser in size as can be seen in the surface and the cross-sectional images. There was still some degree of nanoscale porosity separating the columnar growth features in the P-DCMS coating as shown in Figure 4.5b.

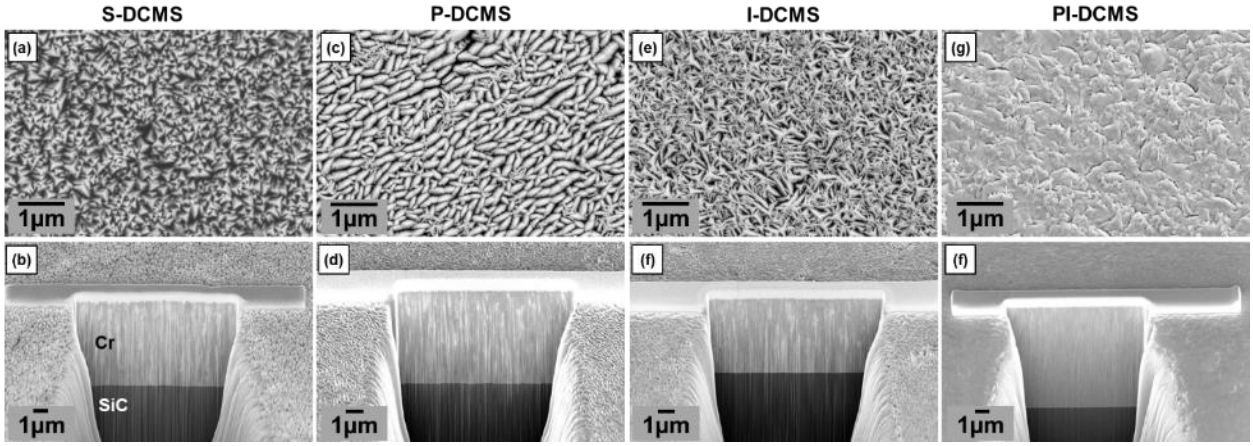

Figure 4.4: Plan-view and cross-sectional SEM images of the (a, b) S-DCMS, (c, d) P-DCMS, (e, f) I-DCMS, and (g, h) PI-DCMS coatings.

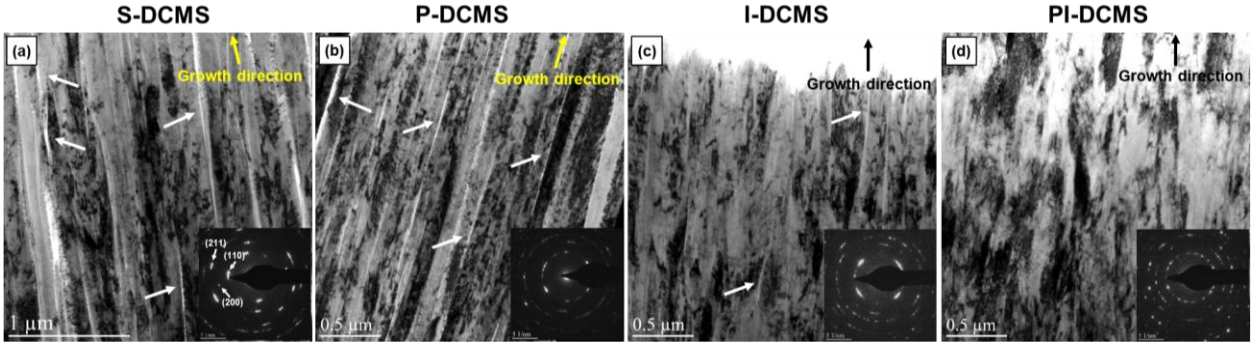

Figure 4.5: BF TEM images and SAED patterns (inset) of the (a) S-DCMS, (b) P-DCMS, (c) I-DCMS, and (d) PI-DCMS coatings. Images were taken from the central region of each coating. Arrows indicate the presence of intercolumnar porosity.

The surface morphology of the I-DCMS coating was similar to that of the S-DCMS coating, but with a more compacted appearance and a dispersion of fine pyramidal structures (Figure 4.4e). The size of the columnar structures in the I-DCMS coating were also comparable to the S-DCMS coating but the nanoscale porosity content was lower. Finally, in the PI-DCMS coating, individual columnar structures were not visible in the plan-view SEM image (Figure 4.4g). Measurements of the porosity level via image analysis is complicated by the diffraction contrast present in the bright

field TEM images, spatial variations in sample thickness, and the presence of curtaining artifacts produced during preparation of the TEM specimens by FIB milling. However, the measurements suggest that the porosity content of the coatings is less than 1.5%.

The cross-sectional TEM image of the PI-DCMS coating (Figure 4.5d) shows that the widths of the columnar structures are much larger than those of the other types of DCMS coatings. The PI-DCMS coating seemed fully dense and devoid of any intercolumnar porosity. Furthermore, high magnification TEM images showed the substructure within the columnar grains of the S-DCMS, P-DCMS, and I-DCMS coatings. Each column consists of a feather-like structure containing a central core and numerous crystallites protruding from the core at an angle, similar to a dendritic structure that form during solidification [99,100]. These feather-like substructures were not observed in the high-density PI-DCMS coating.

The plan-view and cross-sectional SEM images in Figure 4.6 show the surface morphology and microstructure of the HiPIMS and B-HiPIMS coatings. The surface morphology of the HiPIMS coating closely resembled the I-DCMS coating with the addition of star-shaped islands dispersed throughout the surface. The HiPIMS coating exhibited very fine growth morphology including the feather-like crystallites. The surface morphology of the B-HiPIMS coating was distinct from any of the other types of coatings. The as-deposited surface was smooth without discrete columnar features or island formations.

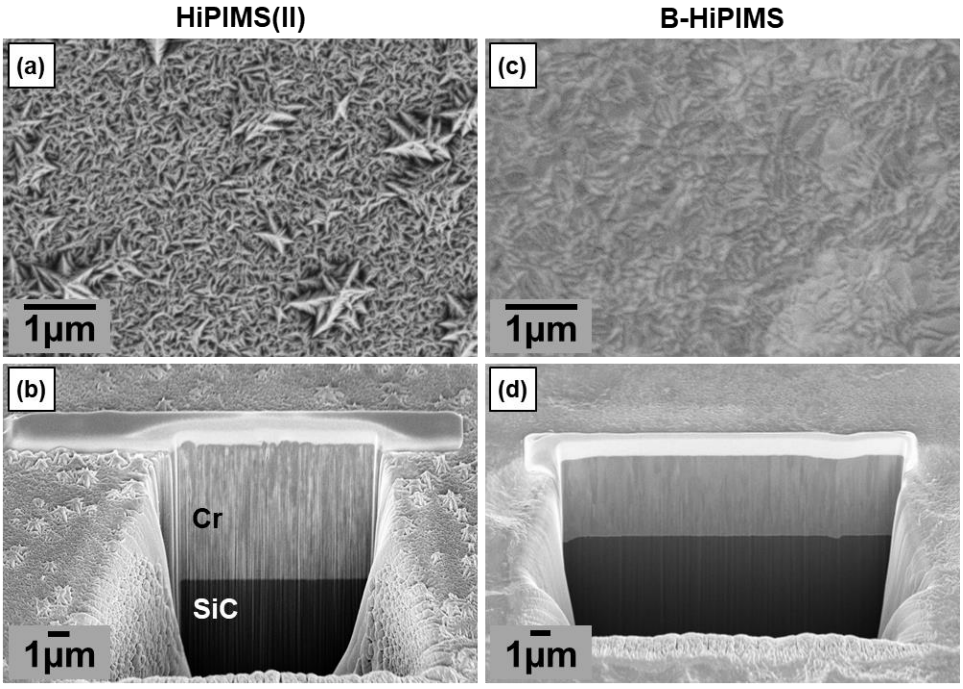

Figure 4.6: Plan-view and cross-sectional SEM images of the (a, b) HiPIMS and (c, d) B-HiPIMS coatings.

TEM imaging of the HiPIMS(II) coating (Figure 4.7a) revealed the coating to contain fine grains with intercolumnar porosity, which is atypical of coatings deposited with HiPIMS. For the B-HiPIMS coating, TEM imaging (Figure 4.7b) showed that the coating is fully dense with larger grains relative to the other coating types. The large grains comprising the B-HiPIMS microstructure are further illustrated by the DF TEM images in Figure 4.8, where it can be seen that the many of the large grains (~ 500 nm width × 4 µm length) grow continuously through the entire coating thickness, whereas the grains within the S-DCMS coating were fine with a higher aspect ratio (~ 150 nm width × 2 µm). The DF TEM images also show that in both DCMS and HiPIMS coatings, finer grains are present near the interface originating from numerous nucleation sites on the substrate surface and eventually coarsening through competitive growth as deposition progresses.

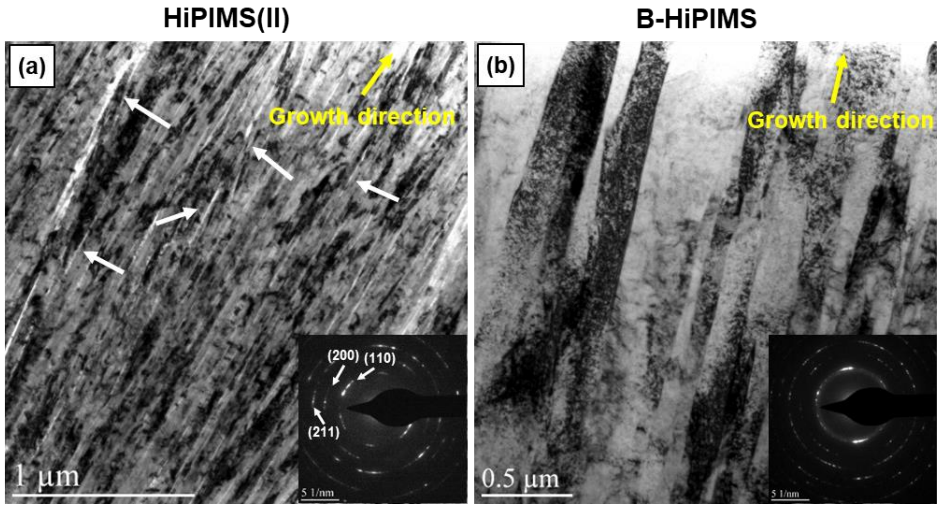

Figure 4.7: BF TEM images and SAED patterns (inset) of the (a) HiPIMS and (b) B-HiPIMS coatings. Images were taken from the central region of each coating. Arrows indicate the presence of intercolumnar porosity.

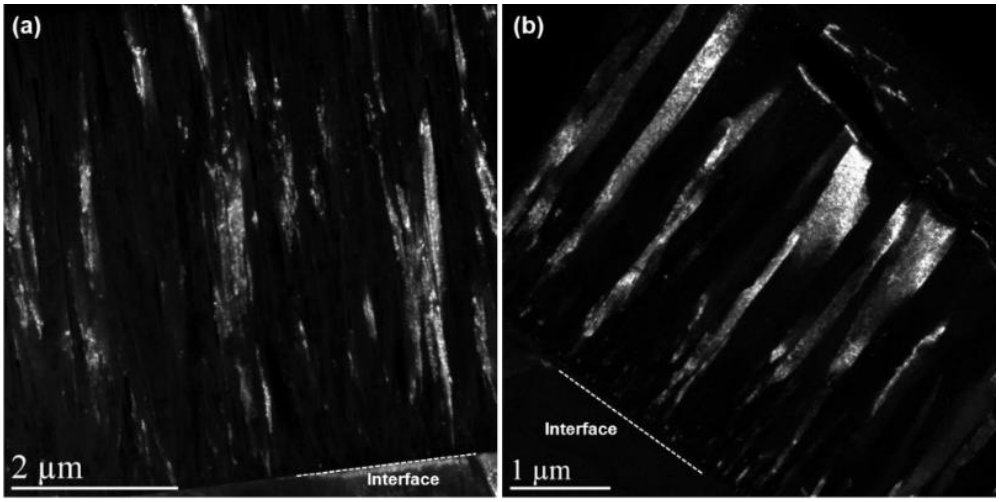

Figure 4.8: DF TEM images with a {110} reflection illuminated showing the differences in grain size between the (a) S-DCMS and (b) B-HiPIMS coatings.

The surface roughness of the six Cr coatings produced in collaboration with Vendor II was measured using AFM. The surface roughness averaged over three AFM scans from an area of 150 µm × 150 µm for the six coatings and uncoated SiC is shown in Figure 4.9. Surface roughness of a coating can be an important parameter for tribological and heat transfer considerations. As expected, the S-DCMS process produces the roughest surface due to the presence of many surface asperities. The lack of adatom mobility generated during S-DCMS deposition produces a coating

that grows conformally to the substrate surface. The other deposition processes, all which have varying degrees of ion bombardment or atomic mobility, produce smoother surfaces, with R_a values of about 50 nm. The densification and surface diffusion that occur under these conditions reduce the effects of the underlying substrate on the surface roughness of the film.

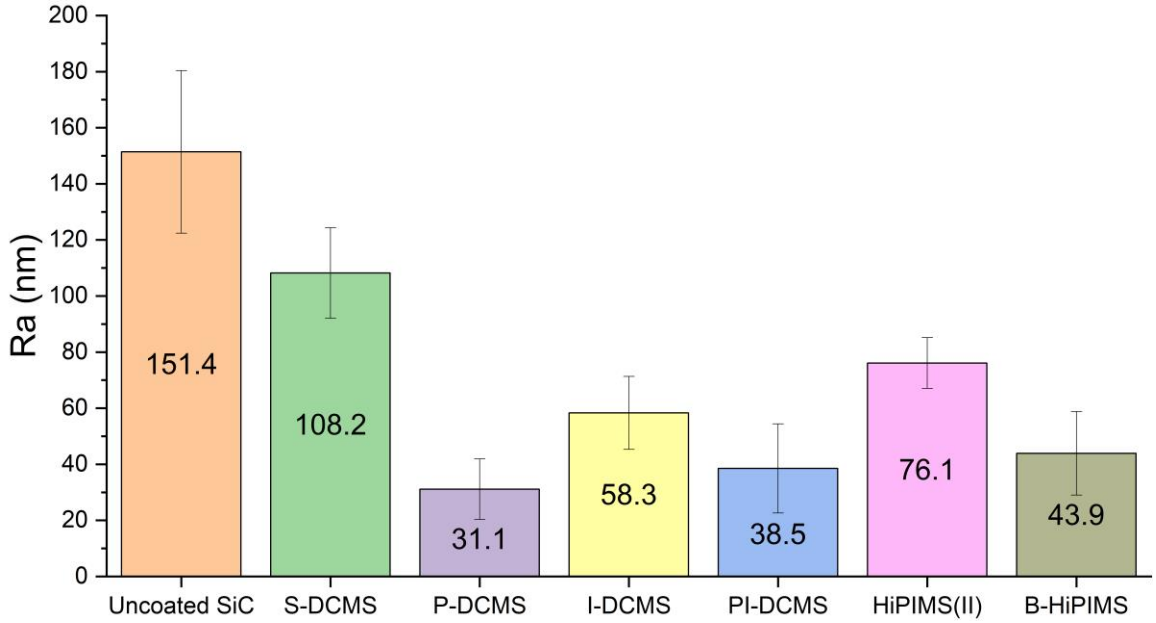

Figure 4.9: Surface roughness (R_a) of the six Cr coatings produced in collaboration with Vendor II compared to the uncoated SiC substrate.

4.3.3 Analysis of coating texture and residual stress

XRD patterns from the six coatings deposited by Vendor II are shown in Figure 4.10a. For three of the coatings (S-DCMS, I-DCMS, HiPIMS(II)), the strongest observed diffraction peak originated from the SiC substrate rather than the Cr coating. In general, these coatings exhibited a slight (211) texture. It was observed that the P-DCMS and B-HiPIMS coatings demonstrate a strong (110) texture, while the PI-DCMS coating exhibited a more random orientation distribution. The texturing of the B-HiPIMS coating can also be visualized via the orientation map (Figure 4.10b) illustrating that most of the grains favor a (110) orientation with respect to the growth

direction of the coating. Texturing is confirmed via the pole figures in Figure 4.10c showing high intensity of (110) planes aligned along the growth direction.

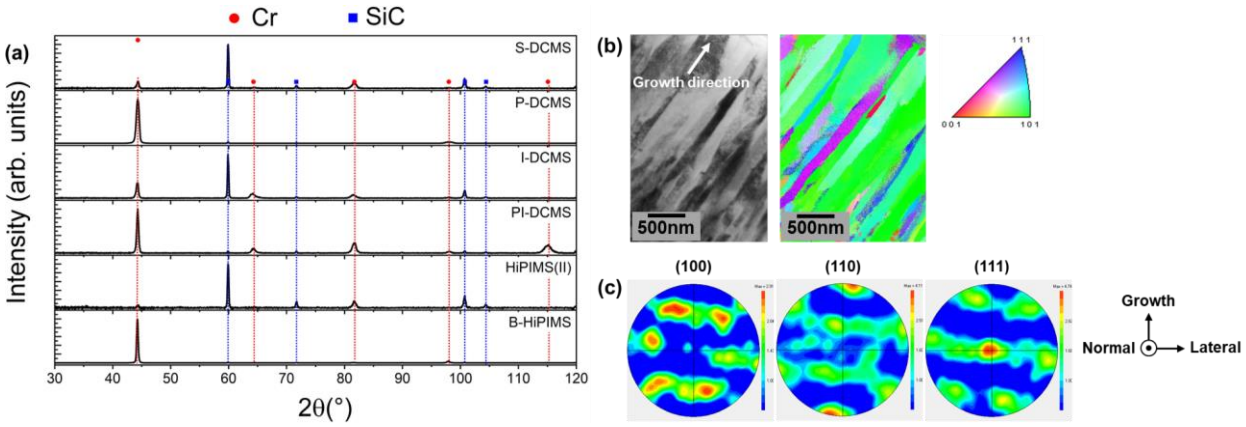

Figure 4.10: (a) XRD patterns of the six Cr coatings produced in collaboration with Vendor II; (b) Virtual BF STEM image and inverse pole figure map from the B-HiPIMS coating; (c) Pole figures from the B-HiPIMS coating.

The residual stress of the six coatings produced by Vendor II was measured using the $\sin^2\psi$ technique. Example plots of d-spacing vs. $\sin^2\psi$ are shown in Figure 4.11. For the B-HiPIMS coating, the analysis technique produced ideal results with a good linear fit. The plot of d-spacing vs. $\sin^2\psi$ for the I-DCMS coating exhibited significant non-linear behavior. The strong non-linearity indicates that the assumption of biaxial stress state for the XRD residual stress measurement technique is not valid. It is believed that there were strong local stress gradients through the coating thickness. As the ψ tilt angle is varied at each measurement step, the depth of x-ray beam penetration is also altered, changing the interaction volume of the coating material for each data point and leading to the uncertainties when a stress gradient is present. Other coatings deposited with a DCMS method also exhibited this non-linear behavior. The residual stress calculation was still completed for these coatings as a semi-quantitative measure of the stress. Residual stress values measured for the magnetron sputtered Cr coatings from Vendor II are shown in Table 4.3. All DCMS coatings exhibited tensile residual stresses on the order of a few hundred MPa. In the case of the HiPIMS processes, the coating deposited with conventional HiPIMS

possessed a tensile residual stress while the B-HiPIMS coating exhibited a relatively large compressive stress.

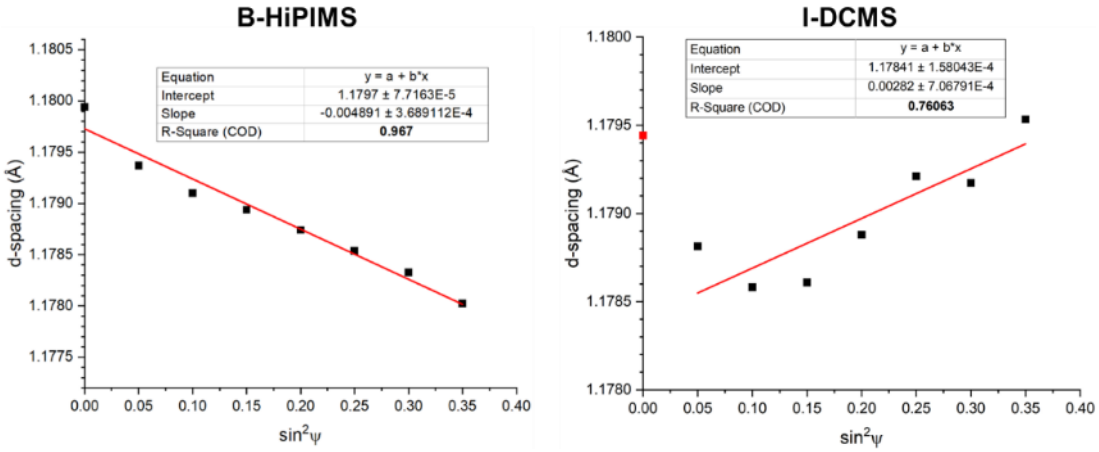

Figure 4.11: Representative plots of interplanar d-spacing vs. sin2ψ for residual measurement for two types of Cr coatings.

Table 4.3: Measured residual stress values for the second generation of magnetron sputtered Cr coatings (negative sign represents compressive stress).

Coating process	Residual stress (MPa)
S-DCMS	140
P-DCMS	380
I-DCMS	180
PI-DCMS	220
HiPIMS(II)	100
B-HiPIMS	-790

4.3.4 Effects of deposition method on microstructure, texture, and residual stress

Micro/nanostructural characterization using SEM and TEM imaging showed different surface morphologies, columnar grain structures, and porosity levels depending on the deposition conditions. The presence of a pulsed target voltage or ion beam bombardment significantly influenced the final microstructure of the coating. In the S-DCMS process, the ionization fraction of sputtered atoms is low, and the depositing atoms have limited mobility (i.e., low kinetic energy)

upon arrival at the substrate surface. The low atomic mobility during deposition produces a microstructure consisting of fine, fibrous growth pattern containing nanoscale intercolumnar porosity. The positive reverse pulses incorporated in P-DCMS deposition induce ionization of the sputtered flux and thereby increase the mobility of depositing atoms toward the substrate surface [51]. The increased mobility was reflected in the P-DCMS microstructure where the columnar grains were coarsened, although some degree of intercolumnar porosity was still present.

The influence of ion bombardment on the coating microstructure was also evident. Since the target voltage characteristics in I-DMCS process are identical to the S-DCMS process, the microstructure was generally similar. However, the ion bombardment introduced additional densification of the coating microstructure, as evidenced by compaction of the pyramidal surface features and reduction in porosity level. The combined effects of the pulsed target voltage and ion bombardment (i.e., PI-DCMS) resulted in the coarsened columnar grains and denser microstructure.

It was anticipated that the HiPIMS coating would show higher density compared to the four types of DCMS coatings. However, the HiPIMS coating shared notable microstructural similarities with the S-DCMS coating, namely very fine columnar grains with intercolumnar porosity. One reason for the microstructure is the absence of a substrate bias during deposition. Applying a negative bias to the substrates during deposition promotes coating densification by accelerating the ionized sputtered flux toward the substrates, causing the ions to impinge with greater energy. This is particularly beneficial for HiPIMS deposition where a large fraction of the sputtered flux is ionized [47]. It is believed that the microstructure of the HiPIMS coating can be significantly improved by applying negative potential to the substrates along with optimized HiPIMS pulsing parameters (e.g., pulse length, pulse frequency).

The B-HiPIMS process produced Cr coatings with a smooth surface, high density, and relatively large grains (~500 nm in width), which were attributed to the energetic deposition process enhanced by positive reverse pulses. The positive reverse pulses applied to the sputter target accelerate the sputtered ions away from the target and toward the substrates with additional energy promoting densification and grain growth. Therefore, it is reasonable to say that the positive target pulses have at least a partially analogous effect to a negative voltage bias applied to the substrate in that both promote densification by increasing the kinetic energy of ions impinging on the substrate.

The effects of the positive target pulse were also reflected in the texturing of the coatings. There were two Cr coatings that incorporated a positive pulse, P-DCMS and B-HiPIMS, which exhibited a strong (110) texture. The positive pulse increases the mobility of atoms on the substrate surface. Therefore, the growth of coating layers tends to favor the lowest surface energy orientation, which is the (110) orientation for bcc Cr. This observation is in good agreement with the previous study by Gautier [101] where the (110) orientation was favored in magnetron sputtered Cr coatings at lower substrate temperatures and higher substrate biases, also supporting the hypothesis that positive target pulses provide similar effects as a negative substrate bias. It is interesting to note that the (110) texturing effect was reduced when the positive pulsing was combined with ion-assisted deposition in the PI-DCMS coating since the collision cascades caused by the ion bombardment disturbed the crystal growth, resulting in a randomly oriented crystallographic structure.

Tensile stresses are commonly found in coatings deposited with DCMS processes. These stresses arise during the initial stages of film growth when isolated island growth structures coalesce to form a grain boundary, thereby reducing the total surface energy by generating a strain

within the coating [62,102]. Also, a tensile residual stress is anticipated for a DCMS Cr coating deposited at relatively low argon pressure with limited adatom mobility [98].

The effect of pulsing and ion bombardment during DCMS deposition can be seen by evaluating the measured residual stress values in Table 4.3. Pulsing (i.e., P-DCMS) produces an increase in tensile stress, which may be related to the coarser grain size observed in the P-DCMS process. Ion bombardment reduces tensile stress through the incorporation of excess atoms into the structure via collision cascades and insertion of atoms into grain boundaries, giving rise to compressive stress effects [64,65]. The ion bombardment effect is illustrated by the reduced tensile stress of I-DCMS compared to S-DCMS and PI-DCMS compared to P-DCMS. It should also be noted that the residual stress measured in the coatings also includes a tensile thermal stress related to differing coefficients of thermal expansion for Cr and SiC. Further analysis of thermal stress effects is provided in Chapter 9.

The same ion bombardment mechanisms (collision cascades and grain boundary diffusion) are responsible for the compressive stress in the B-HiPIMS coating. However, in this case the bombarding ions are metallic Cr^+ ions generated during the strong negative pulses rather than Ar^+ ions from an ion source. Clearly, the compressive effects generated by metallic ion bombardment are drastic enough to produce an overall compressive stress in the B-HiPIMS coating, as has also been reported for other coating materials [103–105]. A compressive stress was also anticipated for the HiPIMS coating. However, as previously discussed, the unoptimized parameters and lack of a substrate bias during HiPIMS deposition produced a coating with microstructure and properties atypical of HiPIMS processes. It is hypothesized that compressive residual stresses are desirable for a coating intended for application on SiC-SiC_f fuel cladding. Compressive stresses within the

coating may help offset, fully or partially, the tensile hoop stress generated by the irradiation-induced volumetric swelling of the underlying SiC cladding tube.

4.4 Investigation of interfacial structure and composition at nanometric scale

4.4.1 Simulation of atomic mixing during deposition

Studying the nature of the coating-substrate interface is crucial to develop a broader understanding of coating behavior, as the interface plays a fundamental role in coating adhesion and the response of the film to dimensional changes in the substrate. The SDTrimSP software was used to model the atomic mixing occurring at the interface during the initial stages of deposition. 200 eV was selected as the incident Cr ion energy based on the upper limit of ion energies measured in HiPIMS plasmas using sophisticated diagnostic techniques [106–108]. The simulation was programmed so the 200 eV Cr ions impinged on a monolithic SiC target to a fluence of 5×10^{16} ions/cm^2. The simulation window was 10 nm wide and divided into 200 data points. Dynamic mode was used to conduct the simulation with 1000 steps of 50 incident ions each, and the target composition was updated after each step. The target composition was saved to an output file every 100 steps.

The plots in Figure 4.12a show how the concentration of Cr, Si, and C evolve as a function of depth below the surface as deposition progresses. It is important to note the scale of the x-axis, which shows that all deposition-induced compositional changes are limited to the first 10 nm below the surface. These plots show how the elemental concentration profiles become broader during the initial stages of deposition but eventually reach a state of maximum width that is maintained during the latter stages. A similar concept is illustrated in Figure 4.12b, which shows how the composition state evolves across four stages of deposition (selected from the data in Figure 4.12a). The earliest stage primarily involves the implantation of Cr into SiC. Because the threshold

displacement energies for Si and C are in the range of 20–40 eV [83], each incident ion can only generate a few atomic displacements before the majority of its energy has dissipated. The resulting implantation depth of 200 eV Cr into SiC is only 1 nm. After this stage, the implanted Cr atoms can be mixed further into SiC, along with the deposition of additional Cr on the surface. This can be observed in the second stage in Figure 4.12b, where the Cr-Si-C mixing region has become wider, and the near-surface region has become almost 100% Cr. Once the Cr surface layer reaches a thickness of about 2 nm, the energy of incident Cr ions is fully dissipated within this layer, and no further mixing can occur. This is illustrated in the third and fourth stages of Figure 4.12b, where the width of the concentration profiles remains constant, and the only mechanism active is deposition of Cr on the surface. The final concentration profiles produced by the simulation predict a deposition-induced atomic mixing layer 2–3 nm in thickness.

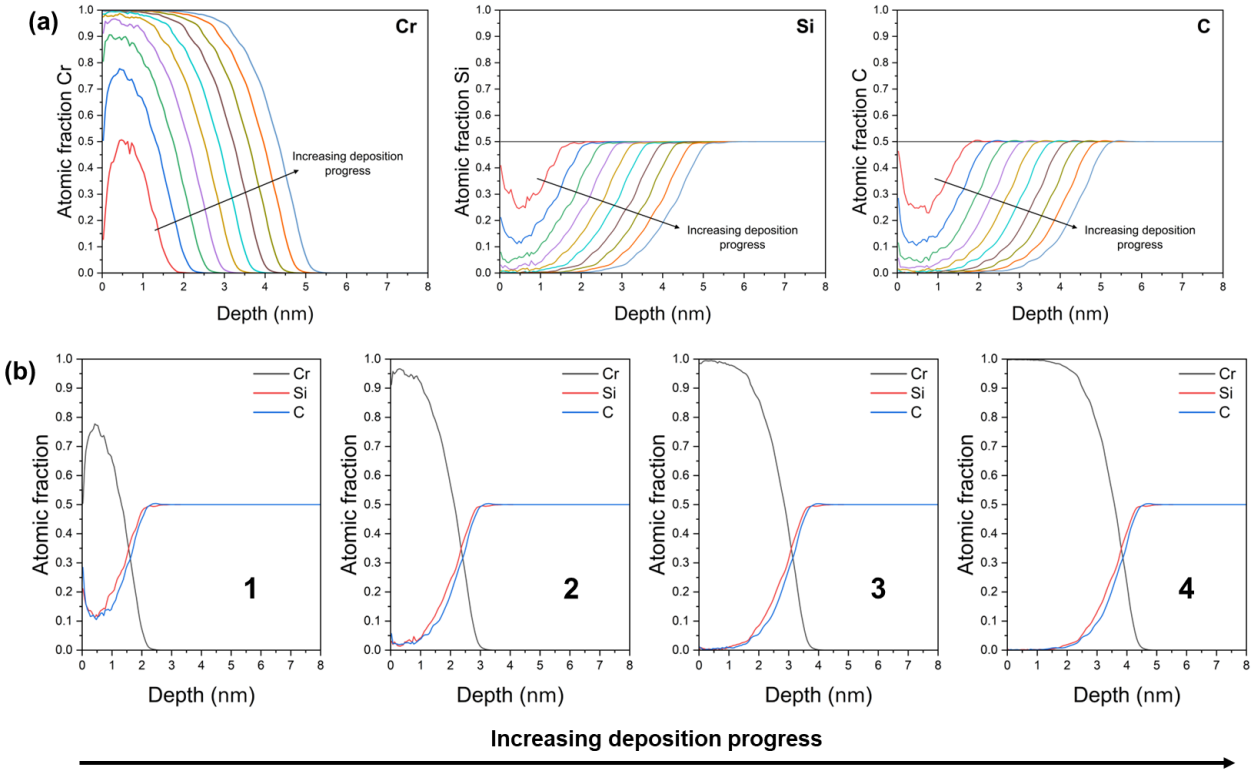

Figure 4.12: (a) Plots showing the evolution of Cr, Si, and C concentration as a function of depth as deposition progresses. Each line represents a fluence increase of 5×10^{15} ions/cm^2 until the final fluence of 5×10^{16} ions/cm^2 is reached; (b) Cr, Si, and C concentration profiles across four stages of deposition. The early stages are dominated by ion implantation and mixing, while the latter stages are dominated by deposition.

4.4.2 High resolution imaging of interface

High resolution transmission electron microscopy (HRTEM) was performed on a Thermo Scientific Talos F200X (S)TEM in the Electron Microscopy Laboratory at Idaho National Laboratory to image the nanoscale interfacial features of select magnetron sputtered Cr coatings. Imaging was performed on the P-DCMS and B-HiPIMS samples, with the assumption that the P-DCMS reasonably representative coatings deposited by other DCMS processes, for the purposes of such nanoscale examinations. Comparing these samples allows for the elucidation of effects of energetic deposition (i.e., B-HiPIMS) on the interfacial structure. An HRTEM image of the DCMS interface is shown in Figure 4.13a along with a magnified image of the interface in Figure 4.13b. The vertical features in the SiC present almost perpendicular to the interface are stacking faults

within the cubic SiC lattice. Lattice planes in both Cr and SiC can be seen, and it is observed that the planes travel uninterrupted in both materials until they meet at the interface. Similar images of the B-HiPIMS interface are shown in Figure 4.15c and d. Here, the Cr lattice planes are separated from the SiC by a discrete layer approximately 2.5 nm in thickness. Based on the contrast of this layer, it is likely that its composition is Cr-rich. The thickness of the observed layer is in good agreement with the length scale of atomic mixing predicted by the SDTrimSP simulation discussed in the previous section. This suggests that this layer is the region of mixing between Cr and SiC. Molecular dynamics simulations across different metallic systems have also show that HiPIMS deposition can produce a coating-substrate intermixed region on the order of a few nanometers [106,109,110].

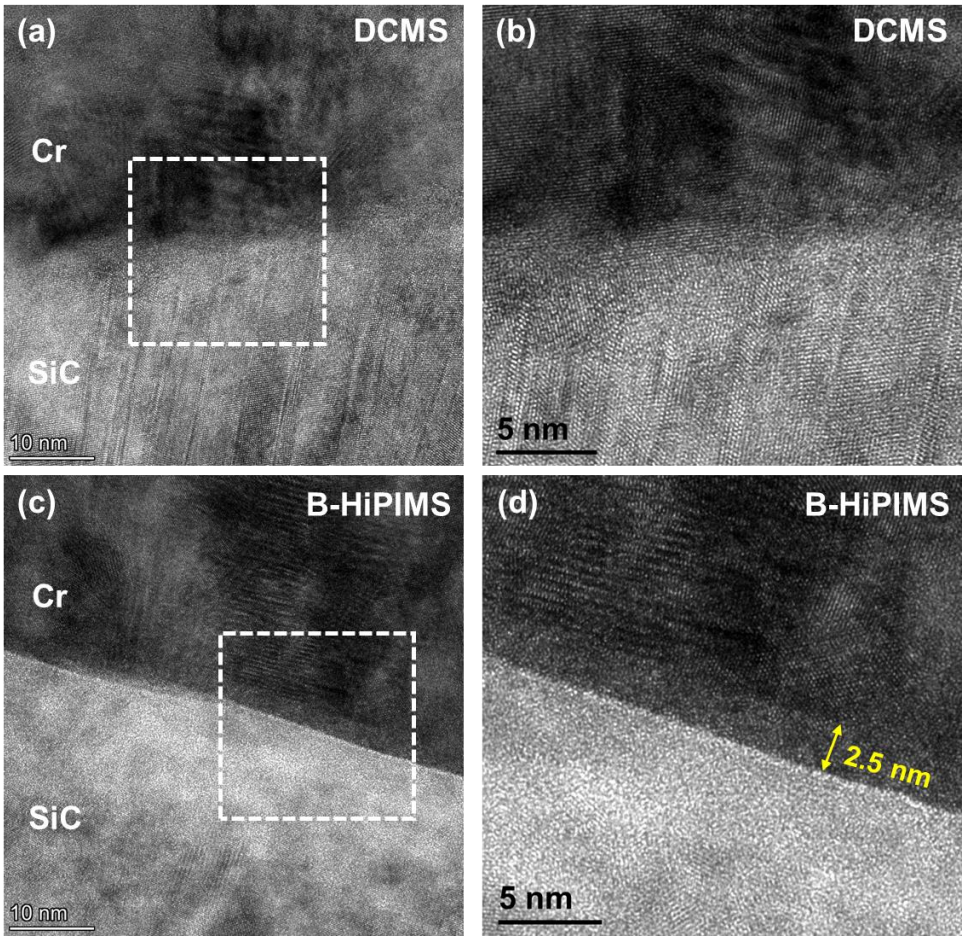

Figure 4.13: (a) HRTEM image of the Cr-SiC interface in the DCMS Cr coating; (b) HRTEM image of the region boxed in (a); (c) HRTEM image of the Cr-SiC interface in the B-HiPIMS Cr coating; (d) HRTEM image of the region boxed in (c).

HRTEM imaging also revealed the isolated presence of another layer at a few locations at the interface in some coatings (Figure 4.14). However, the size and morphology of this layer was markedly different than the Cr-SiC mixing region observed at the B-HiPIMS interface. Figure 4.14 shows a HRTEM image, electron diffraction patterns, and EDS spectra of this isolated interfacial layer present between Cr and SiC. The Cr and SiC diffraction patterns show distinct spots corresponding to the crystalline phases, while the diffraction pattern from the interface band exhibits largely diffuse rings, indicating that the layer is nanocrystalline or even amorphous. The EDS spectra from the interface bands shows strong signals from Si and O, suggesting that this interface band is an oxide layer on the surface of the SiC substrate. Like many materials, SiC is

known to form a native oxide on the surface in ambient conditions that can be either crystalline or amorphous [111]. It is possible that the oxide layer also includes some C (SiO_xC_y), or it may be stoichiometric SiO_2. The oxide layer was observed at the interface of many of the Cr coatings but always in localized areas rather than as a continuous band. This suggests that the *in situ* cleaning of the substrates using either plasma cleaning or ion milling inside the deposition chamber is able to remove most, but not all, of the native oxide layer on the surface of SiC.

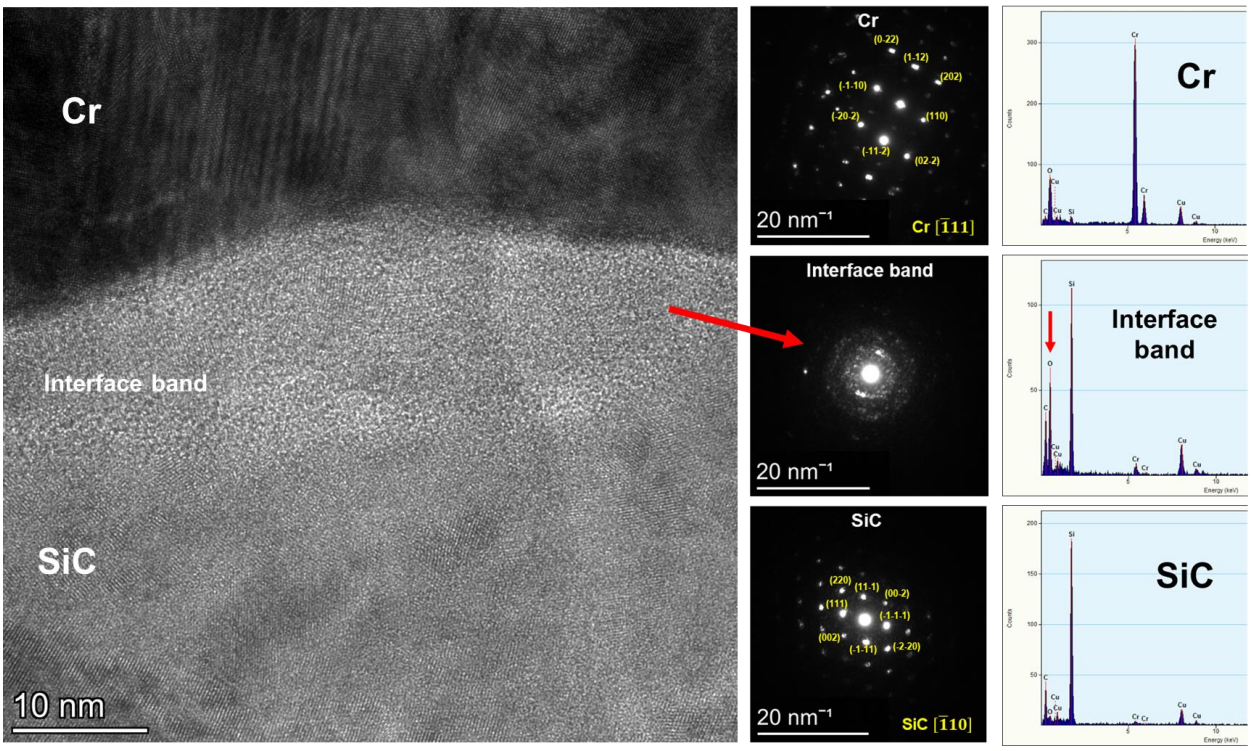

Figure 4.14: HRTEM image (left) of a DCMS interface at a location where the interface band is present between Cr and SiC. The electron diffraction patterns (center) show that the interface band is amorphous, and the EDS spectra (right) show that the interface band is primarily composed of Si and O. The red arrow in the spectrum from the interface band indicates the O peak.

4.4.3 EELS analysis of chemical bonding

The chemical bonding between Cr and SiC was investigated using electron energy loss spectroscopy (EELS). The B-HiPIMS and DCMS samples were selected for analysis to compare the nature of interfacial bonding between two coatings produced with two starkly different sputtering energy regimes. EELS measurements were performed on a FEI Titan probe-corrected

200 kV STEM instrument in the Irradiated Materials Characterization Laboratory (IMCL) at Idaho National Laboratory. EELS spectrum imaging was performed in 34 nm × 34 nm regions across the interfaces of the two coatings. High-resolution spectra were captured from the Cr, Si, and C core-loss regions along with wider-range spectra containing all three core loss regions to facilitate elemental quantification. Measurements were performed in drift-corrected DualEELS mode [112] allowing for the simultaneous collection of low-loss and core-loss spectra. Collection of the zero-loss peak enables improved data processing techniques such as correction of energy shifts and removal of plural scattering artifacts related to sample thickness. All EELS data processing was performed using the Gatan DigitalMicrograph software.

Figure 4.15a shows a low magnification annular dark field STEM (ADF-STEM) image at the interface of the B-HiPIMS coating with the spatial drift correction and spectrum imaging regions indicated. A magnified version of B-HiPIMS spectrum imaging area is shown in Figure 4.15b. A similar spectrum imaging area was chosen in the DCMS sample as well. The spectrum imaging areas were composed of an array of 34 × 34 pixels with low-loss and core-loss EELS spectra collected at each pixel. Prior to data analysis, a series of post-processing steps were applied to make the data suitable for analysis. First, the pre-edge background was subtracted from all spectra using the standard power law function [113]. Second, plural scattering was removed using the Fourier-ratio method [114]. Plural scattering arises when an electron experiences multiple inelastic collisions as it passes through a TEM foil and is directly influenced by the sample thickness. The relative sample thickness can be quantified in terms of the inelastic mean free path λ. The relative sample thickness (t/λ) is calculated by,

$$\frac{t}{\lambda} = -\ln\left(\frac{I_0}{I_t}\right) \qquad \text{(Eq. 4.1)}$$

where t is the sample thickness, I_0 is the integrated intensity of the zero loss peak, and I_t is the integrated intensity of the entire spectrum [115]. For example, a t/λ value of one suggests that on average each electron experiences one inelastic scattering event while traveling through the specimen thickness. t/λ values of less than one are generally preferred for EELS measurements. Figure 4.15c shows relative thickness maps of the DCMS and B-HiPIMS spectrum imaging regions. The B-HiPIMS sample is noticeably thinner than the DCMS sample. However, after removing plural scattering effects from the spectra, any artifacts caused by differences in sample thickness are negated and results from the two samples can be reliably compared.

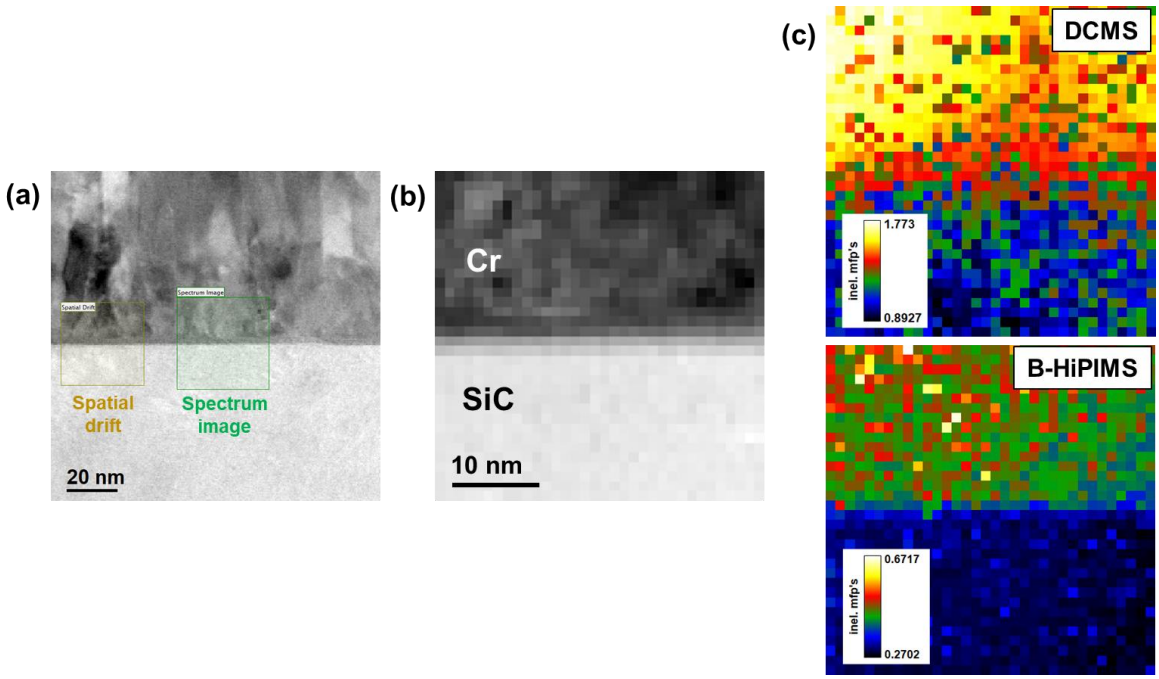

Figure 4.15: (a) Low magnification ADF-STEM reference image of the B-HiPIMS interface with spectrum imaging and drift correction regions for EELS indicated; (b) B-HiPIMS interface EELS spectrum imaging area composed of 34 × 34 pixels; (c) Relative thickness maps (t/λ) computed using the log-ratio method.

With EELS spectrum imaging, it is possible to map elemental concentrations by using the integrated intensities of core-loss signals for each element and known cross sections for inner shell scattering [115]. Cr, Si, and C quantification maps for both samples are shown in Figure 4.16. In both samples, there is a clear delineation between the Cr coating and SiC substrate. In B-HiPIMS,

the concentration of Cr drops off abruptly, while in DCMS there is a more gradual decrease in the Cr signal. However, this Cr profile is most likely an artifact of the FIB milling process used to prepare the TEM lamella or the orientation of the interface during the EELS measurement. A slight overlap between Cr and SiC may be present in the final TEM sample after FIB milling and depending on the area selected for analysis and the orientation of the interface at this location, the electron beam may interact with the overlapped Cr and SiC, resulting in the appearance of a more diffuse interface as seen in the DCMS sample.

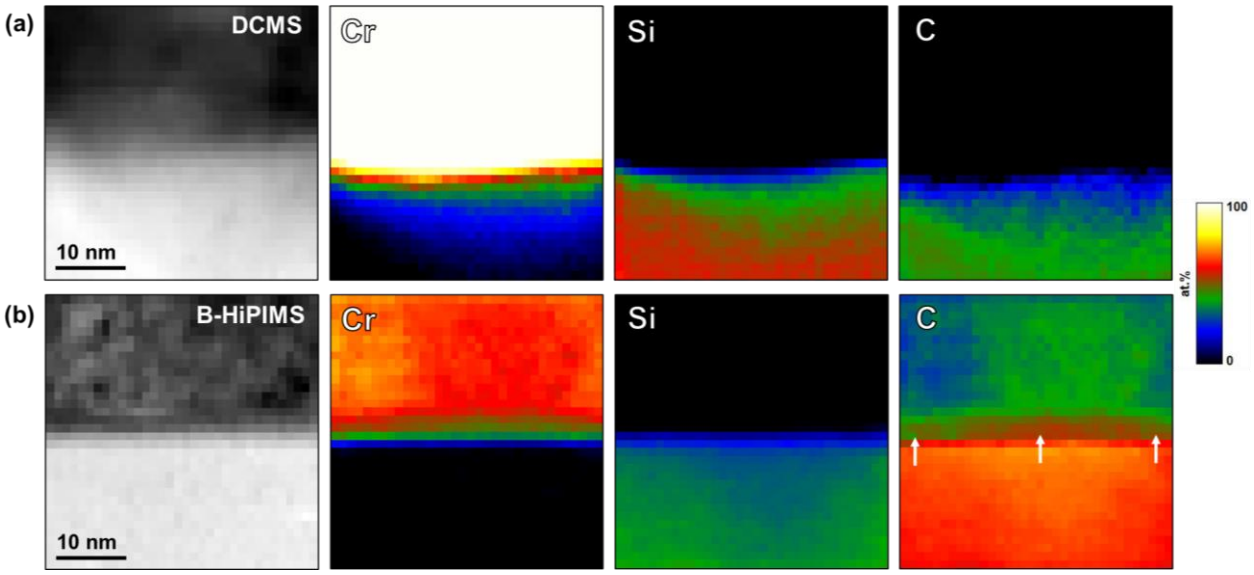

Figure 4.16: Reference spectrum images and EELS elemental quantification maps for (a) DCMS and (b) B-HiPIMS with the deposition-induced mixing region indicated by the arrows in the C map.

The most interesting piece of information that can be gathered from the elemental quantification maps is the distribution of C in the B-HiPIMS Cr coating. The arrows in Figure 4.16b identify a C-enriched band on the Cr side of interface. The thickness of this C-enriched layer corresponds well with the deposition-induced mixing region predicted via the low energy ion beam mixing simulation in Section 4.4.1 and observed via HRTEM imaging in Section 4.4.2, indicating that this C-enriched band is the atomic mixing layer. The mapping also shows the presence of C in the B-HiPIMS Cr coating well away from the interface. However, this is most likely is an

experimental artifact related to hydrocarbon contamination of the TEM lamella. STEM-EDS analysis at the interface of other Cr-coated SiC samples, regardless of coating type, also tended to show excess C within the coating, providing another piece of evidence to suggest that the C observed in EELS of the B-HiPIMS coating is not inherent to the sample. The distinct band of C enrichment immediately adjacent to the interface and good agreement of the layer thickness with the mixing simulation and HRTEM imaging contribute to the high confidence in the identification of this band as the deposition-induced mixing layer. The EELS quantification results suggest that the atomic percentage of C in this region is nearly 50 at. %. However, it is likely that the EELS quantification is overestimating the C concentration, as the measured concentration of C in SiC is greater than 60%. Nevertheless, the qualitative (or semi-quantitative) trends are still valid.

It is also interesting to note that the atomic mixing layer appears to be primarily composed of Cr and C. The ion mixing simulation in Section 4.4.1 predicted approximately equivalent mixing of Si and C, but as mentioned previously, this simulation only considers ballistic collision effects. Chemical potential gradients may also be generated during the recovery of local thermal spikes produced by ion bombardment and provide a driving force for atomic motion [57]. At the deposition temperature of 250 °C, it is expected that C is mobile on account of its small atomic size and ability to diffuse interstitially, whereas Si is likely much less mobile [116]. Also, C has a strong chemical affinity for Cr and can form very stable carbide compounds ($Cr_{23}C_6$, Cr_7C_3, Cr_3C_2) [117]. These factors may explain why C seems to have been mixed into the B-HiPIMS Cr coating to a greater degree than Si.

The elemental mapping results provide a starting point for further investigation of chemical bonding via analysis of the features of core-loss ionization edges. In EELS measurements, the strongest signal produced by Cr is a two-peak ionization edge consisting of the L_2 and L_3 peaks

corresponding to interactions with electrons in $2p_{1/2}$ and the $2p_{3/2}$ orbitals [118]. The doublet peak structure is typical of transition metals, and the peaks are commonly referred to as "white lines" [119]. An example Cr-$L_{2,3}$ edge with the pre-edge background subtracted is shown in Figure 4.17. Analysis of the fine structure of peak features such as shifting of peak centers and the ratio of integrated intensities of L_3 and L_2 peaks can provide valuable information about the nature of chemical bonding between and valence states of the atoms [118].

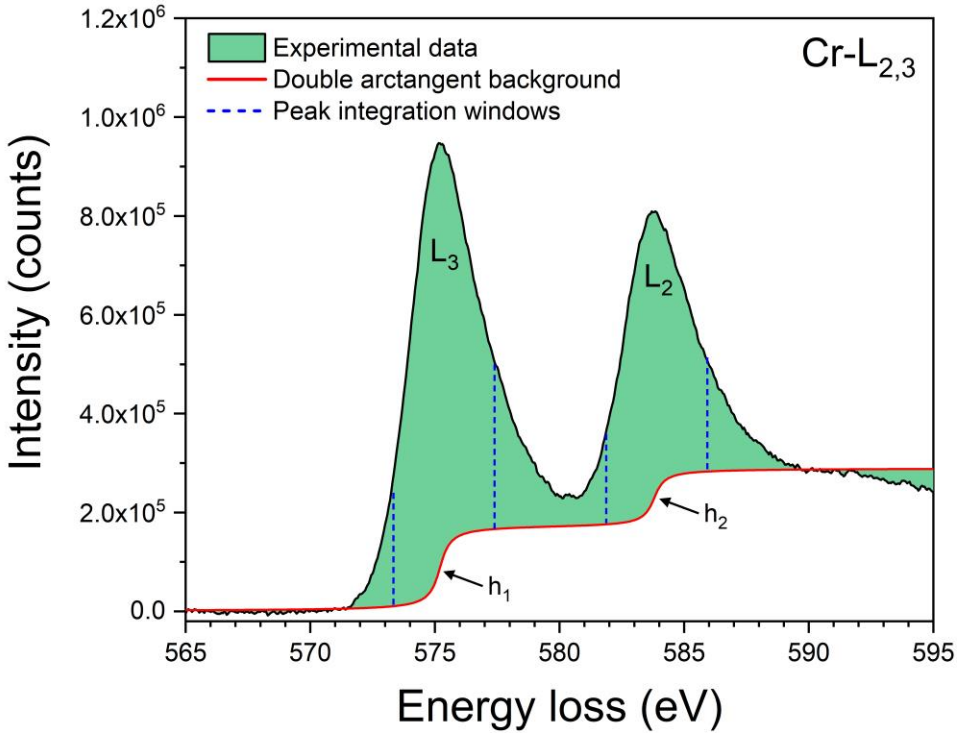

Figure 4.17: Example Cr-$L_{2,3}$ edge collected from EELS measurements of the B-HiPIMS sample with double arctangent background fitting and integration window used for intensity ratio calculation.

To calculate the L_3/L_2 area ratio, the spectral background intensity must be accurately accounted for, as each ionization edge also produces an increase in the background intensity. The most common ways to model the continuum background under the doublet peaks are by using either a two-step linear function [120] or a double arctangent function [121]. In this work, the double arctangent function was used to fit the background under the Cr-$L_{2,3}$ edge. For fitting the

background accurately, the ratio between the magnitude of the two vertical steps (h_1 and h_2) underneath the L_3 and L_2 peaks must be equivalent to the L_3/L_2 peak area ratio. To meet this criterion, background fitting was conducted in a iterative manner following the procedure of Daulton and Little [118]. The upper baseline of the double arctangent function was set to the intensity of the data point 5.8 eV past the L_2 peak maximum. The initial ratio of step heights was initially set to 2:1, matching the theoretical occupancy between $2p_{3/2}$ and $2p_{1/2}$ electrons [118]. The L_3/L_2 ratio was calculated using this background fitting and 4 eV-wide integration windows centered at the maximum of each peak. Then, the ratio of step heights was adjusted to be equivalent to the L_3/L_2 ratio while keeping the upper arctangent baseline fixed at its initial position. The L_3/L_2 ratio was calculated again, and the procedure was repeated until the step height ratio and L_3/L_2 ratio converged to a single value. It was found that only three or four iterations were necessary to achieve convergence. All background fitting and L_3/L_2 ratio calculations were completed using the script developed for DigitalMicrograph by Mitchell [122]. An example double arctangent background function and peak integration windows are shown along with the experimental Cr-$L_{2,3}$ edge in Figure 4.17.

To study how the bonding character of Cr changes near the interface of the coatings, the Cr L_3/L_2 ratio was analyzed as a function of position. Six positions were selected, with the first position in the Cr coating far away from the interface and the final position at the interface between Cr and SiC. Figure 4.18a shows the six analysis positions. To improve the signal-to-noise ratio, the cumulative spectrum from the entire row of pixels corresponding to each position was analyzed. The evolution of the L_3/L_2 ratio with respect to position (i.e., decreasing distance from the Cr/SiC interface moving from position 1 to 6) is shown in Figure 4.18b for both samples. The magnitude of the L_3/L_2 ratio for both B-HiPIMS and DCMS is in good agreement with previous

work, where values between about 1.4–1.6 have been reported for metallic Cr depending on instrumental parameters and analysis procedures [118,123,124]. It is interesting to compare the evolution of the L_3/L_2 ratio between the two samples. Firstly, the L_3/L_2 ratio in DCMS does not exhibit significant variation across all analysis positions. In B-HiPIMS, there is little variation in the L_3/L_2 ratio, followed by a noticeable decrease in the positions closest to the interface where the highest C concentration had been observed in the elemental mapping. Secondly, the L_3/L_2 ratio values are consistently lower in DCMS than B-HiPIMS.

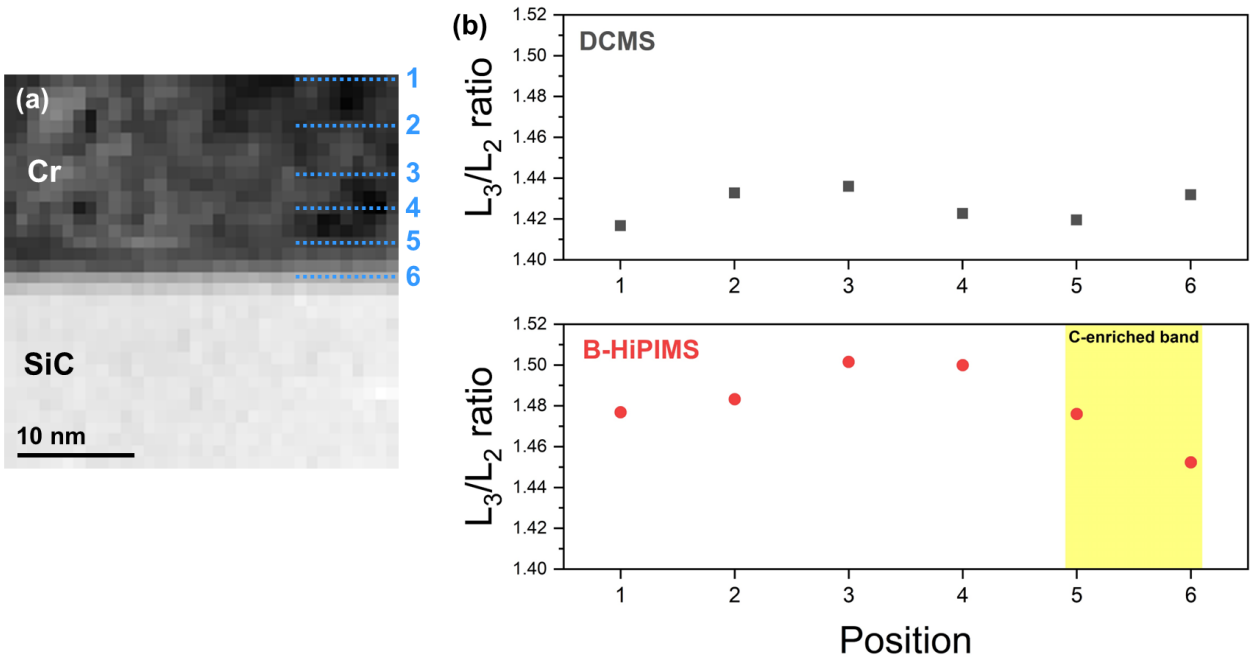

Figure 4.18: (a) Reference spectrum image area from B-HiPIMS with markings indicating the six positions where the Cr L_3/L_2 ratio was calculated. Similar positions were analyzed for the DCMS sample; (b) Plot of the Cr L_3/L_2 ratio as a function of position for both samples with the location of the C-enriched band in B-HiPIMS highlighted. The scale of both plots is identical.

The elemental maps in Figure 4.16b show that far away from the interface in the DCMS coating, the composition is effectively 100% Cr. Therefore, it can be said that the L_3/L_2 ratio at Position 1 in the DCMS sample represents near-ideal metallic bonding in pure chromium (for the current set of measurement and analysis procedures used) with a Cr^0 valence state and only Cr atoms as nearest-neighbors. Because the composition of the DCMS coating is highly Cr-rich even

near the interface with SiC, the L_3/L_2 ratio remains largely unchanged at all analyzed positions. In B-HiPIMS, the most notable aspect of the L_3/L_2 ratio evolution is its decreasing value in the positions near the interface (Position 4 to Position 6). While the number of studies involving L_3/L_2 analysis of Cr-C compounds is limited, there is a consensus in literature that Cr-C mixtures tend to have a lower L_3/L_2 ratio than metallic Cr^0, regardless of whether the compound is a crystalline, ordered compound ($Cr_{23}C_6$, Cr_7C_3, Cr_3C_2) or a disordered Cr-C_x solid solution [118,124–126].

While the oxidation state of Cr in B-HiPIMS is still Cr^0, the presence of C atoms alters the local bonding environment which manifests as a small decrease in the L_3/L_2 ratio. The decrease in L_3/L_2 ratio observed here between Position 1 and Position 6 was approximately 0.03. Daulton and Little reported a decrease of 0.027 between Cr and $Cr_{23}C_6$ using a similar data analysis procedure [118]. The slight increase in L_3/L_2 ratio from Positions 1 and 3 could potentially be due to the presence of O which makes the bonding character of Cr more ionic and tends to increase the L_3/L_2 ratio [118,127]. Finally, given that the L_3/L_2 analysis is very sensitive to minute changes in spectral features, one cannot be conclusive with regards to reason for the differences in magnitude of L_3/L_2 ratio between the DCMS and B-HiPIMS coatings.

A similar analysis was also carried out for C-K edge spectra collected from both samples. The C-K edge was analyzed as a function of position, with the first position located in the SiC substrate far away from the interface and the final position located in the Cr coating. These positions are illustrated in Figure 4.19a. In EELS measurements, the C-K edge is composed of two primary peaks, a peak at 284 eV corresponding to the π bonding state of C (i.e., sp^2 hybridized or graphite-like bonding) and a peak at 290 eV corresponding to the σ bonding state of C (i.e., sp^3 hybridized or diamond-like bonding).

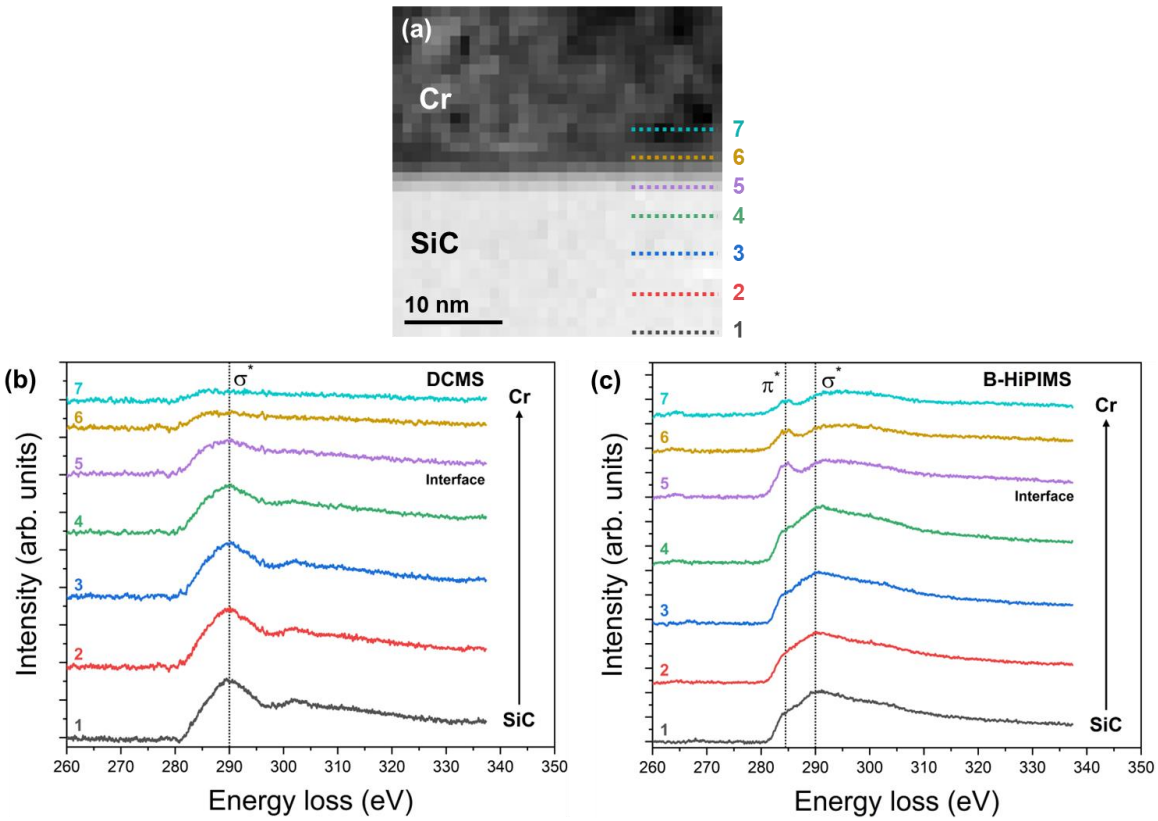

Figure 4.19: (a) Reference spectrum image area from B-HiPIMS with markings indicating the seven positions where the C-K edge was extracted. Similar positions were analyzed for DCMS; (b) C-K edges for the DCMS sample collected at the seven positions indicated in (a); (c) C-K edges for the B-HiPIMS sample collected at the seven positions indicated in (a).

The C-K spectra from the DCMS coating are shown in Figure 4.19b where σ-bonding peak is dominant while there is no intensity corresponding to the π bonding state. 3C-SiC possesses the zinc blende crystal structure, analogous to the diamond crystal structure with half of the atoms replaced with a different element. It can also be thought of as two interpenetrating face-centered cubic lattices of Si and C. Given the similarity of 3C-SiC to the diamond lattice, it is not surprising that the σ-bonding peak is the principal peak in the C spectrum, which is in good agreement with EELS studies of SiC [128–130]. The peak shape remains unchanged with respect to position until the interface is reached, and then the signal rapidly diminishes due to the absence of C within the DCMS Cr coating.

A different C bonding behavior is observed in the B-HiPIMS coating, particularly near the interface. Figure 4.19c shows that within the C-enriched layer on the Cr side of the interface (Positions 5 and 6), a peak corresponding to the π-bonding state appears while the σ-bonding peak intensity is reduced. This indicates that near the interface, C is no longer bonded in a perfect SiC crystal, and its hybridization state has changed to a more graphite-like character. The π-bonding peak remains visible even within the B-HiPIMS Cr coating even farther away from the interface (Position 7), suggesting that the C present within the coating has graphite-like bonding. The bonding of C is likely a combination of C-C bonds and C-Cr bonds. Other studies of transition metal-C mixtures have shown that the presence of a metal can promote formation of sp^2 clusters [131].

The precise structural nature of the deposition-induced Cr-C mixing layer at the B-HiPIMS interface is unknown. Although the equilibrium solubility of C in bcc Cr is small and many stable Cr-carbide phases exist, these phases have complex crystal structures and rigid stoichiometries [117]. Therefore, owing to poor kinetics at the relatively low deposition temperature of 250 °C, the formation of ordered carbides is unlikely. Instead, it is more likely that the mixing layer exists in a metastable form, such as crystalline CrC [132], supersaturated bcc Cr [133], or even an amorphous Cr-C mixture [134]. It has been shown that co-deposition of bcc metals with C can resulted in highly supersaturated solutions of C in the host metal [133,135,136]. In the situation considered here, the source of C comes from the substrate rather than from a sputter target, but it is also well known that the stochastic nature of ion beam mixing can produce supersaturated crystalline phases and amorphous mixtures with non-equilibrium compositions [19,137]. In the literature, high resolution studies of HiPIMS interfaces have not been extensive, but there have

been reports of nanoscale amorphous layers formed between steel substrates and metallic films [138,139].

4.4.4 STEM-EDS quantification of interfacial mixing

The EELS analysis described in the previous section was supported with STEM-EDS measurements to quantify the extent of deposition-induced interfacial mixing. The EELS analysis was focused on just one interface region in each coating. STEM-EDS allows for compositional analysis over a larger area to provide better statistical measurements. The STEM-EDS measurements were performed in the Electron Microscopy Laboratory at Idaho National Laboratory on a Thermo Scientific Talos F200X (S)TEM instrument. The microscope was equipped with a Super-X EDS system with four in-column detectors allowing for rapid collection of EDS maps. EDS maps were collected at multiple locations across the DCMS and B-HiPIMS interfaces.

A representative ADF-STEM image and EDS chemical maps are shown in Figure 4.20a. The HyperSpy v2.0 Python package was used to analyze the EDS data [140]. Each map was split into five vertical sections, and the compositional data was averaged in the horizontal direction within each section to improve the signal-to-noise ratio of the data. The division of the data into five analysis sections is illustrated in Figure 4.20b. The data was then analyzed as a function of distance starting in the Cr coating and ending in SiC substrate. The degree of atomic mixing at the interface is directly related to the width of the interface obtained from elemental concentration profiles. To quantify the interface width, a logistic function of the form,

$$y = \frac{a}{1+e^{-k(x-x_c)}} \qquad \text{(Eq. 4.2)}$$

was fit to the Cr and C composition profiles [141,142]. In this equation, y represents concentration, and x represents the distance. Graphically, the logistic curve has an upper and lower baseline

separated by a vertical step. The fitting parameters are a, k, and x_c where a represents the height of the function, k represents the width of the step, and x_c represents the midpoint position of the step. An example Cr concentration profile with logistic fitting is shown in Figure 4.20c.

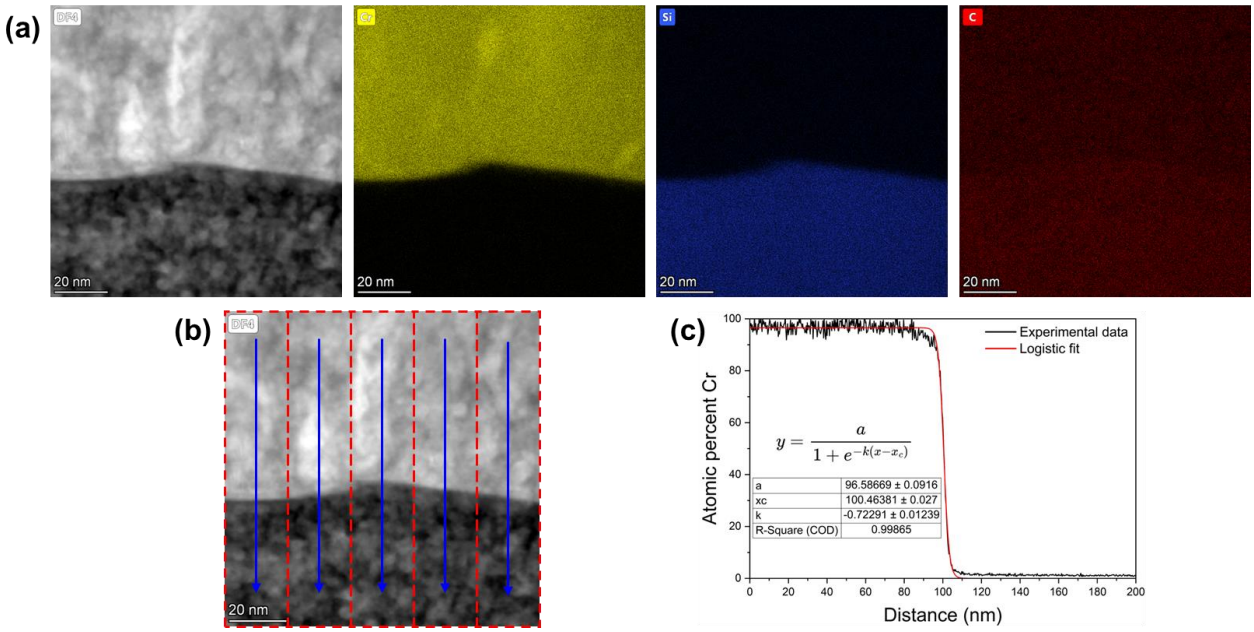

Figure 4.20: (a) Example ADF-STEM image at the B-HiPIMS Cr interface for EDS mapping and corresponding elemental maps for Cr, Si, and C; (b) Separation of EDS data into five line scans of equal width; (c) Representative Cr concentration profile with logistic fitting.

The logistic fitting parameter k ("steepness parameter") serves as a direct quantification of the interface width. A greater absolute value of the steepness parameter suggests the vertical step of the logistic function is sharper and can be interpreted as a lower interface width and in turn degree of atomic mixing. At least ten Cr and C concentration profiles were analyzed for each sample. Plots of the calculated steepness parameters are shown Figure 4.21. On average, the Cr and C steepness parameters are higher in DCMS than B-HiPIMS. This suggests that the concentration gradients of Cr and C are sharper, and there is less mixing in DCMS than B-HiPIMS. This is consistent with the EELS analysis discussed in the previous section. There is still some scatter in the data that may be due to actual local variations or the interface orientation at the measurement area, but repeating the mapping at multiple locations allows for improved statistical confidence in

the data. A statistical hypothesis test (two-sample *t*-test) could verify the statistical significance of the greater steepness parameters in DCMS compared to B-HiPIMS (i.e., the *t*-test was one-sided). The *t*-tests on both the Cr and C steepness parameters returned *p*-values less than 0.05, indicating the difference between DCMS and B-HiPIMS is statistically significant in both datasets. It should be noted that the difference in steepness parameters corresponds to only a few nanometers of true distance, but it is clear that on average, there is greater mixing in B-HiPIMS than DCMS.

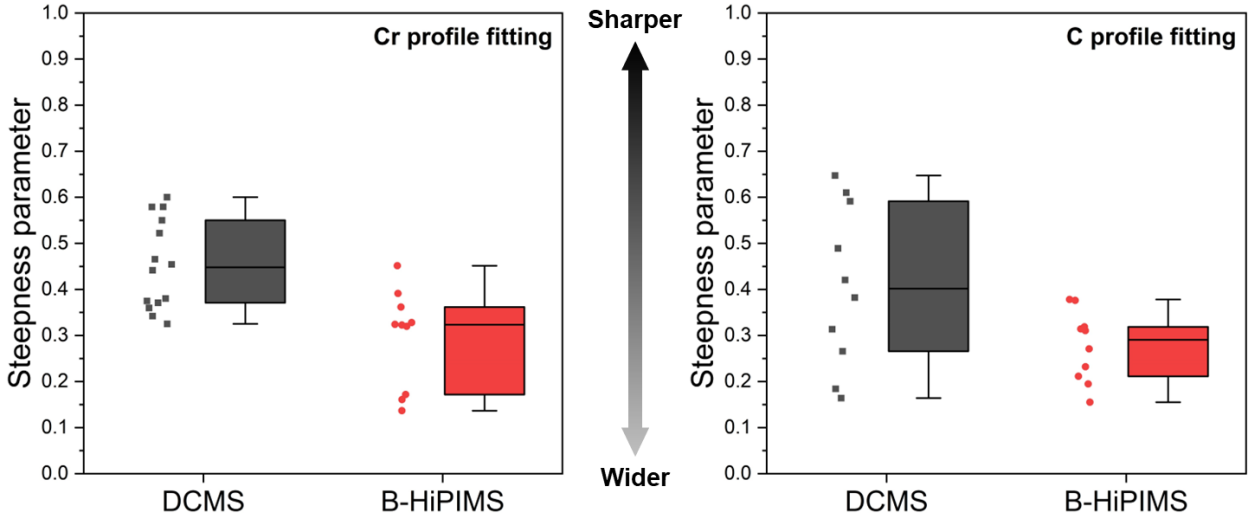

Figure 4.21: Scatter and box plots of Cr and C concentration profile steepness parameters for the DCMS and B-HiPIMS samples determined by logistic fitting. Each data point represents the fitting of a single concentration profile.

4.4.5 Effects of energetic deposition on interfacial characteristics

The results presented in the preceding sections clearly demonstrate how the energetic deposition of a HiPIMS or B-HiPIMS process can alter the state of the interface compared to conventional DCMS deposition. Although the excellent adhesion of HiPIMS coatings is often attributed to the presence of a mixing layer, few researchers have investigated the mixing layer in detail, and most studies have involved metallic substrates [59,138,139,143,144] as opposed to the ceramic SiC substrate observed in this work. The combination of nanoscale imaging and chemical analysis techniques used in this work to study the DCMS and B-HiPIMS interfaces provide a

comprehensive understanding of how interfacial characteristics vary between the two deposition methods in this materials system.

The ion beam mixing simulation in Section 4.4.1 predicted a 2–3 nm thick Cr-SiC interaction layer, which is consistent with molecular dynamics simulations of energetic sputter deposition that have shown mixing layers on the same scale [106,109,110]. The HRTEM imaging in Section 4.4.2 shows very good agreement with the mixing simulation, and a 2.5 nm-thick mixing layer was observed at the B-HiPIMS interface. Chemical bonding within the mixing layer was studied further via EELS spectral imaging in Section 4.4.3, which showed that the mixing layer formed on the Cr-rich side of the interface also contained a considerable amount of C. This suggests that C is a more mobile atomic species during deposition compared to Si. STEM-EDS compositional measurements were performed as a supplement to the EELS analysis by quantifying the extent of atomic mixing at the DCMS and B-HiPIMS interfaces across multiple areas. Statistical analysis of the EDS data confirms that the degree of mixing in B-HiPIMS is greater than DCMS. This multi-technique investigation thoroughly demonstrates how energetic B-HiPIMS deposition alters the makeup of the interface. The atomic mixing layer has consequences in terms of the coating adhesion (Section 5.1) and the stress evolution and interdiffusion behavior at elevated temperatures (Section 6.3).

5. Mechanical Behavior of As-Deposited Coatings

This chapter features direct content from the following journal article first-authored by the PhD candidate:

K. Quillin, H. Yeom, T. Dabney, E. Willing, K. Sridharan, "Microstructural and nanomechanical studies of PVD Cr coatings on SiC for LWR fuel cladding applications," *Surface and Coatings Technology* 441 (2022) 128577.

5.1 Scratch adhesion test

Scratch testing was performed to evaluate the adhesion of the magnetron sputtered Cr coatings and also to assess the cohesion within the coating. The tests were performed by traversing the tip of a 120° sphero-conical diamond probe on the sample surface with varying loads. The tip vertical position remained fixed while the sample moved in the horizontal plane at a velocity of 0.3 mm/s. The downward force on the probe was progressively increased by adding weight on top of the probe every five seconds. A schematic diagram of the scratch test is shown in Figure 5.1. The adhesion strength of the coatings was determined semi-quantitatively by identifying the stage (and the force) of the scratch test at which the coating began to delaminate. The maximum applied load on the system for the samples investigated in this research was 2250 g. In addition to determining the failure load, the scratched regions were examined after the test using SEM to study the failure mechanisms in different types of coatings.

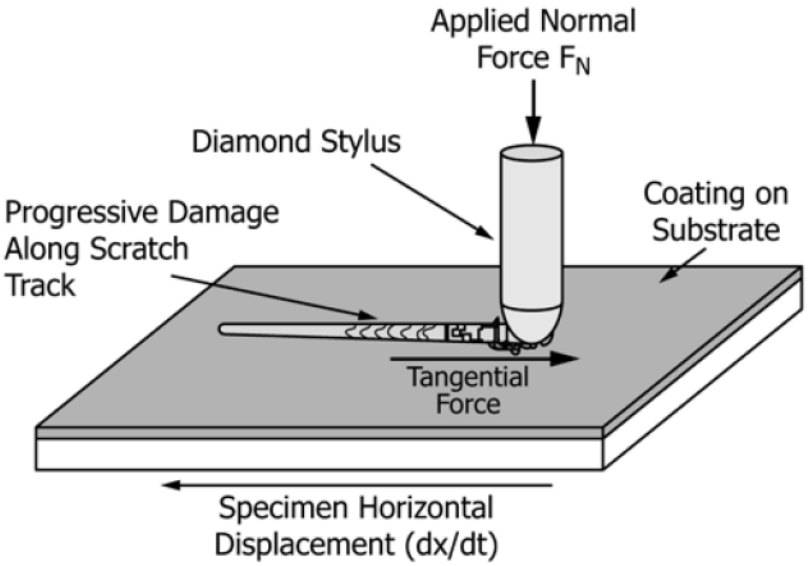

Figure 5.1: Schematic diagram of the progressive scratch test used in this research [145].

The measured delamination loads for the magnetron sputtered Cr coatings are shown in Table 5.1. Two coatings, S-DCMS and B-HiPIMS, did not delaminate at the maximum applied load, indicating that the necessary load to cause debonding is greater than 2250 g. The remaining coatings appear to be split into two categories of adhesion behavior. Both Vendor I coatings and P-DCMS and PI-DCMS from Vendor II had relatively low failure loads. Meanwhile, the I-DCMS and HiPIMS coatings from Vendor II had moderate delamination loads of above 1000 g. One important factor influencing adhesion could be the nature of the SiC substrate cleaning prior to deposition. Both Vendor I and Vendor II performed *in situ* cleaning of the substrates once the samples were loaded, and the deposition chamber was pumped to a vacuum. Vendor I used a plasma-based cleaning process, while Vendor II used ion milling. It is possible that the plasma cleaning performed by Vendor I was not as effective in removing surface-level contaminants or oxides, leading to a reduced adhesion strength. From these results, it seems that pulsing the sputter target voltage during DCMS deposition has a detrimental effect on adhesion as both the P-DCMS and PI-DCMS coatings have low failure loads. It is difficult to make any further determinations on the factors influencing adhesion. Adhesion can be influenced by many factors such as atomic

structure at the interface, residual stress, hardness, porosity, intergranular cohesion, and coating thickness [146].

Table 5.1: Delamination load for the magnetron sputtered Cr coatings measured using scratch testing.

Coating process	Coating manufacturer	Delamination load (g)
S-DCMS	Vendor II	> 2250
P-DCMS	Vendor II	400
I-DCMS	Vendor II	1100
PI-DCMS	Vendor II	500
HiPIMS	Vendor II	1800
B-HiPIMS	Vendor II	> 2250
S-DCMS	Vendor I	500
HiPIMS	Vendor I	800

SEM images of scratches representing the types of deformation observed on different coating variants are shown in Figure 5.2. For the coatings which did not delaminate at the maximum applied of load 2250 g, only consistent plastic deformation was observed, as shown in Figure 5.2a. For coatings that did delaminate, two distinct failure modes were observed depending on the cohesion of the coating. Stronger coating cohesion was observed in the I-DCMS and HiPIMS coatings which delaminated at moderate loads. Minimal cracking was observed within or around the edges of the scratches prior to delamination. Once delamination occurred, the edges of the scratch are smooth and uniform with no cracks branching outward from the coating along the edges of the scratch, as can be seen in Figure 5.2b. This finding indicates that the cohesion of these coatings is strong, and the coating fails in a uniform manner while the microstructure remains intact in undeformed regions.

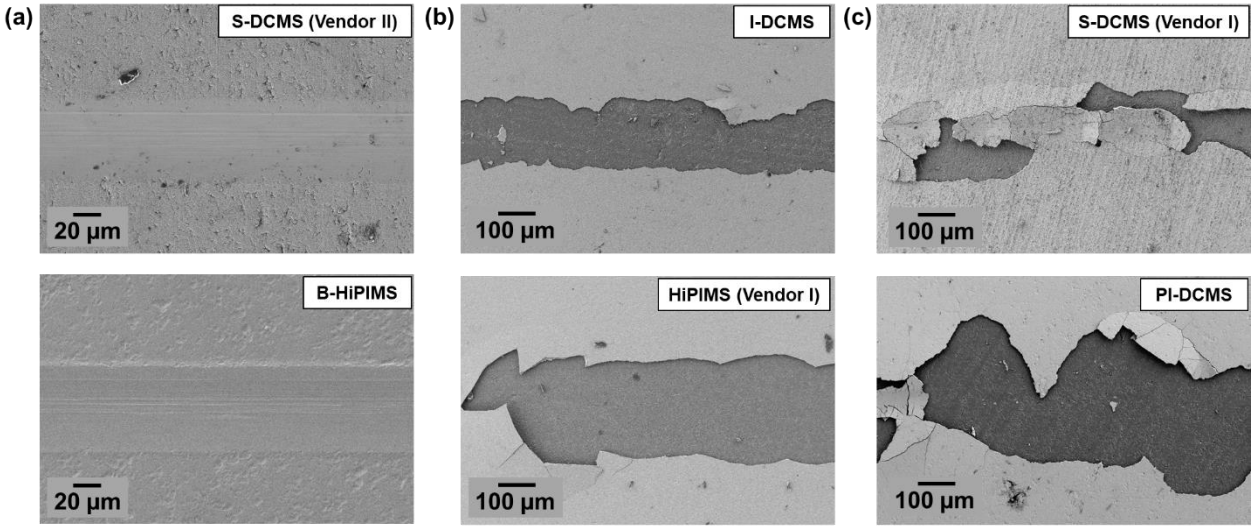

Figure 5.2: SEM images of scratches representing different types of deformation behavior: (a) Coatings where only plastic deformation occurred without delamination from the substrate; (b) Coatings where delamination occurred but strong coating cohesion was observed; (c) Coatings which delaminated and exhibited poor cohesion.

A different behavior was observed in coatings that had a lower adhesion strength, shown in Figure 5.2c. In these coatings, it was observed that extensive cracking occurs prior to complete delamination. Cracks initiating at the scratch and traveling both parallel and perpendicular to the scratch direction were observed. After delamination, the edges of the coating are much more irregular and jagged. Many cracks were initiated at the edges of the scratches and seen to propagate into the coating. This indicates that the cohesion in these coatings is poor. The presence of intercolumnar porosity and weak intergranular bonding may both contribute to the weak cohesion in the coating microstructure.

5.2 High load nanoindentation

5.2.1 Mechanical property measurement and analysis of deformation behavior

Nanoindentation testing was performed to investigate the effect of coating microstructure on the mechanical properties and deformation behavior of the Cr coatings. Conventionally, nanoindentation loads are on the order of 1–10 mN. For coatings studied in this research, it was found that low indentation loads produced indents with depths on the same order of magnitude of

the surface roughness of the coatings, resulting in unreliable data. Therefore, higher indentation loads were used to negate surface roughness effects. By indenting to depths much greater than the surface roughness, the results become less scattered and comparisons between samples can be made reliably. A high load transducer equipped with a diamond Berkovich probe was used to create nano-indents on the as-deposited surface of the coatings with the indentation axis oriented normal to the sample surface. The indentations were conducted in a 4 × 6 grid with the indent centers spaced 50 μm apart using load-controlled mode with peak loads between 4–625 mN. The hardness and elastic modulus were calculated using the Oliver-Pharr method [78]. Although the traditional Oliver-Pharr analysis is subject to uncertainties for a relatively soft film on a hard substrate [147], these errors can be mitigated by measuring the true contact area after indentation [148].

Load-displacement curves at a peak load of 625 mN collected during nanoindentation tests for the Cr coatings produced by Vendor II are shown in Figure 5.3a. The maximum penetration depth of the indenter was between 1.5–2 μm. SEM images of the indents showed that the nano-indents were well-defined, but cracks initiated at the indent corners for the P-DCMS, I-DCMS, and HiPIMS coatings. An example of the observed cracking is shown in Figure 5.3b. FIB-SEM cross-sectional examination of the cracks revealed that the crack propagation occurred along the intercolumnar boundaries (Figure 5.3c). This observation implies weak cohesion strength between the individual columnar structures, leading to fracture by decohesion emanating from the indent corners due to higher stress concentration. The deformed columar grains underneath the nano-indent on the P-DCMS coating are shown in Figure 5.3d. The localized deformation is evident under the center of the indent where the columnar grains have buckled near the surface. However, the grains near the edges of the indent expereinced minimal deformation and remained intact.

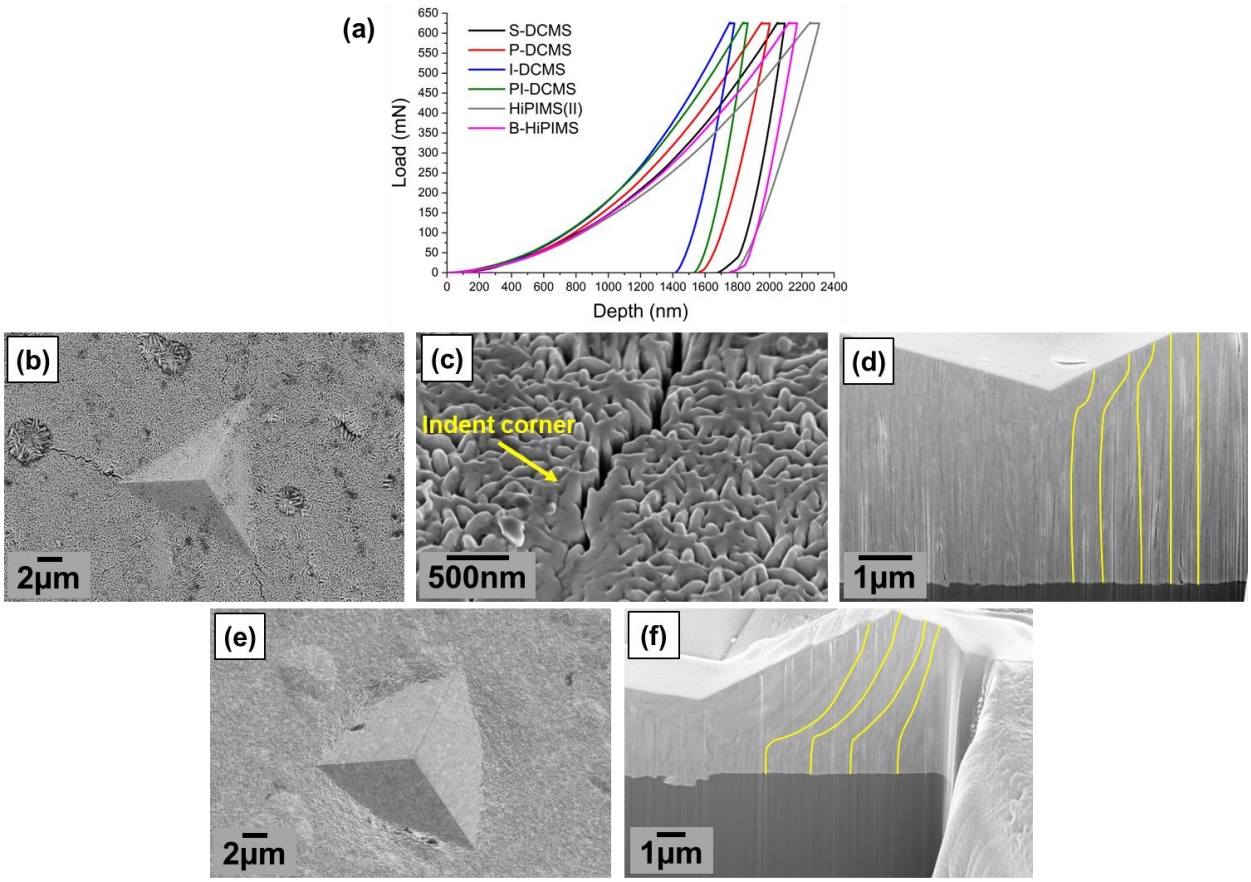

Figure 5.3: (a) Nanoindentation load-displacement curves collected at a peak load of 625 mN for the six coating types; (b) SEM image of 625 mN indent on the P-DCMS coating exhibiting cracks initiated at indent corners; (c) High magnification SEM image of a crack emanating from an indent corner on the P-DCMS coating; (d) Cross-section of 625 mN indent on the P-DCMS coating. Markings show the deformation pattern of the columnar grains; (e) SEM image of the 625 mN indentation on the B-HiPIMS coating showing material pile-up; (f) Cross-section of 625 mN indent on the B-HiPIMS coating. Markings show the deformation pattern of the columnar grains.

Material pile-up around the nano-indents was observed in the PI-DCMS and B-HiPIMS coatings, which is manifested as outward bowing of the indent edges as shown in Figure 5.3e. The plastic flow of the columnar grains in the B-HiPIMS coating was identified underneath the indent (Figure 5.3f). The FIB cross-sectional image shows deformed grains with very high curvature through the coating thickness. The extent of deformed material encompasses a much larger volume than observed in the P-DCMS indent cross section. Cross-sectional TEM imaging of a indent conducted to a peak load of 576 mN was performed to further examine deformation in the B-

HiPIMS coating. BF and DF TEM images of the indent cross section are shown in Figure 5.4. The TEM images illustrate extensive plastic deformation in the B-HiPIMS coating, as indicated by the grains under the center of the indent having bent at nearly a 90° angle relative to the growth direction. Refinement of the columnar grains can be observed in the pile-up regions away from the center of the indent.

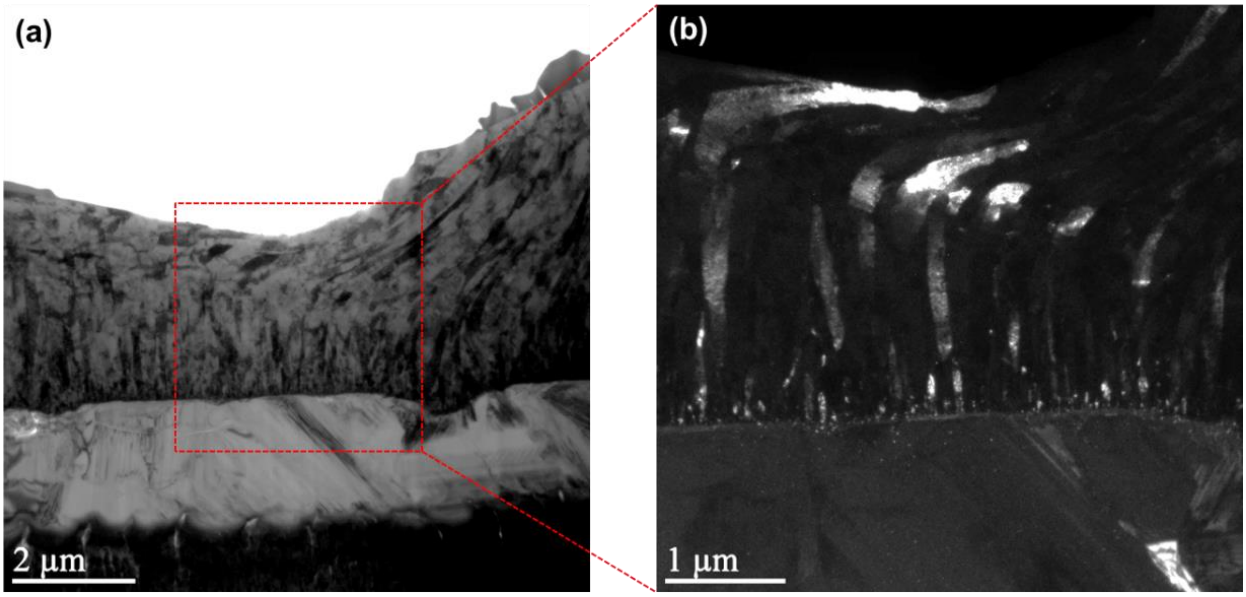

Figure 5.4: (a) Cross-sectional BF TEM image of an indent on the B-HiPIMS coating with 576 mN peak load; (b) DF TEM image of the area indicated by the red outlined box in (a) showing extensive deformation of the columnar grains.

Material pile-up around the indent is indicative of the deformation mechanism at play in the coating. As the grains under compression deform during indentation, the material underneath can be displaced outward along the sides of the indenter. When this occurs, the true indenter contact area becomes greater than the depth-calibrated contact area determined by the nanoindentation instrument [149]. Therefore, pile-up can cause errors in determination of the contact area [150]. The AFM images (Figure 5.5) show the dependence of pile-up formation during nanoindentation on the coating deposition method. An AFM image of an indentation without pile-up is shown in Figure 5.5a. In comparison, Figure 5.5b illustrates how the pile-up areas in the B-HiPIMS coating

are raised above the original surface of the coating. Figure 5.5c illustrates the increase in contact area caused by pile-up (shown in yellow) compared to the depth-calibrated contact area (A_{inst}) determined by the instrument, indicating the importance of the analysis of indentation pile-up behavior in the determination of the true contact area and associated hardness and elastic modulus.

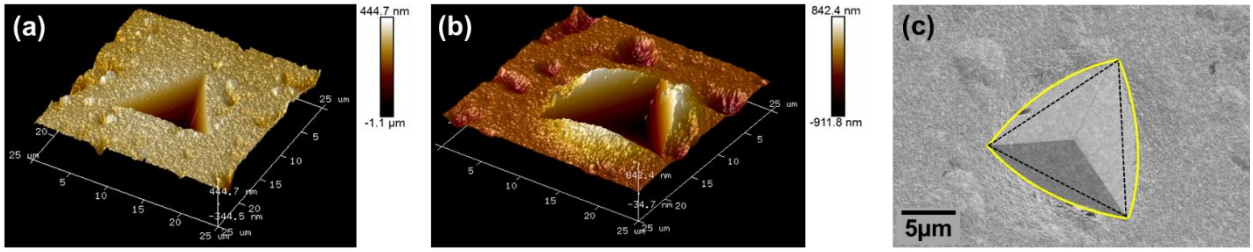

Figure 5.5: AFM images of indents on the (a) I-DCMS coating exhibiting no pile-up and (b) B-HiPIMS coating with pile-up; (c) SEM image of an indent on the B-HiPIMS coating showing the true contact area in yellow, and the contact area determined via the instrument'

The true contact area (A_{true}) of the indents was measured graphically using the ImageJ software. The ratio of A_{true}/A_{inst} was determined, where a ratio greater than one indicates the presence of pile-up, implying that the instrument underestimates the actual contact area. The A_{true}/A_{inst} ratios for each coating are summarized in Table 5.2. The PI-DCMS and B-HiPIMS coatings show ratios greater than one and the other coatings have ratios equal to one or slightly lower.

Table 5.2: Mechanical properties measured using nanoindentation and calculated parameters of the six Cr coating variants produced in collaboration with Vendor II.

Sample	A_{true}/A_{inst}	Hardness (GPa)	Elastic modulus (GPa)	H/E	W_{pl}/W_{tot}
S-DCMS	0.97	5.33 ± 0.85	248.5 ± 24.7	0.0252	0.822
P-DCMS	1.00	7.47 ± 0.55	227.5 ± 9.4	0.0379	0.769
I-DCMS	0.98	8.55 ± 0.34	284.2 ± 23.5	0.0366	0.770
PI-DCMS	1.18	6.92 ± 0.24	328.8 ± 12.0	0.0262	0.793
HiPIMS(II)	0.92	6.53 ± 0.43	154.0 ± 8.7	0.0463	0.735
B-HiPIMS	1.26	4.60 ± 0.24	269.7 ± 19.4	0.0204	0.808

The mechanical properties, specifically hardness and elastic modulus, of the coatings were measured using the method developed by Oliver and Pharr [151]. The indentation hardness is defined as:

$$\frac{P_{max}}{A} \quad \text{(Eq. 5.1)}$$

where P_{max} is the peak load and A is the contact area. The elastic modulus was determined from the reduced modulus (E_r) calculated by the instrument as:

$$E_r = \frac{1}{\beta}\frac{\sqrt{\pi}}{2}\frac{S}{\sqrt{A}} \quad \text{(Eq. 5.2)}$$

where β is a factor correcting for the indenter shape (β = 1.034 for a Berkovich probe) and S is the contact stiffness determined from the initial portion of the unloading curve. The elastic modulus of the coating (E) is then calculated from the following equation:

$$\frac{1}{E_r} = \frac{1-\nu^2}{E} + \frac{1-\nu_i^2}{E_i} \quad \text{(Eq. 5.3)}$$

where ν is Poisson's ratio and the subscript i indicates the properties of the indenter. The elastic modulus and Poisson's ratio for the diamond indenter are 1140 GPa and 0.07, respectively. A Poisson's ratio of 0.21 was used for all Cr coatings [152].

It is important to note that both hardness and elastic modulus have a dependence on contact area in the nanoindentation tests. Therefore, any error in the measurement of the contact area will propagate to final values of hardness and modulus. In calculating the hardness and elastic modulus of the coatings, the contact area measured from the SEM images was used instead of the depth-calibrated contact area to decrease the error in contact area originating from the instrument and any substrate effects. The average hardness and modulus values are summarized in Table 3. The hardness of the coatings is in good agreement with previously published values for magnetron sputtered Cr coatings [96,153,154]. The large standard deviation in the S-DCMS coating can be attributed to the high surface roughness of the coating leading to greater scatter in the measured values. Most coatings have elastic moduli similar to that of bulk Cr (~ 250 GPa). Of the six coating

types investigated, HiPIMS and PI-DCMS exhibited the lowest and highest modulus values, respectively.

In addition, the *H/E* ratio for each coating was calculated from this dataset to be used as an indicator of pile-up behavior (Table 3). It has been reported that materials with a lower *H/E* ratio tend to exhibit pile-up ($A_{true}/A_{inst} > 1$), while materials with a higher *H/E* ratio tend to show sink in ($A_{true}/A_{inst} < 1$) [155]. In materials with a lower *H/E* ratio, plastic deformation occurs more readily, resulting in the formation of a larger plastic zone around the indenter and subsequent pile-up formation [156]. This trend is consistent with the observations for the six coatings investigated; PI-DCMS and B-HiPIMS exhibited material pile-up, and both showed lower *H/E* ratios than other coatings. Although the S-DCMS coating also had a low *H/E* ratio, pile-up behavior was not observed. This will be discussed further in the next section.

Finally, the load-displacement curves were analyzed to calculate the fraction of the plastic work done during nanoindentation. The plastic work fraction is considered a parameter corresponding to the ductility of a material. First, the total work of indentation (W_{tot}) is calculated using the area under the loading portion of the curve. The elastic work portion (W_{el}) is the area under the unloading portion of the curve. This illustrated in Figure 5.6. Therefore, plastic work is $W_{pl} = W_{tot} - W_{el}$, and the fraction of plastic work is simply W_{pl}/W_{tot} [157]. More ductile materials are expected to show large values of W_{pl}/W_{tot} while brittle materials typically have values less than 0.5 [158]. The average fraction of plastic work for each coating is summarized in Table 3. The coatings exhibiting material pile-up (PI-DCMS and B-HiPIMS) showed low *H/E* ratios but high W_{pl}/W_{tot} values.

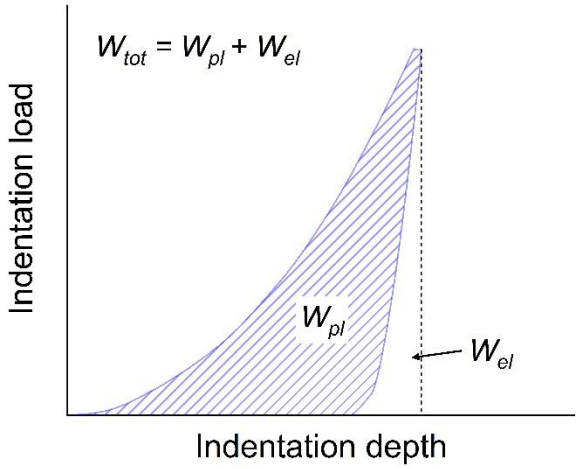

Figure 5.6: Qualitative load-displacement curve with definitions of plastic and elastic work.

Similar nanoindentation experiments were conducted on the S-DCMS and HiPIMS coatings produced in collaboration with Vendor I. The S-DCMS coating produced by Vendor I has mechanical properties comparable to the S-DCMS coating produced by Vendor II on account of their similar microstructures. Since both coatings have fully dense microstructures, it is most reasonable to compare the Vendor I HiPIMS coating to the Vendor II B-HiPIMS coating. While both coatings have elastic moduli similar to that of bulk Cr (~ 270 GPa), the HiPIMS coating is significantly harder with values approaching10 GPa, compared to about 5 GPa for the B-HiPIMS coating. The extremely fine grain size of the HiPIMS coating is the most likely contributor to the higher hardness. The difference in mechanical response between the two coatings is illustrated in the load-displacement curves shown in Figure 5.7a. The higher *H/E* ratio of the HiPIMS coating compared the B-HiPIMS leads to less indent pile-up, as shown in Figure 5.7b.

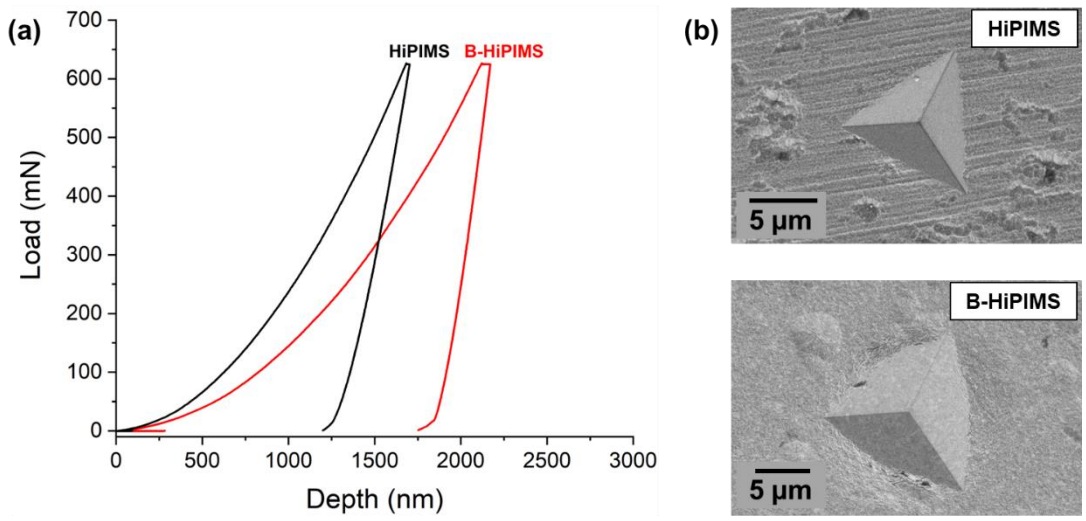

Figure 5.7: (a) Load-displacement curves for the B-HiPIMS and Vendor I HiPIMS coatings; (b) SEM images of 625 mN indents on the indicated coating types.

5.2.2 Effect of microstructure on nanomechanical behavior

From the standpoint of the reactor application, it is desirable for the Cr coatings to possess sufficient ductility to accommodate the stress evolution from swelling of the underlying SiC cladding during operation. Additionally, the coating should have good tribological properties to resist grid-to-rod fretting originating from flow-induced vibration of the fuel cladding and any wear during the insertion of the cladding in the reactor system.

Although plastic deformation of a coating can be limited if it contains porosity, a clear trend between hardness and porosity was not identified. Ion bombardment of the substrate during deposition increased the hardness of the coating as in the case of I-DCMS coating which showed the highest hardness among the six types of the Cr coatings. When pulsing was combined with ion bombardment (PI-DCMS process), the hardness decreased slightly, due to larger grains induced by the pulsing effect. A similar result was also observed in the B-HiPIMS coating where the microstructure was very dense but showed the lowest hardness due to the larger grain size. It is noted that residual stresses could also influence the pile-up behavior, which subsequently affects the mechanical property measurements as discussed previously.

Porosity content influenced the elastic modulus of the coatings, with coatings containing nanoscale porosity showing relatively lower moduli. During nanoindentation, it is likely that the intercolumnar defects in the coating matrix become sealed at the peak load and elastically recover during unloading. This hypothesis is also useful to explain the low modulus of the HiPIMS coating, where the presence of a higher volume fraction of fine intercolumnar pores resulted in sponge-like elastic response during unloading.

It is interesting to note that the S-DCMS coating did not exhibit pile-up although its low *H/E* ratio relative to the other coatings suggest that it should be susceptible to pile-up. It is hypothesized that the significant amount of intercolumnar porosity in the S-DCMS coating acted as a mechanical buffer to mitigate pile-up formation around the nano-indent. Some of the displacement from nanoindentation was consumed to seal the porosity present in the coating instead of plastic deformation of the columnar grains. This explanation can also be applied to the other coatings with significant porosity levels. For example, in the porous P-DCMS coating (Figure 5.3d) it was found that only local regions of the grains were deformed but much of the material under the center of the indent had been densified. The fully dense B-HiPIMS coating exhibited more extensive deformation around the nano-indent as there was no porosity to act as a buffer, and material was forced to deform outward along the indenter (Figure 5.3f). Qualitative examinations of coating ductility can be drawn from characterization of material pile-up and calculation of plastic work fraction during nanoindentation. The presence of pile-up and high plastic work fractions in PI-DCMS and B-HiPIMS coatings are indicators of plasticity and suggest these types of coating may perform favorably when subjected to the tensile hoop stress generated by swelling of SiC under neutron irradiation.

5.3 Elevated temperature nanoindentation and indentation creep test

The nanoindentation system used in this research is also equipped with an elevated-temperature stage which allows for indentation testing up to 500 °C, which was used for elevated temperature measurements and indentation creep tests. In the high temperature stage, the sample was clamped between two plates which heated the sample from the top and bottom. An argon cover gas was flowed into the space between the two plate heaters to minimize oxidation during high temperature exposure. Figure 5.8 shows the results of an indentation test at room temperature and 500 °C on the Vendor I HiPIMS Cr coating. The hardness decreased by about 1 GPa at 500 °C. This result initially suggests that the mechanical properties and wear resistance of the Cr coating should not be dramatically affected by the elevated temperature inside the reactor core.

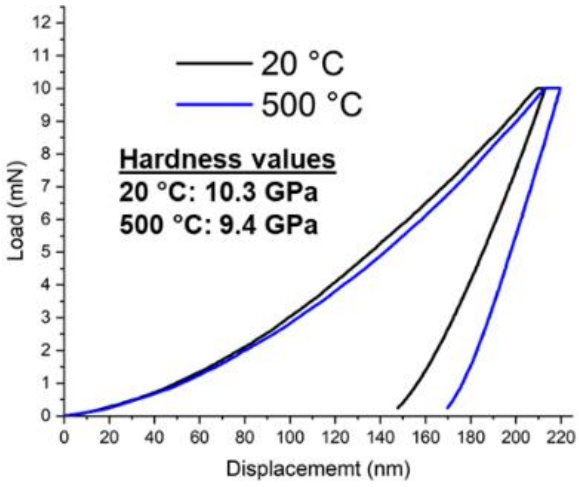

Figure 5.8: Nanoindentation load-displacement curves collected at 10 mN peak load and resulting hardness values for tests at 20 ºC and 500 °C on the HiPIMS Cr coating.

The elevated temperature nanoindentation stage also provides the opportunity to conduct creep testing. A continuous stiffness measurement (CSM) test method was used to conduct creep tests. At the loads and displacements relevant to nanoindentation, the effects of thermal drift can be quite considerable, especially when the need arises to conduct an indentation lasting more than a few seconds, such as for a creep test. In the CSM technique, a small oscillation is applied to the nominal

load setpoint, and the resulting shift in displacement amplitude is monitored [79]. Through this process, the instrument continuously measures the contact stiffness, accounts for the effects of thermal drift, and provides a precise measurement of displacement which is needed for an indentation creep test.

During an indentation creep test, the indenter is held at a constant load for an extended period, normally at least 300 seconds. Displacement (*h)* and hardness (*H*) are both measured as a function of time. The indentation strain rate $\dot{\varepsilon}_i$ is defined as $\dot{h}/h$ where $\dot{h}$ is the instantaneous time derivative of the displacement [159]. Using the power law creep equation:

$$\dot{\varepsilon} = A\sigma^n e^{(-Q_c/RT)} \quad \text{(Eq. 5.4)}$$

the creep stress exponent (*n*) can be calculated from the slope of a plot of ln ($\dot{\varepsilon}$) vs. ln (*H*) where the instantaneous hardness is assumed to be representative of the stress (σ) [160]. The creep exponent is a parameter often used to determine the creep mechanism (e.g., dislocation glide, climb, grain boundary diffusion). If tests are conducted across a range of temperatures, the creep activation energy (Q_c) can also be calculated.

An indentation creep test was conducted on the Vendor I HiPIMS Cr coating and an annealed bulk Cr control sample. The test was conducted at room temperature and 500 °C with a load of 10 mN and 600 s hold time. The difference in hardness and grain size between bulk Cr (3 GPa hardness) and the HiPIMS coating (10 GPa hardness) results in slightly different mechanical responses during the creep test. Figure 5.9a shows the measured displacement during the creep test. The displacement is greater in the bulk Cr due to its lower hardness. In order to calculate the indentation strain rate, the displacement vs. time data were fit to an empirical equation [161]:

$$h = h_i + a(t - t_i)^{0.5} + b(t - t_i)^{0.25} + c(t - t_i)^{0.125} \quad \text{(Eq. 5.5)}$$

where h_i and t_i are the depth and time at the onset of creep and a, b, and c are fitting constants. The indentation strain rate is shown in Figure 5.9b. Similarly, strain rates are greater in the bulk Cr. An interesting finding is that the strain rate drops to zero for both samples are room temperature. It is hypothesized that this is due to the mechanical recovery of the material imparting an upwards force on the indenter and essentially counteracting any creep effects. This mechanical recovery occurs more quickly in the HiPIMS coating, again most likely due to its higher hardness. Plots of ln $(\dot{\varepsilon})$ vs. ln (H) used for the calculation of the creep exponent (n) are presented in Figure 5.9c. The creep exponent for bulk Cr at 500 °C was roughly $n \approx 8$. This value suggests that the creep deformation occurs via dislocation motion, which is expected for a coarse-grained material well below its melting point [162]. For the HiPIMS coating, the creep exponent was approximately $n \approx 24$. This large value of n is indicative of what is called power-law breakdown where the mechanisms at play are less understood [162], but in this case, the creep of the HiPIMS coating can be considered as negligible.

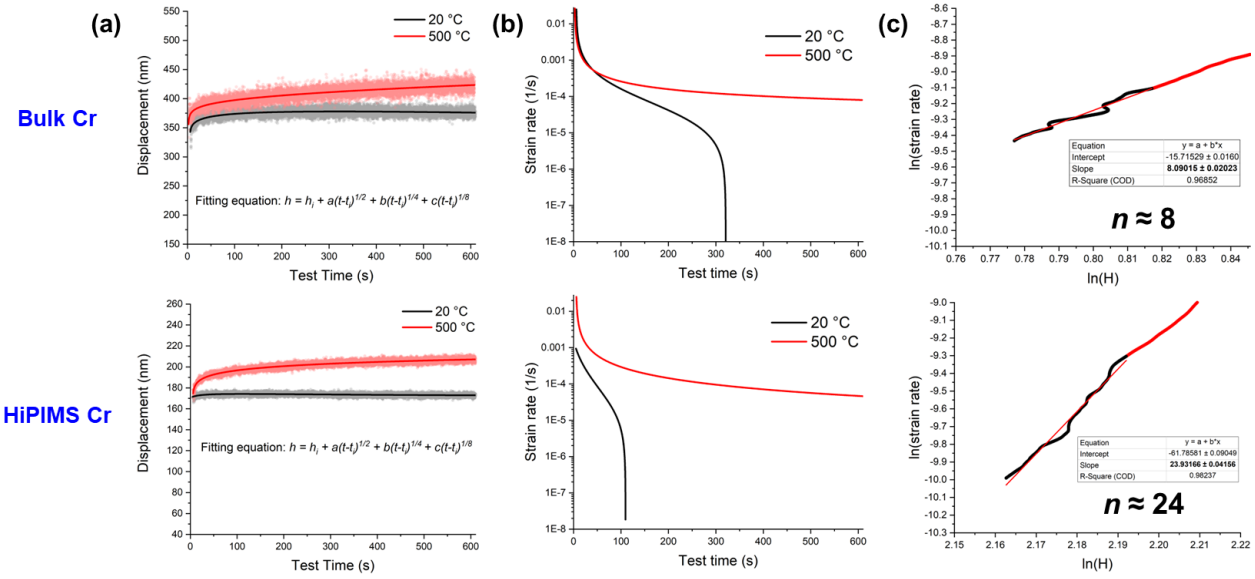

Figure 5.9: Results from nanoindentation creep testing of bulk Cr and HiPIMS Cr at room temperature and 500 °C: (a) Measured displacement values during the creep experiment, (b) Calculated strain rates, (c) Plots of $ln\ (\dot{\varepsilon})$ vs. ln (H) used for the calculation of the creep exponent

(n) at 500 °C. A creep exponent of n = 8 indicates creep is controlled by dislocation motion, and an exponent of n = 24 indicates creep of the material is negligible.

5.4 Nanoscratch wear tests

As a preliminary investigation of the tribological properties of the Cr coatings, nano-scratch wear tests were conducted using the nanoindentation instrument equipped with a lateral force transducer and 1 μm cono-spherical diamond probe. In the nano-scratch test, the probe traverses across the sample surface while maintaining a specified load and velocity. Displacements and forces are measured in the normal and lateral directions. From this data, the coefficient of friction (defined as lateral force/normal force) can be calculated. After the test, the probe was used in scanning-probe mode to image the surface topography of the wear scar.

For the nano-scratch test, the load was set at 1 mN, the probe velocity was 0.67 μm/s, and the total scratch length was 10 μm. The probe made four total passes across the same scratch track. The test was conducted on the S-DCMS and B-HiPIMS coatings. Figure 5.10a shows scanning probe microscopy images of the resulting wear scars after the nano-scratch test. Height profiles collected across the wear scar at the locations indicated in Figure 5.10a are plotted in Figure 5.10b. It is clear that the depth and width of the wear scar are larger in the S-DCMS coating compared to B-HiPIMS. The smoother surface and strong intercolumnar cohesion in the B-HiPIMS coating improved its tribological performance by reducing friction (or resistance to sliding motion) and preventing the creating of microscale debris. The friction coefficient calculated during the nano-scratch test is shown in Figure 5.10c. Both coatings have approximately the same coefficient of friction on average. However, the coefficient of friction for the S-DCMS coating varied over a much wider range (i.e., higher scatter) than for the B-HiPIMS coating due to the higher surface roughness and weak intercolumnar cohesion.

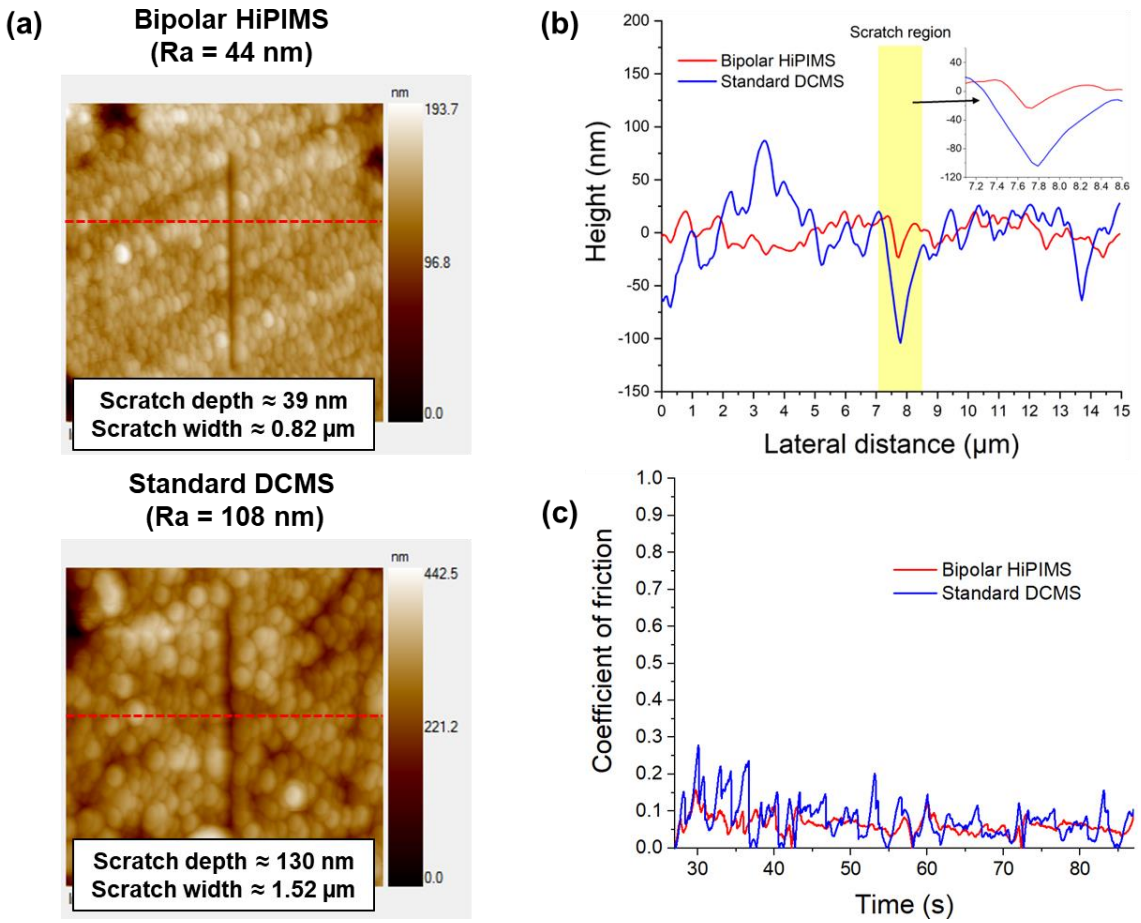

Figure 5.10: (a) Scanning probe microscopy images of the resulting wear scars on the S-DCMS and B-HiPIMS coatings after the nano-scratch test. Red lines indicate the location where height profiles were collected; (b) Profilometry data from the locations marked in red in (a) with the scratch cross section highlighted and plotted in the inset; (c) Coefficient of friction calculated continuously during the test.

6. *In Situ* High Temperature X-Ray Diffraction Experiments

This chapter features direct content from the following journal article first-authored by the PhD candidate:

K. Quillin, H. Yeom, X. Pu, D. Frazer, K. N. Sasidhar, K. Sridharan, "Effects of elevated temperature exposure on the residual stress state and microstructure of PVD Cr coatings on SiC investigated via in situ X-ray diffraction and transmission electron microscopy," *Materials Science and Engineering: A* 879 (2023) 145273.

6.1 Experiment description

Prior studies of the Cr-coated SiC system including the work presented in the preceding sections have focused on characterization and testing of coating materials at ambient conditions. *In situ* high temperature experiments can provide valuable insight into the evolution of microstructure and residual stress in the coatings and the interactions between Cr and SiC. For example, *in situ* experiments can be used to understand how a coating will perform at reactor operating conditions and how its characteristics may change after prolonged exposure at high temperatures.

In situ XRD techniques have previously been used to study thin films at elevated temperatures [163–168]. In addition to measuring stress at elevated temperatures, these techniques have also been applied to study crystallization and phase transformations in certain coating materials [165,168] . Furthermore, analysis of the diffraction peak intensity and broadening over time provides information about changes in the features of coating microstructure, such as defect density, grain size, and crystallographic texture. *In situ* XRD experiments have also been used to examine the formation of new phases that develop through the interdiffusion and chemical reaction of two compounds [169,170]. While the Cr-SiC system has not been studied via *in situ* methods, there is a moderate body of existing work concerned with the interdiffusion and phase formation between Cr and SiC [10,171–174]. The previous work has mainly involved Cr-SiC diffusion

couple experiments, identification of the Cr-C and Cr-Si phases formed in the reaction layer, and analysis of the diffusion pathways in relation to the ternary phase diagram.

In situ XRD experiments were performed by the author at the Irradiated Materials Characterization Laboratory (IMCL) at Idaho National Laboratory using a Malvern Panalytical Empyrean diffractometer equipped with an Anton Paar HTK 1200N heating chamber. Measurements were conducted in the Bragg-Brentano geometry using a Cu Kα X-ray source (λ = 1.5406 Å) operated at 45 kV and 40 mA. The fully enclosed heating chamber was pumped down to a pressure on the order of 0.001 Pa to minimize sample oxidation at elevated temperatures. Samples were placed on an alumina stage inside the heating chamber. To account for the thermal expansion of the stage at elevated temperatures, the stage height was automatically adjusted by the instrument's software to maintain proper sample alignment,

Three experimental temperatures relevant to LWRs were selected: 300 °C, 700 °C, and 1200 °C. 300 °C represents the LWR normal operating temperature, while 700 °C is a temperature that the cladding may experience during power transient conditions. The highest experimental temperature, 1200 °C, is considered the onset of an accident condition that may occur due to loss of coolant in the reactor. For these high temperature studies, the heater was ramped at a rate of 10 °C/min to reach the test temperatures. XRD measurements were initiated as soon as the experimental temperature was reached. New samples were used for each experiment. 2θ scans and residual stress measurements were performed at evenly spaced time intervals throughout the duration of the test. The 2θ scans and residual stress measurements were conducted sequentially, followed by a waiting period. For the 1200 °C tests, no residual stress measurements were performed. Approximately twenty 2θ scans and residual stress measurements were performed during each experiment. The wait time between measurements varied depending on the total

duration of the test. Scans were also performed at room temperature before and after the elevated temperature portion of the experiments. Table 6.1 summarizes the temperatures and hold times for the *in situ* XRD experiments.

Table 6.1: Experimental matrix for the *in situ* XRD experiments. Separate B-HiPIMS and DCMS samples were tested at each condition.

Temperature (°C)	Hold time (h)	Scans performed	Approximate wait time between measurements (h)
300	84	2θ, residual stress	4
700	16	2θ, residual stress	0.75
1200	3	2θ	0

The 2θ scans and residual stress measurements were performed in accordance with the procedure described in Section 2.2. The scanning time was doubled for DCMS samples due to a lower diffracted X-ray intensity. To account for errors in the residual stress measurements associated with the uncertainty of peak fitting, error analysis of the residual stress data was conducted and is described in Appendix E. After the high temperature exposure, the microstructure of the samples was characterized using (S)TEM, EDS, and electron diffraction. CALPHAD-based thermodynamic calculations were performed using Thermo-Calc 2022b software to predict phase evolution due to the interdiffusion between the Cr coating and SiC substrate. The thermodynamic data pertaining to the ternary Cr-Si-C system was obtained from the commercially available SGTE alloy solutions v6 (SSOL6) database, which is primarily based on the assessment by Du et al. [175].

6.2 300 °C *in situ* XRD study

6.2.1 Microstructural characterization

Bright field TEM images of the B-HiPIMS Cr and DCMS Cr coatings taken after the *in situ* XRD experiment at 300 °C are shown in Figure 6.1. As expected, given this relatively low

temperature in relation to the melting point of Cr, no changes were observed in the coating microstructure, grain size, or interface structure. In the B-HiPIMS coating, columnar grains were observed, and many grains were observed to grow uninterrupted through nearly the entire coating thickness, similar to the as-deposited microstructure. Fine, fibrous grains separated by narrow regions of intercolumnar porosity were observed in the DCMS coating, very similar to the as-deposited microstructure.

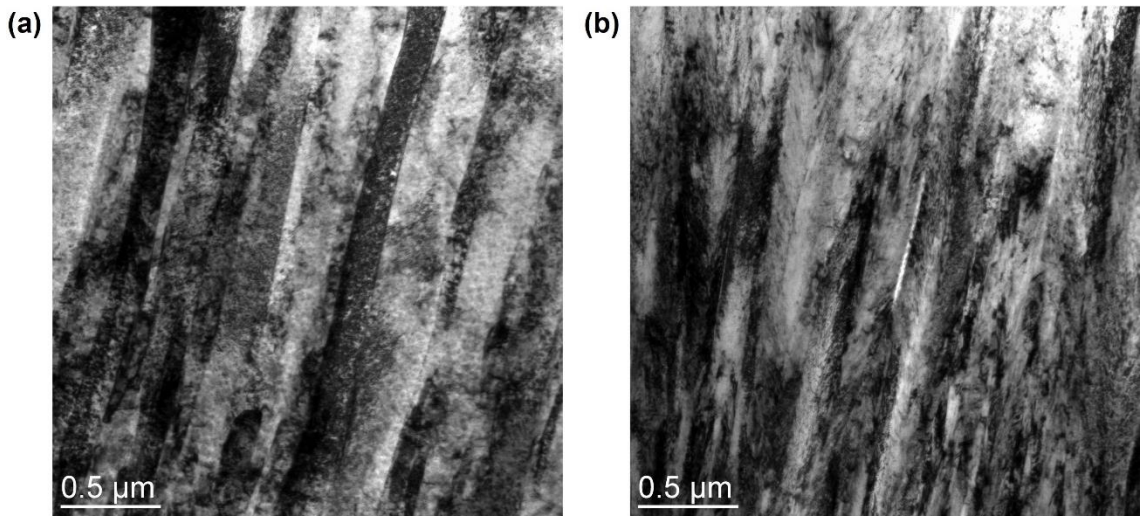

Figure 6.1: BF TEM images of the (a) B-HiPIMS and (b) DCMS coatings after 84 hours at 300 °C.

6.2.2 2θ scans

Figure 6.2 shows a selection of the 2θ patterns collected during the 300 °C experiments conducted for a duration of 84 hours. The patterns labeled "25 °C-start" and "25 °C-end" represent the measurements taken before and after the elevated temperature portion of the experiment. "300 °C-0 h" and "300°C-84 h" indicate the first and last scans taken at 300 °C, respectively. Peaks originating from the β-SiC substrate were observed in the diffraction patterns of both the B-HiPIMS and DCMS samples due to X-rays penetrating through the full Cr coating thickness and reaching the SiC substrate. The B-HiPIMS coating exhibited a strong (110) texture, and the intense Cr (110) peak dominated the diffraction pattern. Patterns collected from the DCMS sample showed

a lower signal-to-noise ratio and lower intensity relative to B-HiPIMS on account of the higher surface roughness and porosity of the DCMS coating. The magnified view of the Cr (110) peak presented in Figure 6.2 shows the evolution of the peak location at 300 °C and at room temperature before and after the experiment. At 300 °C, the peak location is shifted to a lower angle due to thermal expansion of the lattice and the corresponding increase in d-spacing. A quantitative analysis of peak characteristics (e.g., location, width, relative intensity) was conducted via peak fitting.

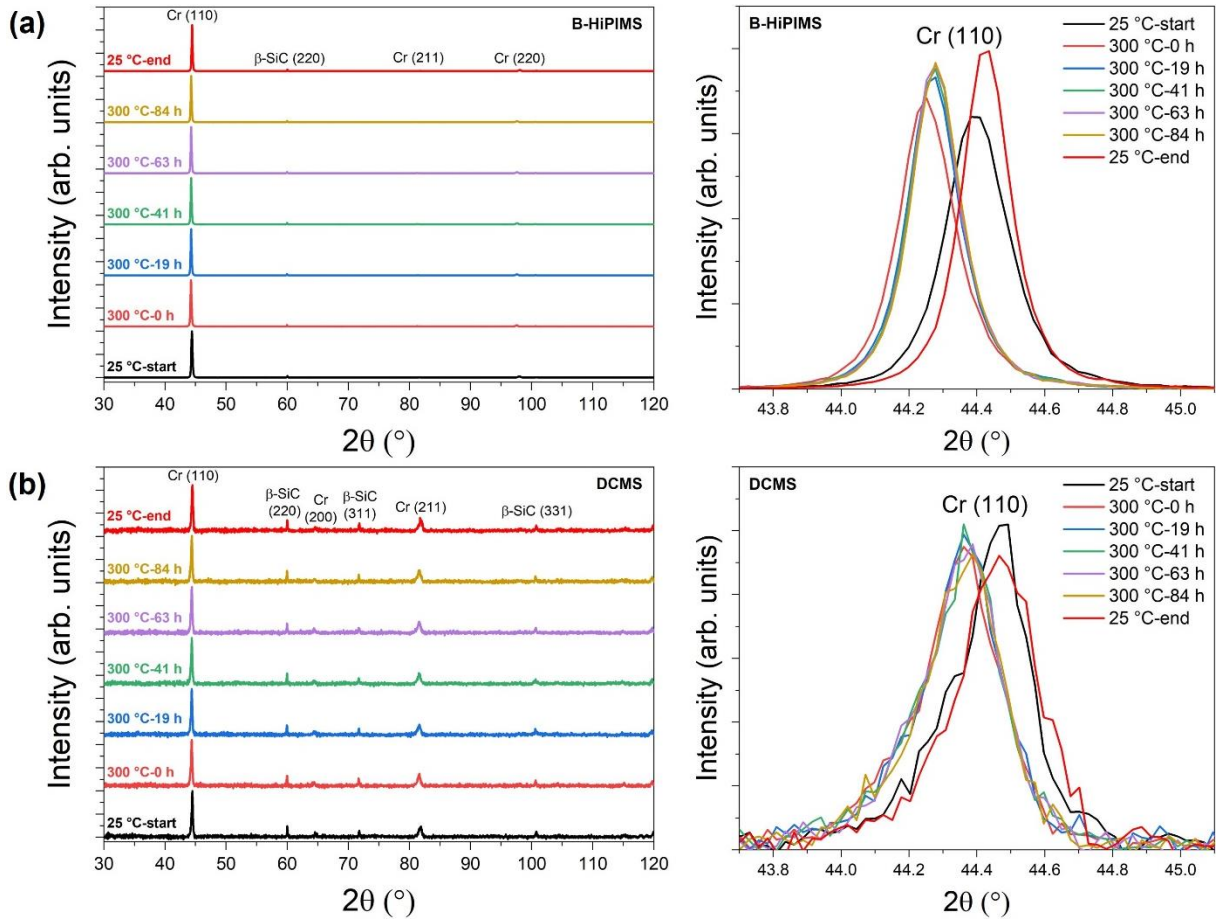

Figure 6.2: 2θ XRD patterns and magnified view of the Cr (110) diffraction peak signals collected during the 300 °C experiment as a function of time for the (a) B-HiPIMS coating and (b) DCMS coating.

The diffraction peak analysis including peak location, full width at half maximum (FWHM), and texture coefficient for the Cr coatings at 300 °C are shown in Figure 6.3. For both coatings,

the Cr (110) peak shifted marginally to a higher 2θ angle during the course of the 300 °C experiment (Figure 6.3a). This is due to a change in stress state in the coatings causing a change in lattice parameter. The peak shift was larger during the initial stages of the test and became more gradual during the remainder of the experiment. The magnitude of the initial peak shift in the B-HiPIMS coating was about twice as large as in the DCMS coating. In addition, the B-HiPIMS peak is at a lower angle than the DCMS peak, indicative of its higher compressive stress state.

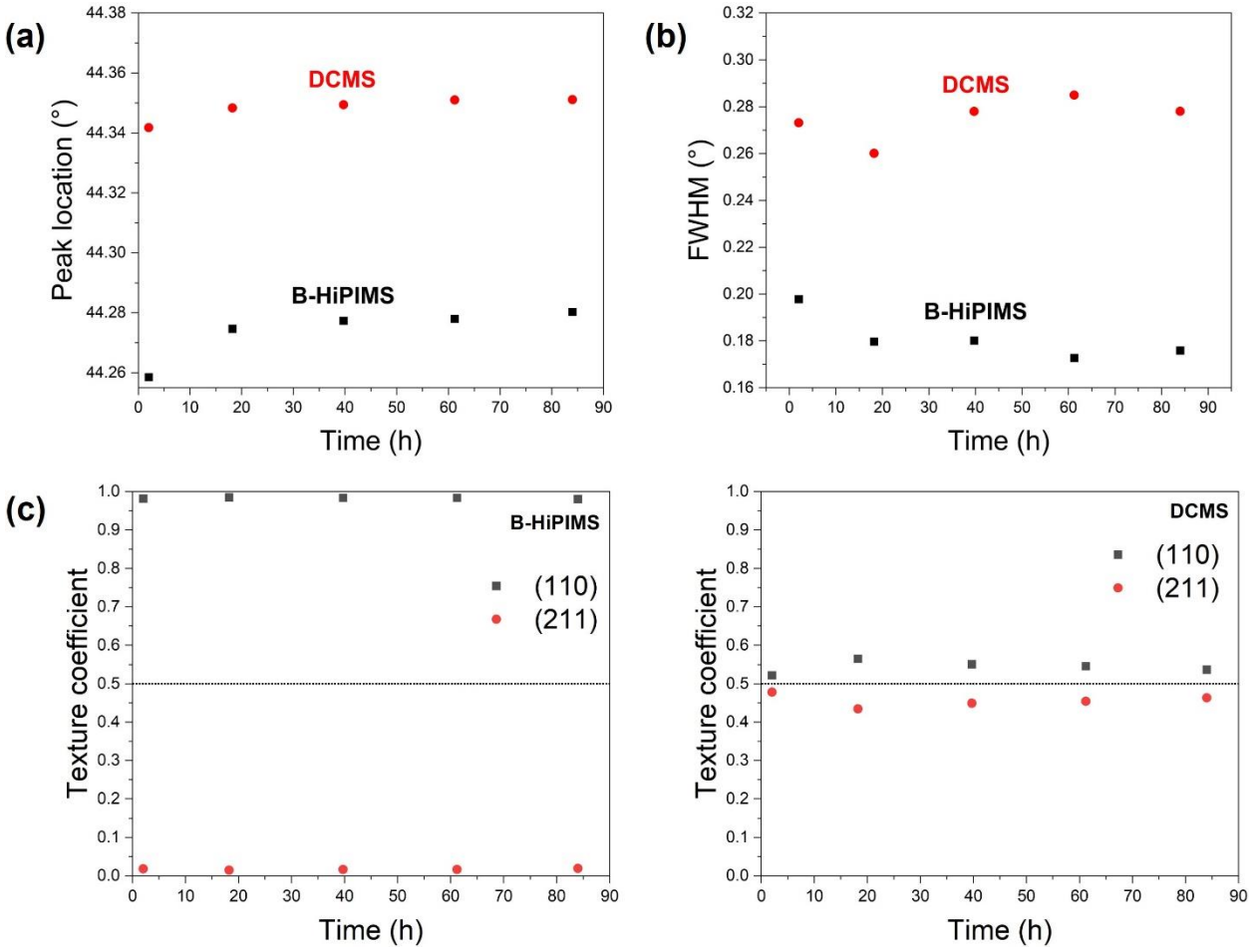

Figure 6.3: Evolution of (a) Cr (110) peak location, (b) Cr (110) peak FWHM, and (c) texture coefficient for the B-HiPIMS and DCMS coatings at 300 °C. The dotted line in the texture coefficient plots represents the texture coefficient value for a randomly oriented crystal structure.

The evolution of the Cr (110) peak width (FWHM) for the two coatings at 300 °C is shown in Figure 6.3b. The width of the (110) peak in the B-HiPIMS coating gradually decreased over time.

It is known that many factors influence peak broadening including strain, defect density, and grain size [176]. The gradual decrease in peak width for the B-HiPIMS sample is attributed to a reduction in stress and defect density as the coating anneals over time at 300 °C. For the DCMS coating, the peak width remains essentially constant over time, an indication that the stress state and defect density in the coating are not changing to a significant extent. The greater FWHM of the Cr (110) peak in the DCMS coating compared to B-HiPIMS is due to the finer grain size, a higher number density of defects, and inhomogeneous stress state of the DCMS coating.

Lastly, the texture in the coatings was compared by using the texture coefficient. The texture coefficient is defined as,

$$\delta_{hkl} = \frac{I_{hkl,exp}/I_{hkl,0}}{\sum_{hkl} I_{hkl,exp}/I_{hkl,0}} \quad \text{(Eq. 6.1)}$$

where the I_{hkl} is the intensity of a specific diffraction peak, and the subscript *exp* indicates the experimental values and the subscript *0* indicates the theoretical values for a random orientation distribution [101]. A texture coefficient is calculated for each *hkl* plane that is analyzed. In a completely random crystalline structure, the value of the texture coefficient is equal for every *hkl* plane. This value depends on how many diffraction peaks are included in the analysis. In this case, because two sets of peaks were included in the texture analysis the texture coefficient for a randomly oriented crystal structure is 0.5.

Figure 6.3c shows the calculated texture coefficients for the B-HiPIMS and DCMS coatings over time at 300 °C. For both coatings only the (110) and (211) peaks offered intensities consistently high enough for analysis across all measurements. As confirmed by room temperature measurements, strong (110) texturing is exhibited in the B-HiPIMS coating, which is also reflected in the value of the texture coefficient being close to unity. The (110) preferred orientation of the B-HiPIMS is expected based on the moderate substrate heating and ion acceleration during

deposition providing sputtered atoms sufficient mobility to grow in the lowest energy orientation, which is (110) for bcc Cr [177]. In comparison, atomic mobility during DCMS deposition is low, and the resulting structure is much more randomly oriented as indicated by both the (110) and (211) planes possessing a texture coefficient close to 0.5. As mentioned previously, 300 °C is not a high enough temperature for any significant diffusion or crystalline rearrangement to occur in Cr, therefore value of the texture coefficient is constant over time for both samples.

6.2.3 Residual stress measurements

The residual stress evolution in the B-HiPIMS and DCMS coatings at 300 °C is shown in Figure 6.4. As determined in previous work [76,178], the initial residual stress state of the B-HiPIMS coating is compressive, and the DCMS coating is tensile. This is also in good agreement with previous studies of magnetron sputtered Cr coatings [11,179]. Generation of interstitials through collision cascades produced by ion bombardment and incorporation of excess atoms within grains via grain boundary diffusion lead to the compressive stress in the B-HiPIMS coating [63]. In comparison, tensile stress is generated during DCMS deposition by coalescence of crystalline islands to minimize surface area during the initial stages of growth [62]. These stress states were maintained throughout the duration of the 300 °C experiment. A slight wavelike or oscillating behavior is observed in the residual stress data, which is attributed to temperature fluctuations of the sample heating stage causing small changes in sample position, which shifted peak location slightly. The error bars for the stress data were calculated by propagating the error from linear fitting of the d-spacing vs. $\sin^2\psi$ plot. The error calculation procedure is detailed in Appendix E. In general, the error in the calculated residual stress values was determined to be about ± 10%.

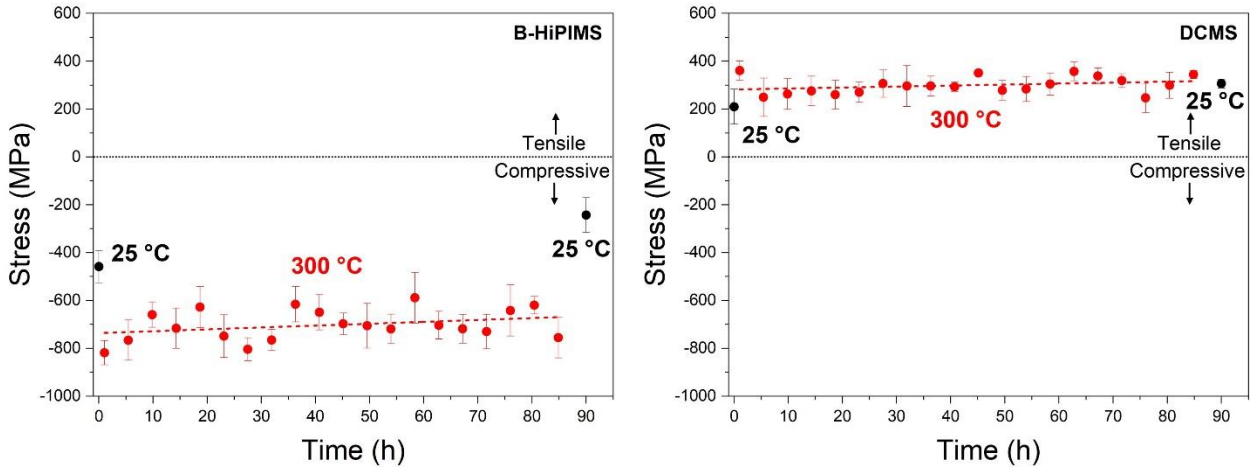

Figure 6.4: Residual stress evolution in the B-HiPIMS and DCMS coatings during the 300 °C experiment, also including the measurements conducted at room temperature before and after the test. The dotted line represents linear fitting of the 300 °C data.

In the B-HiPIMS coating, it is observed that the residual stress at 300 °C becomes more compressive compared to the initial value at room temperature. Over time, however, the stress in the B-HiPIMS sample gradually became less compressive (i.e., moving toward zero). It is believed that the deposition-induced defects that initially generate the large compressive stress were slowly being annihilated over time at 300 °C which results in stress relief. Then upon cooling of the sample from 300 °C back to room temperature, the stress shifts back to a less compressive value. The stress relief that occurred at 300 °C is visualized by comparing the data points measured at room temperature before and after the experiment, where the residual stress measured at 25 °C after the experiment has shifted closer to zero compared to the initial value. In comparison, the DCMS coating exhibits a tensile residual stress for the entire duration of the 300 °C experiment. The magnitude of the stress remains relatively constant and does not appear to vary throughout the test. It could be speculated that the stress trends slightly in tensile direction, which is consistent with the behavior of the Cr (110) peak location shown in Figure 6.3a.

6.3 700 °C *in situ* XRD study

6.3.1 Microstructural characterization

TEM images of the B-HiPIMS and DCMS coatings after the 700 °C experiment are shown in Figure 6.5. For the B-HiPIMS coating, there were clear indications of recrystallization and grain growth. The coating microstructure consists of large, equiaxed grains about 1 µm in size in place of the originally columnar grains. Because the recrystallization temperature for metals is generally about one-third to one-half of the melting point (in Kelvin), it was anticipated that microstructural changes would occur given that 700 °C is approximately 45% of the melting point of pure Cr. A chemical interaction region between Cr and SiC approximately 1 µm in width was observed at the interface. Three distinct phases (labeled Phase 1, 2, 3) were identified within this region and are shown in Figure 6.5b. Voids were also formed throughout the interaction region. The voids (10–100 nm size) were primarily observed within the newly formed phase nearest the Cr coating (Phase 1) and along the boundary between Phase 1 and the Cr coating. These voids may be a result of the Kirkendall effect where unequal diffusion rates in opposite directions create an excess of vacancies on one side of the interface which coalesce in the form of voids [174,180].

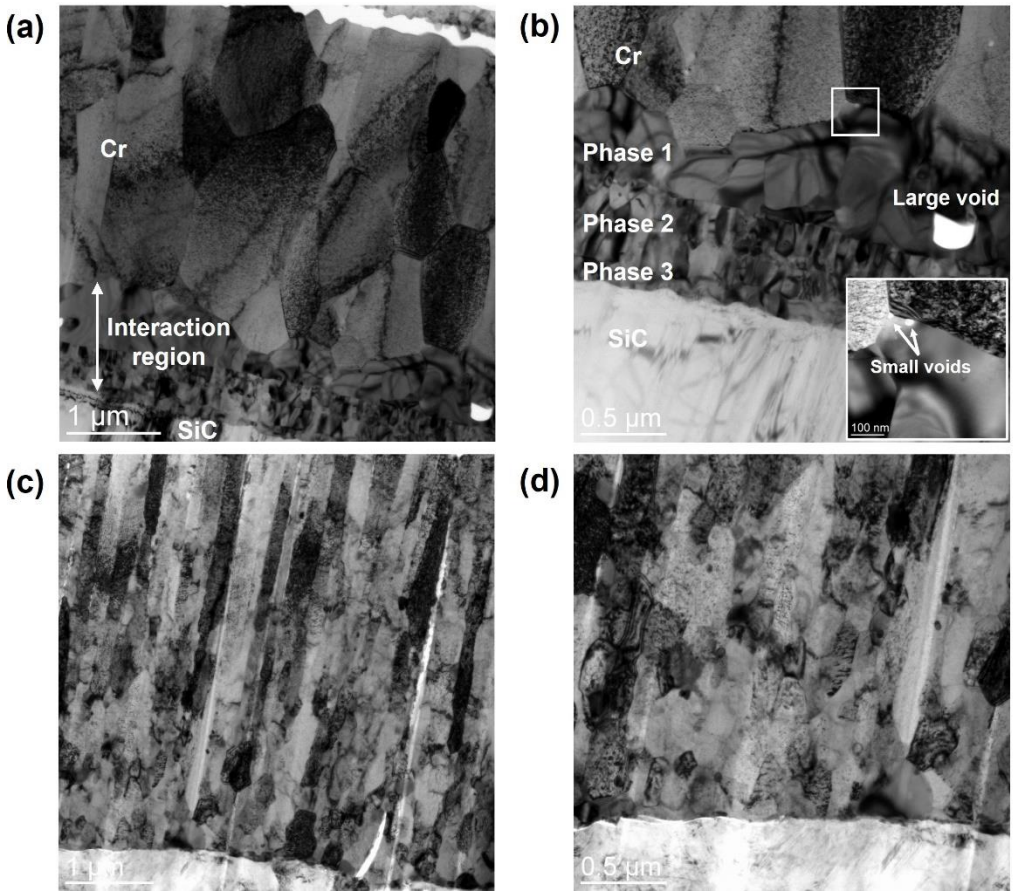

Figure 6.5: (a) BF TEM image of the B-HiPIMS Cr coating after 16 hours at 700 °C; (b) BF TEM image of the B-HiPIMS Cr coating interface showing the presence of three new phases and formation of voids. The inset plot shows a magnified view of the region enclosed by the box; (c) BF TEM image of the DCMS Cr coating after 16 hours at 700 °C; (d) BF TEM image of the DCMS Cr coating interface.

Microstructural changes were also observed in the DCMS coating after the 700 °C experiment (Figure 6.5c) but to a lesser extent than in the B-HiPIMS coating. The initial fibrously-packed microstructure of the as-deposited coating transitioned to a more columnar structure consisting of sightly coarser grains. Although the amount of intercolumnar porosity was reduced, some localized regions of porosity were still observed. The interaction region at the interface of the DCMS coating could not be clearly delineated, and distinct phase boundaries could not be observed in TEM images. In contrast to the B-HiPIMS sample, no voids were observed near the interface of the DCMS coating after the 700 °C experiment.

CALPHAD modeling of the Cr-Si-C system was performed to predict phase formation at the Cr coating/SiC substrate interface. A calculated isothermal phase diagram for the Cr-Si-C system at 700 °C is shown in Figure 6.6a. The thermodynamic calculation indicates that the formation of many Cr-C and Cr-Si phases is possible via the interaction of Cr and SiC as well as a ternary $Cr_5Si_3C_x$ phase. In addition, the quantitative fractions of equilibrium phases expected along the dotted line (joining the two end-compositions of the diffusion couple) in the phase diagram were calculated and are shown in Figure 6.6b**.** The dotted line pertains to compositions with equimolar contents of Si and C. In other words, it represents the composition pathway that would be traversed by the system in a situation where there is equal diffusivity of Si and C during the interdiffusion.

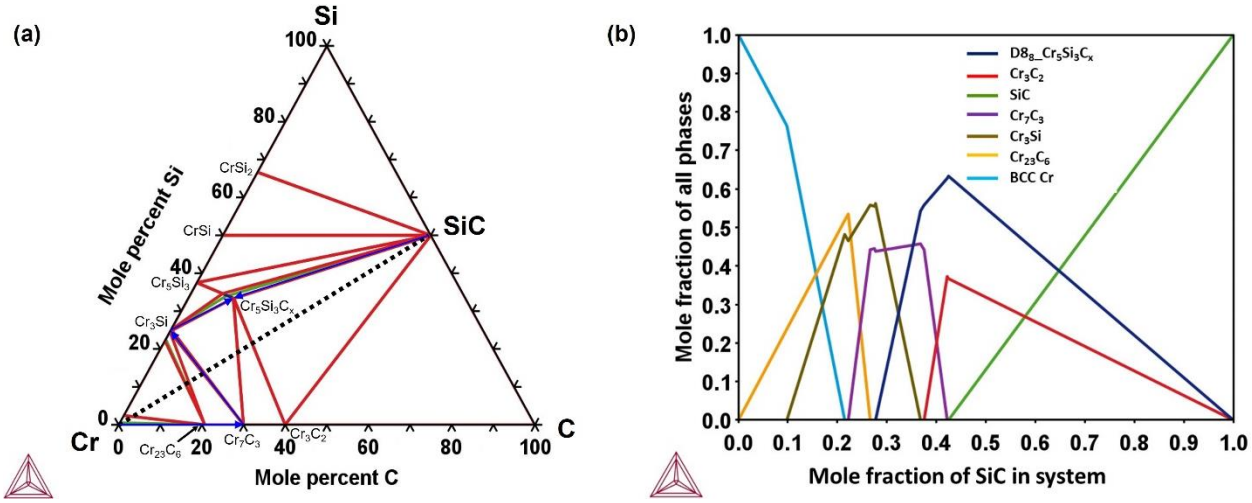

Figure 6.6: (a) Calculated isothermal phase diagram for the Cr-Si-C system at 700 °C. The black dotted line represents the path with equimolar concentrations of Si and C. The true diffusion path determined from experimental observations is indicated by the blue arrows; (b) Calculated equilibrium phase fractions along the path marked by the dotted line in (a).

STEM-EDS point scans and line profiles were performed to analyze the composition of the interfacial phases that were observed in Figure 6.5b. Table 6.2 summarizes the composition of the three new phases averaged from several EDS point scans. These results show that Phase 1 (phase nearest the Cr coating) contains significant C content and minimal Si content, indicating this is likely a Cr-C phase. Phase 2 contains a moderate amount of Si and minimal C, suggesting this

compound is a Cr-Si phase. Phase 3 (nearest the SiC substrate) contains both Si and C in addition to Cr.

Table 6.2: Average composition values (in atomic percent) for the three new phases observed in the B-HiPIMS Cr coating determined by EDS point measurements and possible phases considering the measured composition and ternary phase diagram.

	Cr	**Si**	**C**	**Possible Phases**
Phase 1	71.08	0.46	28.45	$Cr_{23}C_6$, Cr_7C_3, Cr_3C_2
Phase 2	77.02	19.82	3.15	Cr_3Si, Cr_5Si_3
Phase 3	64.13	29.62	6.23	$Cr_5Si_3C_x$

The Cr, Si, and C composition profiles extracted from the EDS line scan shown in Figure 6.7a agree with the results of the point scans from Table 6.2 indicating that within the reaction layer, C content is greatest near the Cr coating, and Si content is greatest near the SiC interface. Based on these measurements and the possible phases from the Cr-Si-C ternary phase diagram, the three phases were identified as Cr_7C_3, Cr_3Si, and $Cr_5Si_3C_x$. Because of inherent limitations associated with measuring atomic concentrations of light elements by EDS, electron diffraction patterns were also collected to confirm the presence of the Cr_7C_3, Cr_3Si, and $Cr_5Si_3C_x$ phases identified from the EDS analysis. Indexed CBED patterns for the three phases are shown in Fig. 8b. The patterns were able to be accurately indexed knowing the theoretical crystal structures and lattice parameters of the three phases, confirming their identity to be Cr_7C_3, Cr_3Si, and $Cr_5Si_3C_x$. The formation of these phases is also predicted by the thermodynamic calculations shown in Figure 6.6b where Cr_7C_3, Cr_3Si, and $Cr_5Si_3C_x$ are present in equilibrium near the Cr-rich side of the diagram.

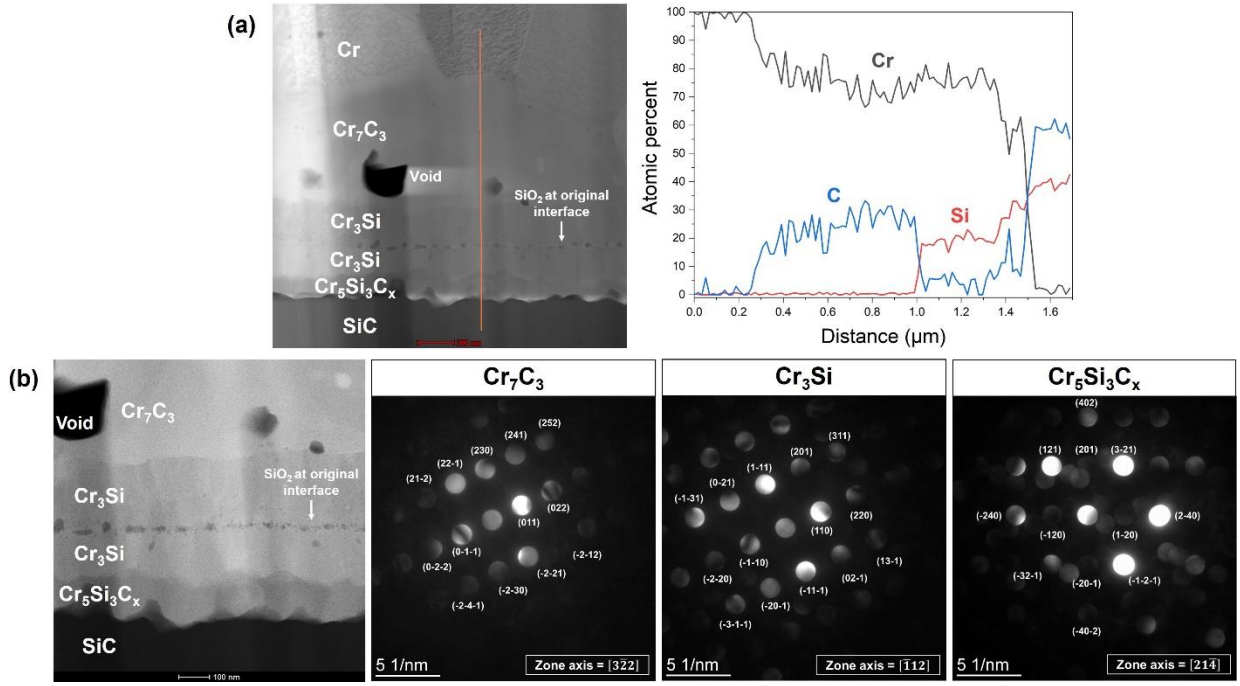

Figure 6.7: (a) HAADF STEM image of the interface in the B-HiPIMS Cr coating after the 700 °C experiment and corresponding EDS line scan data (in atomic percent) taken from the location marked in the image; (b) High magnification HAADF STEM image of the interface in the B-HiPIMS Cr coating after the 700 °C experiment and CBED patterns from the three new observed phases.

HAADF STEM images of the interface in the B-HiPIMS Cr coating revealed a line of circular particles running parallel to the interface within the Cr_3Si layer as seen in Figure 6.7a. Compositional analysis of these particles showed high concentrations of Si and O. Also, the distance from the layer of particles to the coating surface was measured and was noted to be identical to the as-deposited coating thickness. It is suggested that the particles are remnants of the native SiO_2 layer on the surface of the SiC substrate that were not fully removed during plasma or ion beam cleaning of the substrates in the vacuum chamber prior to deposition. This line of particles can be used as a reference marker to evaluate the relative diffusion of various atomic species across the interface between Cr coating and SiC substrate. Based on this approach, it appears that C is that fastest diffusing species, as the Cr_7C_3 layer extends almost 1 μm into the Cr coating from the original interface. The formation of Cr_3Si extends to only a few hundred

nanometers from the original interface in both directions, indicating the diffusion of Si into Cr and Cr into SiC is a slower process relative to the diffusion of C. These observations agree with the previously published work showing Cr-C phases tend to form nearest to the Cr layer and Cr-Si phases tend to form closer to the substrate [10,172,174,180]. By considering the identified phases and the order of the observed interfacial layers, the interdiffusion pathway with respect to the Cr-Si-C phase diagram was determined and is indicated by the blue arrows in Figure 6.6a.

Similar characterization was performed for the DCMS sample after the 700 °C experiment as shown in Figure 6.8. As suggested by the BF TEM images in Figure 6.5b, no distinct interaction layer was formed between the DCMS Cr coating and SiC substrate. This is confirmed by the EDS line scan across the coating/substrate interface. However, through further examination of the near-interface composition via EDS point scans, it was found that certain grains contained elevated C concentration, but these grains were isolated and were not present in a continuous layer near the interface. It is also interesting to note that Kirkendall voids near the interface were absent. It appears that the coating was partially debonded due to thermal stresses generated during the test, suggesting lower adhesion strength of the coating compared to the B-HIPIMS coating.

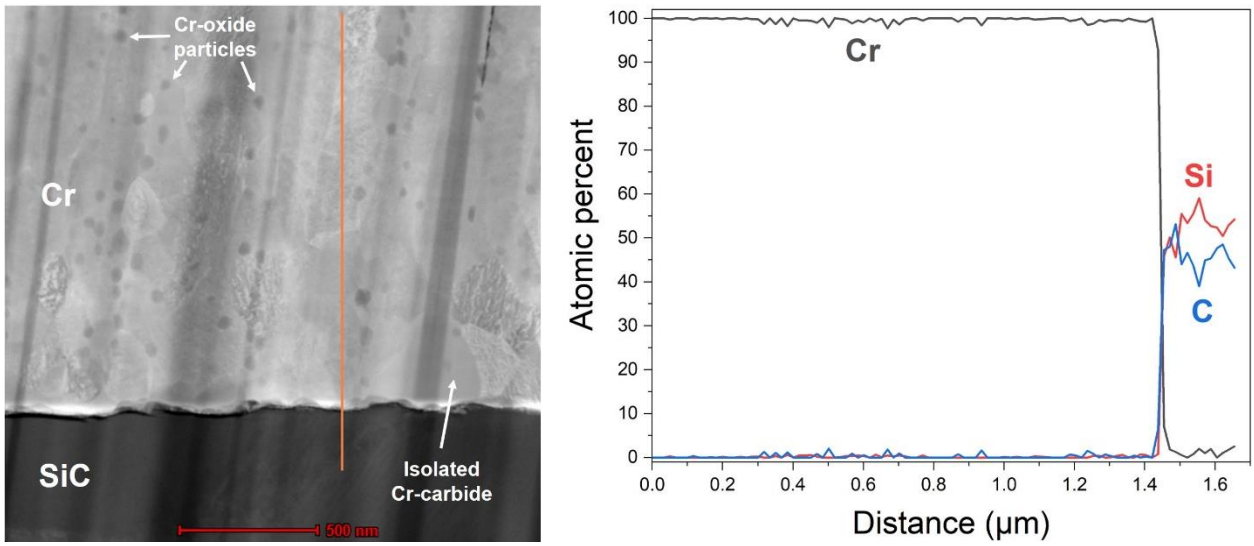

Figure 6.8: HAADF STEM image of the interface in the DCMS Cr coating after the 700 °C experiment and corresponding EDS line scan data (in atomic percent) taken from the location marked in the image.

Another observation was the presence of small particles approximately 50 nm in diameter dispersed throughout the DCMS coating. Compositional analysis of these particles showed that the particles were composed of Cr and O. It is believed that these particles are a Cr-oxide phase that formed during the 700 °C experiment due to the penetration of residual oxygen in the XRD heating chamber through the porous intercolumnar boundaries of the DCMS microstructure. A similar effect has been observed in water corrosion testing of the DCMS Cr coating where the intercolumnar boundaries were oxidized below the surface of the coating [178]. It is illustrative to note that oxide particles were not observed in the B-HiPIMS coating due to its more densified microstructure.

6.3.2 2θ scans

Full 2θ patterns and magnified views of the Cr (110) peak for the 700 °C XRD scans are shown in Figure 6.9. The patterns labeled "700 °C-0 h" indicates the first scan performed at 700 °C, while "700 °C-16 h" indicates the final scan at 700 °C. Similar to the 300 °C experiments, the Cr (110) peak dominates the B-HiPIMS diffraction pattern, while the DCMS pattern exhibits additional Cr

peaks and peaks originating from the SiC substrate. The magnified view of the (110) peak shows that there are changes in both the peak location and peak width after the 700 °C experiment. It was also observed that the intensity of the (110) peak increased over time in samples of both coatings. Additionally, new peaks not associated with either the Cr coating or SiC substrate were observed.

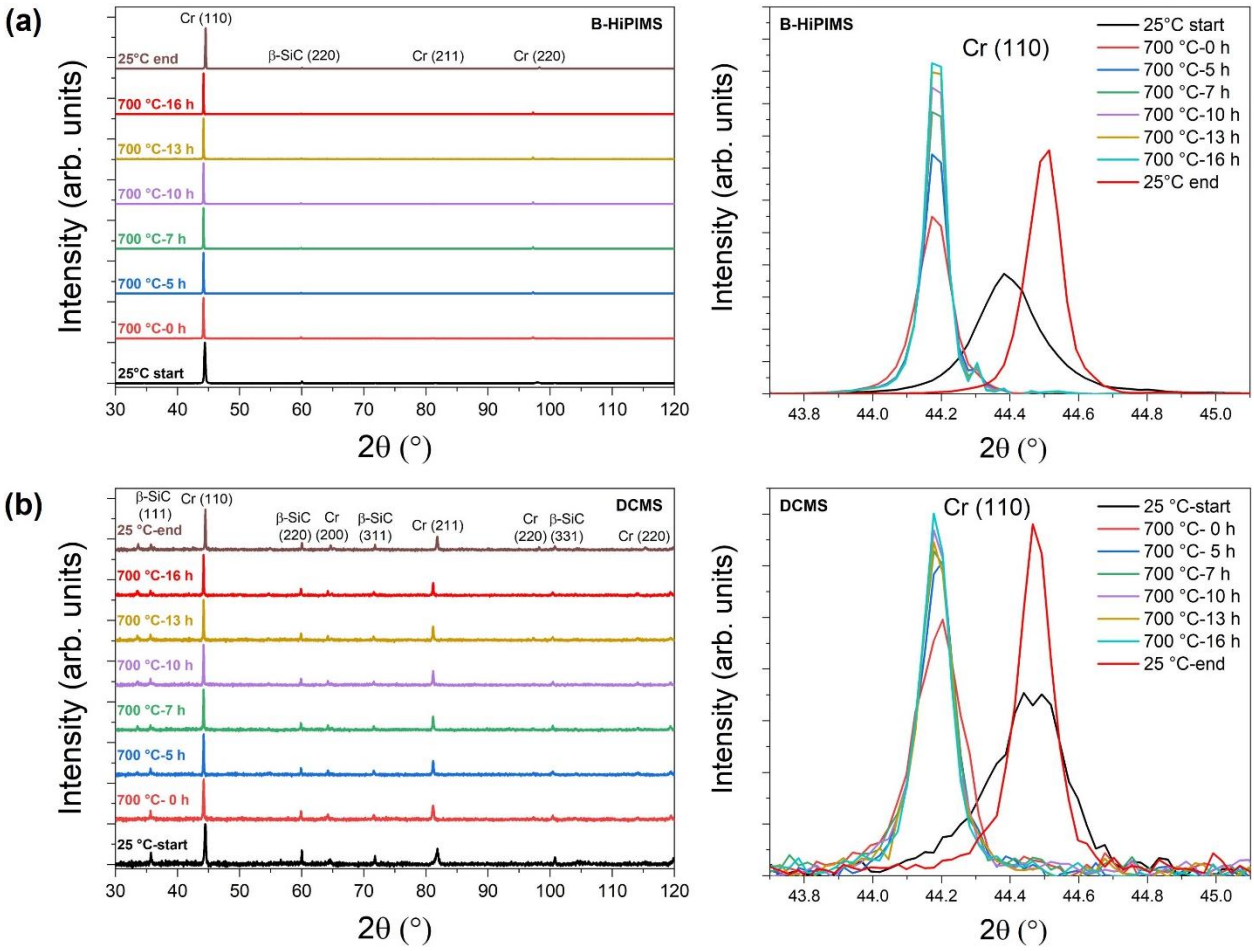

Figure 6.9: 2θ XRD patterns and magnified view of the Cr (110) diffraction peak signals collected during the 700 °C experiment as a function of time for the (a) B-HiPIMS coating and (b) DCMS coating. Unlabeled peaks correspond to Cr-Si-C compounds.

New peaks began to emerge after about four hours exposure at 700 °C. XRD patterns of the B-HiPIMS and DCMS coatings taken at room temperature after the 700 °C experiment are shown in Figure 6.10. Based on the phases that were identified via STEM-EDS and electron diffraction characterization of the B-HiPIMS coating, tabulated diffraction data from the ICDD was used to

index the new peaks. The process of indexing the diffraction peaks was complicated by the fact that many of the potential phases have diffraction peaks with 2θ values very close to one another and peak shifting caused by thermal expansion. Despite this, all new peaks appearing in the B-HiPIMS diffraction pattern were positively identified as originating from a Cr-C, Cr-Si, or Cr-Si-C phase. The indexed peaks are also in agreement with the thermodynamic calculations discussed earlier. In comparison, many of the new peaks observed in the B-HiPIMS diffraction pattern were not found in the DCMS diffraction pattern since the interdiffusion in the DCMS sample at 700 °C was limited.

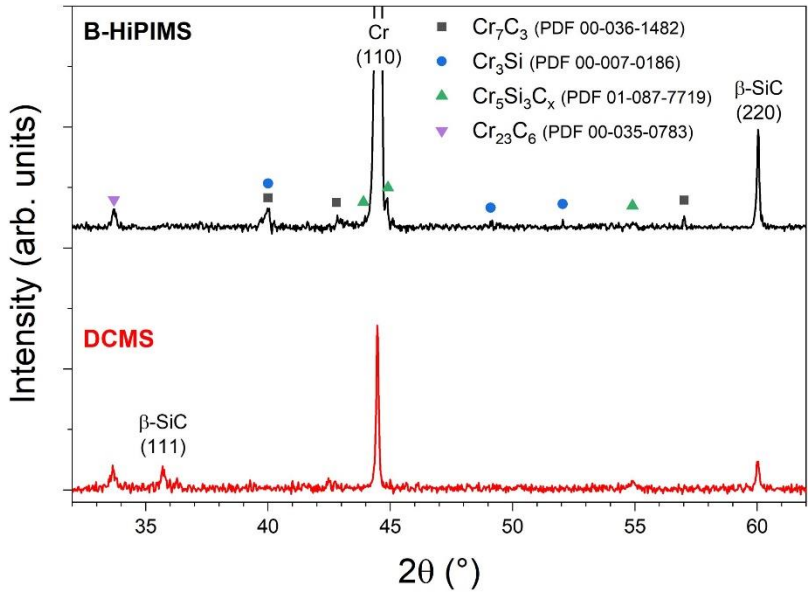

Figure 6.10: Diffraction patterns from the B-HiPIMS and DCMS coating taken at room temperature after the 700 °C experiment.

The peak analysis for (110) peak location, FWHM, and texture for the 700 °C experiments is shown in Figure 6.11. The B-HiPIMS and DCMS samples exhibited opposite trends for the evolution of the Cr (110) peak location. For B-HiPIMS, the peak shifted to a higher angle initially and eventually remained constant due to a steadily increasing tensile stress (as detailed in the following section). The (110) peak shifted to a lower angle in the DCMS coating over time. However, the residual stress in the DCMS coating remained largely constant over time at 700 °C,

indicating that there may be another factor influencing the peak location besides the residual stress, such as the incorporation of oxygen or formation of Cr-oxide along the intercolumnar boundaries as was observed in Figure 6.8. Both coating types showed a decreasing peak width over time, likely due to an increase in grain size and reduction in defect density. Lastly, the texture of both coatings, shown in Figure 6.11c, did not change drastically from the results at 300 °C. The strong (110) preferred orientation in the B-HiPIMS coating was maintained at 700 °C and slightly increased over time. This suggests that even though recrystallization and grain growth occurred within the coating, the strong texture is not altered and may even tend to become more exaggerated as grains of other orientations are superseded by the faster growing (110) orientation. At 700 °C, the crystalline structure of the DCMS coating maintains its randomly oriented state, in agreement with the microstructural observations, suggesting that significant crystalline rearrangement did not occur in the DCMS coating at 700 °C.

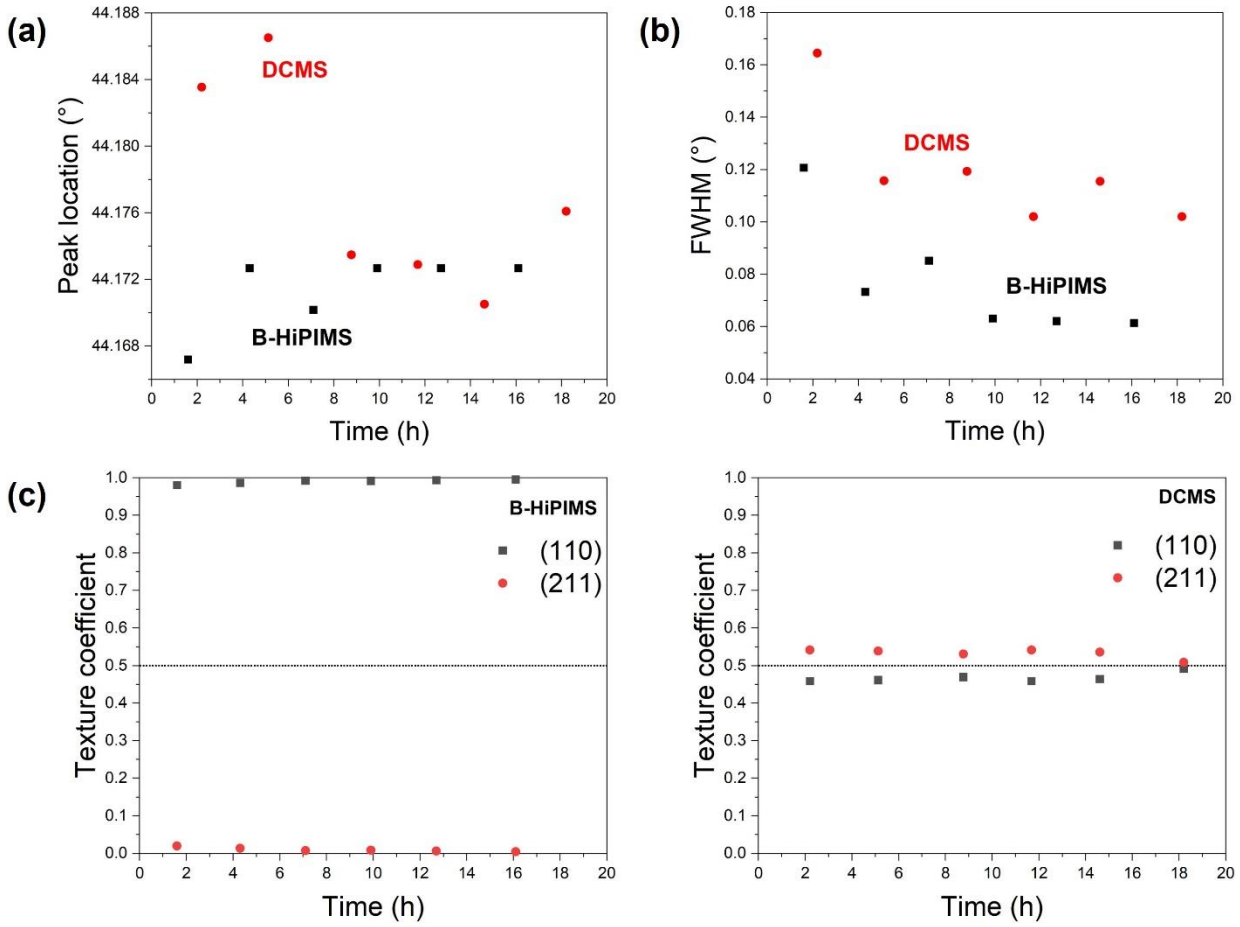

Figure 6.11: Evolution of the (a) Cr (110) peak location, (b) Cr (110) peak FWHM, and (c) texture coefficient for the B-HiPIMS and DCMS coatings at 700 °C. The dotted line in the texture coefficient plots represents values for a randomly oriented crystal structure.

6.3.3 Residual stress measurements

The evolution of residual stress for the two coating types at 700 °C is shown in Figure 6.12. The magnitude of the error bars is slightly higher compared to the 300 °C data due to greater variability at the higher experimental temperature. It is interesting to note that in contrast to the 300 °C experiment, the residual stress in the B-HiPIMS coating transitioned to a tensile state immediately upon reaching 700 °C. There is also a clear trend of increasing tensile stress in the B-HiPIMS coating over time at 700 °C. Upon cooling from 700 °C back to room temperature, there is an additional increase in tensile stress. However, the residual stress of the DCMS coating at 700 °C is similar to the results observed in the 300 °C experiment. The magnitude of the residual stress

does not change significantly upon heating or cooling of the sample, and the stress remains relatively constant for the duration of the 700 °C portion of the experiment.

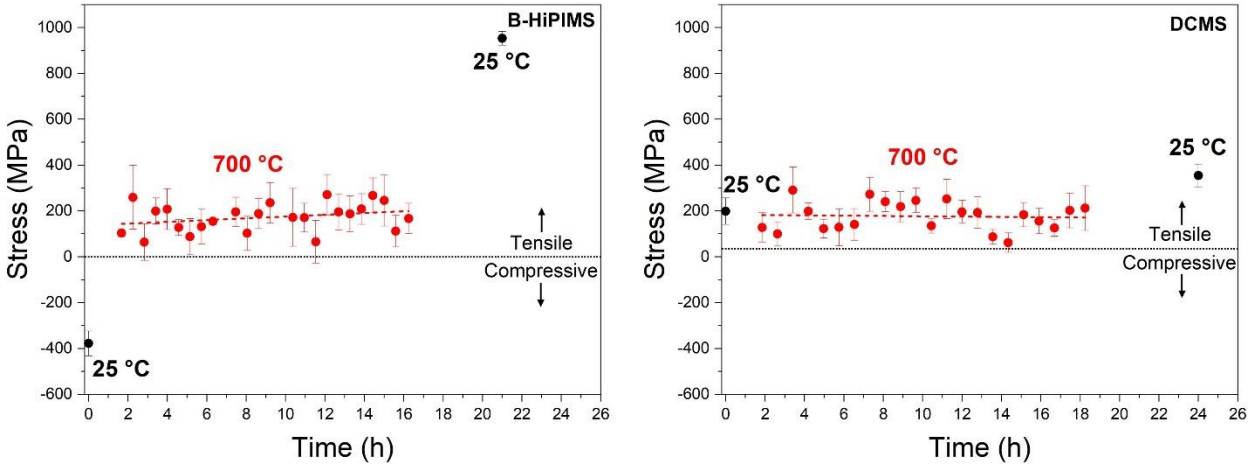

Figure 6.12: Residual stress evolution in the B-HiPIMS and DCMS coatings during the 700 °C experiment, also including the measurements conducted at room temperature before and after the test. The dotted line represents linear fitting of the 700 °C data.

6.4 Role of thermal stress

Thermal stresses in a coating are typically generated when a coating is deposited on a substrate with a different coefficient of thermal expansion (CTE) at elevated temperature [90]. The thermal stress in the coating can be calculated using the equation,

$$\sigma_{th} = \frac{E_f}{(1-\nu_f)}(\alpha_f - \alpha_s)(T_d - T_0) \qquad \text{(Eq. 6.2)}$$

where E_f, ν_f, and α_f are the elastic modulus, Poisson's ratio, and CTE for the film, and α_s is the CTE for the substrate. T_d is the deposition temperature, and T_0 is the temperature at which the thermal stress is being calculated. To calculate the thermal stresses present at the temperatures relevant to this work, thermal expansion coefficients of 6.0 × 10^{-6}/K and 4.0 × 10^{-6}/K were used for Cr [91] and SiC [31], respectively. For the B-HiPIMS and DCMS coatings, elastic moduli of 270 GPa and 205 GPa had been measured by nanoindentation [76,178] and were used for the thermal stress calculation. A value of 0.21 was used for the Poisson's ratio of Cr [77]. The

deposition temperatures of the B-HiPIMS and DCMS coatings were 250 °C and 120 °C, respectively.

At room temperature, the thermal stress component in both coating types is tensile due to the thermal expansion coefficient of Cr being greater than that of the SiC substrate. Upon returning to ambient conditions after deposition, the thermal contraction of the Cr coating is constrained by the SiC substrate, producing a tensile stress in the coating. The magnitude of the thermal stress present at room temperature in the B-HiPIMS and DCMS coatings is calculated to be approximately 150 MPa and 50 MPa, respectively. The total residual stress in a coating is the sum of the intrinsic deposition-induced stress, thermal stress, and other stresses originating from microstructural effects [181]:

$$\sigma_{tot} = \sigma_{dep} + \sigma_{th} + \sigma_{other} \quad \text{(Eq. 6.3).}$$

As reported earlier, compressive residual stress is present in the B-HiPIMS coating at room temperature. This stress value reflects the aggregate of the thermal stress and deposition-induced stress components. Given that the thermal stress is known, the stress contribution from deposition effects can be calculated by subtracting the thermal stress from the total measured residual stress. Therefore, the magnitude of the deposition-induced stress in the B-HiPIMS coating is approximately -600 MPa. This is in agreement with previous studies where deposition processes incorporating energetic ion bombardment, such as ion-assisted DCMS, HiPIMS, and B-HiPIMS, have been shown to give rise to compressive stresses through the impingement of energetic ions that promote grain boundary diffusion and induce collision cascades [63]. These mechanisms lead to the incorporation of excess atoms within the crystal structure, creating compressive stresses. In comparison, the deposition-induced stress component in the DCMS coating is tensile, with a magnitude of about 250 MPa.

The thermal stress effect is reflected in the residual stress measurements on the B-HiPIMS coating at 300 °C shown in Figure 6.4. Because the experimental temperature of 300 °C is greater than the deposition temperature of the B-HiPIMS coating, the thermal stress transforms from approximately 150 MPa (tensile) at room temperature to about -50 MPa (compressive), a net change of -200 MPa. This explains the increase in compressive stress from room temperature to 300 °C. Then over time at 300 °C, the thermal stress contribution remains constant as the deposition-induced stress is gradually relieved through recovery processes occurring within the coating [182], producing a decrease in compressive stress. At the end of the experiment as the sample cools to room temperature, the thermal stress reverts to its original tensile state, which produces a change in stress equal and opposite to the change in stress observed between the initial 25 °C data point and the first data point at 300 °C.

Similar thermal effects were anticipated during the 700 °C experiment with the B-HiPIMS coating, but the trend in residual stress was different from the results obtained in the 300 °C experiments. In contrast to the increase in compressive stress observed upon heating from room temperature to 300 °C, it was found that tensile stress increased in the B-HiPIMS coating at 700 °C. Based on the thermal stress calculation, a net change in stress of -450 MPa was expected, clearly in disagreement with the measured data. This indicates there is another factor in addition to thermal and deposition-induced effects altering the stress in the coating. It was reasoned that the microstructural evolution observed in the B-HiPIMS coating at 700 °C, both grain growth and phase evolution at the coating/substrate interface, contributed to the overall residual stress of the coating.

It has been previously reported that tensile stresses can be generated during recrystallization of thin films during deposition at temperatures near half of the melting point of the coating material

[102,183,184]. Stress is generated by a reduction in the number density of grain boundaries leading to densification of the coating and reduction in volume. While these effects are typically considered during film deposition, this mechanism of stress evolution is also valid for a post-deposition thermal treatment of a coating, as in the case of the 700 °C experiment in this work. From the work of Chaudhari [184], the tensile stress produced by the rearrangement of grain boundaries can be estimated by,

$$\sigma = \frac{2E}{1-\nu}\Delta v_{ex}\left(\frac{1}{D_0} - \frac{1}{D}\right) \quad \text{(Eq. 6.4)}$$

where Δv_{ex} is the excess volume per unit area present at a grain boundary, and D_0 and D are the initial and final grain diameters. Following the approach of Misra [185], a value of 0.1 nm can be used for Δv_{ex}. Based on the TEM imaging of the B-HiPIMS coating performed in this work, the values of D_0 and D are estimated as 0.2 µm and 1 µm, respectively. From these values, a tensile stress of approximately 300 MPa is expected to be generated during recrystallization, which is in reasonable agreement with the measured values shown in Figure 6.12. The use of the equation from Chaudhari [184] also predicts increasing tensile stress as recrystallization and grain growth progress (i.e., increasing value of D), which is also in agreement with the trend observed in stress for the B-HiPIMS coating at 700 °C. Lastly, additional stress contributions related to different molar volumes, thermal expansion coefficients, and elastic moduli related of the new phases formed at the interface between the Cr coating and SiC substrate may also be playing a role.

It is worth noting that there was the large increase in tensile stress for the B-HiPIMS observed when cooling from 700 °C to room temperature. As mentioned previously, the stress of the B-HiPIMS coating did not follow the expected trend upon heating from room temperature to 700 °C. However, the increase in tensile stress upon cooling at the end of the experiment does match with the expected behavior based on the thermal stress contribution, where a net increase in tensile

stress of almost 500 MPa should occur. It is believed that the recrystallization of the B-HiPIMS coating essentially "resets" the thermal processing history of the coating, and the effects of the deposition performed at 250 °C are readily negated, making 700 °C the new baseline temperature for thermal stress considerations.

6.5 1200 °C *in situ* XRD study

Due to complications with the 1200 °C experiment on the B-HiPIMS coating relating to the thermal expansion of the alumina sample holder, the analysis at this temperature focused on the DCMS coating. Seven 2θ scans were performed on the DCMS coating during the three-hour hold time at 1200 °C. No residual stress measurements were performed due to the disappearance of Cr peaks (due to the consumption of metallic Cr due to diffusion) during the early stages of high temperature exposure. A 1200 °C isothermal phase diagram for the Cr-Si-C system determined by CALPHAD is shown in Figure 6.13a. The phase diagram only differs slightly from the previously determined 700 °C diagram, and therefore, the calculated equilibrium phase fractions across the path of equimolar Si and C composition (shown in Figure 6.13b) are also similar to those at 700 °C.

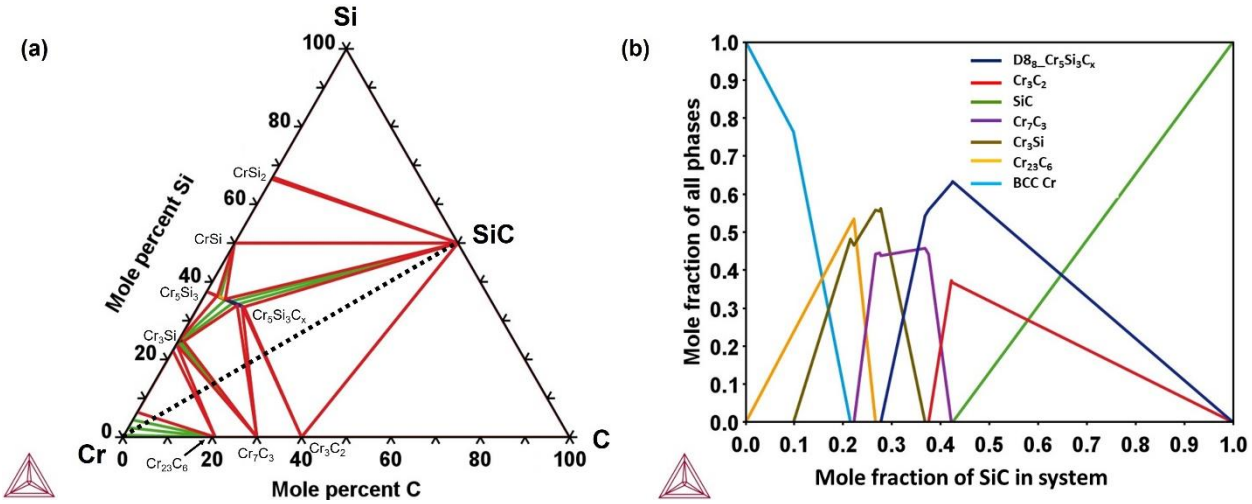

Figure 6.13: (a) Calculated isothermal phase diagram for the Cr-Si-C system at 1200 °C. The black dotted line represents the path with equimolar concentrations of Si and C; (b) Calculated equilibrium phase fractions along the path marked by the dotted line in (a).

The diffraction patterns collected at 1200 °C are shown in Figure 6.14a. Many new peaks corresponding to the emergence of new phases was observed immediately at 1200 °C, indicating that significant chemical interaction between the Cr coating and the underlying SiC substrate had occurred during the ramp-up period. Most of the new diffraction peaks observed were associated with the same phases observed at 700 °C (Cr_7C_3, Cr_3Si, and $Cr_5Si_3C_x$). In addition to these phases, multiple peaks corresponding to the Cr_3C_2 phase were also identified. The formation of this carbide phase is predicted by the thermodynamic calculations presented in Figure 6.13b where Cr_3C_2 is the final carbide to form as interdiffusion progresses on account of its lower Cr content relative to the other stable carbide phases.

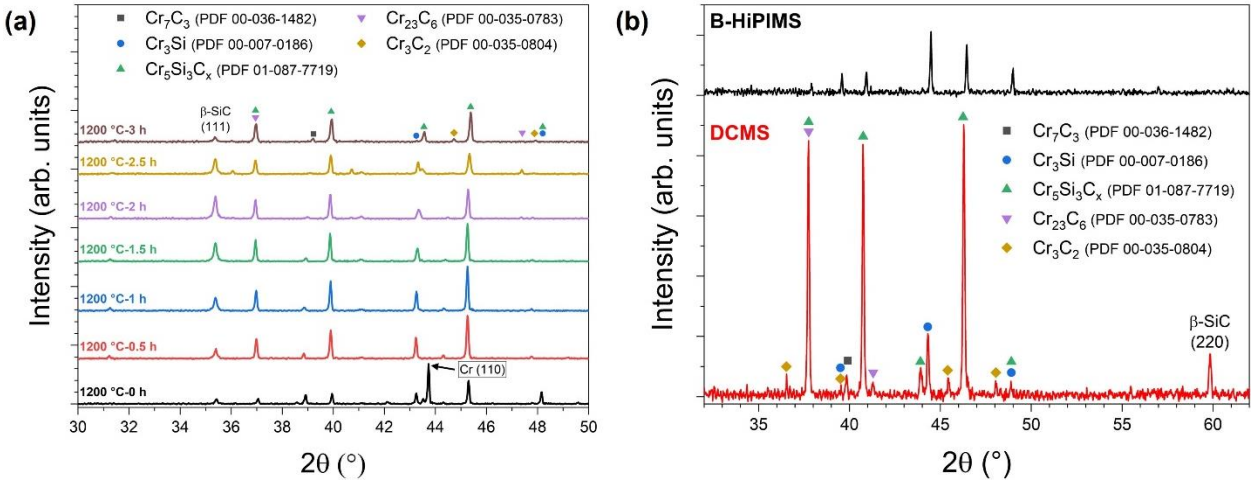

Figure 6.14: (a) Diffraction patterns from the DCMS Cr coating at 1200 °C with major peaks indexed; (b) Indexed diffraction pattern from the B-HiPIMS and DCMS Cr coatings taken at room temperature after three hours at 1200 °C.

The presence of these peaks can be seen clearly in Figure 6.14b, which is an indexed diffraction pattern from the DCMS coating taken at room temperature after the 1200 °C experiment. These findings are in good agreement with previous studies of the interdiffusion of Cr and SiC [10,172,174,180]. Figure 6.14b also shows the diffraction pattern from the B-HiPIMS sample after the experiment, and although the diffracted intensity from the sample is lower, it is observed that many of the peaks found in the DCMS diffraction pattern are identical to those of the B-HiPIMS diffraction pattern. Similar to the 700 °C experiment, precise identification of some diffraction peaks was difficult due to overlap of peaks of many possible phases, and the potential for peak shifting due to stresses or instrumental effects.

It is noted that the Cr (110) peak is the strongest in the first diffraction pattern measured at 1200 °C, indicating there is still a substantial amount of the Cr coating still intact. However, the Cr (110) peak has completely disappeared in the second diffraction pattern collected at 1200 °C. The approximate time between the measurement of the first and the second diffraction patterns was only 30 minutes, indicating that the entire Cr coating was consumed within an hour at 1200

°C via interaction with the SiC substrate, although some thickness ofthe coating was likely consumed during the ramp-up phase of the experiment.

6.6 Influence of deposition process

This work has revealed a few important differences between the B-HiPIMS and DCMS coatings in regards to evolution of microstructure and residual stress at elevated temperatures. First, the degree of grain growth that occurred in the DCMS coating at 700 °C was much less than that experienced by the B-HiPIMS coating. The important factors limiting grain growth in the DCMS coating are the intercolumnar porosity present within the coating microstructure and inadequate cohesion between grain boundaries. These factors will limit the extent of grain growth that can occur by inhibiting diffusion across boundaries. For example, consider a single columnar growth structure comprised of many fine, fibrous grains and separated from neighboring columns by a narrow band of porosity. Then at 700 °C, the fibrous grains may coalesce to form a single columnar grain, but due to the porosity, growth of this grain cannot progress beyond this point. This can be visualized in Figure 6.8b, where it is observed that the fibrous grains comprising the as-deposited DCMS microstructure have been replaced by coarser columnar grains, but the columnar grains are still divided by intercolumnar porosity. In contrast, the dense B-HiPIMS coating behaves in a manner more akin to a bulk material where grain boundary migration can occur readily and facilitate grain growth.

Another significant difference between the B-HiPIMS and DCMS coatings is that extent of interdiffusion between Cr and SiC at the interface. The B-HiPIMS coating exhibited 1 μm interaction layer formed at the interface over 16 hours at 700 °C, while in the DCMS coating, there were only isolated areas near the interface showing interdiffusion. The DCMS sample after the 700 °C experiment showed that the coating debonded slightly from the SiC substrate. Because the

coating and substrate were no longer in intimate contact mass transport across the interface could not take place, and interdiffusion only occurred in localized regions where bonding was maintained. It is generally understood that B-HiPIMS deposition processes produce a greater degree of interfacial mixing via the impingement of energetic ions on the substrate in the early stages of deposition [59,109]. The characterization of the B-HiPIMS interface in Section 4.4 confirms that there is a Cr-SiC mixing layer present. A pre-mixed interfacial layer in the B-HiPIMS coating enhances adhesion of the coating and facilitates interdiffusion between the coating and substrate, leading to the formation of a uniform interaction layer. The presence of Kirkendall voids in the B-HiPIMS coating but not the DCMS coating also demonstrates that the extent of mass transport across the B-HiPIMS interface was much greater.

The last point to be addressed is the behavior of the residual stress in the DCMS coating. While the B-HiPIMS coating exhibited clear trends of stress relief at 300 °C and increasing tensile stress at 700 °C, for the DCMS coating the stress remained relatively constant at both temperatures. It is speculated that the intercolumnar porosity, inhomogeneous microstructure, and inadequate adhesion of the DCMS coating cause the residual stress to remain constant over time. It is well known that the residual stress of PVD coatings tends to vary through the coating thickness [186–188]. Given that the stress likely varies spatially through the DCMS coating, and the microstructure contains porosity with grains arranged in a more disordered fashion, it is difficult for the stress state to change in a uniform manner throughout the coating. Although the stress may vary in localized regions of the coating, the measured residual stress values represent a volume-averaged stress, and overall, there is no net effect on the residual stress throughout the coating. In contrast, the coherent, dense microstructure of the B-HiPIMS coating leads to more uniform and coordinated evolution in stress. Finally, it should also be noted that the DCMS coating does not

follow the changes in stress that would be expected due to the thermal effects covered in the previous section. It is possible that due to the poor adhesion of the coating and associated debonding at the interface may alleviate stress buildup in the coating. Consequently, the stress is not strongly influenced by thermal expansion or contraction of the SiC substrate.

6.7 Considerations for in-reactor performance

There are a few key findings that provide insight into the performance of Cr-coated SiC fuel cladding in LWRs. This work shows that the B-HiPIMS Cr coating maintains its beneficial compressive residual stress at 300 °C (the approximate LWR operating temperature). During reactor operation, the SiC cladding will experience volumetric swelling due to the formation of radiation-induced defects [37,189]. Consequently, a coating deposited on the outer surface of the cladding will experience a tensile stress as the SiC cladding swells. Based on this consideration, it is121elieveed that the compressive stress present in the B-HiPIMS coating at 300 °C would be beneficial to offset the radiation-induced tensile stress effects. The tensile stress present in the DCMS coating could be detrimental, as the tensile stresses from swelling combined with deposition-induced tensile stress will produce an additive effect. This may increase the likelihood of coating failure, especially given the poor adhesion of the DCMS coating. The gradual stress relief observed in the B-HiPIMS coating over time at 300 °C is also viewed as a beneficial feature that may improve the ductility of the coating, which is also necessary for the coating to be able to accommodate stresses and deform without cracking or delamination.

The other important consideration is the behavior of the coating at 1200 °C. In this work it was found that the Cr coating was completely consumed via interaction with the SiC substrate within about one hour at 1200 °C. Furthermore, it is noted that these experiments were conducted in an inert environment, while in a real nuclear reactor accident scenario, the coating will also be

consumed from the outer surface via the oxidation reaction with high temperature steam. The effect of the Cr-SiC interdiffusion layer on the steam oxidation performance of the Cr-coated SiC system has not been widely studied [10]. SiC is likely expected to experience surface degradation in the steam environment, but in accident scenarios it is likely that it will maintain its structural integrity. However, the effect of the Cr-SiC interaction layer on the oxidation behavior and mechanical stability of the cladding should be evaluated. Future work could also include mechanical testing of the Cr coating samples after elevated temperature exposure to assess how the evolution in microstructure, residual stress, and interfacial composition have influenced the mechanical properties and adhesion of the coatings.

7. Hydrothermal Corrosion Testing

This chapter features direct content from the following journal articles first-authored by the PhD candidate:

K. Quillin, H. Yeom, T. Dabney, M. McFarland, K. Sridharan, "Experimental evaluation of direct current magnetron sputtered and high-power impulse magnetron sputtered Cr coatings on SiC for light water reactor applications," *Thin Solid Films* 716 (2020) 138431.

K. Quillin et al., "Evolution of corrosion product layer on Cr films in prototypical PWR water chemistry and flow conditions," *npj Materials Degradation* (2024), in preparation.

7.1 Static water corrosion

Hydrothermal corrosion tests were performed using a static water autoclave. These experiments were intended as initial evaluations of corrosion performance to screen out poorly performing coatings and deposition technologies. Photographs of the autoclave system and Inconel sample fixtures are shown in Figure 7.1. Tests were performed at 360 °C (to approximately simulate LWR temperatures) and 18.6 MPa in deionized (DI) water for a total period of 30 days. The tests were interrupted at intermediate intervals to measure the weight change of samples and refresh the water. The dissolved oxygen content of the water prior to test was measured to be about 5 ppm, but this likely changes over the course of the test as the solubility of oxygen in water changes during temperature ramping and because oxygen is consumed through interaction with the samples and walls of the autoclave chamber. A degassing step was performed during ramping of the system to remove dissolved oxygen. While these conditions do not represent the exact in-reactor operating conditions, they do provide a mechanistic understanding of hydrothermal corrosion effects and a relative comparison of materials' performance. It should be noted that water chemistry, primarily dissolved oxygen and hydrogen concentrations and radiation can have significant effects on corrosion rates.

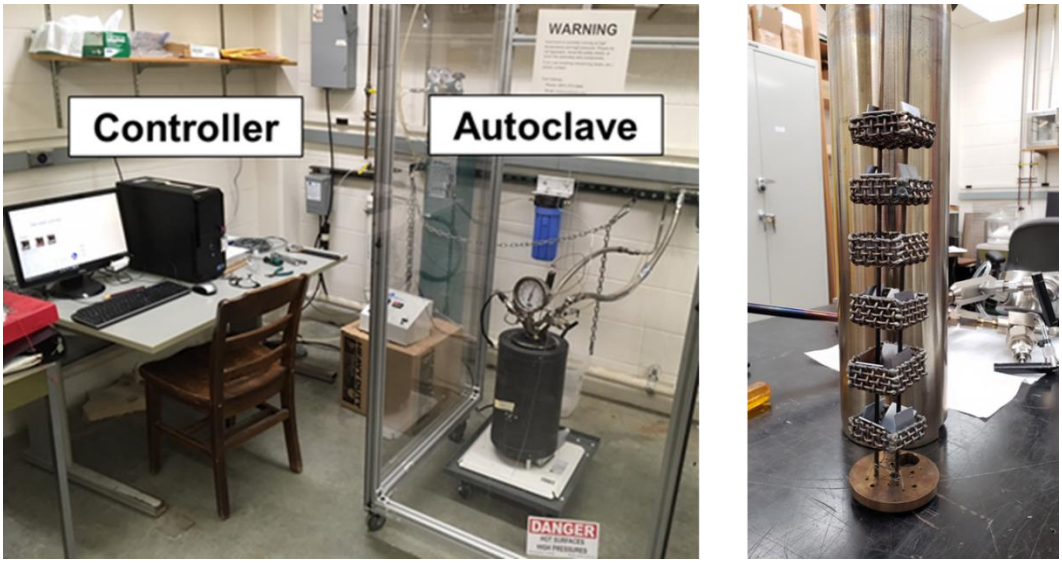

Figure 7.1: Photographs of the static water autoclave system and sample fixture used for evaluating hydrothermal corrosion performance of the coated samples.

The first autoclave testing campaign included the DCMS and HiPIMS Cr coatings produced by Vendor I. Zircaloy-4 coupons were included during the test to provide a reference for current LWR cladding alloys and served as a standard test material so any experimental irregularities could be identified. Uncoated CVD SiC coupons were also tested as control samples to provide a baseline for comparison of the efficacy of coating materials. Four replicates of each sample type were included at the beginning of the test, and at each time interval, one replicate was removed from the test as a representative sample for that specific time step. Weight change results are presented in the units of weight change per unit surface area. This allowed for normalization of the data for samples of different sizes or slightly different coated areas. Since uncoated CVD SiC coupons were included during the autoclave test (i.e., the weight change per area of SiC is known), it was possible to isolate the weight change induced by the coating material alone using the following equation:

$$\Delta W_{\text{coating}} = \Delta W_{\text{sample}} - \frac{\Delta W_{\text{SiC}}}{A_{\text{SiC}}}(2lt + 2wt + lw)_{\text{SiC}} \qquad \text{(Eq. 7.1)}$$

where ΔW is the weight change in mg, A_{SiC} is the surface area of SiC, l, t, and w represent the dimensions of the coated SiC coupon. $\Delta W_{coating}$ is then divided by the known surface area of the coated surface to calculate the weight change per unit area.

The first-generation DCMS Cr and HiPIMS Cr coatings performed well in the 30-day autoclave test. Both coatings remained adhered throughout the test. The weight change of the samples is presented in Figure 7.2 along with Zr-4 reference samples and uncoated CVD SiC. As expected, CVD SiC lost weight during the corrosion experiment via dissolution of SiO_2. The weight gain of the Cr coatings was much less than that of the Zr-4 reference coupons. The DCMS Cr coating showed a weight gain roughly three times higher than the HiPIMS Cr coating. This result is attributed to the presence of intercolumnar porosity within the S-DCMS coating wich leads to greater microscopic surface area and permeation of corrosive species.

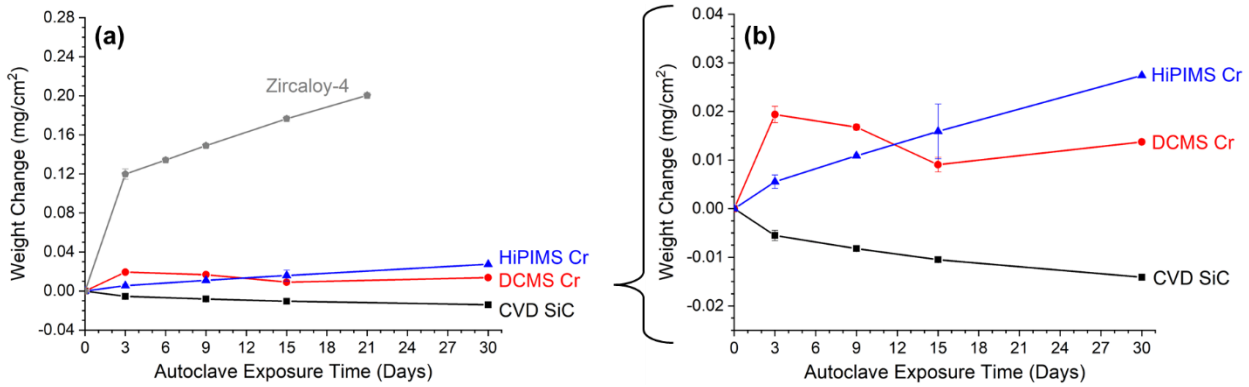

Figure 7.2: Weight change results from the autoclave hydrothermal corrosion tests: (a) CVD SiC, DCMS Cr, and HiPIMS Cr data compared to standard Zircaloy-4 coupons and (b) expanded view of data in (a) shown for clarity.

After the initial three-day interval, the DCMS coating showed a transient weight loss trend over the next two time-intervals (up to 15 days) of exposure in the autoclave test. It is speculated that this transient weight loss may have resulted from weakly-bonded columnar grains on the surface of the DCMS coatings that may have detached from the coating matrix due to the volumetric expansion associated with intercolumnar oxidation. On the other hand, the denser and

defect-free microstructure of HiPIMS coatings may have provided for a more effective barrier to penetration of water into the coating resulting in gradual weight gain without exhibiting the transient weight loss behavior. Experimental evidence to support this explanation conclusively would require more frequent removal of samples from the autoclave tests followed by characterization to understand the relationship between the transient weight loss and the microstructure of the DCMS and HiPIMS coatings. It is noted that the 30-days duration of the test is relatively short compared to the life cycle of the fuel cladding, so the trends observed in this study may be regarded as behaviors and trends exhibited in initial stages of hydrothermal corrosion of the coatings.

The corrosion rate of CVD SiC from this study is in agreement with previously published data (summarized by Yang [38] and Kim [39]), although it is towards the lower end of the reported range. This is likely due to the discrepancy between researchers in corrosion test conditions, water chemistry, and microstructure of SiC. Oxidation of Zircaloy-4 has been widely studied, and the oxidation rate in this study agrees with the published literature [190,191]. The oxidation rates of the PVD Cr coatings agree with results from previous studies in which PVD Cr-coated Zr-alloy samples were exposed to PWR conditions in a long-term autoclave test [192,193]. In BWR-hydrogen water chemistry (150 ppm dissolved H_2), Raiman et al. [8] reported a weight gain for their PVD Cr coating, similar to the weight gains measured in this study.

Photographs of the Cr-coated samples after the 30-day test are shown in Figure 7.3. The surface color changed from metallic gray to the green-gold which is indicative of Cr_2O_3. SEM and XRD characterization of the samples showed no changes in the surface morphology or phases for CVD SiC or either of the Cr coatings. The oxide layer on the Cr samples was too thin to be detected by

either SEM or XRD. Therefore, STEM was performed to measure the oxide layer thickness and characterize coating microstructure for autoclave-tested samples.

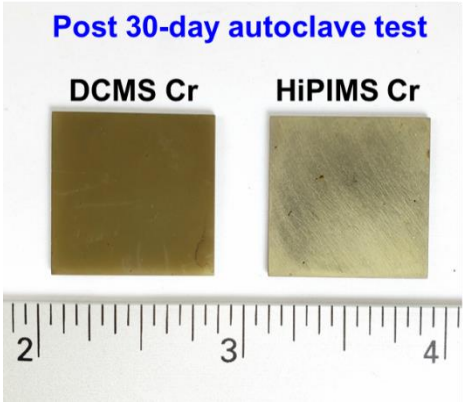

Figure 7.3: Photograph of the DCMS and HiPIMS Cr coatings after the 30-day autoclave test. Both samples showed the green-gold surface color indicative of Cr_2O_3.

STEM examination of the autoclave-tested Cr-coated samples showed the thin surface oxide layer formed during the autoclave test. The oxide layer thickness on the surface was approximately 20-30 nm for both types of Cr coatings, as can be seen in Figure 7.4a and b. The oxide layer stoichiometry of Cr_2O_3 was confirmed by EDS analysis. As mentioned previously, the columnar defects in the DCMS coatings provide pathways which allow water to penetrate and oxidize the inner surfaces of intercolumnar regions during the autoclave test. Oxide formation was in fact observed in these intercolumnar regions well below the coating surface for these DCMS coatings (Figure 7.4d). An EDS line-scan across the intercolumnar region confirms the presence of an extremely thin Cr_2O_3 layer between columnar grains of the DCMS Cr microstructure.

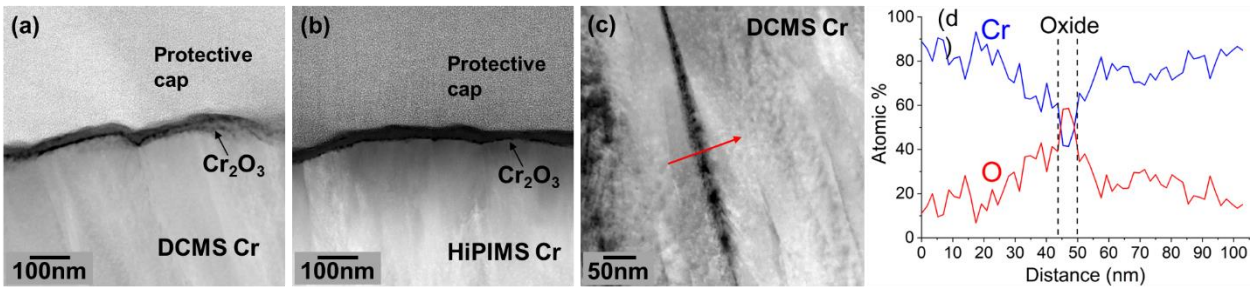

Figure 7.4: HAADF-STEM images of (a) DCMS Cr and (b) HiPIMS coating surfaces after 30 days autoclave exposure. Both coatings formed a 20-30 nm thick Cr_2O_3 surface layer. (c) Oxide formation in the intercolumnar regions in the interior of the DCMS Cr coating. (d) The EDS line-scan across the columnar grains confirming the formation of oxide phase in the intercolumnar region.

The long-term effects of the oxide formation in the intercolumnar regions of the DCMS coating is not known at this point. It is possible that water may penetrate through the entire thickness of the coating, reaching the substrate and weakening the coating/substrate interface in long-term corrosion scenarios. Another possibility is that as the fine columnar defects become oxidized, a self-healing effect occurs where the columnar gaps become sealed by the growing higher specific volume of the oxide and no further water penetration can occur. An extended autoclave test is necessary to identify the effects of the nanoscale intercolumnar porosity. Substrate heating during deposition may prevent formation of the intercolumnar porosity by providing adatoms with enough thermal energy to fully densify the microstructure and thereby prevent any detrimental effects associated with the intercolumnar regions.

Surface roughness of the samples was quantified using AFM surface scanning after each interval of the autoclave test. The resulting data is shown in Figure 7.5. No clear trends for roughness evolution are evident for any of the samples. The CVD SiC samples, which experience material removal showed no significant change in surface roughness, a result that is supported by the work of Kim et al. [194]. The roughness of the HiPIMS coating is lower than the DCMS coating, and both coatings maintain their roughness values during the 30-day autoclave exposure, in part due to the fine grain sizes of the coating. It is also worth noting that while the initial surface

roughness of DCMS. The relatively short timescale of the autoclave test precludes any conclusions regarding correlations between surface roughness and corrosion, but it is worth noting that surface roughness plays a role in the heat transfer parameter, critical heat flux, which is important for fuel cladding surfaces during high temperature accident scenarios.

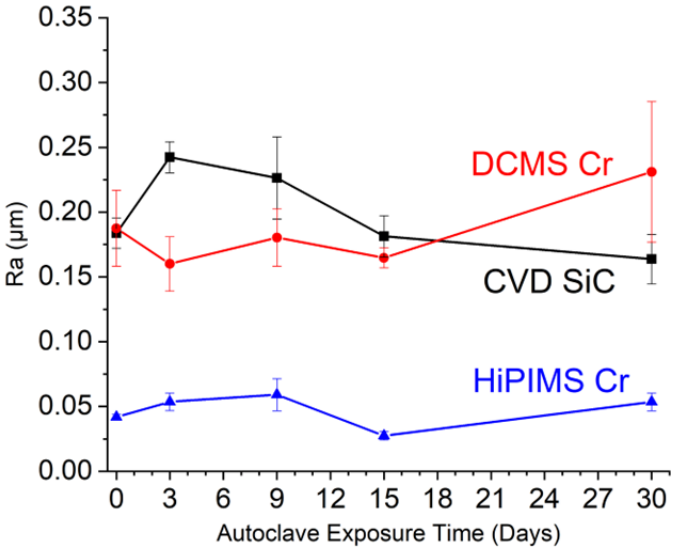

Figure 7.5: Surface roughness evolution during the autoclave test as measured by AFM.

A second hydrothermal corrosion test was conducted on the four DCMS (S-DCMS, P-DCMS, I-DCMS, PI-DCMS), HiPIMS(II), and B-HIPIMS coatings. The experimental conditions and procedure were identical to the first corrosion experiment. Bulk Cr samples were also included in the experiment as a baseline. Two replicates of each sample were included in the test and all samples were tested for the full 30-day period. Photographs of the samples after the corrosion test are shown in Figure 7.6. The P-DCMS, PI-DCMS, and HiPIMS(II) Cr coatings exhibited delamination after the initial three-day interval of the experiment. Therefore, these samples were not included in the subsequent stages of the corrosion test. The poor performance of the HiPIMS(II) coating produced by Vendor II is likely due to the use of an unoptimized set of deposition parameters compared to the Vendor I HiPIMS coating, where optimized parameters were used and resulted in good coating performance. The I-DCMS coating remained adhered after

three days, but visual examination revealed the coating was in the initial stages of buckling, and the coating was also removed from the test. For the delaminated coatings, the failure mechanism appears to be a mechanical failure rather than a corrosion-driven failure. The S-DCMS and B-HiPIMS coatings remained fully adherent and protective throughout the full 30-day test.

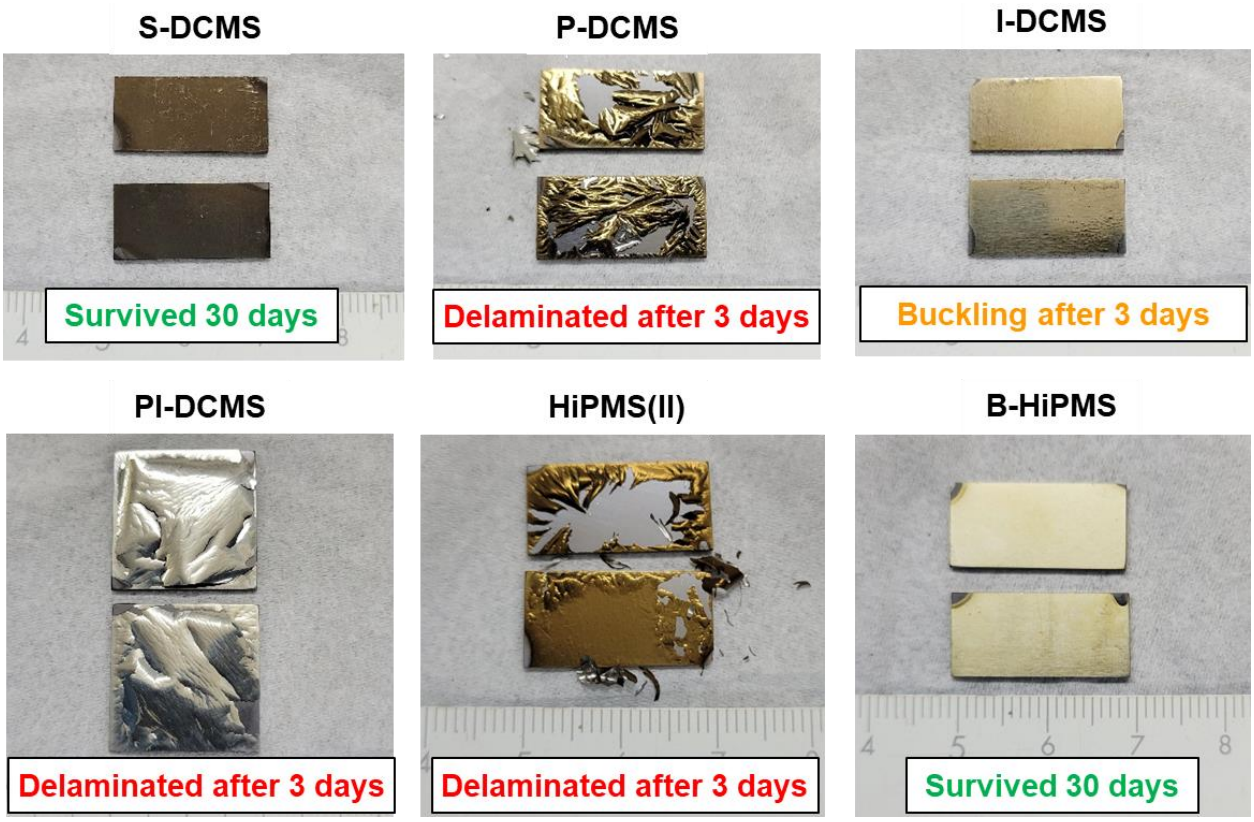

Figure 7.6: Photographs of the six variants of magnetron sputtered Cr coatings produced in collaboration with Vendor II after autoclave exposure.

The weight change of the S-DCMS and B-HiPIMS coatings during the 30-day corrosion test is shown in Figure 7.7 along with uncoated SiC and bulk Cr reference samples. The S-DCMS coating shows an abnormally large weight gain during the initial three-day period. It is believed that fine debris originating from other samples in the autoclave became attached to the S-DCMS samples leading to excessive weight gain. The B-HiPIMS coating performed very well in the corrosion test, exhibiting a weight gain similar to that of bulk Cr due to the dense microstructure and strong adhesion of the coating.

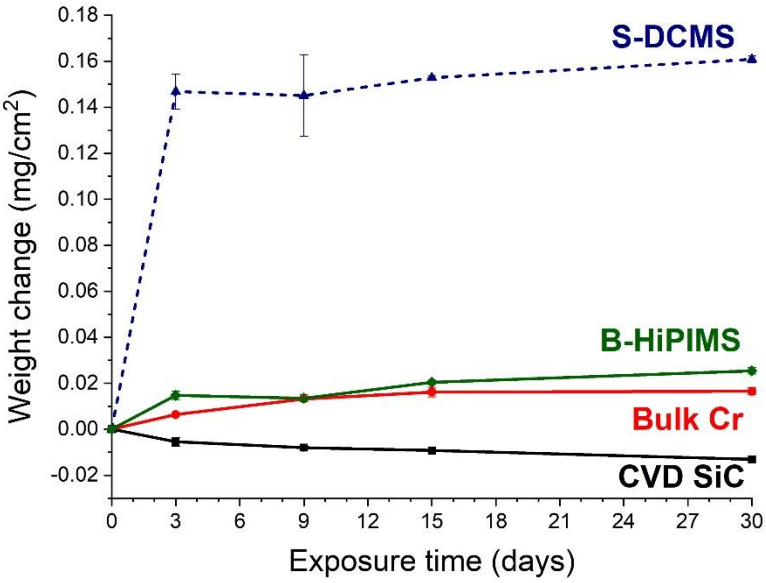

Figure 7.7: Weight change plot for the S-DCMS and B-HiPIMS coatings during the 30-day hydrothermal corrosion test along with those of uncoated SiC and bulk Cr reference samples.

It is also interesting to compare coating performance in the autoclave corrosion test to the coating-substrate adhesion behavior evaluated via the progressive scratch test outlined in Section 5.1. The main failure mode of the coatings inside the autoclave appeared to be debonding (or delamination) of the film from the substrate. Therefore, it is expected that there would be some relationship between the scratch test delamination load and coating performance in the autoclave. Table 7.1 provides a comparison between the performance of the Cr coatings in the autoclave and the scratch test delamination loads. For the coatings produced by Vendor II, there is a relatively good correlation between the coating adhesion in the autoclave and the delamination load. Coatings with higher delamination loads tended to remain well adhered in the autoclave. The coatings with lower delamination loads likely have insufficient adhesion strength to withstand the thermal stresses generated during the autoclave test. Interestingly, for the DCMS and HiPIMS coatings deposited by Vendor I, the delamination loads were relatively low, but both coatings performed well in the autoclave test. One reason for this could be the different substrate cleaning

processes used by the two vendors. Vendor I used a plasma cleaning process while Vendor II used an ion milling process.

Table 7.1: Summary of coating performance in the 30-day static autoclave hydrothermal corrosion test and delamination loads measured in the progressive scratch test (repeated from Table 5.1).

Coating process	Coating manufacturer	Autoclave performance	Scratch test delamination load (g)
S-DCMS	Vendor I	Well adhered	600
HiPIMS	Vendor I	Well adhered	800
S-DCMS	Vendor II	Well adhered	> 2250
P-DCMS	Vendor II	Delaminated after 3 days	400
I-DCMS	Vendor II	Buckling after 3 days	1100
PI-DCMS	Vendor II	Delaminated after 3 days	500
HiPIMS(II)	Vendor II	Delaminated after 3 days	1800
B-HiPIMS	Vendor II	Well adhered	> 2250

It should also be noted that there are fundamental differences in the way in which the scratch test and autoclave test influence the coating. In the scratch test, the coating area surrounding the indenter will experience a multi-axial stress state, and during the early stages of the test, the coating experiences the brunt of the load, while the interface will not get probed until the load is increased. Therefore, the structure and mechanical properties of the coating, including density, hardness, and residual stress, will play a role in the coating behavior in the scratch test. Resultingly, many different scratch failure mechanisms are possible depending on the specific combination of cohesive and adhesive strengths of a particular coating (as described in Section 5.1), and failure is possible in a coating with weak cohesion before the load of the scratch ever reaches the interface. In the autoclave, all stress generation is related to the thermal expansion mismatch between Cr and SiC. Consequently, the stress will be greatest at the interface, and the interface strength will be the primary factor that governs coating behavior, which is why the only failure mode observed in the autoclave test was interfacial debonding.

Based on the results of the two autoclave corrosion tests, comprising eight different types of magnetron sputtered Cr coatings, the best-performing coating types can be identified. The DCMS and HiPIMS Cr coatings produced in collaboration with Vendor I and the B-HiPIMS coating produced in collaboration with Vendor II were selected based on their good adhesion and low weight gain in the 30-day hydrothermal corrosion test. Figure 7.8 shows a weight change plot for the three down-selected coatings. All three coatings gained weight via the formation of a passive oxide layer and successfully prevented the hydrothermal corrosion of the SiC substrate.

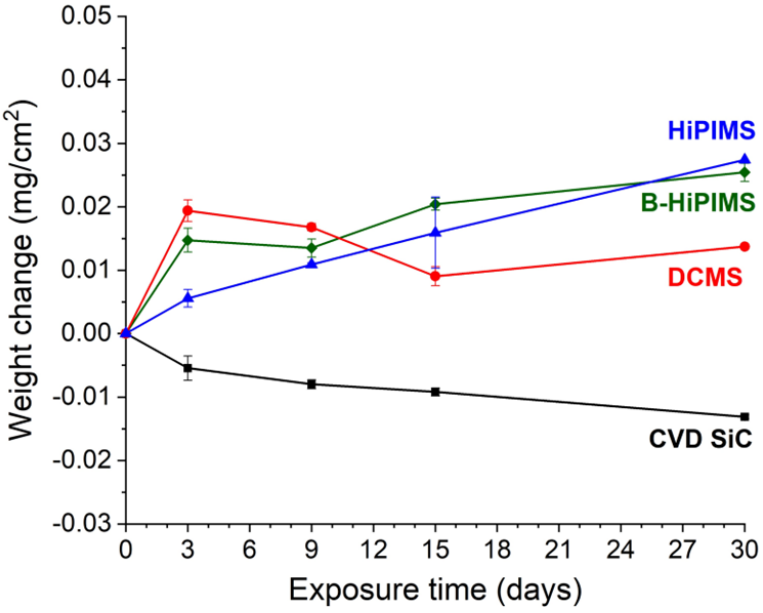

Figure 7.8: Weight change plot for the three best-performing coatings compiled from the two autoclave hydrothermal corrosion tests.

7.2 PWR flow loop corrosion test

The autoclave corrosion test offers a relatively convenient method to quickly evaluate the performance of different coatings but does not provide the most accurate replication of the in-reactor corrosive environment, where there are conditions of coolant flow and active chemistry control. In flow conditions, the corrosion products are being continually removed from the material-coolant interface, thereby minimizing the possibility of corrosion being restricted by

solubility limit considerations in the coolant. Additionally, flow-assisted erosion/corrosion may also play in mechanically destabilizing thin coatings. Corrosion tests were therefore performed in a PWR flow loop at the General Electric Research Center to simulate the real reactor condition more closely. Flow loop hydrothermal corrosion experiments involve the continuous cycling of the high temperature water and constant monitoring and control of the water chemistry, similar to commercial reactor systems. The test temperature and pressure were 330 °C and 13.1 MPa, respectively, and the volumetric flow rate of the water was 40 cm^3/min. The water chemistry was continuously controlled to have 3.5 ppm of dissolved hydrogen gas. With these conditions, the corrosion test is regarded as being more similar to a PWR environment [4]. Two flow loop experiments were performed. The first test was performed for a duration of three months and included the DCMS and HiPIMS coatings produced by Vendor I. No weight change data was collected in the first test. Uncoated CVD SiC and B-HiPIMS samples were included in the second test, which was one month in duration and included weight change measurements. Both tests were run continuously with no removal of the samples at intermediate time steps.

In the three-month flow loop test, both the DCMS and HiPIMS coatings produced by Vendor I remained adhered to the SiC substrate. This trend is consistent with the results observed in the one-month static autoclave test. Figure 7.9a shows a photograph of the two samples after the flow loop test. The surface of both samples is a deep purple-gold color, which may be indicative of a different oxide layer thickness in comparison to the green-gold color of the samples after the 30-day static autoclave test. Additionally, in contrast to the autoclave experiment, the surface of the Cr coatings after the flow loop test did exhibit noticeable changes in surface morphology. A uniform dispersion of fine particles was observed on the surface of both Cr coatings, as can be seen in Figure 7.9b. The homogeneous morphology of the surface layer suggests that this phase is

an oxide layer than has grown on the surface of the Cr coatings rather than contaminant particles or oxide that has dissolved in the water and plated out on the surface during cooling of the system. The HAADF-STEM images in Figure 7.9c show the oxide layer that has formed on the surface of both coatings. The morphology of the oxide appears pyramidal and jagged, and the oxide layer thickness was in the range of 50–100 nm. Lastly, ASTAR nanoscale orientation mapping was performed in one near-surface region of the DCMS coating to identify the crystal structure of the corrosion product phase and generate a phase map. The ASTAR mapping area and subsequent phase map are shown in Figure 7.9d. The quality of the phase map is slightly reduced due to sample preparation artifacts, but the analysis clearly identified the presence of rhombohedral Cr_2O_3 on the surface of the bcc Cr coating. The rhombohedral phase is based on the corundum prototype crystal structure and is the expected equilibrium phase structure for Cr_2O_3 [195].

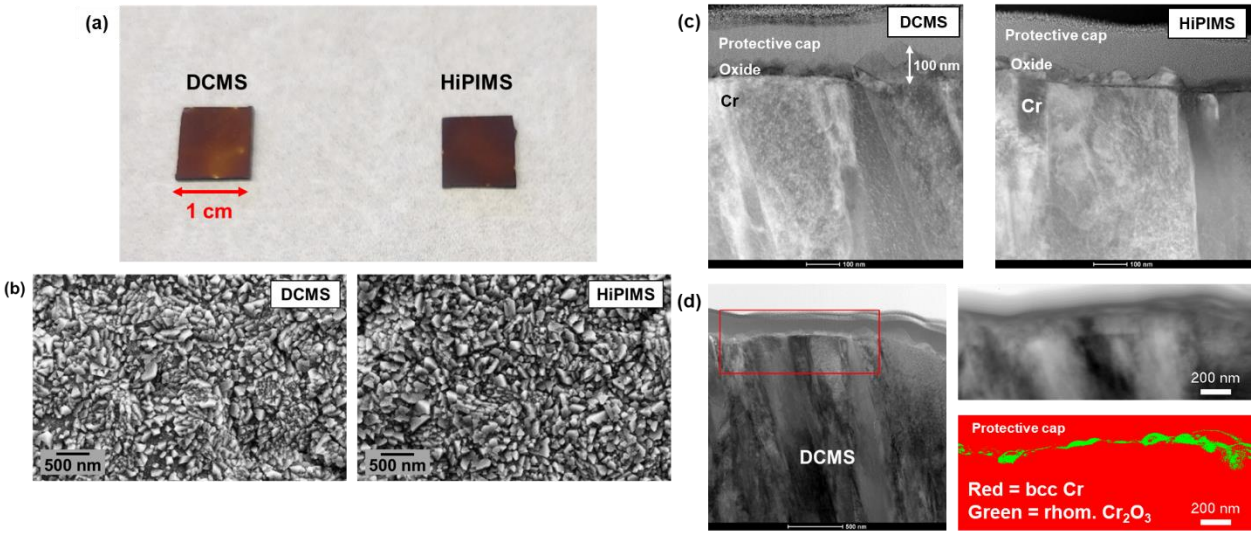

Figure 7.9: (a) Photograph of the Vendor I DCMS and HiPIMS Cr coatings after three months of exposure in the PWR flow loop; (b) SEM images of the surface of the two coatings after PWR flow loop exposure; (c) Cross-sectional HAADF-STEM images of the near-surface regions of the two coatings after PWR flow loop exposure; (d) BF STEM image of the DCMS coating with the box indicating the ASTAR mapping area and the ASTAR virtual BF STEM image and phase map.

The uncoated CVD SiC and B-HiPIMS Cr coatings performed as expected in the one-month flow loop test. Photographs of the SiC and B-HiPIMS samples after one month of exposure are

shown in Figure 7.10. The appearance of the SiC did not visibly change while the B-HiPIMS surface color became green-gold. The appearance of B-HiPIMS after the PWR flow loop test was very similar to the Cr-coated samples tested in the static autoclave. Although the exact thickness of the oxide layer on the B-HiPIMS Cr sample is unknown, the fact that the surface appearance is the same as the autoclave samples that were also tested for one month suggests that the color of the exposed samples is a function of the oxide layer thickness due to thin film interference effects rather than composition. The average weight change of CVD SiC in the PWR flow loop test was about -0.005 mg/cm^2, and the weight change of B-HiPIMS was about 0.005 mg/cm^2. A detailed comparison of the results of the static autoclave and PWR flow loop hydrothermal corrosion tests is provided in the next section.

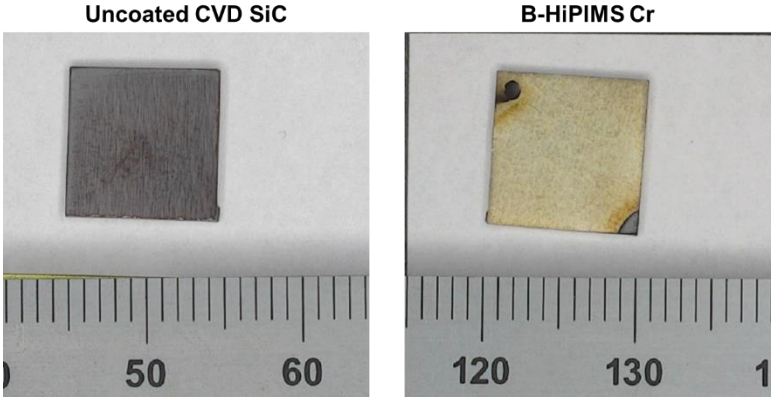

Figure 7.10: Photographs of uncoated CVD SiC and B-HiPIMS Cr samples after one month of exposure in the PWR flow loop.

7.3 Effect of water chemistry and flow on corrosion behavior

The test conditions of the static autoclave and PWR flow loop allow for elucidation of the effects of water chemistry and coolant flow on corrosion performance. These aspects include the kinetics of corrosion reactions and the thickness, morphology, and chemistry of the oxide layer. Figure 7.11a shows a comparison of weight change data for the two types of samples (uncoated CVD SiC and B-HiPIMS Cr) that were tested in both corrosion conditions (static autoclave and

PWR flow loop) for 30 days. The magnitude of SiC weight loss and Cr weight gain are both greater in the static autoclave. As mentioned in Section 7.1, it is known that the water inside the static autoclave contains some amount of dissolved oxygen gas when the test begins, whereas the flow loop coolant contains predominantly dissolved hydrogen (Section 7.2). Because both the dissolution of SiC (via the formation of SiO_2) and oxidation of Cr (Cr metal forming Cr_2O_3) involve reactions with oxygen, it is not surprising that corrosion reactions are accelerated when dissolved oxygen is present. This is in agreement with previous studies of the effects of water chemistry on corrosion of SiC [4,40] and Cr [8,13]. However, it should be noted that for Cr, its passivation behavior can be lost in highly oxygenated conditions (e.g., dissolved oxygen concentration greater than about 1 ppm), where Cr_2O_3 is no longer stable [13,196]. A flow loop corrosion test was also performed under oxygen-rich conditions, and it was observed that the Cr coating was fully consumed via corrosion within seven days. More details of the corrosion test in highly oxygenated conditions are provided in Appendix B.

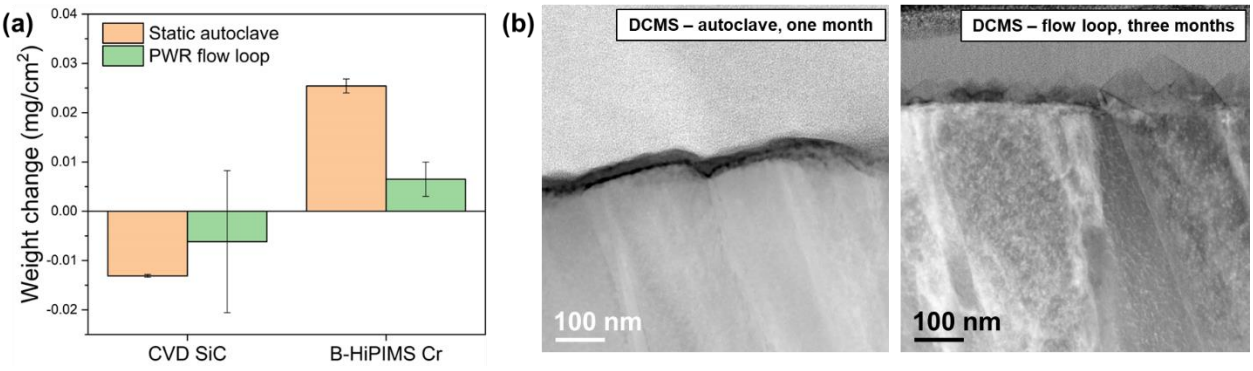

Figure 7.11: (a) Comparison of weight change data for uncoated CVD SiC and the B-HiPIMS Cr coating that were tested for 30 days in the static autoclave and PWR flow loop; (b) HAADF-STEM images comparing surface oxides on the DCMS Cr coating samples that were tested for 30 days in the static autoclave and three months in PWR flow loop.

The two different test conditions also produce oxide layers with different characteristics. A side-by-side comparison of the oxide layers formed on the DCMS Cr coating in the two corrosion tests is shown in Figure 7.11b. The DCMS coating exposed in the static autoclave formed an oxide

layer with a uniform thickness and morphology and has the appearance of a conformal thin film. The oxide layer formed during the flow loop test is thicker and composed of individual pyramidal grains with a more jagged morphology. There are multiple variables to be considered in this comparison, including exposure time, water chemistry, and flow rate. The thicker oxide on the flow loop-tested sample can be attributed to the longer duration of the flow loop test. It is possible the test duration and flow also influence the oxide morphology. The oxide layer may grow uniformly during the initial stages of oxidation, and the pyramidal grains might only emerge later. Coolant flow could also influence the oxide growth morphology. Weakly attached hydroxide species may be preferentially detached from the surface by the flowing coolant, or the growth of pyramidal oxide grains could be favored in certain directions due to shadowing effects.

The final aspect that can be compared is the composition of the surface corrosion layer formed during the two hydrothermal corrosion tests. XPS was used to investigate the chemical bonding states of Cr and O in the near-surface regions of the DCMS and HiPIMS coatings after one month exposure in the static autoclave and three months exposure in the PWR flow loop. Prior to collection of XPS data, hydrocarbons were removed from the sample surface using 30 seconds of *in situ* Ar^+ milling. High resolution scans of the Cr 2p, O 1s, and C 1s energy ranges were performed. All scans were aligned to the C 1s peak at 285.0 eV to account for minor charging effects.

Spectra from the Cr $2p_{3/2}$ portion of the Cr 2p energy range for both coating types and corrosion conditions are shown in Figure 7.12a. For each plot, the coating type is the same, and the corrosion condition is varied. It can be observed that the position, width, and shape of the Cr 2p peak is different between the two corrosion conditions, suggesting that the composition of the oxide layer is altered. A similar conclusion can be drawn from the comparison of O 1s spectra in Figure 7.12b.

The O 1s spectra from the autoclave-tested samples tend to be shifted to a higher binding energy and a have a larger shoulder on the higher energy side of the main peak. The peak shift could be related to the oxide thickness, oxide stoichiometry, or charging artifacts that were not properly accounted for [197,198]. Figure 7.12c shows a comparison of Cr 2p and O 1s spectra for the DCMS and HiPIMS coatings both tested in the PWR flow loop. The peak locations and shapes are very similar for the two types of samples, suggesting that the oxide layer chemistry is most dependent on the corrosion test conditions rather than the coating type and validating XPS as a reliable technique to evaluate the chemical state of the oxide layer.

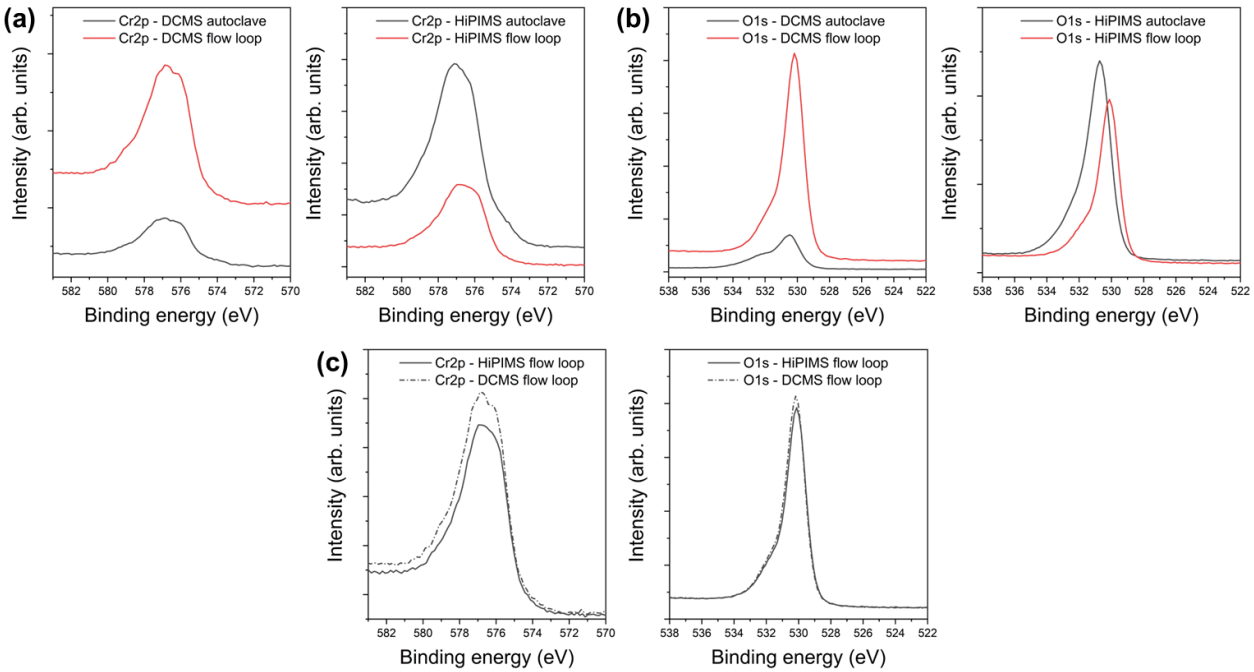

Figure 7.12: (a) XPS comparison of Cr $2p_{3/2}$ spectra from the DCMS and HiPIMS coatings after exposure in the two corrosion tests; (b) XPS comparison of O 1s spectra from the DCMS and HiPIMS coatings after exposure in the two corrosion tests; (c) XPS comparison of Cr $2p_{3/2}$ and O 1s spectra for samples exposed in the same corrosion conditions.

A more quantitative assessment of the oxide layer composition can be made by deconvoluting the XPS spectra and identifying the individual chemical states contributing to the experimental data. For a Cr-based oxide layer, the most common chemical states are metallic Cr (Cr^0), Cr^{3+} in Cr_2O_3, and Cr^{3+} in $Cr(OH)_3$ [198,199]. XPS analysis of these chemical states is complicated by the

electronic structure of Cr_2O_3, which exhibits muliplet splitting. In this case, the single chemical state of Cr_2O_3 requires fitting of five underlying peaks [198]. The five peaks can be fit using the set of peak constraints (area ratios, FWHM values, and peak positions) via the procedure from Biesinger et al. [198]. The metallic Cr and $Cr(OH)_3$ chemical states can be fit with single peaks. The relative amounts of the different chemical states are determined by taking the ratio of the peak area for that chemical state to the sum of all peak areas. In the case of the Cr_2O_3 multiplet structure, the total Cr_2O_3 fraction is just the sum of the five multiplet peak contributions. All peak fitting was performed using the Spectra Data Processor v8.0 software [200]. The typical Shirley function was used to remove the spectral background.

Figure 7.13 shows the peak deconvolution for the oxide layers formed on the DCMS and HiPIMS coatings in the static autoclave and PWR flow loop corrosion tests. Reasonably good fitting was achieved by using the five-peak Cr_2O_3 multiplet structure and single peaks corresponding to metallic Cr and $Cr(OH)_3$. The typical peak positions and the relative amounts of the different chemical states are summarized in Table 7.2. All peak positions are in good agreement with other XPS studies of Cr-oxide compounds [198,199,201,202]. All samples had a low fraction of metallic Cr, indicating that practically all the Cr on the surface has undergone a reaction with the coolant. The most interesting comparison is between the samples of the same coating type tested in the different corrosion environments. The values in Table 7.2 show that Cr_2O_3 is the predominant species for all samples. However, the samples exposed in the PWR flow loop contain a much greater amount of Cr_2O_3 compared to the same coating type tested in the static autoclave. The values show very good agreement between the two flow loop-tested samples. For the autoclave-tested samples, this analysis suggests that there is a bit more $Cr(OH)_3$ content in the HiPIMS sample, but the trend of greater Cr_2O_3 content in the flow samples is clear.

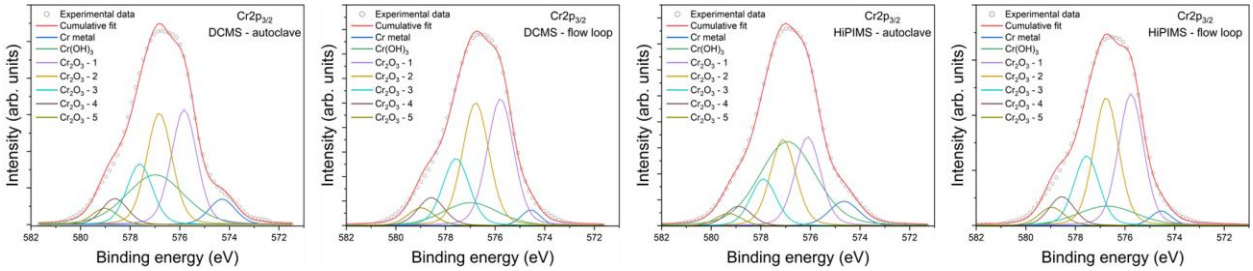

Figure 7.13: Peak deconvolution of Cr $2p_{3/2}$ spectra for the DCMS and HiPIMS coatings in both corrosion environments.

Table 7.2: Chemical state analysis of Cr from the DCMS and HiPIMS oxide layers based on the peak deconvolution in Figure 7.13. The peak position is the average position across all samples. The relative percentages are calculated by using the integrated peak areas. The total Cr_2O_3 percentage is the sum of the five multiplet peaks. The Cr_2O_3 peak position is the weighted average position of five multiplet peaks.

Chemical state	Peak position (eV)	DCMS – autoclave	DCMS – flow loop	HiPIMS – autoclave	HiPIMS – flow loop
Cr metal	574.3	5.6%	2.7%	6.1%	2.7%
$Cr(OH)_3$	577.3	24.1%	11.3%	39.5%	10.5%
Cr_2O_3 (total)	576.8	70.3%	86.0%	54.4%	86.8%

A similar analysis can be conducted using the O 1s spectra from the same samples. The O 1s spectra can be broken down into three contributions corresponding to the Cr-oxide, Cr-hydroxide, and adsorbed water (i.e, a hydrated oxide) [203–205]. The peak deconvolutions are shown in Figure 7.14. The three-peak deconvolution provided very good fit quality for all four samples. The average peak positions and relative percentages of the different chemical states are given in Table 7.3. Theoretically, the relative amounts of oxide and hydroxide determined from the O 1s fitting should be similar to the values determined via the Cr 2p fitting, but it can be seen the fraction of oxide determined using O 1s is consistently lower than when using Cr 2p. However, the qualitative trend of greater oxide fraction in the flow loop samples still holds for the O 1s chemical state assessment. This may suggest that there is some systematic error in the quantification of the different chemical states, but the trends observed in the Cr 2p analysis are valid. One point to note is that some researchers have mentioned that a portion or all of the hydroxide peak may be due to

defective sites in the main oxide [198,206]. Also, it could be assumed that all adsorbed water is incorporated into the oxide lattice, in which case the fraction of water could be added to the fraction of oxide, bringing the relative amount closer to what was determined in the Cr 2p analysis.

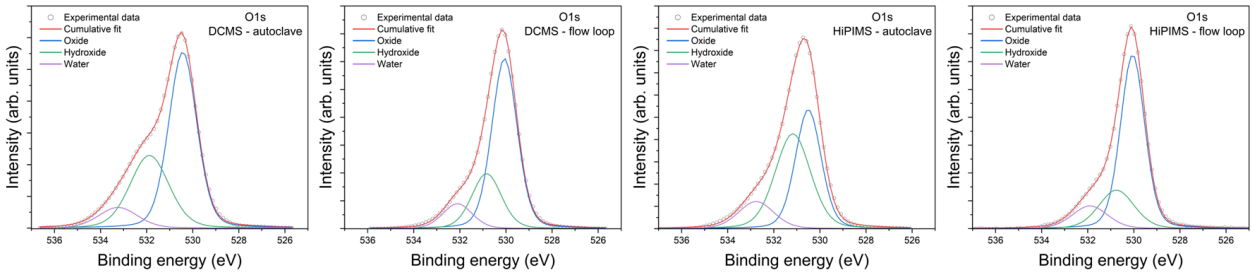

Figure 7.14: Peak deconvolution of O 1s spectra for the DCMS and HiPIMS coatings in both corrosion environments.

Table 7.3: Chemical state analysis of O from the DCMS and HiPIMS oxide layers based on the peak deconvolution in Figure 7.14. The peak position is the average position across all samples. The relative percentages are calculated by using the integrated peak areas.

Chemical state	Peak position (eV)	DCMS – autoclave	DCMS – flow loop	HiPIMS – autoclave	HiPIMS – flow loop
Oxide	530.3	57.7%	64.7%	41.6%	66.1%
Hydroxide	531.1	32.9%	24.3%	45.4%	21.3%
Adsorbed water	532.5	9.4%	11.0%	13.0%	12.6%

The XPS analysis of the oxide layers clearly shows that the $Cr(OH)_3$ content is greater in the samples tested in the autoclave. Two variables must be considered in the comparison between the coated samples tested in the static autoclave and flow loop, test duration and water chemistry. First, it is possible that the high hydroxide content in the oxide layers formed in the autoclave test are related to the test duration. It may be easier for hydroxides to form during the initial stages of oxidation that then gradually react to form oxides. There is some evidence to support the early formation of hydroxides that may explain why the hydroxide contribution in the one-month autoclave test is greater than in the three-month flow loop test [205,207]. The water chemistry in the two corrosion environments is likely also playing a role. It is known that the autoclave coolant contained at least some amount of dissolved oxygen and does not have continuous chemistry

control. The presence of free oxygen may promote the presence of other ions in the coolant that could favor hydroxide formation. In the PWR flow loop, hydrogen is the primary dissolved species, which may restrict chemical reactions to only occur between Cr and water molecules and promote oxide formation.

To conclude, both the static autoclave and PWR flow loop are effective means to evaluate the hydrothermal corrosion performance of Cr-coated SiC. The flow loop test offers a more realistic simulation of the in-reactor corrosive environment by incorporating continuous chemistry control and hydrogen addition to coolant, as well as flow of the coolant. Through these corrosion tests, the best performing Cr coatings, namely the DCMS and HiPIMS coatings produced by Vendor I and the B-HiPIMS coating from Vendor II, could be identified. These coatings remained adherent for the full extent of the autoclave and flow loop tests and were effective in mitigating the hydrothermal corrosion of the underlying SiC through the formation of a passivating Cr_2O_3 layer on the Cr coating surface. One aspect not addressed by these experiments is the effect of irradiation on corrosion behavior. Irradiation can accelerate corrosion by enhancing near-surface diffusion through the generation of point defects and radiolyzing the coolant [18]. Water radiolysis can generate oxidative species, such as hydroxides, peroxides, and oxygen radicals [18]. A corrosion experiment incorporating water radiolysis was planned but could not be completed (details in Appendix C). Overall, the results of this chapter show that the Cr coatings should remain protective as long as the coating remains adhered. However, it should be noted that Cr may not be fully protective in an oxygen-rich environment (see Appendix B).

8. Radiation Damage Effects in Cr-coated SiC

This chapter features direct content from the following journal articles first-authored by the PhD candidate:

K. Quillin, K. N. Sasidhar, M. W. Qureshi, H. Yeom, I. Szlufarska, K. Sridharan, "Unusual nanoscale amorphization of metallic chromium interfacing with SiC under high energy irradiation," *Acta Materialia* (2024), under review.

K. Quillin et al., "Structural evolution and mechanical behavior of a Cr coating on SiC under high energy ion irradiation," *Journal of Nuclear Materials* (2024), in preparation.

8.1 Experiment description

To study the effects of irradiation on the Cr coating and the Cr/SiC interface, a 5 mm × 10 mm × 1 mm samples of the B-HiPIMS Cr-coated SiC (coating thickness ~ 4.3 μm) were irradiated at the Argonne Tandem Linac Accelerator System (ATLAS) located at Argonne National Laboratory. Irradiation was conducted using 80 MeV Xe^{26+} ions at a sample temperature of 350 °C with the sample surface fixtured normal to the direction of the ion beam. The extremely high incident ion energy was selected so the ion could penetrate through the entire Cr coating thickness and perturb the Cr/SiC interface. The beam was defocused and aligned to irradiate half of the sample, producing an unirradiated reference region that experienced the same thermal history as the irradiated region. An illustration of the irradiated sample is shown in Figure 8.1a. The beam current was measured by a National Electrostatics Corporation (NEC) Faraday cup (model FC18), and the shape of the beam was determined by a NEC beam profile monitor (model BPM81). The beam profile was approximately a two-dimensional Gaussian shape with a horizontal and vertical spread of σ_x = 1.4 mm and σ_y = 1.1 mm, respectively and a peak ion flux of $1.9 \times 10^{12}/cm^2 \cdot s$. The sample was irradiated for 4.5 hours to reach an ion fluence of $3.0 \times 10^{16}/cm^2$.

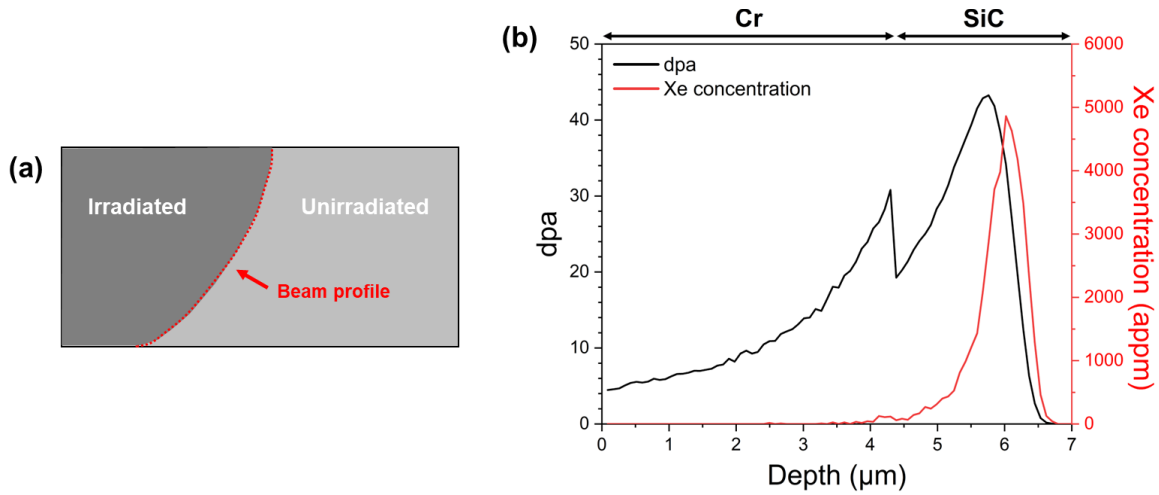

Figure 8.1: (a) Illustration of the irradiated B-HiPIMS Cr sample; (b) SRIM-2013 calculations of dpa and implanted Xe concentration as a function of depth below surface produced in Cr-SiC by 80 MeV Xe^{26+} ion irradiation to a fluence of $3.0 \times 10^{16}/cm^2$.

The SRIM-2013 software package was used to compute the radiation damage profile produced in the Cr-SiC coating-substrate system by the 80 MeV Xe^{26+} ion irradiation [80]. Threshold displacement energies of 40 eV, 35 eV, and 21 eV were used for Cr, Si, and C, respectively [82,83]. A two-layer target consisting of a 4.3 μm thick Cr layer followed by a SiC layer was created using the SRIM user interface. The number of displacements per atom (dpa) was calculated from the SRIM output following the procedure of Stoller et al. [81]. The dpa generated in the Cr-SiC bilayer and implanted Xe concentration as a function of depth are shown in Figure 8.1b. The considerably high incident ion energy produces a radiation damage region that extends through the entire Cr coating and perturbs the Cr-SiC interface. The damage level at the interface is 20–30 dpa, and Xe is implanted to a depth about 1.5 μm below the interface into SiC.

8.2 Irradiation-induced defects in Cr coating

The effects of radiation damage on the structure of the B-HiPIMS Cr coating were evaluated using TEM-based methods. In a pure metal, the primary effects of irradiation are the formation of point defects (vacancies and interstitials) and defect clustering in the form of voids and dislocation loops [18]. It should be noted that prior to irradiation, there are pre-existing defects in the as-

deposited coating. Figure 8.2a shows a BF STEM image of the reference B-HiPIMS sample. The visible defects appear to be a random assortment of dislocations and dislocation loops (appearing as small dark spots) with no preferred orientation. The presence of this nanoscale defect structure has been observed in other PVD coatings [208,209] and may be promoted by the non-equilibrium and layer-by-layer growth nature of sputter deposition, especially considering the low energy ion bombardment that occurs during HiPIMS and B-HiPIMS deposition.

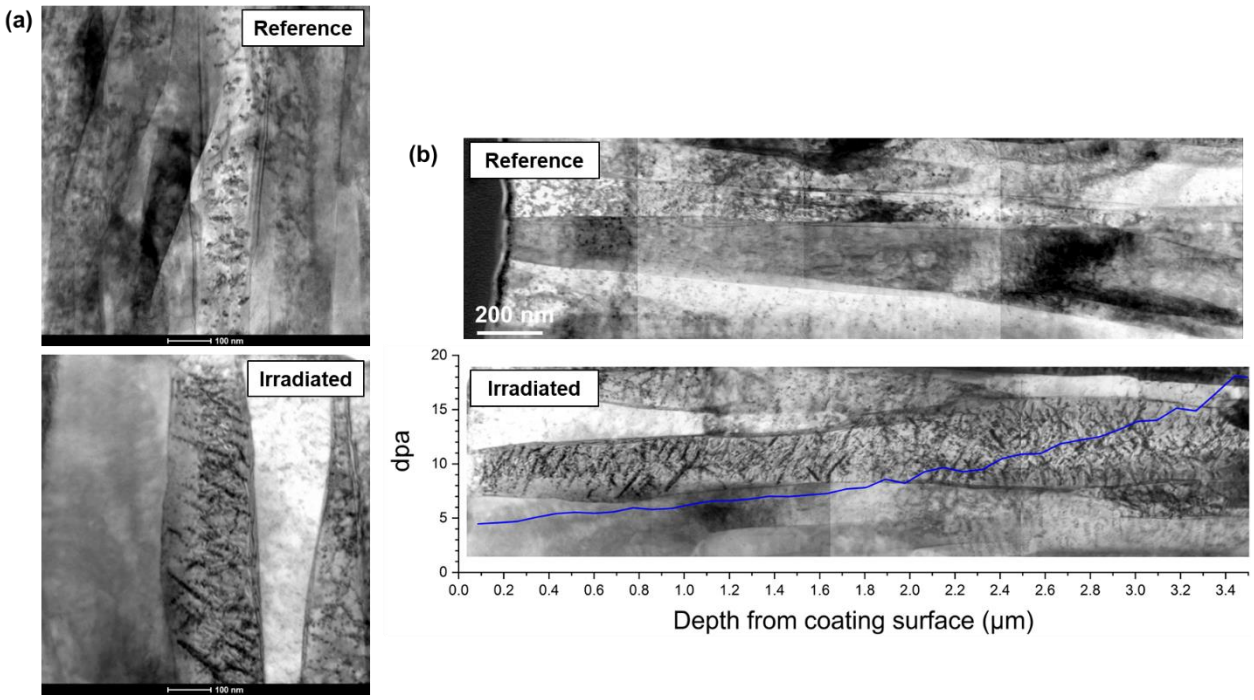

Figure 8.2: BF STEM images of defects in the reference and irradiated columnar structure of B-HiPIMS samples; (b) Stitched BF STEM images as a function of depth from the coating surface for the reference and irradiated B-HiPIMS samples with the dpa profile overlayed on the image of the irradiated sample.

Figure 8.2a also shows the defect structure in the irradiated columnar grain structure of the B-HiPIMS coating, which has clearly been altered by radiation damage. The central grain in the imaged area contains many defect structures oriented at the same angle of inclination with respect to the longitudinal axis of the grain. Closer inspection of these defect structures reveals that they are not single dislocations, but oriented chains composed of multiple dislocation loops. In Figure

8.2b, multiple BF STEM images are stitched together to show how the defects evolve as a function of depth from the coating surface. In the unirradiated B-HiPIMS reference sample, the defect density appears to be mostly uniform throughout the coating thickness. In the irradiated sample, the defect density increases farther away from the coating surface. This is in line with the simulated damage profile, overlayed on the image of the irradiated sample in Figure 8.2b, which shows a trend of increasing dpa deeper into the coating, resulting in a greater defect density.

The ASTAR nanoscale orientation mapping system was used to identify the crystal direction along which the dislocation loop chains are oriented. Figure 8.3a shows the ASTAR mapping area which includes two grains where the dislocation loop chains can be clearly observed. The orientation angle of the dislocation loop chains with respect to the growth axis of the columnar grains was measured and is in the range of 50–65°, as shown in Figure 8.3b. ASTAR mapping outputs three orientation maps, with each map representing the orientation of the grains with respect to each of the major sample axes. The sample axes are defined in the virtual BF STEM image in Figure 8.3c. X and y are the horizontal and vertical directions in the plane of the TEM sample, and z is the direction through the thickness of the same (parallel to the electron beam). Figure 8.3c also shows arrows indicating two distinct features which can be used for positional referencing in the real space image. The two grains of interest for orientation analysis are also labeled in Figure 8.3c. Orientation maps with respect to the y and z sample axes are shown in Figure 8.3d along with the crystal directions parallel to the corresponding sample direction for the two grains of interest. Both grains are oriented similarly with respect to the vertical direction in the sample plane (y sample axis) with orientations close to [111] but are oriented differently in the z direction by an angle of about 90°.

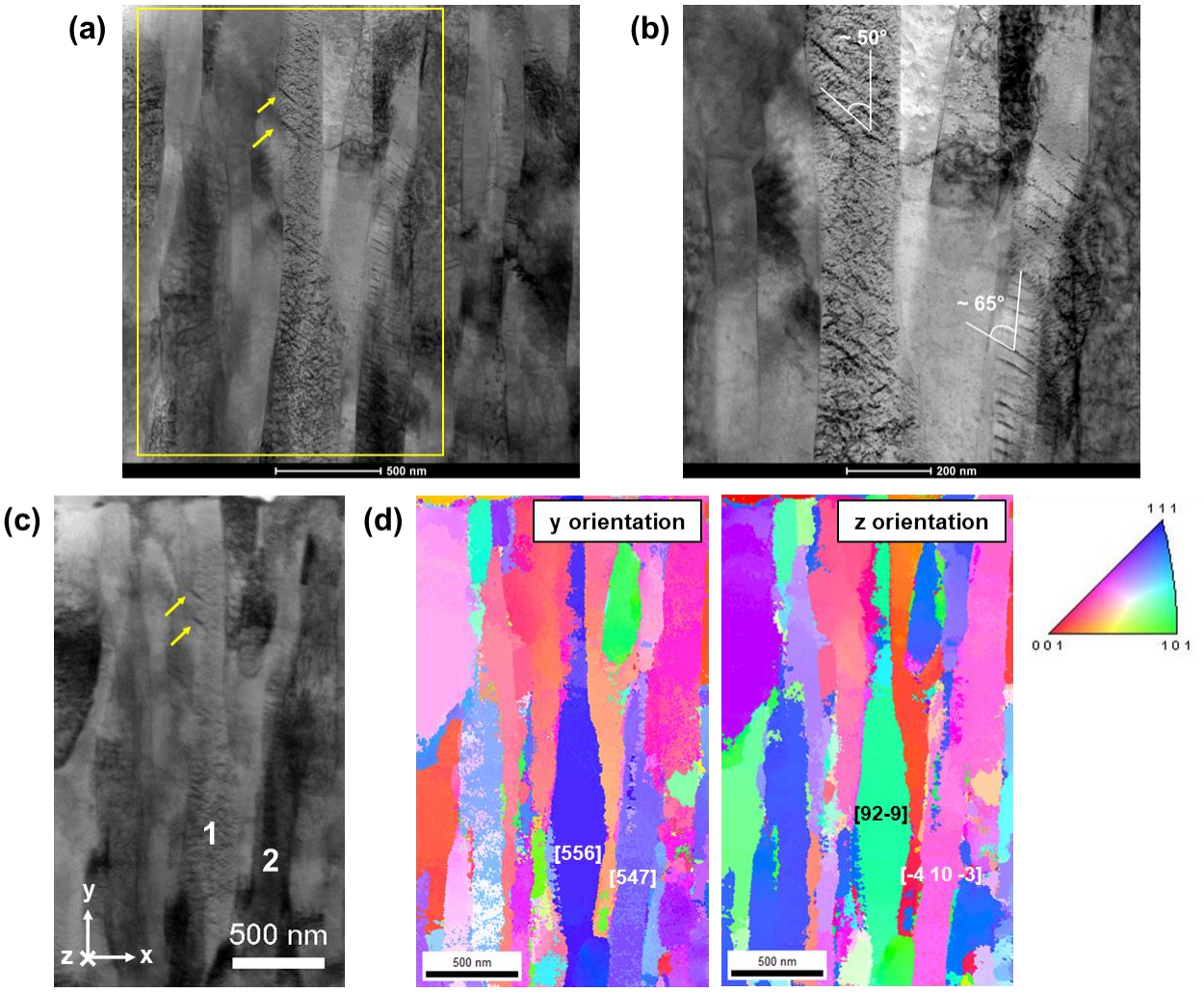

Figure 8.3: (a) BF STEM image of the irradiated B-HiPIMS Cr coatings with the yellow box indicating the ASTAR mapping region and arrows pointing to identifying features for location referencing in the virtual ASTAR STEM image; (b) Higher magnification BF STEM image showing oriented dislocation loop chains and angular measurement of the inclination of the chains with respect to the growth direction of the grains; (c) Virtual BF STEM image collected via the ASTAR mapping with the arrows indicating the same features indicated by the arrows in (a). The sample coordinate system is shown in the lower left, and the two grains of interest are indicated (1 and 2); (d) IPF maps with respect to the y and z sample directions with labels indicating the crystal orientations of the two grains of interest.

The orientation of the dislocation loop chains can be identified by finding which crystal direction forms an angle of about 50° in the y direction with respect to the orientation of the grains. Because the direction of the dislocation loop chains lies in the sample plane, it also must be normal to the z orientation direction of the grain. This way, the list of possible crystalline directions can

be reduced, and self-consistency can be ensured. Following this procedure, it was found that the defect chains are aligned along a <100> direction in the two grains of interest. There is also a second set of defect chains that are less obvious in the BF STEM images that intersect the main <100> chains at an angle of 55–60°, which are most likely aligned along <111> directions.

While dislocation loop formation has been observed in irradiated PVD Cr coatings [210,211], no prior reports of oriented loop chains could be found. There have been many reports of oriented defect clusters (often termed chains, strings, or rafts) in other irradiated bcc metals, such as Fe and W [212–216]. In a few studies, the orientation direction of the defect chains has been identified as <100>, in agreement with this study. One possible explanation for the development of <100>-oriented chains is that due to their low atomic packing density, the <100> directions can accommodate the greatest degree of volume expansion caused by crystal defects [217] The Burgers vectors of dislocation loops in bcc metals tends to be a mixture of a/2<111> and a<100> that seems to strongly depend on the irradiation dose and temperature [218]. The accepted mechanism for the formation of oriented dislocation loop chains is related to elastic interactions between neighboring loops where a shared orientation can develop through dislocation glide and rotation [219,220]. It is possible that most of the loops observed in the Cr coating have a Burgers vector of a/2<111>, as dislocations of this type are more mobile, especially at low temperatures, and would have the ability to undergo the transformations for defect alignment [218]. However, a detailed TEM investigation incorporating many sample tilting steps would be necessary to confidently identify the Burgers vector of the observed loops. Lastly, because the development of oriented defects depends on internal strain fields, the pre-existing residual stress of the B-HiPIMS coating may also be playing a role in the formation of the defect structures.

While dislocation loops seemed to be the primary type of defect formed in Cr by irradiation, some voids less than 5 nm in diameter were also observed. TEM images of voids are shown in Figure 8.4. Because very little Xe is implanted in the Cr coating, these voids are likely true cavities (i.e., empty space formed via clustering of vacancies) rather than gas bubbles. Dislocation loops can be formed via clustering of either vacancies or interstitials, while voids are larger vacancy clusters. Interstitials also tend to be more mobile than vacancies, offering one explanation as to why loop formation is favored over voids. The irradiation temperature was on the very low end of the void swelling regime for Cr, and the high fraction of grain boundary area in the Cr coating may limit vacancy clustering by acting as defect sinks [221].

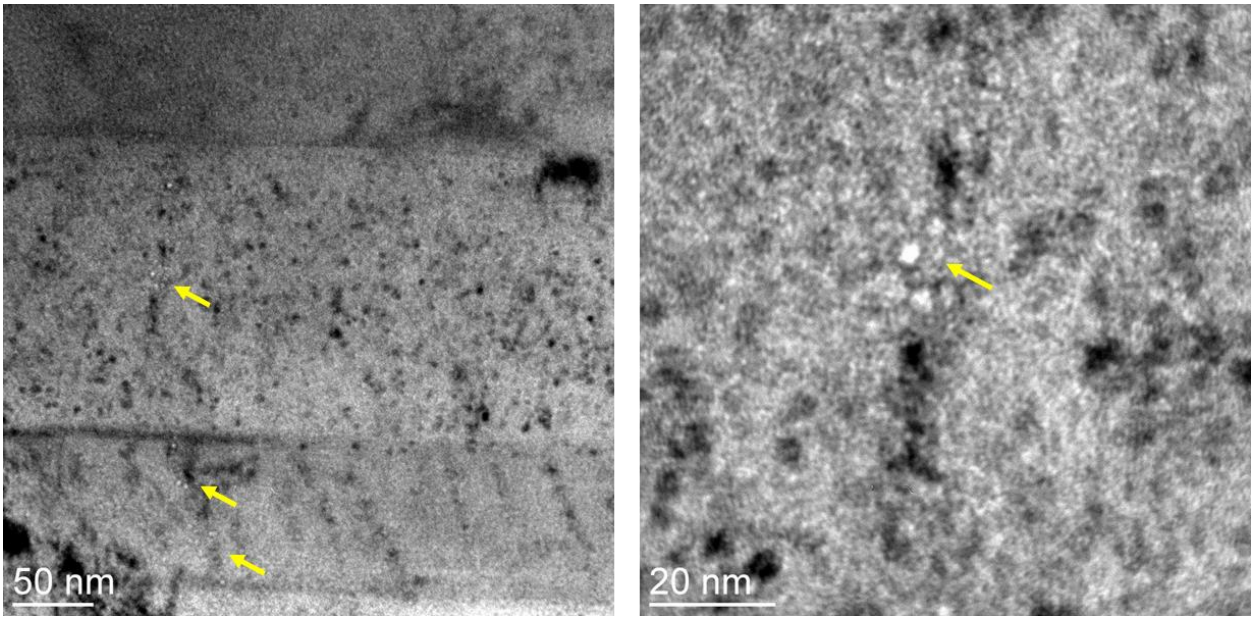

Figure 8.4: BF TEM images of the irradiated B-HiPIMS Cr coating with arrows indicating voids.

8.3 Effects of irradiation on Cr-SiC interface

8.3.1 Characterization of interfacial evolution via transmission electron microscopy

After the irradiation experiment, transmission electron microscopy analysis of the interface in the unirradiated reference region and irradiated region was performed to evaluate the effect of the high energy Xe^{26+} irradiation on the interfacial structure. Figure 8.5a shows a BF TEM image of

the Cr-SiC interface within the unirradiated region, which experienced solely thermal effects during the irradiation experiment. Given the relatively low irradiation temperature (350°C) and short irradiation time, no structural changes were observed in this region compared to the as-deposited coating [222]. In contrast, the structure of the interface was substantially altered by irradiation, as shown in Figure 8.5b. Specifically, two new phases were observed near the Cr-SiC interface: an amorphous band with approximate thickness of only 20 nm and a 5 nm-thick crystalline phase that separated the amorphous phase and the SiC substrate. The amorphous structure was confirmed via HRTEM imaging and electron diffraction as shown in Figure 8.5c and d.

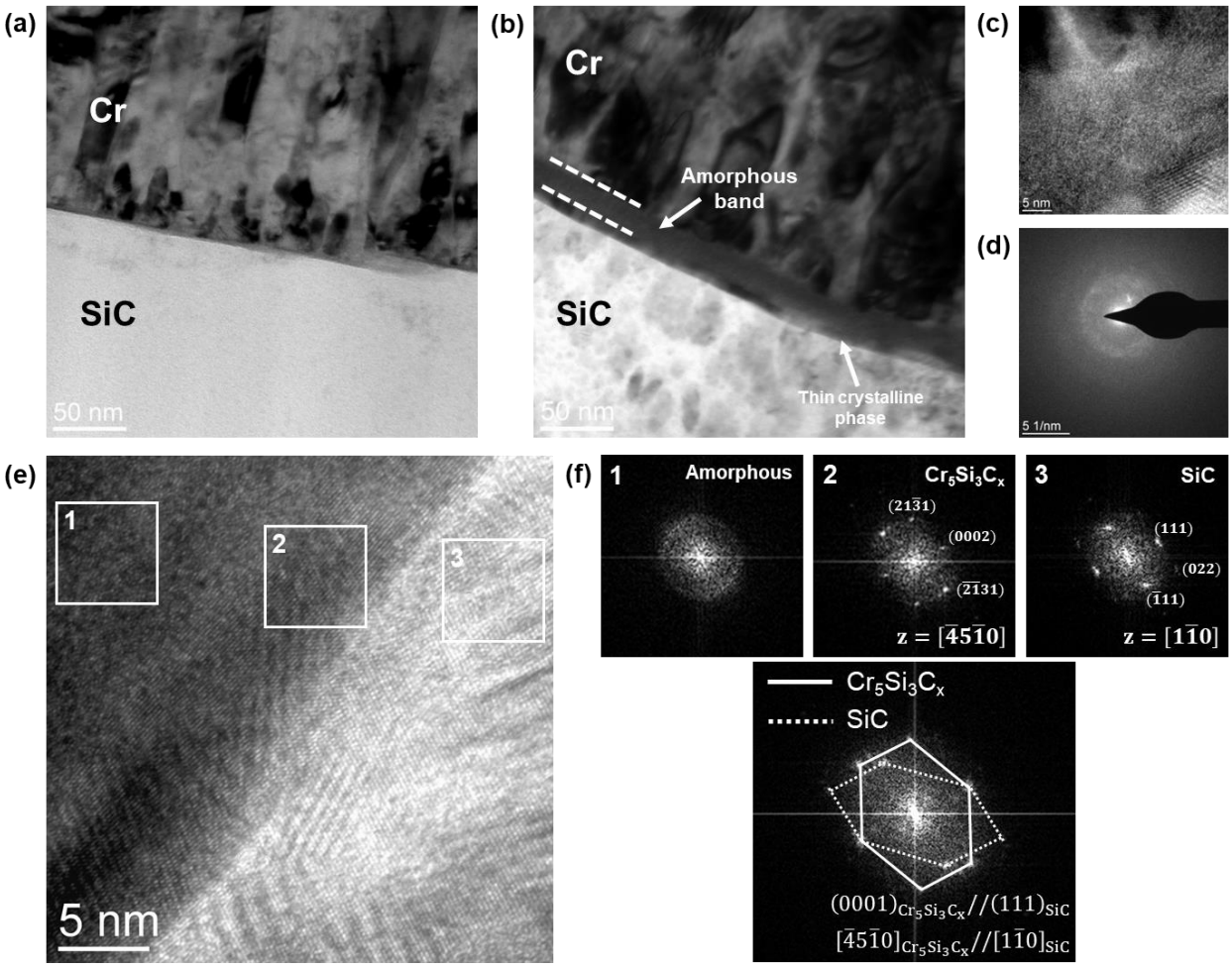

Figure 8.5: (a) BF TEM image at the interface of the unirradiated reference region; (b) BF TEM image of the interface of the irradiated sample showing the amorphous band formed at the Cr-SiC interface; (c) HRTEM image centered on the amorphous phase; (d) Electron diffraction pattern of the amorphous phase exhibiting diffuse rings typical of an amorphous structure; (e) HRTEM image of the interface between the amorphous phase and SiC with FFT locations boxed; (f) FFTs taken from the boxed locations in (e) and overlaid FFT patterns from the $Cr_5Si_3C_x$ and SiC phases illustrating the orientation relationship.

Fast Fourier Transform (FFT) analysis of the HRTEM image was conducted to identify the thin crystalline phase present between the amorphous band and SiC. FFT patterns calculated from the amorphous band, crystalline phase, and SiC substrate are presented in Figure 8.5f. Indexing the FFT pattern of the crystalline phase against the known crystal structures of the possible intermetallic and carbide phases of the Cr-Si-C system indicates that the crystalline phase is $Cr_5Si_3C_x$. This ternary phase has a hexagonal close packed (hcp) crystal structure (space group

193, $P6_3/mcm$) [223] and has been commonly observed on the SiC-rich side of Cr-SiC diffusion couples [172,222,223]. Additionally, the FFT analysis revealed an orientation relationship between the $Cr_5Si_3C_x$ phase and the SiC substrate illustrated by the overlaid FFT patterns shown in Figure 8.5f. We found the basal planes of the hexagonal close packed (hcp) $Cr_5Si_3C_x$ phase to be oriented parallel to the {111} planes of the zinc blende SiC structure (analogous to two interpenetrating face centered cubic lattices of Si and C). The alignment of these close-packed families of planes between hcp and face centered cubic (fcc) phases in combination with the alignment of the $< 11\bar{2}0 >_{hcp}$ and $< 1\bar{1}0 >_{fcc}$ directions is commonly observed in fcc to hcp phase transformations [224,225]. From the FFT analysis, it can be determined that the close-packed planes lie parallel to each other, but the $[\bar{4}5\bar{1}0]$ direction of the hexagonal ternary phase is aligned parallel to the $[1\bar{1}0]$ direction of the cubic SiC phase. This corresponds to a 19° deviation from the typical orientation relationship. The atypical orientation relationship observed between the cubic SiC substrate and hexagonal $Cr_5Si_3C_x$ phase may be due to strain generated by the lattice mismatch at the interface and the presence of interstitial carbon altering the closest-packed direction within the hexagonal crystal structure [225]. It is also possible that within small volumes of materials orientation relationships may be altered with respect to their bulk counterparts due to competition between volume, strain, and interfacial free energies [225].

In addition to structural characterization, STEM-EDS was used to analyze the compositional distribution of Cr, Si, and C in the interfacial region after irradiation. Compositional profiles measured via EDS line scans are shown in Figure 8.6a. These measurements indicate that the amorphous layer in the irradiated sample is on the Cr-rich side of the interface. Additionally, the Si and C profiles indicate that both elements are present in the amorphous layer in concentrations of at least 10 at. %. The Si composition profile exhibits a uniform gradient between the SiC

substrate and amorphous layer. The slope of the Si gradient is shallower compared to the reference sample (region of sample that experienced similar thermal effects but not irradiation effects). In contrast, the C profile does not follow a uniform gradient between the SiC substrate and amorphous layer. Rather, a narrow region of C depletion in the area that corresponds to the crystalline $Cr_5Si_3C_x$ phase and C enrichment within the amorphous band can be observed. These observations suggest that radiation damage has notably altered the compositional makeup of the interface, and these are conclusively not purely thermal diffusion effects.

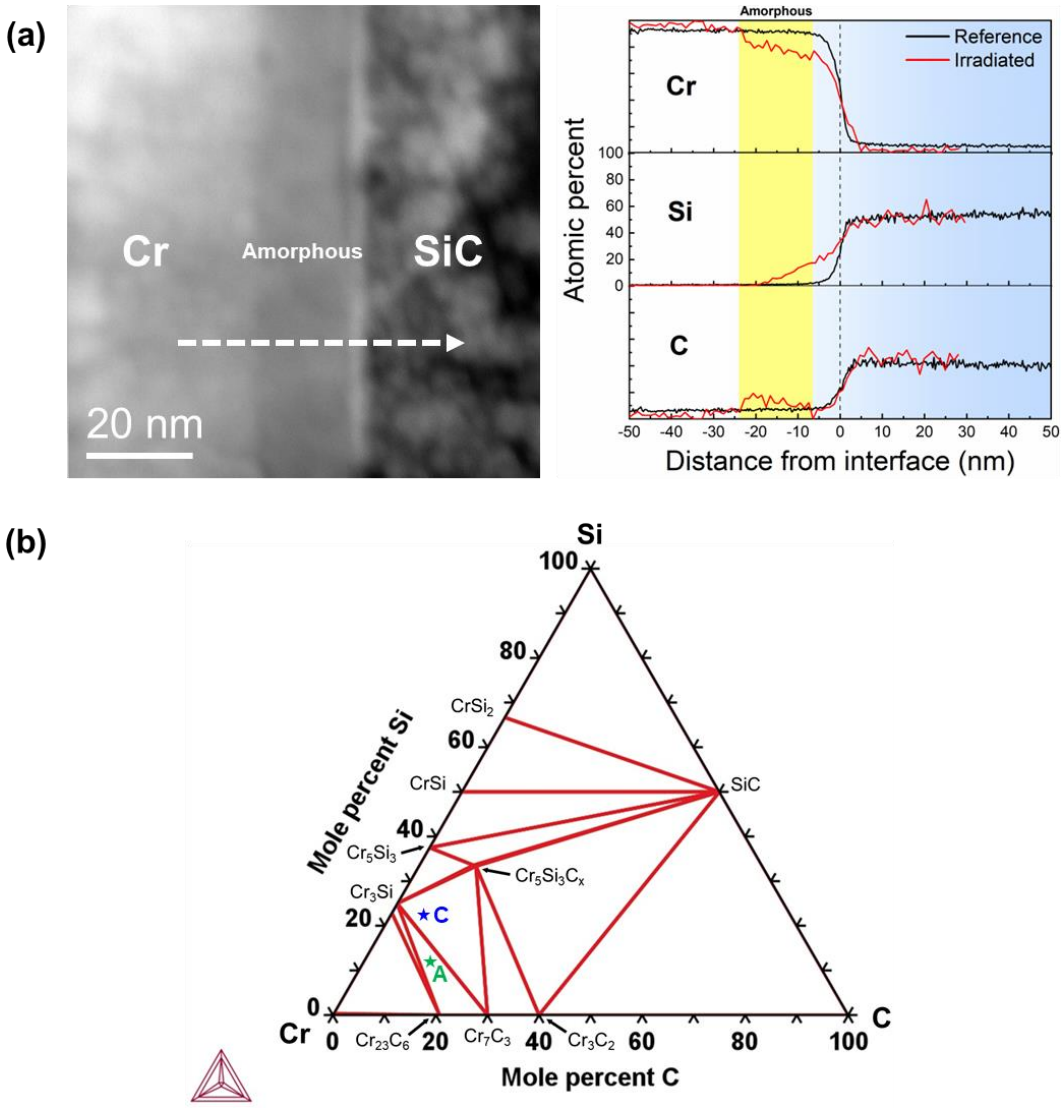

Figure 8.6: (a) HAADF STEM image showing the location of the EDS line scan in the irradiated sample and Cr, Si, and C composition profiles measured in the reference and irradiated samples with the location of the amorphous band in the irradiated sample indicated; (b) Calculated isothermal phase diagram for the Cr-Si-C system at 300 °C with the points A and C marking the average compositions of the amorphous and crystalline layers, respectively.

An equilibrium ternary phase diagram for the Cr-Si-C system at 300 °C (approximate irradiation temperature) with markings indicating the average compositions of the amorphous and the thin $Cr_5Si_3C_x$ interfacial layers measured from STEM-EDS is shown in Figure 8.6b. Obviously, the phase diagram does not predict the formation of an amorphous phase, as the multiple silicide and carbide phases are more thermodynamically stable, and the amorphous phase observed after

irradiation is undoubtedly metastable. For the composition corresponding to the $Cr_5Si_3C_x$ layer (point C in Figure 8.6b), the phase diagram shows that at equilibrium, there should be three co-existing phases (Cr_3Si, Cr_7C_3, $Cr_5Si_3C_x$), with the appropriate compositional partitioning (compositions of the three phases are represented by the vertices of the bounding three-phase field). However, it is also clear from the experimental results that such equilibrium compositional partitioning has not taken place. Instead, only the ternary $Cr_5Si_3C_x$ compound with a significant deviation from the equilibrium stoichiometry (i.e., a metastable composition) was observed to form. To understand the formation of these metastable phases and the extent of radiation-induced mixing, we have used a combination of computational approaches that include ballistic simulations of ion beam mixing, density functional theory (DFT) calculations of defect formation energies, and CALPHAD-based thermodynamic modeling to assess phase stability in the Cr-Si-C system under irradiation.

8.3.2 Ballistic transport-induced interfacial mixing

The SDTrimSP software package [85–87] was used to perform a dynamic ion beam mixing simulation to investigate the effect of radiation damage and the resulting ballistic transport of atoms across the interface. In effect, this simulation captures the temporal composition-depth distribution as irradiation progresses. To make more efficient use of computational resources, a narrow target consisting of 500 nm of Cr followed by SiC was built, rather than running the simulation for the entire Cr coating thickness. In support of this approach, it was determined using SRIM that near the Cr-SiC interface the incident ion energy is reduced from 80 MeV to approximately 8 MeV, which was then used as the energy for the incident Xe ions in the SDTrimSP mixing simulation. The dynamic simulation was conducted in 400 fluence steps of $0.0075 \times 10^{16}/cm^2$ each until the final ion fluence of $3.0 \times 10^{16}/cm^2$ was reached, with the target composition

updated after each fluence step. After every 40 fluence steps, the program generated a data output file containing the concentration of each element (Xe, Cr, Si, C) as a function of depth within the simulation window.

Figure 8.7a shows how the distributions of Cr, Si, and C evolve as irradiation progresses through continually increasing levels of ion fluence as a function of depth. Due to the lower threshold displacement energies and lower mass of Si and C compared to Cr, the extent of displacement of these elements into Cr can be observed to be greater than that of Cr into SiC. As one would expect, the mixing range becomes progressively wider with increasing ion fluence. The simulated final elemental distributions after irradiation to a fluence of $3.0 \times 10^{16}/cm^2$ are shown in Figure 8.7b. The skewed nature of intermixing with a greater extent observed on the Cr-side of the interface is in good agreement with the STEM-EDS measurements (Figure 8.6a).

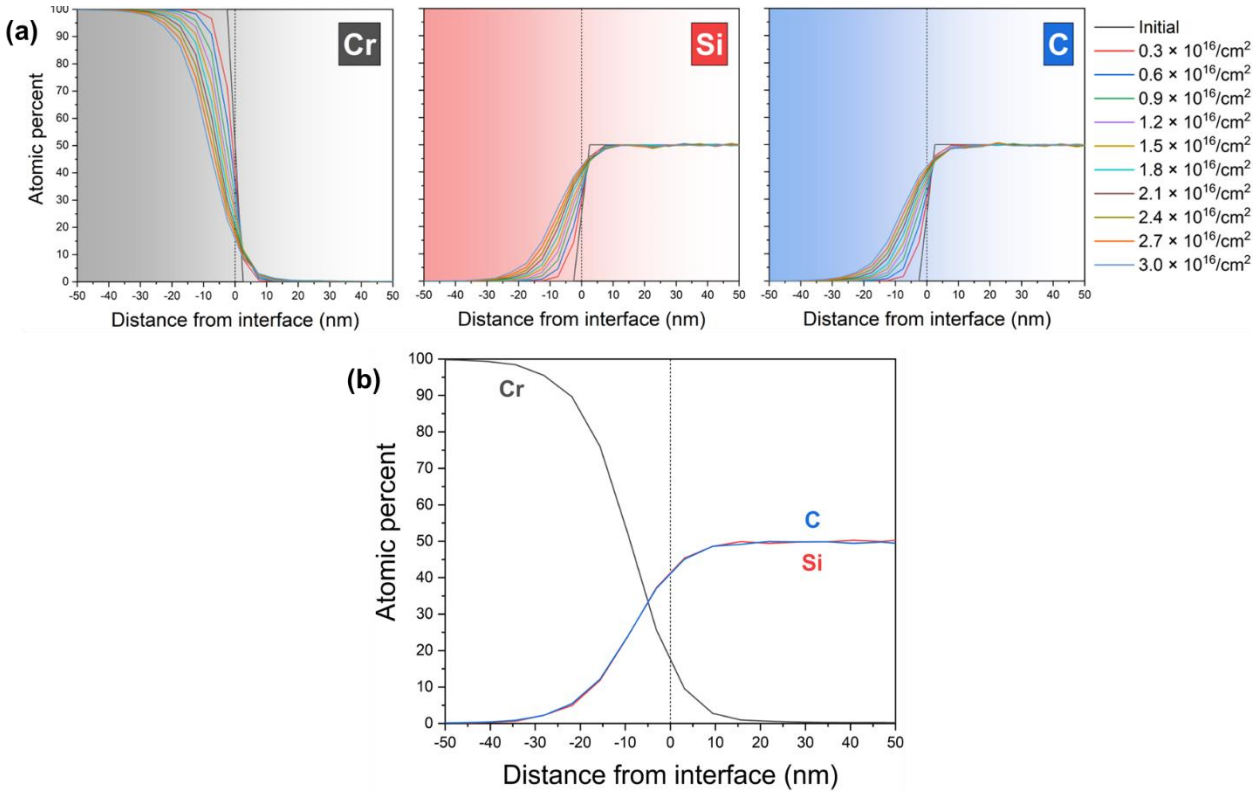

Figure 8.7: (a) Evolution of elemental composition profiles at the interface with increasing ion fluence as simulated by the SDTrimSP software. The dashed line represents the position of the original Cr-SiC interface prior to irradiation; (b) Final composition of the interface as predicted by the SDTrimSP software for an ion fluence of $3.0 \times 10^{16}/cm^2$.

The results of the ion beam mixing simulation further show that intermixing distances of tens of nanometers are possible for Si and C via ballistic collisions. This finding is also in good agreement with the Si composition profile measured via STEM-EDS shown in Figure 8.6a. One should note however that the experimentally measured C profile does not perfectly follow the smooth composition gradient predicted by the mixing simulation. The experimental C profile from Figure 8.6a exhibited a C depleted area near the interface followed by a C enriched region in the amorphous layer. The ion beam simulation does not predict this feature of C distribution since it does not take any thermodynamic properties of the system into account, which could be providing the driving force for C to segregate into the amorphous layer. Based on the results of the ion beam mixing simulation, it can be reasoned that Si and C atoms are being forced into the body-centered

cubic (bcc) Cr phase through irradiation-induced collision cascades. The next question that arises pertains to the relative thermodynamic stability of point defects (self and foreign element interstitials and vacancies) within the Cr and SiC phases. To address this, density functional theory (DFT) calculations were performed to determine the formation energies of the point defects within the two phases.

8.3.3 Ab initio calculations of point defect formation

DFT calculations were performed (courtesy Computational Materials Group, University of Wisconsin-Madison) using the Vienna Ab initio Simulation Package (VASP) code [226]. The generalized gradient approximation (GGA) with Perdew-Burke-Ernzerhof (PBE) was employed in its spin polarized form [227,228]. The projected augmented wave approach with a plane-wave energy cutoff of 450 eV was set to construct the wave function. For structural optimization and defect calculations, a supercell of 2×2×2 containing 64 atoms for cubic SiC and 4×4×4 containing 128 atoms for body-centered cubic Cr was selected with Monkhorst-Pack k-point mesh [229] of 6×6×6 and 3×3×3, respectively. The conjugate gradient method was used for optimization of the structure without imposing any symmetry. Formation energy of defects (E_{for}) in 3C-SiC and bcc Cr was calculated as,

$$E_{for} = E_{def} - E_{per} + \sum n_i \mu_i, \qquad \text{(Eq. 8.1)}$$

where E_{def} and E_{per} represent the total energy of defective and perfect supercell, n_i is the number of atoms of type *i* removed or added due to the defect, and μ_i is the chemical potential of atom type *i*. For intrinsic SiC defects, μ_i was calculated using an approach similar to the one used by Shrader *et al.* [230]. Here, the reported formation energies of defects involving Si and C are calculated using the μ_i at the midpoint where the deviation of chemical potential from the bulk phase are equal

for both Si and C. The formation energy for Cr defects have been calculated by taking the μ_i in Cr-rich condition.

The crystal structure of the cubic 3C-SiC possesses a zinc blende structure where C is bonded to four equivalent Si atoms, forming corner sharing CSi_4 tetrahedra. Two types of vacancies exist in SiC: silicon vacancy (V_{Si}) and carbon vacancy (V_C) which are surrounded by four C and Si neighbors, respectively. There are numerous interstitial sites where an additional defect atom can be situated. Some of these configurations are identified based on their surrounding environment i.e., the tetrahedrally coordinated interstitial sites, where the interstitial atom is surrounded by the four Si atoms (I_{TSi}) or C atoms (I_{TC}). Another configuration is the hexagonal interstitial site (I_{Hex}) which lies in the center of a hexagon formed by alternating Si and C atoms. Yet another possibility is a split configuration (I_{sp}) in which the interstitial atom splits the bonds between lattice atoms and shares the lattice site. These split configurations, also known as dumbbells, can be oriented along the <100> or <110> directions [231]. All of these configurations are depicted in Figure 8.8a. DFT was used to calculate the formation energies of Cr, Si, and C interstitials for each possible point defect configuration. The formation energy of the most stable defect configuration for each interstitial atom along with the vacancy energies is shown in Table 8.1. The most stable interstitial defects are found to be <110> split dumbbells for Si_I and Cr_I and <100> split dumbbell for C_I.

For the Cr phase, <111> dumbbell, octahedral, tetrahedral, and trigonal interstitial sites [232] are considered for Cr, Si, and C defects within a bcc Cr lattice (Figure 8.8b). For Si_I and Cr_I, the <111> dumbbell site is most energetically favorable, while for C_I, the octahedral site is favorable (Table 8.1). The calculated formation energies are in good agreement with previously reported values for self-interstitials atoms (SIAs) in SiC [230] and Cr [232].

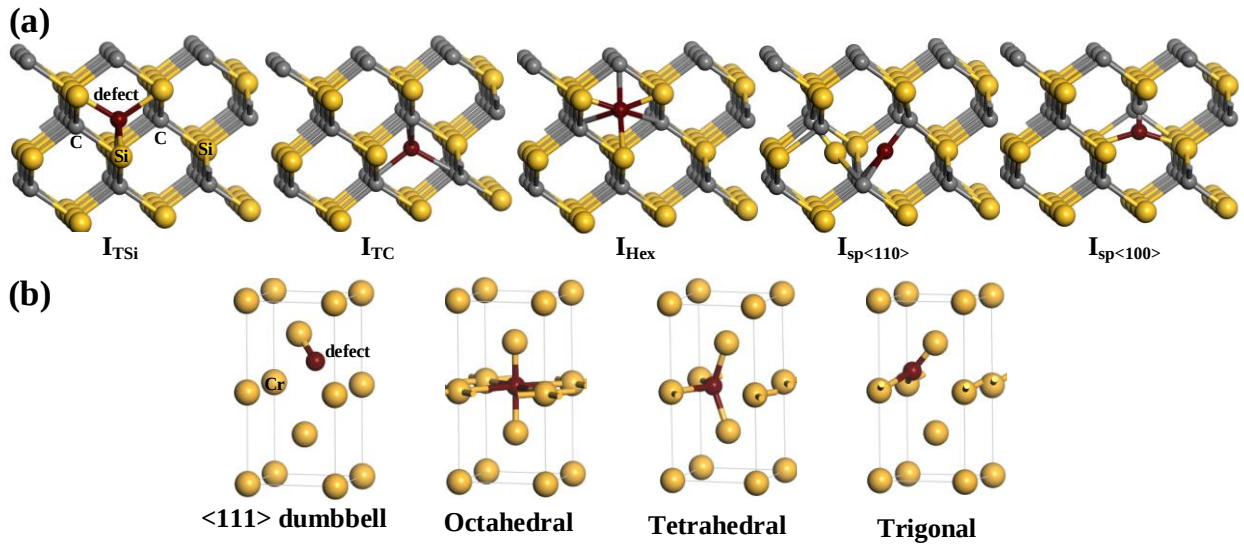

Figure 8.8: All possible interstitial defect configurations in (a) 3C-SiC, and (b) bcc Cr.

Table 8.1: Formation energies (in units of eV) for the most stable configurations of Cr, Si, and C point defects in 3C-SiC and bcc Cr.

Defect	**SiC**	**Cr**
$\mathbf{C_I}$	6.730	2.161
$\mathbf{Si_I}$	8.975	5.620
$\mathbf{Cr_I}$	6.418	6.073
$\mathbf{V_{Si}}$	7.410	
$\mathbf{V_C}$	4.415	
$\mathbf{V_{Cr}}$		4.113

An interesting observation that can be made from Table 8.1 is that the defect formation energies for all three elements are lower in Cr than in SiC. This suggests that once embedded in Cr as a consequence of irradiation, there will be no thermodynamic driving force for the defects to migrate out of the Cr phase. In other words, both the intrinsic SIAs generated via direct radiation damage of Cr and the extrinsic ballistically-mixed Si and C interstitial atoms originating from the SiC

substrate will remain in Cr. SIAs in SiC also have a tendency to migrate toward defect sinks (in this case, the Cr-SiC interface), which may provide another source of point defects injected into Cr [233].

8.3.4 Thermodynamic basis for amorphization of Cr

The incorporation of point defects with positive energies of formation into Cr leads to additional stored energy within the host phase [234–236]. The total amount of stored energy is dependent on the concentration of defects. For ion irradiated metals, the stored energy is typically on the order of a few to tens of kJ/mol [235,237]. Using the point defect formation energies calculated via DFT, an estimate of the additional energy stored in the Cr phase can be made as a function of defect concentration.

In the following discussion, the thermodynamic basis underlying the irradiation-induced nanoscale amorphization of the Si and C-containing bcc Cr is described. CALPHAD-based metastable equilibrium calculations were performed to determine an 'amorphization temperature' for the irradiated Cr-Si-C bcc solid solution as a function of irradiation-induced point defect concentrations. In these metastable equilibrium calculations, formation of various chromium silicides and chromium carbides (as found in the equilibrium phase diagram in Fig. 3b) is suppressed. In other words, the relative thermodynamic stability of the bcc Cr-Si-C solid solution with respect to an amorphous phase of the same composition is evaluated. This was done under the assumption that diffusional kinetics at the irradiation temperature (350°C) is too slow to allow any compositional redistribution that is necessary for the formation of the different equilibrium phases. Thus, the compositional distribution generated by the irradiation-induced ballistic collisions is assumed to be frozen, and no further redistribution occurs.

To simulate an irradiated Cr-Si-C mixture, additional enthalpic contributions that arise from the presence of point defects as a function of their concentrations have been calculated from the DFT-calculated point defect energies presented in Table 8.1. These contributions were then added to the Gibbs energy of the equilibrium bcc Cr-Si-C solid solution obtained from the equilibrium Cr-Si-C thermodynamic assessment [175]. A linear variation of the irradiation enthalpy as a function of the respective point defect concentrations has been considered. Specifically, irradiation enthalpy ΔH_{irrad} has been defined as $\Delta H_{irrad} = \sum_i x_i E_i$, where x_i is the atomic percent of a point defect i and E_i is the DFT-calculated formation energy per atomic percent of the point defect. This definition holds under the assumption that mutual interactions between defects at the dilute concentrations considered here are negligible, and that they are independent of the overall Si/C content in the bcc lattice. On the other hand, the amorphous phase has been modeled (in accordance with [238]) by extrapolating the thermodynamic interaction parameters of the high temperature liquid phase to temperatures below the equilibrium melting point.

Figure 8.9a shows the variation of the amorphization temperature for a pristine, unirradiated Cr-Si-C solid solution as a function of Si and C content while keeping the concentration of the third element fixed at 10 at. % (i.e., compositions of Cr-xSi-10C and Cr-10Si-xC). The extremely high transition temperatures imply that they represent a melting phenomenon rather than amorphization, as expected for a Cr-based solid solution. The same calculations were repeated with a range of irradiation enthalpies added to the crystalline Cr phase. A substantial reduction in amorphization temperature corresponding to increasing amounts of irradiation enthalpy, representing a progressive destabilization of the crystalline phase was observed. The results corresponding to an irradiation enthalpy of 12 kJ/mol are shown in Figure 8.9b. This amount of irradiation enthalpy was found to be necessary to yield an amorphization temperature of about

350°C, the irradiation temperature for our experiment, for the range of typical compositions considered in this study. In fact, for the amorphous band composition as measured in the STEM-EDS data (Cr-10Si-15C), the amorphization temperature drops down to ~320°C at the irradiation enthalpy of 12 kJ/mol (Figure 8.9b). In other words, the amorphous phase of this composition becomes thermodynamically more stable than an irradiated crystalline phase with this amount of irradiation enthalpy below 320°C.

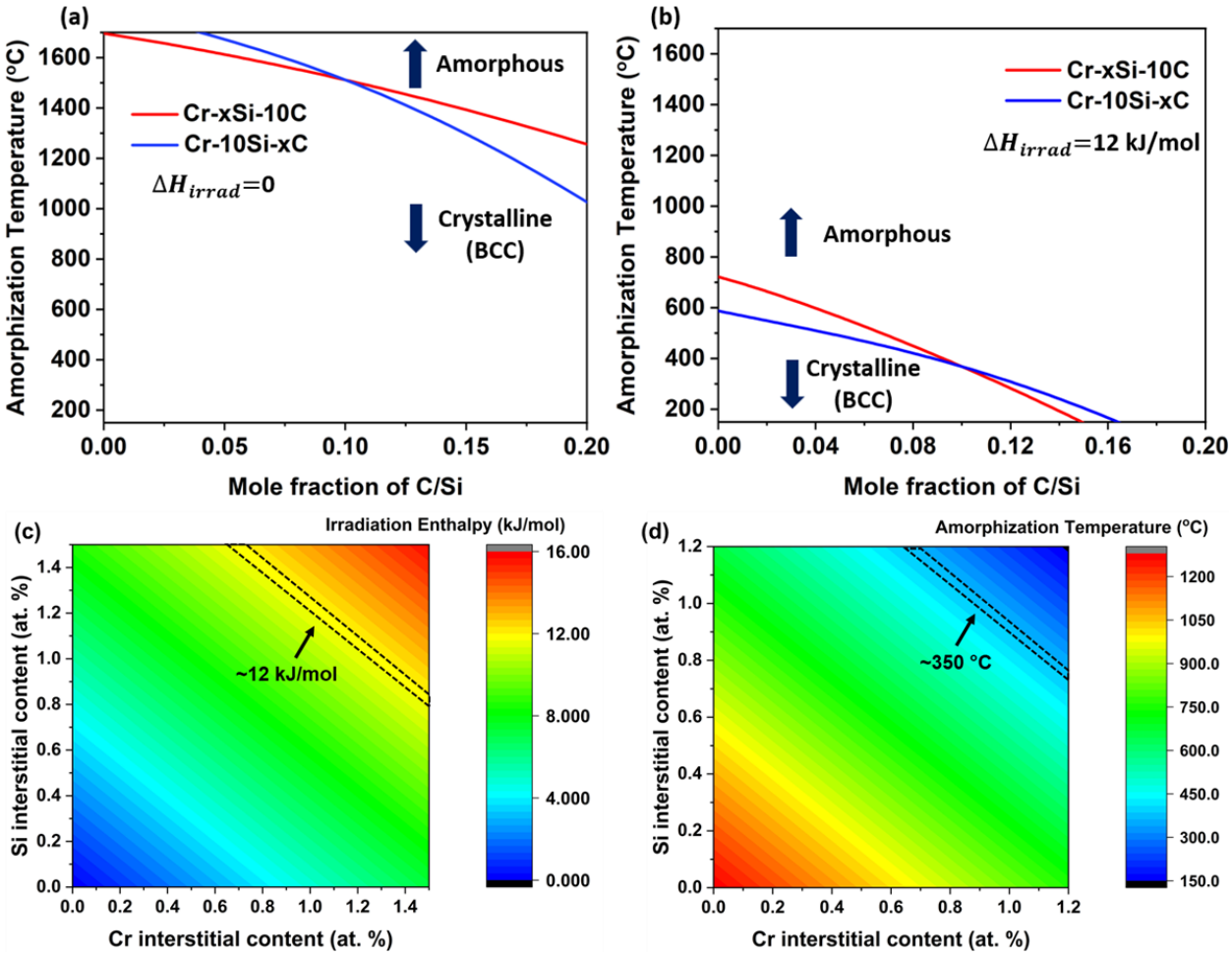

Figure 8.9: Metastable crystalline-amorphous transition temperatures calculated for (a) no irradiation enthalpy and (b) 12 kJ/mol of irradiation enthalpy added to the crystalline Cr phase. The amorphization temperature is plotted as a function of both C and Si content, while keeping the concentration of the third element fixed; (c) Irradiation enthalpy calculated as a function of Cr self-interstitial and Si interstitial defect concentrations in a Cr lattice for an overall composition of Cr-10Si-15C; (d) Amorphization temperature plotted as a function of Cr and Si interstitial defect concentrations for an overall composition of Cr-10Si-15C. The respective defect enthalpies have been taken from the DFT calculations reported above. Mutual defect interactions have been neglected at these defect concentrations, resulting in a linear dependence between irradiation enthalpy and defect concentration.

Figure 8.9c shows the typical concentrations of point defects essential to introduce this amount of irradiation enthalpy, and Figure 8.9d shows the corresponding amorphization temperature variation for an overall alloy composition of Cr-10Si-15C and irradiation enthalpy of 12 kJ/mol. The two types of point defects in the bcc solid solution, namely Cr self-interstitials and Si interstitials have been arbitrarily chosen for illustration purposes. One or more of the different

point defects discussed in the preceding section could contribute to the irradiation enthalpy. It can be seen from the region highlighted in Fig. 6c that a total defect concentration of about 2 at. % (as a combination of Cr and Si interstitials) is required for introducing an irradiation enthalpy of 12 kJ/mol. About the same concentration of point defects is necessary to bring the amorphization temperature down to 350°C in a Cr-10Si-15C alloy (Figure 8.9d). This concentration of point defects and magnitude of stored energy is commensurate with the damage level produced by the high energy irradiation [235,237].

A fundamentally important point that can be noted from these results is that the amorphization temperature decreases steadily as a function of C and Si content in the alloy system (Figure 8.9a and b). This implies that for a given point-defect concentration in the alloy, increasing amounts of C and Si favor amorphous phase formation over the crystalline phase. In other words, the increasing intrinsic stability of the amorphous phase itself increases with increasing C and Si content. It has been well established from numerous investigations on metallic glasses that elements with mutually strong thermodynamic affinities (i.e., elements forming very stable intermetallic compounds with high negative enthalpies of formation) are most effective glass formers when subjected to appropriate processing [239,240]. The increasing tendency for amorphization with increasing Si or C content is in agreement with the strong thermodynamic affinity between Cr-Si and Cr-C as attested by the number of stable intermetallic compounds formed between the two pairs of elements.

In addition to the amorphous phase formation, the presence of the thin crystalline $Cr_5Si_3C_x$ phase between the amorphous layer and SiC is a point of interest. From the STEM-EDS measurements shown in Figure 8.6a, the approximate composition of the crystalline band places the system in the three-phase region bounded by Cr_7C_3, Cr_3Si, and $Cr_5Si_3C_x$. However, due to the

limited diffusion kinetics at the relatively low irradiation temperature of 350 °C, the elemental partitioning necessary to form the three equilibrium phases is not possible. Instead, a partitionless nucleation of the ternary, non-stoichiometric $Cr_5Si_3C_x$ phase appears to occur. This is akin to several partition-free precipitation reactions observed in systems under conditions of restricted kinetics [241–243]. From STEM-EDS results in Figure 8.6, the concentration of C in $Cr_5Si_3C_x$ (< 10 at. %) was found to be less than the C concentration in the amorphous phase (~ 20 at. %), which is in agreement with previous work showing that the maximum C content in $Cr_5Si_3C_x$ is 11 at. % [223]. Based on the trends of amorphization temperature vs. composition shown in Figure 8.9, it is evident that both Si and C concentrations of at least 10 at. % are necessary for amorphization in Cr, suggesting that the lack of C within the $Cr_5Si_3C_x$ phase necessitates it to maintain its crystallinity while regions of greater C content undergo amorphization.

8.4 Mechanical behavior of irradiated Cr-SiC

8.4.1 Nanoindentation testing

Nanoindentation testing was performed to evaluate the effects of irradiation on the mechanical properties and understand the deformation behavior on the B-HiPIMS Cr coating. The nanoindentation measurements were performed in displacement-controlled mode to a depth of 2 µm to ensure the indentation size was similar to those on the as-deposited coatings described previously in Section 5.2. A 6 × 6 grid of indents was performed on the reference and irradiated B-HiPIMS samples. To account for the effects of indentation pile-up, SEM imaging of the residual indents was performed, and the true contact area was measured using the ImageJ software.

The raw nanohardness data is shown in Figure 8.10a. Both datasets have notable scatter, and it is not clear if irradiation has affected the coating hardness. SEM images of representative indents on the reference and irradiated B-HiPIMS samples are shown in Figure 8.10b. Similar to the as-

deposited B-HiPIMS coating, both samples exhibit indentation pile-up and show no signs of brittle failure. As discussed in Section 5.2, the extent of pile-up was assessed by taking the ratio of the true contact area measured via SEM imaging (A_{SEM}) to the contact area determined by the nanoindentation instrument using the conventional Oliver-Pharr method (A_{inst}). The measured pile-up ratios for the two samples are shown Figure 8.10a. On average, the magnitude of pile-up was greater in the reference sample compared to the irradiated sample. The A_{SEM} values were then used to correct the hardness data in the manner described in Section 5.2,

$$\frac{P_{max}}{A_{SEM}} \qquad \text{(Eq. 8.2)}$$

which is the same as Equation 5.1 (repeated here for clarity). In the corrected hardness data in Figure 8.10a, it can be noted that data scatter is substantially reduced in both datasets by applying the pile-up area correction. Because the conventional Oliver-Pharr method is unable to account for the effects of pile-up, measuring the true contact area via SEM is able to negate the systematic error in the Oliver-Pharr method [149]. With the corrected data, it becomes clear that irradiation has caused a hardness increase of about 0.5 GPa in the B-HiPIMS Cr coating. The reference region is slightly softer than the as-deposited B-HiPIMS coating which could be due to minor stress relief and defect annealing taking place during the sample heating during irradiation.

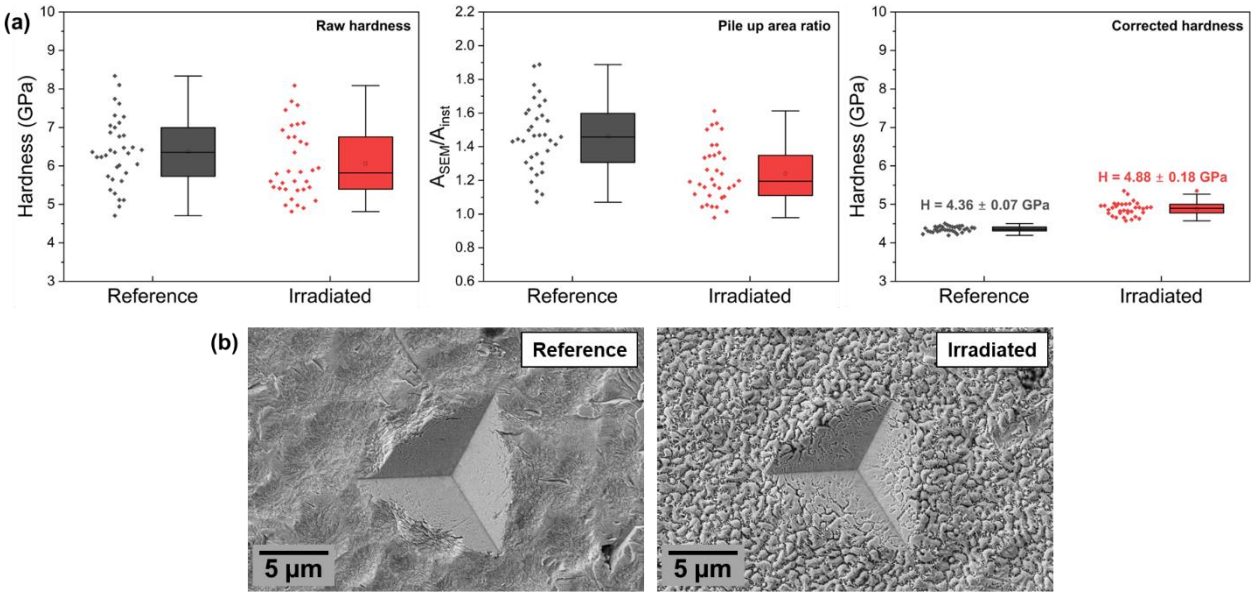

Figure 8.10: (a) Plots of the raw hardness data, pile up ratio, and corrected hardness data; (b) SEM images of nanoindents on the reference and irradiated B-HiPIMS samples used to measure the true contact area.

The deformation of the columnar grains within the irradiated Cr coating were also investigated via cross-sectional TEM imaging. A side-by-side comparison of indent cross sections from the as-deposited and irradiated B-HiPIMS coatings is shown in Figure 8.11. Although no indent cross section was performed on the unirradiated reference region that experienced that same thermal history as the irradiated region, it is assumed that the deformation behavior of that region is quite similar to the as-deposited coating. To briefly recap the findings from the as-deposited sample (fully detailed in Section 5.2), extensive deformation of the columnar grains was observed underneath the indentation. Some grains were deformed up to an angle of almost 90° with respect to their original orientation, and all grains appeared to deform coherently in a ductile, plastic manner. A coherent bending of columnar grains can also be observed in the indent on the irradiated sample. However, the extent of deformation is clearly less than for the as-deposited sample, as illustrated by the yellow traces in Figure 8.11. The behavior of the irradiation-induced dislocation

loop chains within the deformed grains could not be determined because the heavily deformed microstructure underneath the indentation made it difficult to locate the loops within these regions.

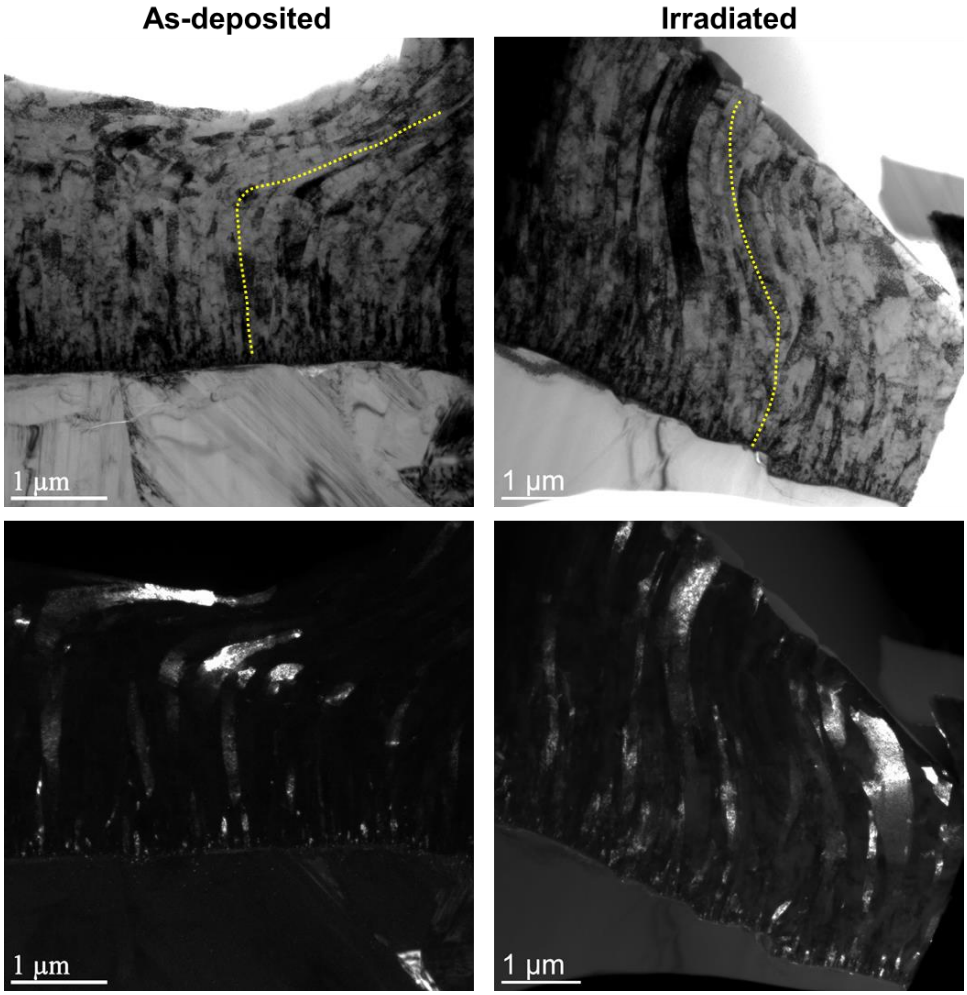

Figure 8.11: BF and DF TEM images of indent cross sections from the as-deposited and irradiated B-HiPIMS samples. Yellow lines show the shapes of the deformed grains. The indentation loads were 576 mN and 650 mN for the indents on the as-deposited and irradiated samples, respectively.

The results of the nanoindentation and subsequent characterization of the irradiated B-HiPIMS coating clearly show that radiation damage has caused an increase in coating hardness. The dislocation loops formed under irradiation (Section 8.2) act as obstacles to dislocation motion and increase in resistance to plastic deformation. This is illustrated by the decrease in columnar bending observed in the indentation cross section on the irradiated sample and also helps explain why the extent of pile-up (quantified by the pile-up area ratio) is less in the irradiated sample

compared to the reference region. The result is a 0.5 GPa increase in coating hardness, which is in line with other reports of irradiated Cr coatings [210,244].

8.4.2 In situ microcantilever bending

An *in situ* microcantilever bending experiment was performed at the Irradiated Materials Characterization Laboratory at Idaho National Laboratory to study the effect of irradiation on the mechanical behavior of the B-HiPIMS Cr interface. PFIB milling was used to fabricate two sets of ten cantilevers near the edge of the sample in the irradiated and unirradiated reference regions, as illustrated in Figure 8.12a. High current milling was used to clear an area with enough space to allow the picoindenter probe to reach the cantilevers without contacting the rest of the sample and create an area thin enough for cantilever fabrication. A prepared area after rough trenching but prior to cantilever shaping is shown in Figure 8.12b. The sample was mounted on a 45° pre-tilted specimen holder so milling could be performed in both top-down and head-on geometries by rotating the sample by 180° inside the instrument and tilting the sample by an extra 7°.

Cantilever shaping was conducted with a series of decreasing milling currents starting with 4 nA. The first step of cantilever shaping is shown in Figure 8.12c. Cantilevers were fabricated such that at least 1 µm of the SiC substrate was included at the base end of the cantilever, and rest of the cantilever was composed of the B-HiPIMS Cr coatings. Some of the coating thickness was gradually lost during the milling steps, but generally at least 3 µm of Cr was retained. The cantilever geometry is illustrated in Figure 8.12d. The cantilevers were fabricated to have a square cross section approximately 1 µm × 1 µm. The final cantilevers had a total length of about 4 µm (3 µm Cr + 1 µm SiC), resulting in an aspect ratio (length:width) of 4:1, which is in the typical range of cantilever geometries used by other researchers [245–248]. The cantilevers were not pre-

notched at the interface. Images of finished cantilevers viewed from the top down and head on are shown in Figure 8.12e and f.

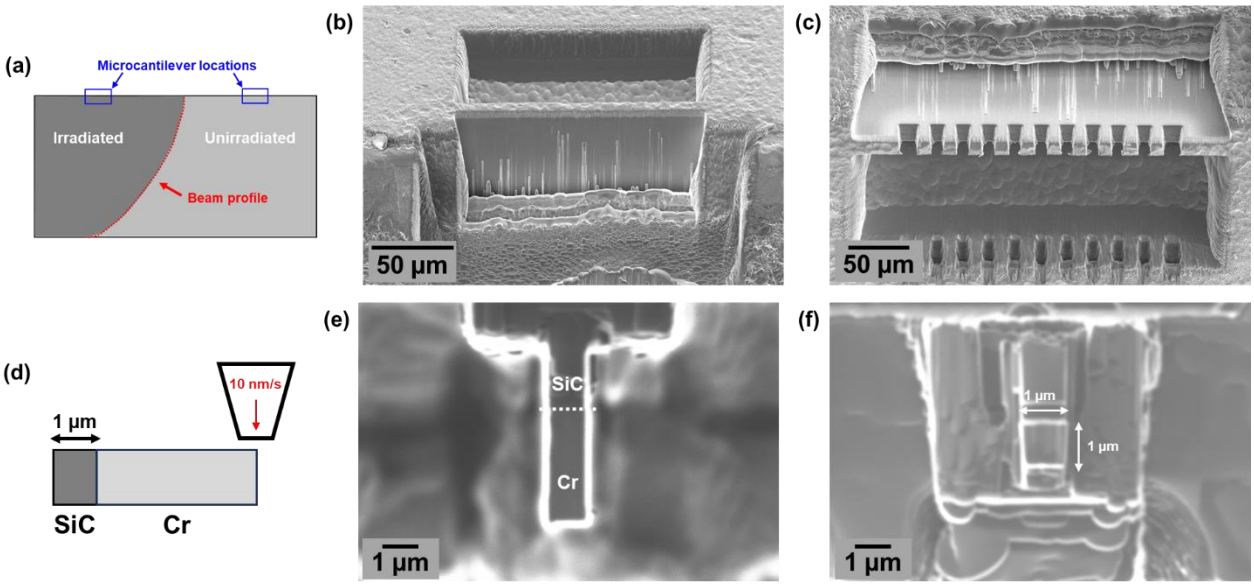

Figure 8.12: (a) Illustration of the irradiated B-HiPIMS Cr sample with microcantilever locations marked; (b) SEM image of rough trenching for microcantilever fabrication; (c) SEM image of initial fabrication of microcantilever profiles; (d) Drawing of microcantilever viewed from side showing incorporation of Cr/SiC interface in the cantilever and 1 µm diamond flat punch; (e) Top-down FIB image of a finished microcantilever with dotted line indicating position of the interface; (f) Head-on FIB image of a finished microcantilever with cross section dimensional measurements.

Microcantilever bending was performed using a Hysitron PI 88 picoindenter installed inside a FEI Quanta 3D FIB/SEM instrument. This *in situ* instrumental setup allows for simultaneous collection of load-displacement data and video recording during the bending experiments. The picoindenter was equipped with 1 µm diamond flat punch that was used to bend the cantilevers at a rate of 10 nm/s. Cantilevers were bent until it visibly fractured into two pieces or until the load dropped to zero. The load-displacement data can be converted into stress-strain using the known dimensions of the cantilevers. The stress (σ) for a cantilever with a rectangular cross section is calculated by,

$$\sigma = \frac{6PL}{wh^2} \qquad \text{(Eq. 8.3)}$$

where P is the load, L is the distance between the loading point and the base of the cantilever, and w and h are the width and height of the cantilever [249]. The elastic modulus (E) is needed to calculate strain and can be determined by,

$$E = \frac{4PL^3}{wh^3\delta} \quad \text{(Eq. 8.4)}$$

where δ is the displacement [249]. Then, the strain (ε) can easily be found from,

$$\varepsilon = \frac{\sigma}{E} \quad \text{(Eq. 8.5).}$$

In the reference and irradiated regions, five cantilevers were tested at room temperature, and five were tested at 300 °C. Unfortunately, the data from the 300 °C experiments could not be used due to a plethora of experimental issues. Of the room temperature tests, all five were successful in the reference region, and three were successful in the irradiated region.

Representative stress-strain curves from the *in situ* bending of reference and irradiated cantilevers are shown in Figure 8.13a. Due to the small cross-sectional area of the cantilevers, the resulting stresses are on the order of GPa, which is typical for micromechanical experiments [11,245]. The failure strain of the cantilevers was 1% or less, which equates to displacements in the range of 10–100 nm. One interesting feature of the stress-strain curves, most often observed in the bending of reference cantielvers, is a plateau in the intermediate strain ranges where increasing displacement is not met with a large increase in load followed by a steep increase in load leading up to failure. This could be a consequence of the cantilever geometry being composed of dissimilar materials that respond differently to the loading conditions. During the early stages of the test most of the load will be localized in Cr, which is relatively soft and ductile compared to SiC and could deform steadily without a sharp increase in load. This is indicated by regime (1) in Figure 8.13a. When the SiC at the base of the cantilever begins to deform, and sharp load increase would be

expected followed by fracture soon after due to the brittleness of SiC, as indicated by regime (2) in Figure 8.13a.

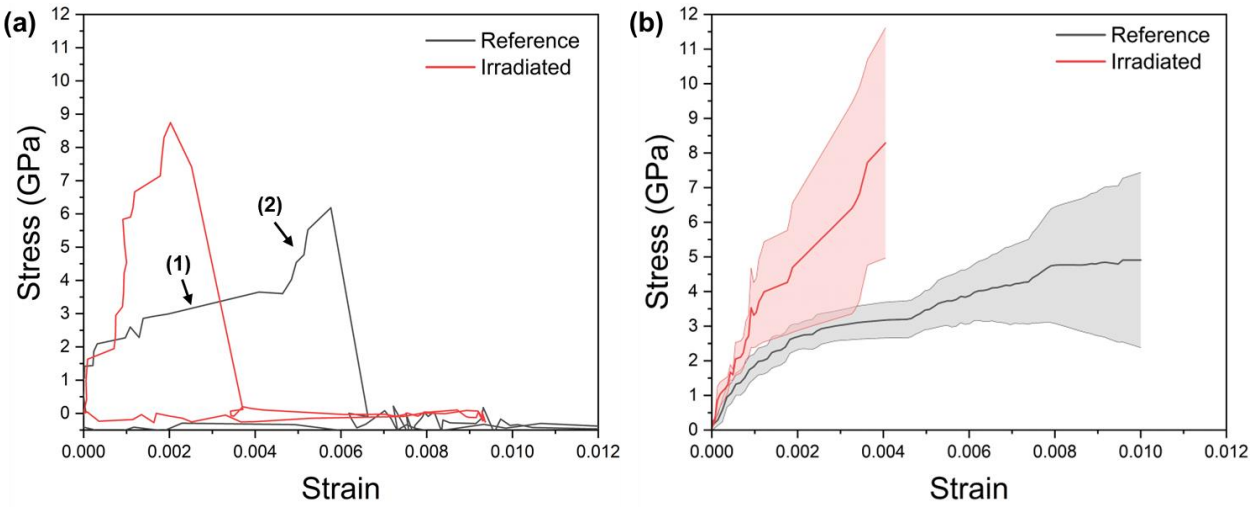

Figure 8.13: (a) Representative stress-strain curves from the microcantilever bending tests on the reference and irradiated samples. Locations (1) and (2) indicated regimes dominated by the deformation of Cr and SiC, respectively; (b) Averaged stress-strain data for the reference and irradiated cantilevers up to the point of failure. The solid line represents the mean, and the shaded bands represent the standard error.

Stress-strain data averaged from all cantilever replicates is shown Figure 8.13b. This plot shows that on average, the failure stress is higher and failure strain is lower in the irradiated cantilevers. It can also be observed that the stress in the irradiated cantilevers rises at a faster rate as strain increases, which is likely due to the presence of irradiation-induced defects and consequent hardening in the B-HiPIMS Cr coating described in the previous section. The failure stress and failure strain data are summarized in Table 8.2. The lower strain and higher stress at failure are typical indicators of irradiation-induced embrittlement. It should be noted that the standard deviation of the data, particularly the failure stress data, is relatively high due to the small number of tests and large degree of variability associated with conducting sophisticated tests on such a small scale.

Table 8.2: Average cantilever failure strain and failure stress with standard deviations.

	Failure strain	Failure stress (GPa)
Reference	0.0070 ± 0.0019	5.22 ± 3.30
Irradiated	0.0025 ± 0.0013	6.13 ± 2.55

The failure behavior of the cantilevers was assessed via post-test SEM imaging. The sample was rotated and tilted inside the SEM chamber so the cantilever could be imaged from the side to view crack propagation. Images of the reference cantilevers after bending are shown in Figure 8.14a. At the point of failure, some cantilevers fully broke into two pieces leaving only the base of the cantilever, while other cantilevers fractured but did not fully break. For the cantilevers that remained attached, it was observed that cracking primarily occurred within the SiC cantilever base and occasionally right at the Cr/SiC interface. Failure was never observed in the B-HiPIMS Cr coating, providing another indication that the cohesive strength of the coating is very high. The fact the failure rarely occurred at the interface also suggests that the adhesion of the B-HiPIMS coating is quite strong and corroborates the results of scratch tests from Section 5.1. If cantilevers were fabricated from one of the Cr coating types that demonstrated weaker adhesion, it is possible that interfacial failure would be the dominant mechanism. In the work of Mouche et al. [11], they observed that some Cr/SiC cantilevers failed in a ductile manner via plastic deformation of the Cr coating, which was not observed in this study. All failures appeared to be driven by the SiC substrate. The same failure mechanism was observed in the irradiated cantilevers, as shown in Figure 8.14b.

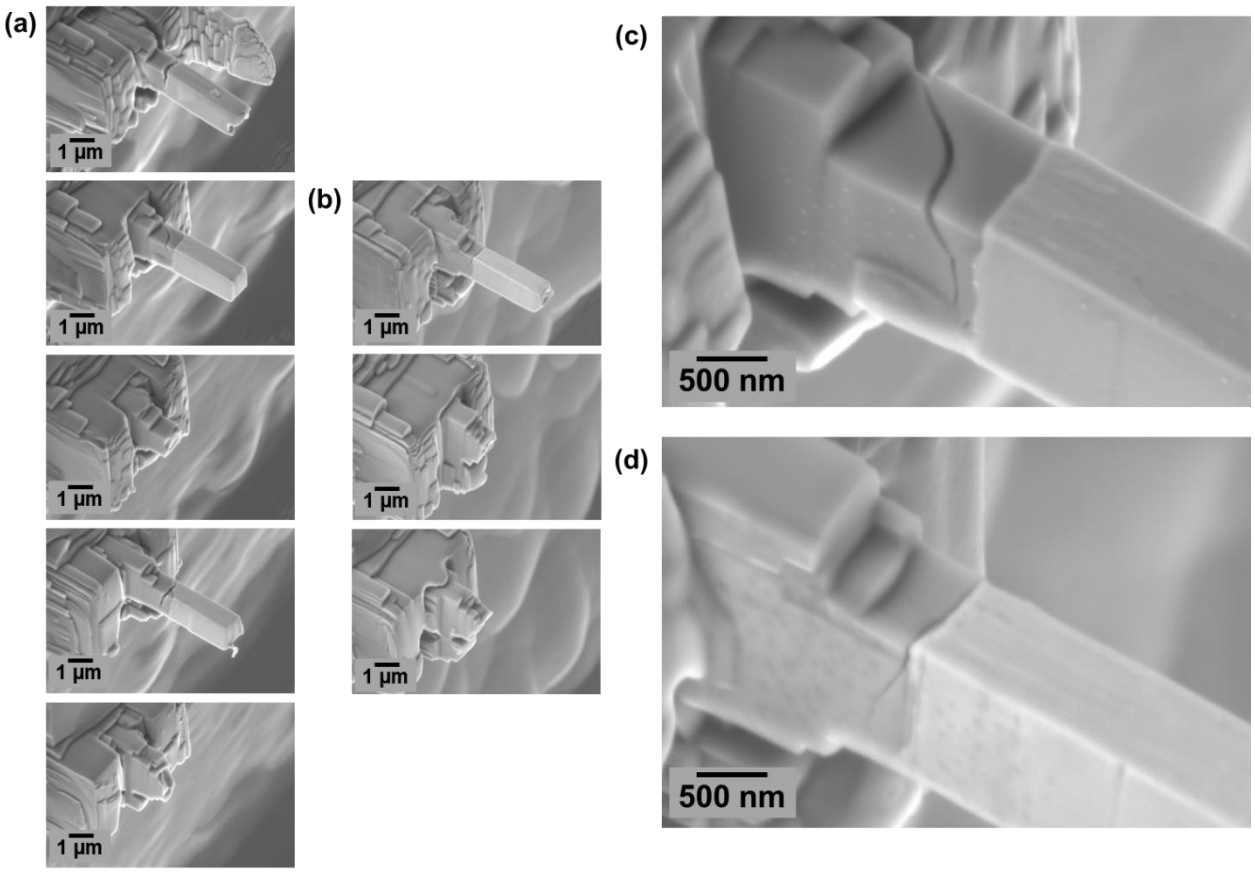

Figure 8.14: SEM images of tested (a) reference and (b) irradiated microcantilevers; Higher magnification SEM images of (c) reference and (d) irradiated microcantilevers showing cracking in the SiC.

It is not known if there is any relationship between the fracture mode and whether the cantilever separated into two pieces or not. Due to the sample geometry, *in situ* videos of the bending tests could only be captured from the head-on view, so real-time viewing of crack propagation was not possible. Figure 8.14c and d show higher magnification SEM images of cantilever fracture and are representative of the SiC substrate failure mechanism. In the irradiated cantilever (Figure 8.14d), it appears that the crack may have initiated at the interface and then propagated within the SiC rather than continuing along the interface. The influence of the irradiation-induced amorphous layer at the Cr/SiC interface (Section 8.3) on cantilever deformation is not precisely known. One attraction of nanostructured materials containing amorphous phases is increased strength and toughness, but this seems to be dependent on the materials system [250,251]. It is possible that the

presence of the amorphous layer is at least partially responsible for the greater average stress in the irradiated cantilevers.

It is unlikely that the irradiation-induced defects within the Cr coating (Section 8.2) play a major role in the deformation behavior of the cantilevers because the Cr appears to undergo very little plastic deformation and is not the site of failure, but these defects could also contribute to the higher stress. It is hypothesized that the main factor influencing cantilever embrittlement is radiation damage in the SiC substrate. From the dpa profile in Figure 8.1, it is known that the peak radiation damage occurs about 1.5 μm into the SiC, and much of this region has been incorporated in the base of the cantilevers. The effects of irradiation on the mechanical behavior of SiC have been studied extensively. There is good agreement that irradiation produces a slight hardness increase in SiC, but the effects on flexural strength and fracture toughness are more variable [31]. There is some data to suggest that fracture toughness decreases under irradiation at temperatures less than 400 °C [31]. Because cracking in the SiC is the main mode of cantilever failure, it is believed that a combination of increased hardness and decreased fracture toughness of SiC caused by radiation damage led to the embrittlement of the irradiated Cr-SiC cantilevers. Finally, it should be noted that the irradiation implants about 0.5 at. % of Xe into SiC near the radiation damage peak. Although no Xe bubble formation was observed in the SiC, the effects of dissolved gas on embrittlement of SiC (similar to hydrogen embrittlement in metals [18]) cannot be definitively ruled out.

8.5 Summary of irradiation effects on Cr-coated SiC

The high energy irradiation of the B-HiPIMS Cr sample provides valuable insight into the potential effects of radiation damage in the Cr coating and at the Cr/SiC interface. The defects formed in the coating by radiation damage are primarily organized dislocation loops in the

columnar grains that tend to cluster in oriented chains. These defects lead to an increase in coating hardness. At the interface, intrinsic radiation damage in Cr and mixing of Si and C atoms into Cr synergistically destabilize the crystalline phase and result in the formation of an amorphous Cr-Si-C mixture. Microcantilever testing revealed that irradiation results in embrittlement of the interface, a finding that is mainly attributed to radiation damage in SiC.

One aspect of these results that should be considered is the difference in dose rate between ion and neutron irradiation. Ion irradiation experiments typically produce dose rates three or four orders of magnitude greater than in-reactor neutron dose rates [18]. The material response to irradiation can be different depending on the dose rate which influences the number of overlapping collision cascades and defect recovery rates [18]. Also, the irradiation experiment in this work produced a dpa level on the very upper end of what would be encountered in a typical LWR [15], creating more atomic disorder within the coating and at the interface than would be experienced in the true reactor scenario. One neutron irradiation experiment was conducted on an unoptimized Cr coating and is detailed in Appendix D. The interfacial phenomenon may be particularly influenced by the high dose rate and damage level that created extremely far-from-equilibrium conditions and enhanced amorphization.

With these factors in mind, it can be argued that irradiation does not seem to have a drastic detrimental effect on the properties and performance of Cr-coated SiC, at least for the B-HiPIMS Cr coating which displays excellent behavior in the as-deposited condition. Even at the high level of radiation damage, the Cr coating hardens only slightly and maintains its plasticity, as indicated by the presence of indentation pile-up and absence of indentation-induced cracking. The interfacial amorphous layer formed under irradiation did not appear to degrade the strength of the B-HiPIMS

interface, and it is predicted that the extent of amorphization would be lower under neutron irradiation compared to this experiment.

9. Conclusions

SiC-SiC$_f$ composites offer considerable potential as accident tolerant fuel cladding materials in LWRs. However, SiC as a material exhibits hydrothermal corrosion under normal reactor operating conditions, via the formation of water soluble Si-O-H compounds. Chromium coatings 5–10 µm thick deposited by magnetron sputtering methods have been investigated for mitigation of hydrothermal corrosion of SiC in LWR water coolant. Four DCMS processes and two HiPIMS processes involving different power densities, target pulse cycles, and mechanisms of ion bombardment were investigated for the deposition of these Cr coatings on SiC. This research focused on a holistic understanding of the phenomena governing the relationships between deposition process characteristics, the resulting structure of the Cr coatings and Cr-SiC interface, mechanical properties and deformation behavior including the evolution of residual stresses within the coatings during elevated temperature exposure, resistance to hydrothermal corrosion including the evolution of passive films, and nanoscale morphological and compositional changes in the coating and interface under irradiation.

The fundamental aspects differentiating DCMS and HiPIMS deposition processes are the degree of ionization of sputtered atoms prior to impingement on the substrate surface and the mobility afforded to atoms on the surface of the growing film as a consequence of high power pulses applied to the target during HiPIMS deposition. HRTEM methods were rigorously used to study the effects of energetic deposition on the coating microstructure and nature of the Cr-SiC interface. It was found that regardless of the DCMS process variant used, the columnar grains of the film were separated by regions of nanoscale porosity. In contrast, the two HiPIMS processes used (conventional HiPIMS and B-HiPIMS) resulted in fully dense Cr coatings. The impingement of metallic ions and increased mobility of surface atoms during HiPIMS deposition both promote

densification of the film via atomic peening effects and surface diffusion. It was also observed that energetic deposition altered the structure of the Cr-SiC interface. HRTEM imaging of the B-HiPIMS Cr interface revealed a 2 nm wide deposition-induced mixing layer on the Cr-rich side of the interface. The composition of this layer was analyzed using EELS, and in addition to Cr, a considerable amount of C originating from the SiC substrate was detected, suggesting the occurrence of atomic mixing between Cr and SiC via ion bombardment during the early stages of deposition. This experimentally observed mixing was supported by Monte Carlo simulations of interfacial compositional evolution caused by ion bombardment during irradiation. No mixing layer was observed in DCMS coatings. The presence of this mixing layer at the B-HiPIMS coating interface plays a role in enhanced adhesion by promoting bonding between the coating and substrate and facilitates further mixing between Cr and SiC via thermal diffusion at high temperature.

Given the importance of residual stress in the overall mechanical behavior of a coating, *in situ* XRD experiments were conducted to measure the stress evolution within the DCMS and B-HiPIMS coatings at 300 °C and 700 °C. At 300 °C (approximate reactor operating temperature), the residual stress in the DCMS coating was tensile and did not vary significantly over the course of 84 hours of exposure. The residual stress in the B-HiPIMS was compressive at 300 °C and was gradually relieved over time. The compressive residual stress state is a beneficial coating characteristic that can offset tensile strain generated by volumetric swelling of the underlying SiC cladding under irradiation. At 700 °C, grain growth in the B-HiPIMS Cr coating resulted in a transition to a tensile stress state. Also, a Cr-SiC interdiffusion region consisting of Cr-carbide and Cr-silicide phases formed at the interface. The identity of the phases was confirmed using the XRD peaks, EDS measurements, and electron diffraction, and supported by CALPHAD-based

thermodynamic modeling. The residual stress in the DCMS coating at 700 °C maintained a similar state to that at 300 °C, and interdiffusion was localized to isolated areas at the interface. The lack of intercolumnar cohesion within the coating microstructure and weaker interface of the DCMS coating limited the evolution of residual stress or interaction between the coating and substrate.

The mechanical properties and deformation behavior of the Cr coatings were evaluated using nanoindentation. The hardness of the coatings ranged between 5–10 GPa with variations related to grain size, morphology, and density. Some of the DCMS coatings exhibited cracks emanating from the corners of the indents that propagated along the intercolumnar boundaries, providing more evidence of poor cohesive strength within the DCMS coatings. Cross-sectional TEM imaging of an indent on a DCMS coating revealed that the columns tend to buckle under the center of the indent and the porosity gets sealed off by the force of the indenter. Indents on the B-HiPIMS coating exhibited a phenomenon known as indentation pile-up, indicated by the outward bowing of the indent edges. The coarser (relative to the other coating types) columnar grains of the B-HiPIMS coating were observed to deform in a significantly ductile manner under the force of the indenter, with some grains being bent by almost 90° with respect to their original growth direction. Along with the compressive stress of the B-HiPIMS coatings, the ability of the coating to undergo extensive plastic deformation without fracture underscores the ability of the coating to accommodate dimensional changes of the cladding without catastrophic failure.

Hydrothermal corrosion experiments were conducted in static deionized water at 360 °C for a duration of 30 days with samples being removed at intervals for examination and weight change measurements. The coatings produced by DCMS processes, except the batch produced by the standard DCMS process (S-DCMS) without additional target pulsing or ion bombardment, delaminated (i.e., a mechanical failure rather than a corrosion-induced failure) during the initial

stages of the test, suggesting the adhesion of these films was insufficient. Both conventional HiPIMS and B-HiPIMS coatings remained well-adhered throughout the experiment, an effect that may at least be partially attributed to intermixed layer at the interface. These Cr coatings exhibited weight gained via the formation of a 20–30 nm thick surface oxide layer which successfully prevented corrosion of the underlying SiC. In addition to the surface layer, oxide formation was observed along porous intercolumnar regions below the surface of the conventional DCMS coating. The best performing coatings from the autoclave test (S-DCMS, HiPIMS, B-HiPIMS) were exposed in a second corrosion test conducted for 90 days in a chemistry-controlled flow loop containing dissolved hydrogen gas to simulate PWR conditions. The coatings remained adherent and protective under these conditions as well. It was observed that the rates dissolution of uncoated SiC and oxidation of the Cr coatings was reduced in the flow loop due to the presence of dissolved hydrogen limiting the possible corrosion pathways. Using TEM and XPS, it was determined that the corrosion layers formed on the Cr coatings exposed in the flow loop tended to exhibit a more heterogeneous thickness and morphology and contained greater fraction of Cr-oxide and lower fraction of Cr-hydroxide compared to the corrosion layers formed in the static autoclave. It is most likely that the coolant flow and dissolved hydrogen present in the flow loop influence the corrosion product morphology and composition. Overall, these corrosion tests demonstrate the protective ability of the Cr coatings in a hydrothermal corrosion environment, given coating adhesion is maintained.

To study the effects of irradiation on the coating structure and Cr-SiC interface, a B-HiPIMS sample was irradiated with 80 MeV Xe^{26+} ions to a damage level of 30 dpa at the interface. In the coating, radiation damage produced highly organized linear arrays of dislocation loops oriented along <100> directions within the columnar grains oriented. These defects subsequently produced

an increase in coating hardness by acting as barriers to dislocation motion. Microscopy of indents on the irradiated B-HiPIMS sample revealed that the extent of indentation pile-up and degree of columnar deformation both were reduced after irradiation. Detailed HRTEM in conjunction with FFT analysis showed a 5 nm thick $Cr_5Si_3C_x$ layer adjacent to SiC followed by a 20 nm thick Cr-rich amorphous band at the interface after irradiation. Atomistic simulations coupled with CALPHAD-thermodynamic modeling showed that amorphization is driven by the synergistic effects of radiation damage in the Cr and irradiation-induced mixing of Si and C into Cr. The effect of irradiation on mechanical behavior of Cr-SiC interface was evaluated using *in situ* microcantilever bending experiments. In both unirradiated and irradiated cantilevers, the main failure mechanism was cracking in SiC at the cantilever base, suggesting that amorphization does not significantly weaken the interface. The irradiated cantilevers exhibited a higher average failure stress and lower average failure strain, which is likely to be a combined effect of radiation damage in Cr and SiC.

In summary, this study furthers the understanding of how the energetics of ion impingement on substrate and enhancement in atomic mobility generated during magnetron sputter deposition affect coating structure, properties, and performance. The characterization of the interface using high resolution electron microscopy imaging and analytical techniques provides valuable scientific insight into the nanoscale effects of energetic deposition, which is crucial to expanding the scope of these technologies in industry. This work also addressed the behavior of the Cr-SiC system in different environments including elevated temperatures, hydrothermal corrosion, and irradiation. In particular, the study and elucidation of irradiation-induced amorphization at the Cr-SiC interface can be applicable to other metal-SiC interfaces as interest in the use of SiC as a core component in advanced fission and fusion reactors grows. Through these studies, the key relationships

between deposition process, coating structure, and consequent behavior have been identified in the context of developing an effective coating to mitigate the hydrothermal corrosion of SiC in light water reactors.

References

[1] K.A. Terrani, Accident tolerant fuel cladding development: Promise, status, and challenges, Journal of Nuclear Materials 501 (2018) 13–30. https://doi.org/10.1016/j.jnucmat.2017.12.043.

[2] J. Carmack, F. Goldner, S.M. Bragg-Sitton, L.L. Snead, Overview of the U.S. DOE Accident Tolerant Fuel Development Program, Idaho National Laboratory (INL), 2013. https://www.osti.gov/biblio/1130553.

[3] S.J. Zinkle, K.A. Terrani, J.C. Gehin, L.J. Ott, L.L. Snead, Accident tolerant fuels for LWRs: A perspective, Journal of Nuclear Materials 448 (2014) 374–379. https://doi.org/10.1016/j.jnucmat.2013.12.005.

[4] K.A. Terrani, Y. Yang, Y.-J. Kim, R. Rebak, H.M. Meyer, T.J. Gerczak, Hydrothermal corrosion of SiC in LWR coolant environments in the absence of irradiation, Journal of Nuclear Materials 465 (2015) 488–498. https://doi.org/10.1016/j.jnucmat.2015.06.019.

[5] C.K. Ang, J.R. Burns, K.A. Terrani, Y. Katoh, Examination of Hybrid Metal Coatings for Mitigation of Fission Product Release and Corrosion Protection of LWR SiC/SiC, 2016. https://doi.org/10.2172/1346647.

[6] C.K. Ang, S.S. Raiman, J.R. Burns, X. Hu, Y. Katoh, Evaluation of the First Generation Dual-purpose Coatings for SiC Cladding, 2017. https://doi.org/10.2172/1424435.

[7] C. Ang, C. Kemery, Y. Katoh, Electroplating chromium on CVD SiC and SiCf-SiC advanced cladding via PyC compatibility coating, Journal of Nuclear Materials 503 (2018) 245–249. https://doi.org/10.1016/j.jnucmat.2018.03.009.

[8] S.S. Raiman, P. Doyle, C. Ang, Y. Katoh, K.A. Terrani, Hydrothermal Corrosion of Coatings on Silicon Carbide in Boiling Water Reactor Conditions, CORROSION 75 (2019) 217–223. https://doi.org/10.5006/2997.

[9] P.A. Mouche, C. Ang, T. Koyanagi, P. Doyle, Y. Katoh, Characterization of PVD Cr, CrN, and TiN coatings on SiC, Journal of Nuclear Materials 527 (2019) 151781. https://doi.org/10.1016/j.jnucmat.2019.151781.

[10] K.A. Kane, P.I.M. Stack, P.A. Mouche, R.R. Pillai, B.A. Pint, Steam oxidation of chromium corrosion barrier coatings for sic-based accident tolerant fuel cladding, Journal of Nuclear Materials 543 (2021) 152561. https://doi.org/10.1016/j.jnucmat.2020.152561.

[11] P.A. Mouche, T. Koyanagi, D. Patel, Y. Katoh, Adhesion, structure, and mechanical properties of Cr HiPIMS and cathodic arc deposited coatings on SiC, Surface and Coatings Technology 410 (2021) 126939. https://doi.org/10.1016/j.surfcoat.2021.126939.

[12] P.A. Mouche, A. Evans, W. Zhong, T. Koyanagi, Y. Katoh, Effects of sample bias on adhesion of magnetron sputtered Cr coatings on SiC, Journal of Nuclear Materials 556 (2021) 153251. https://doi.org/10.1016/j.jnucmat.2021.153251.

[13] P.J. Doyle, C. Ang, L. Snead, Y. Katoh, K. Terrani, S.S. Raiman, Hydrothermal Corrosion of First-Generation Dual-Purpose Coatings on Silicon Carbide for Accident-Tolerant Fuel Cladding, Journal of Nuclear Materials 544 (2021) 152695. https://doi.org/10.1016/j.jnucmat.2020.152695.

[14] P.J. Doyle, T. Koyanagi, C. Ang, L. Snead, P. Mouche, Y. Katoh, S.S. Raiman, Evaluation of the effects of neutron irradiation on first-generation corrosion mitigation coatings on SiC for accident-tolerant fuel cladding, Journal of Nuclear Materials 536 (2020) 152203. https://doi.org/10.1016/j.jnucmat.2020.152203.

[15] S.J. Zinkle, G.S. Was, Materials challenges in nuclear energy, Acta Materialia 61 (2013) 735–758. https://doi.org/10.1016/j.actamat.2012.11.004.

[16] Pellet, fuel, U.S. Nuclear Regulatory Commission (2023). https://www.nrc.gov/reading-rm/basic-ref/glossary/pellet-fuel.html (accessed January 29, 2024).

[17] M. Allen, Ten years after Fukushima: could new fuels make nuclear power safer?, Physics World (2021). https://physicsworld.com/a/ten-years-after-fukushima-could-new-fuels-make-nuclear-power-safer/ (accessed January 29, 2024).

[18] G.S. Was, Fundamentals of Radiation Materials Science, Springer New York, New York, NY, 2017. https://doi.org/10.1007/978-1-4939-3438-6.

[19] M. Nastasi, J.W. Mayer, Ion beam mixing in metallic and semiconductor materials, Materials Science and Engineering: R: Reports 12 (1994) 1–52. https://doi.org/10.1016/0927-796X(94)90005-1.

[20] G.S. Was, Ion beam modification of metals: Compositional and microstructural changes, Progress in Surface Science 32 (1989) 211–332. https://doi.org/10.1016/0079-6816(89)90005-1.

[21] B.X. Liu, W.S. Lai, Q. Zhang, Irradiation induced amorphization in metallic multilayers and calculation of glass-forming ability from atomistic potential in the binary metal systems, Materials Science and Engineering: R: Reports 29 (2000) 1–48. https://doi.org/10.1016/S0927-796X(00)00016-4.

[22] K.A. Terrani, Accident tolerant fuel cladding development: Promise, status, and challenges, Journal of Nuclear Materials 501 (2018) 13–30. https://doi.org/10.1016/j.jnucmat.2017.12.043.

[23] B.R. Maier, B.L. Garcia-Diaz, B. Hauch, L.C. Olson, R.L. Sindelar, K. Sridharan, Cold spray deposition of Ti2AlC coatings for improved nuclear fuel cladding, Journal of Nuclear Materials 466 (2015) 712–717. https://doi.org/10.1016/j.jnucmat.2015.06.028.

[24] G. Cheol Lee, H. Noh, H. Yeom, H. Jo, T. Kyun Kim, M. Kim, K. Sridharan, H. Sun Park, Zirconium-silicide coating on zircaloy-4 substrate for accident tolerance: Effects on oxidation resistance and boiling, Annals of Nuclear Energy 126 (2019) 350–358. https://doi.org/10.1016/j.anucene.2018.11.019.

[25] T. Dabney, G. Johnson, H. Yeom, B. Maier, J. Walters, K. Sridharan, Experimental evaluation of cold spray FeCrAl alloys coated zirconium-alloy for potential accident tolerant fuel cladding, Nuclear Materials and Energy 21 (2019) 100715. https://doi.org/10.1016/j.nme.2019.100715.

[26] B. Maier, H. Yeom, G. Johnson, T. Dabney, J. Walters, P. Xu, J. Romero, H. Shah, K. Sridharan, Development of cold spray chromium coatings for improved accident tolerant zirconium-alloy cladding, Journal of Nuclear Materials 519 (2019) 247–254. https://doi.org/10.1016/j.jnucmat.2019.03.039.

[27] J.-C. Brachet, I. Idarraga-Trujillo, M.L. Flem, M.L. Saux, V. Vandenberghe, S. Urvoy, E. Rouesne, T. Guilbert, C. Toffolon-Masclet, M. Tupin, C. Phalippou, F. Lomello, F. Schuster, A. Billard, G. Velisa, C. Ducros, F. Sanchette, Early studies on Cr-Coated Zircaloy-4 as enhanced accident tolerant nuclear fuel claddings for light water reactors, Journal of Nuclear Materials 517 (2019) 268–285. https://doi.org/10.1016/j.jnucmat.2019.02.018.

[28] H. Yeom, B. Maier, G. Johnson, T. Dabney, M. Lenling, K. Sridharan, High temperature oxidation and microstructural evolution of cold spray chromium coatings on Zircaloy-4 in steam environments, Journal of Nuclear Materials 526 (2019) 151737. https://doi.org/10.1016/j.jnucmat.2019.151737.

[29] Y. Yamamoto, B.A. Pint, K.A. Terrani, K.G. Field, Y. Yang, L.L. Snead, Development and property evaluation of nuclear grade wrought FeCrAl fuel cladding for light water reactors, Journal of Nuclear Materials 467 (2015) 703–716. https://doi.org/10.1016/j.jnucmat.2015.10.019.

[30] K. Yueh, K.A. Terrani, Silicon carbide composite for light water reactor fuel assembly applications, Journal of Nuclear Materials 448 (2014) 380–388. https://doi.org/10.1016/j.jnucmat.2013.12.004.

[31] L.L. Snead, T. Nozawa, Y. Katoh, T.-S. Byun, S. Kondo, D.A. Petti, Handbook of SiC properties for fuel performance modeling, Journal of Nuclear Materials 371 (2007) 329–377. https://doi.org/10.1016/j.jnucmat.2007.05.016.

[32] C.P. Deck, G.M. Jacobsen, J. Sheeder, O. Gutierrez, J. Zhang, J. Stone, H.E. Khalifa, C.A. Back, Characterization of SiC–SiC composites for accident tolerant fuel cladding, Journal of Nuclear Materials 466 (2015) 667–681. https://doi.org/10.1016/j.jnucmat.2015.08.020.

[33] T. Koyanagi, Y. Katoh, G. Singh, M. Snead, SiC/SiC cladding materials properties handbook, Nuclear Technology Research and Development, ORNL/TM-2017/385 (2017).

[34] D. Kim, H.-G. Lee, J.Y. Park, W.-J. Kim, Fabrication and measurement of hoop strength of SiC triplex tube for nuclear fuel cladding applications, Journal of Nuclear Materials 458 (2015) 29–36. https://doi.org/10.1016/j.jnucmat.2014.11.117.

[35] P. Wang, F. Liu, H. Wang, H. Li, Y. Gou, A review of third generation SiC fibers and SiCf/SiC composites, Journal of Materials Science & Technology 35 (2019) 2743–2750. https://doi.org/10.1016/j.jmst.2019.07.020.

[36] K.A. Terrani, B.A. Pint, C.M. Parish, C.M. Silva, L.L. Snead, Y. Katoh, Silicon Carbide Oxidation in Steam up to 2 MPa, Journal of the American Ceramic Society 97 (2014) 2331–2352. https://doi.org/10.1111/jace.13094.

[37] Y. Katoh, L.L. Snead, I. Szlufarska, W.J. Weber, Radiation effects in SiC for nuclear structural applications, Current Opinion in Solid State and Materials Science 16 (2012) 143–152. https://doi.org/10.1016/j.cossms.2012.03.005.

[38] H. Yang, X. Li, C. Liu, Y. Zhao, B. Chen, X. Yang, L. Cheng, L. Zhang, Hydrothermal corrosion behavior of SiCf/SiC composites candidate for PWR accident tolerant fuel cladding, Ceramics International 44 (2018) 22865–22873. https://doi.org/10.1016/j.ceramint.2018.09.079.

[39] D. Kim, H.J. Lee, C. Jang, H.-G. Lee, J.Y. Park, W.-J. Kim, Influence of microstructure on hydrothermal corrosion of chemically vapor processed SiC composite tubes, Journal of Nuclear Materials 492 (2017) 6–13. https://doi.org/10.1016/j.jnucmat.2017.05.010.

[40] P.J. Doyle, S. Zinkle, S.S. Raiman, Hydrothermal corrosion behavior of CVD SiC in high temperature water, Journal of Nuclear Materials 539 (2020) 152241. https://doi.org/10.1016/j.jnucmat.2020.152241.

[41] W.-J. Kim, D. Kim, J.Y. Park, Fabrication and material issues for the application of SiC composites to LWR fuel cladding, Nuclear Engineering and Technology 45 (2013) 565–572. https://doi.org/10.5516/NET.07.2012.084.

[42] G.M. Jacobsen, J.D. Stone, H.E. Khalifa, C.P. Deck, C.A. Back, Investigation of the C-ring test for measuring hoop tensile strength of nuclear grade ceramic composites, Journal of Nuclear Materials 452 (2014) 125–132. https://doi.org/10.1016/j.jnucmat.2014.05.002.

[43] T. Koyanagi, Y. Katoh, T. Hinoki, C. Henager, M. Ferraris, S. Grasso, Progress in development of SiC-based joints resistant to neutron irradiation, Journal of the European Ceramic Society 40 (2020) 1023–1034. https://doi.org/10.1016/j.jeurceramsoc.2019.10.055.

[44] A. Baptista, F. Silva, J. Porteiro, J. Míguez, G. Pinto, Sputtering Physical Vapour Deposition (PVD) Coatings: A Critical Review on Process Improvement and Market Trend Demands, Coatings 8 (2018) 402. https://doi.org/10.3390/coatings8110402.

[45] M. Samuelsson, D. Lundin, J. Jensen, M.A. Raadu, J.T. Gudmundsson, U. Helmersson, On the film density using high power impulse magnetron sputtering, Surface and Coatings Technology 205 (2010) 591–596. https://doi.org/10.1016/j.surfcoat.2010.07.041.

[46] P. Panjan, A. Drnovšek, P. Gselman, M. Čekada, M. Panjan, Review of Growth Defects in Thin Films Prepared by PVD Techniques, Coatings 10 (2020) 447. https://doi.org/10.3390/coatings10050447.

[47] K. Sarakinos, J. Alami, S. Konstantinidis, High power pulsed magnetron sputtering: A review on scientific and engineering state of the art, Surface and Coatings Technology 204 (2010) 1661–1684. https://doi.org/10.1016/j.surfcoat.2009.11.013.

[48] J.A. Thornton, Influence of substrate temperature and deposition rate on structure of thick sputtered Cu coatings, Journal of Vacuum Science and Technology 12 (1975) 830–835. https://doi.org/10.1116/1.568682.

[49] J.A. Thornton, High Rate Thick Film Growth, Annu. Rev. Mater. Sci. 7 (1977) 239–260. https://doi.org/10.1146/annurev.ms.07.080177.001323.

[50] J.T. Gudmundsson, Physics and technology of magnetron sputtering discharges, Plasma Sources Sci. Technol. 29 (2020) 113001. https://doi.org/10.1088/1361-6595/abb7bd.

[51] J. Lin, Z.L. Wu, X.H. Zhang, B. Mishra, J.J. Moore, W.D. Sproul, A comparative study of CrNx coatings Synthesized by dc and pulsed dc magnetron sputtering, Thin Solid Films 517 (2009) 1887–1894. https://doi.org/10.1016/j.tsf.2008.09.093.

[52] A. Guglya, Chapter 4 - Ion-beam-assisted deposition of thin films, in: Emerging Applications of Nanoparticles and Architectural Nanostructures, 2018: pp. 95–119.

[53] V. Kouznetsov, K. Macák, J.M. Schneider, U. Helmersson, I. Petrov, A novel pulsed magnetron sputter technique utilizing very high target power densities, Surface and Coatings Technology 122 (1999) 290–293. https://doi.org/10.1016/S0257-8972(99)00292-3.

[54] D. Lundin, K. Sarakinos, An introduction to thin film processing using high-power impulse magnetron sputtering, J. Mater. Res. 27 (2012) 780–792. https://doi.org/10.1557/jmr.2012.8.

[55] B. Wu, I. Haehnlein, I. Shchelkanov, J. McLain, D. Patel, J. Uhlig, B. Jurczyk, Y. Leng, D.N. Ruzic, Cu films prepared by bipolar pulsed high power impulse magnetron sputtering, Vacuum 150 (2018) 216–221. https://doi.org/10.1016/j.vacuum.2018.01.011.

[56] T. Nakano, N. Hirukawa, S. Saeki, S. Baba, Effects of target voltage during pulse-off period in pulsed magnetron sputtering on afterglow plasma and deposited film structure, Vacuum 87 (2013) 109–113. https://doi.org/10.1016/j.vacuum.2012.03.010.

[57] A. Anders, A structure zone diagram including plasma-based deposition and ion etching, Thin Solid Films 518 (2010) 4087–4090. https://doi.org/10.1016/j.tsf.2009.10.145.

[58] J. Alami, P. Eklund, J.M. Andersson, M. Lattemann, E. Wallin, J. Bohlmark, P. Persson, U. Helmersson, Phase tailoring of Ta thin films by highly ionized pulsed magnetron sputtering, Thin Solid Films 515 (2007) 3434–3438. https://doi.org/10.1016/j.tsf.2006.10.013.

[59] A.P. Ehiasarian, J.G. Wen, I. Petrov, Interface microstructure engineering by high power impulse magnetron sputtering for the enhancement of adhesion, Journal of Applied Physics 101 (2007) 054301. https://doi.org/10.1063/1.2697052.

[60] J. Alami, S. Bolz, K. Sarakinos, High power pulsed magnetron sputtering: Fundamentals and applications, Journal of Alloys and Compounds 483 (2009) 530–534. https://doi.org/10.1016/j.jallcom.2008.08.104.

[61] G. Abadias, E. Chason, J. Keckes, M. Sebastiani, G.B. Thompson, E. Barthel, G.L. Doll, C.E. Murray, C.H. Stoessel, L. Martinu, Review Article: Stress in thin films and coatings: Current status, challenges, and prospects, Journal of Vacuum Science & Technology A 36 (2018) 020801. https://doi.org/10.1116/1.5011790.

[62] W.D. Nix, B.M. Clemens, Crystallite coalescence: A mechanism for intrinsic tensile stresses in thin films, J. Mater. Res. 14 (1999) 3467–3473. https://doi.org/10.1557/JMR.1999.0468.

[63] D. Magnfält, G. Abadias, K. Sarakinos, Atom insertion into grain boundaries and stress generation in physically vapor deposited films, Appl. Phys. Lett. 103 (2013) 051910. https://doi.org/10.1063/1.4817669.

[64] M.M.M. Bilek, D.R. McKenzie, A comprehensive model of stress generation and relief processes in thin films deposited with energetic ions, Surface and Coatings Technology 200 (2006) 4345–4354. https://doi.org/10.1016/j.surfcoat.2005.02.161.

[65] P.R. Guduru, E. Chason, L.B. Freund, Mechanics of compressive stress evolution during thin film growth, Journal of the Mechanics and Physics of Solids 51 (2003) 2127–2148. https://doi.org/10.1016/j.jmps.2003.09.013.

[66] E. Chason, B.W. Sheldon, L.B. Freund, J.A. Floro, S.J. Hearne, Origin of Compressive Residual Stress in Polycrystalline Thin Films, Phys. Rev. Lett. 88 (2002) 156103. https://doi.org/10.1103/PhysRevLett.88.156103.

[67] U. Welzel, J. Ligot, P. Lamparter, A.C. Vermeulen, E.J. Mittemeijer, Stress analysis of polycrystalline thin films and surface regions by X-ray diffraction, J Appl Cryst 38 (2005) 1–29. https://doi.org/10.1107/S0021889804029516.

[68] The International XPS Database of XPS Reference Spectra, (n.d.). https://xpsdatabase.net/ (accessed September 28, 2023).

[69] M. Rosso, A. Arafat, K. Schroën, M. Giesbers, C.S. Roper, R. Maboudian, H. Zuilhof, Covalent Attachment of Organic Monolayers to Silicon Carbide Surfaces, Langmuir 24 (2008) 4007–4012. https://doi.org/10.1021/la704002y.

[70] C. Wang, N. Huang, H. Zhuang, Z. Zhai, B. Yang, L. Liu, X. Jiang, Growth of large-scale heteroepitaxial 3C-SiC films and nanosheets on silicon substrates by microwave plasma enhanced CVD at higher powers, Surface and Coatings Technology 299 (2016) 96–103. https://doi.org/10.1016/j.surfcoat.2016.04.070.

[71] L. Sun, C. Han, N. Wu, B. Wang, Y. Wang, High temperature gas sensing performances of silicon carbide nanosheets with an n–p conductivity transition, RSC Adv. 8 (2018) 13697–13707. https://doi.org/10.1039/C8RA02164C.

[72] L. Wang, Z. Chen, B. Wang, Y. Li, R. Zhang, G. Liu, Z. He, D. Fu, H. Wang, X. Xiong, Effect of free carbon on micro-mechanical properties of a chemically vapor deposited SiC coating, Ceramics International 44 (2018) 17118–17123. https://doi.org/10.1016/j.ceramint.2018.06.165.

[73] K. Mogi, T. Ogiwara, M. Suzuki, S. project of Sasj, Sputter Etching Rate Ratio of Si to SiO_2 using Mesh-Replica Method, Journal of Surface Analysis 9 (2002) 514–523. https://doi.org/10.1384/jsa.9.514.

[74] D. Viladot, M. Véron, M. Gemmi, F. Peiró, J. Portillo, S. Estradé, J. Mendoza, N. Llorca-Isern, S. Nicolopoulos, Orientation and phase mapping in the transmission electron microscope using precession-assisted diffraction spot recognition: state-of-the-art results, Journal of Microscopy 252 (2013) 23–34. https://doi.org/10.1111/jmi.12065.

[75] M.E. Fitzpatrick, A.T. Fry, P. Holdway, F.A. Kandil, J. Shackleton, L. Suominen, Determination of residual stresses by X-ray diffraction., Teddington, 2005. https://eprintspublications.npl.co.uk/2391/ (accessed September 22, 2023).

[76] K. Quillin, H. Yeom, T. Dabney, E. Willing, K. Sridharan, Microstructural and nanomechanical studies of PVD Cr coatings on SiC for LWR fuel cladding applications, Surface and Coatings Technology 441 (2022) 128577. https://doi.org/10.1016/j.surfcoat.2022.128577.

[77] H. Baker, Properties of Metals, in: J.R. Davis (Ed.), Metals Handbook Desk Edition, 2nd ed., ASM International, 1998: pp. 114–121. https://doi.org/10.31399/asm.hb.mhde2.a0003086.

[78] W.C. Oliver, G.M. Pharr, An improved technique for determining hardness and elastic modulus using load and displacement sensing indentation experiments, J. Mater. Res. 7 (1992) 1564–1583. https://doi.org/10.1557/JMR.1992.1564.

[79] X. Li, B. Bhushan, A review of nanoindentation continuous stiffness measurement technique and its applications, Materials Characterization 48 (2002) 11–36. https://doi.org/10.1016/S1044-5803(02)00192-4.

[80] J.F. Ziegler, M.D. Ziegler, J.P. Biersack, SRIM – The stopping and range of ions in matter (2010), Nuclear Instruments and Methods in Physics Research Section B: Beam Interactions with Materials and Atoms 268 (2010) 1818–1823. https://doi.org/10.1016/j.nimb.2010.02.091.

[81] R.E. Stoller, M.B. Toloczko, G.S. Was, A.G. Certain, S. Dwaraknath, F.A. Garner, On the use of SRIM for computing radiation damage exposure, Nuclear Instruments and Methods in Physics Research Section B: Beam Interactions with Materials and Atoms 310 (2013) 75–80. https://doi.org/10.1016/j.nimb.2013.05.008.

[82] E10 Committee, Standard Practice for Investigating the Effects of Neutron Radiation Damage Using Charged-Particle Irradiation, ASTM International, 2023. https://doi.org/10.1520/E0521-23.

[83] R. Devanathan, W.J. Weber, Displacement energy surface in 3C and 6H SiC, Journal of Nuclear Materials 278 (2000) 258–265. https://doi.org/10.1016/S0022-3115(99)00266-4.

[84] M.T. Robinson, I.M. Torrens, Computer simulation of atomic-displacement cascades in solids in the binary-collision approximation, Phys. Rev. B 9 (1974) 5008–5024. https://doi.org/10.1103/PhysRevB.9.5008.

[85] A. Mutzke, R. Schneider, W. Eckstein, R. Dohmen, K. Schmid, U.V. Toussaint, G. Badelow, SDTrimSP Version 6.00, Max-Planck-Institut für Plasmaphysik, 2019. https://doi.org/10.17617/2.3026474.

[86] P.S. Szabo, D. Weichselbaum, H. Biber, C. Cupak, A. Mutzke, R.A. Wilhelm, F. Aumayr, Graphical user interface for SDTrimSP to simulate sputtering, ion implantation and the dynamic effects of ion irradiation, Nuclear Instruments and Methods in Physics Research Section B: Beam Interactions with Materials and Atoms 522 (2022) 47–53. https://doi.org/10.1016/j.nimb.2022.04.008.

[87] H. Hofsäss, K. Zhang, A. Mutzke, Simulation of ion beam sputtering with SDTrimSP, TRIDYN and SRIM, Applied Surface Science 310 (2014) 134–141. https://doi.org/10.1016/j.apsusc.2014.03.152.

[88] W.D. Wilson, L.G. Haggmark, J.P. Biersack, Calculations of nuclear stopping, ranges, and straggling in the low-energy region, Phys. Rev. B 15 (1977) 2458–2468. https://doi.org/10.1103/PhysRevB.15.2458.

[89] J.F. Ziegler, J.P. Biersack, The Stopping and Range of Ions in Matter, in: D.A. Bromley (Ed.), Treatise on Heavy-Ion Science: Volume 6: Astrophysics, Chemistry, and Condensed Matter, Springer US, Boston, MA, 1985: pp. 93–129. https://doi.org/10.1007/978-1-4615-8103-1_3.

[90] Y. Pauleau, Generation and evolution of residual stresses in physical vapour-deposited thin films, Vacuum 61 (2001) 175–181. https://doi.org/10.1016/S0042-207X(00)00475-9.

[91] R.B. Roberts, G.K. White, E. Fawcett, Thermal expansion of Cr and Cr-V alloys, Physica B+C 119 (1983) 63–67. https://doi.org/10.1016/0378-4363(83)90167-5.

[92] B. Maier, H. Yeom, G. Johnson, T. Dabney, J. Walters, P. Xu, J. Romero, H. Shah, K. Sridharan, Development of cold spray chromium coatings for improved accident tolerant zirconium-alloy cladding, Journal of Nuclear Materials 519 (2019) 247–254. https://doi.org/10.1016/j.jnucmat.2019.03.039.

[93] J.-C. Brachet, I. Idarraga-Trujillo, M.L. Flem, M.L. Saux, V. Vandenberghe, S. Urvoy, E. Rouesne, T. Guilbert, C. Toffolon-Masclet, M. Tupin, C. Phalippou, F. Lomello, F. Schuster, A. Billard, G. Velisa, C. Ducros, F. Sanchette, Early studies on Cr-Coated Zircaloy-4 as enhanced accident tolerant nuclear fuel claddings for light water reactors, Journal of Nuclear Materials 517 (2019) 268–285. https://doi.org/10.1016/j.jnucmat.2019.02.018.

[94] P.B. Barna, M. Adamik, Fundamental structure forming phenomena of polycrystalline films and the structure zone models, Thin Solid Films 317 (1998) 27–33. https://doi.org/10.1016/S0040-6090(97)00503-8.

[95] Y.C. Feng, D.E. Laughlin, D.N. Lambeth, Formation of crystallographic texture in rf sputter-deposited Cr thin films, Journal of Applied Physics 76 (1994) 7311–7316. https://doi.org/10.1063/1.358019.

[96] A. de Monteynard, F. Schuster, A. Billard, F. Sanchette, Properties of chromium thin films deposited in a hollow cathode magnetron powered by pulsed DC or HiPIMS, Surface and Coatings Technology 330 (2017) 241–248. https://doi.org/10.1016/j.surfcoat.2017.10.006.

[97] A. Ferrec, J. Keraudy, S. Jacq, F. Schuster, P.-Y. Jouan, M.A. Djouadi, Correlation between mass-spectrometer measurements and thin film characteristics using dcMS and HiPIMS discharges, Surface and Coatings Technology 250 (2014) 52–56. https://doi.org/10.1016/j.surfcoat.2014.02.030.

[98] D.W. Hoffman, J.A. Thornton, Internal stresses in sputtered chromium, Thin Solid Films 40 (1977) 355–363. https://doi.org/10.1016/0040-6090(77)90137-7.

[99] B.-K. Jang, H. Matsubara, Microstructure of nanoporous yttria-stabilized zirconia films fabricated by EB-PVD, Journal of the European Ceramic Society 26 (2006) 1585–1590. https://doi.org/10.1016/j.jeurceramsoc.2005.03.248.

[100] A.O. Eriksson, O. Tengstrand, J. Lu, J. Jensen, P. Eklund, J. Rosén, I. Petrov, J.E. Greene, L. Hultman, Si incorporation in Ti1−xSixN films grown on TiN(001) and (001)-faceted TiN(111) columns, Surface and Coatings Technology 257 (2014) 121–128. https://doi.org/10.1016/j.surfcoat.2014.05.043.

[101] C. Gautier, J. Machet, Effects of deposition parameters on the texture of chromium films deposited by vacuum arc evaporation, Thin Solid Films 289 (1996) 34–38. https://doi.org/10.1016/S0040-6090(96)08891-8.

[102] R.W. Hoffman, Stresses in thin films: The relevance of grain boundaries and impurities, Thin Solid Films 34 (1976) 185–190. https://doi.org/10.1016/0040-6090(76)90453-3.

[103] Š. Batková, J. Čapek, J. Rezek, R. Čerstvý, P. Zeman, Effect of positive pulse voltage in bipolar reactive HiPIMS on crystal structure, microstructure and mechanical properties of CrN

films, Surface and Coatings Technology 393 (2020) 125773. https://doi.org/10.1016/j.surfcoat.2020.125773.

[104] I. Fernández-Martínez, J.A. Santiago, Á. Mendez, M. Panizo-Laiz, P. Diaz-Rodríguez, L. Mendizábal, J. Díez-Sierra, C. Zubizarreta, M.A. Monclus, J. Molina-Aldareguia, Selective Metal Ion Irradiation Using Bipolar HIPIMS: A New Route to Tailor Film Nanostructure and the Resulting Mechanical Properties, Coatings 12 (2022) 191. https://doi.org/10.3390/coatings12020191.

[105] R.P.B. Viloan, J. Gu, R. Boyd, J. Keraudy, L. Li, U. Helmersson, Bipolar high power impulse magnetron sputtering for energetic ion bombardment during TiN thin film growth without the use of a substrate bias, Thin Solid Films 688 (2019) 137350. https://doi.org/10.1016/j.tsf.2019.05.069.

[106] M. Kateb, J.T. Gudmundsson, S. Ingvarsson, Effect of substrate bias on microstructure of epitaxial film grown by HiPIMS: An atomistic simulation, Journal of Vacuum Science & Technology A: Vacuum, Surfaces, and Films 38 (2020) 043006. https://doi.org/10.1116/6.0000233.

[107] J. Keraudy, R.P.B. Viloan, M.A. Raadu, N. Brenning, D. Lundin, U. Helmersson, Bipolar HiPIMS for tailoring ion energies in thin film deposition, Surface and Coatings Technology 359 (2019) 433–437. https://doi.org/10.1016/j.surfcoat.2018.12.090.

[108] F. Avino, A. Sublet, M. Taborelli, Evidence of ion energy distribution shift in HiPIMS plasmas with positive pulse, Plasma Sources Sci. Technol. 28 (2019) 01LT03. https://doi.org/10.1088/1361-6595/aaf5c9.

[109] M. Kateb, H. Hajihoseini, J.T. Gudmundsson, S. Ingvarsson, Role of ionization fraction on the surface roughness, density, and interface mixing of the films deposited by thermal evaporation, dc magnetron sputtering, and HiPIMS: An atomistic simulation, Journal of Vacuum Science & Technology A 37 (2019) 031306. https://doi.org/10.1116/1.5094429.

[110] M. Kateb, J.T. Gudmundsson, P. Brault, A. Manolescu, S. Ingvarsson, On the role of ion potential energy in low energy HiPIMS deposition: An atomistic simulation, Surface and Coatings Technology 426 (2021) 127726. https://doi.org/10.1016/j.surfcoat.2021.127726.

[111] C. Önneby, C.G. Pantano, Silicon oxycarbide formation on SiC surfaces and at the SiC/SiO2 interface, Journal of Vacuum Science & Technology A 15 (1997) 1597–1602. https://doi.org/10.1116/1.580951.

[112] J. Scott, P.J. Thomas, M. MacKenzie, S. McFadzean, J. Wilbrink, A.J. Craven, W.A.P. Nicholson, Near-simultaneous dual energy range EELS spectrum imaging, Ultramicroscopy 108 (2008) 1586–1594. https://doi.org/10.1016/j.ultramic.2008.05.006.

[113] R.F. Egerton, Electron Energy-Loss Spectroscopy in the Electron Microscope, Springer US, Boston, MA, 1995. https://doi.org/10.1007/978-1-4615-6887-2.

[114] F. Wang, R. Egerton, M. Malac, Fourier-ratio deconvolution techniques for electron energy-loss spectroscopy (EELS), Ultramicroscopy 109 (2009) 1245–1249. https://doi.org/10.1016/j.ultramic.2009.05.011.

[115] R.F. Egerton, M. Malac, EELS in the TEM, Journal of Electron Spectroscopy and Related Phenomena 143 (2005) 43–50. https://doi.org/10.1016/j.elspec.2003.12.009.

[116] M. Hillert, Phase Equilibria, Phase Diagrams and Phase Transformations: Their Thermodynamic Basis, 2nd ed., Cambridge University Press, Cambridge, 2007. https://doi.org/10.1017/CBO9780511812781.

[117] M. Venkatraman, J.P. Neumann, The C-Cr (Carbon-Chromium) System, Bulletin of Alloy Phase Diagrams 11 (1990) 152–159. https://doi.org/10.1007/BF02841701.

[118] T.L. Daulton, B.J. Little, Determination of chromium valence over the range Cr(0)–Cr(VI) by electron energy loss spectroscopy, Ultramicroscopy 106 (2006) 561–573. https://doi.org/10.1016/j.ultramic.2006.02.005.

[119] J.H. Paterson, O.L. Krivanek, Elnes of 3d transition-metal oxides: II. Variations with oxidation state and crystal structure, Ultramicroscopy 32 (1990) 319–325. https://doi.org/10.1016/0304-3991(90)90078-Z.

[120] D.H. Pearson, C.C. Ahn, B. Fultz, White lines and d-electron occupancies for the 3d and 4d transition metals, Phys. Rev. B 47 (1993) 8471–8478. https://doi.org/10.1103/PhysRevB.47.8471.

[121] P.A. van Aken, B. Liebscher, Quantification of ferrous/ferric ratios in minerals: new evaluation schemes of Fe L23electron energy-loss near-edge spectra, Phys Chem Min 29 (2002) 188–200. https://doi.org/10.1007/s00269-001-0222-6.

[122] D. Mitchell, Double Atan EELS Background, 20150402, v2.0, (2015). http://www.dmscripting.com/double_atan_eels_background.html.

[123] K. Bawane, P. Manganaris, Y. Wang, J. Sure, A. Ronne, P. Halstenberg, S. Dai, S.K. Gill, K. Sasaki, Y.K. Chen-Wiegart, R. Gakhar, S. Mahurin, S.M. Pimblott, J.F. Wishart, L. He, Determining oxidation states of transition metals in molten salt corrosion using electron energy loss spectroscopy, Scripta Materialia 197 (2021) 113790. https://doi.org/10.1016/j.scriptamat.2021.113790.

[124] X. Fan, E.C. Dickey, S.J. Pennycook, M.K. Sunkara, Z-contrast imaging and electron energy-loss spectroscopy analysis of chromium-doped diamond-like carbon films, Appl. Phys. Lett. 75 (1999) 2740–2742. https://doi.org/10.1063/1.125134.

[125] L. Yate, L. Martínez-de-Olcoz, V.I. Ivashchenko, A.V. Pshyk, E. Coy, J. Esteve, A. Lousa, Stabilization of complex orthorhombic o-Cr3C2 thin films under high energetic growth conditions: Experiments and calculations, Journal of Alloys and Compounds 848 (2020) 156373. https://doi.org/10.1016/j.jallcom.2020.156373.

[126] H.-T. Lin, P.K. Nayak, S.-C. Wang, S.-Y. Chang, J.-L. Huang, Electron-energy loss spectroscopy and Raman studies of nanosized chromium carbide synthesized during carbothermal reduction process from precursor Cr(CO)6, Journal of the European Ceramic Society 31 (2011) 2481–2487. https://doi.org/10.1016/j.jeurceramsoc.2010.12.005.

[127] X. Liu, T. Yang, P. Lang, Y. Yao, X. Shen, R. Yu, TEM characterization of an epitaxial CrO2 film deposited by the CVD method and the transition interface, Materials Letters 352 (2023) 135132. https://doi.org/10.1016/j.matlet.2023.135132.

[128] A.J. Leide, L.W. Hobbs, Z. Wang, D. Chen, L. Shao, J. Li, The role of chemical disorder and structural freedom in radiation-induced amorphization of silicon carbide deduced from electron spectroscopy and ab initio simulations, Journal of Nuclear Materials 514 (2019) 299–310. https://doi.org/10.1016/j.jnucmat.2018.11.036.

[129] S. Muto, T. Tanabe, Local structures and damage processes of electron irradiated α-SiC studied with transmission electron microscopy and electron energy-loss spectroscopy, Journal of Applied Physics 93 (2003) 3765–3775. https://doi.org/10.1063/1.1555673.

[130] M. Ishimaru, I.-T. Bae, A. Hirata, Y. Hirotsu, J.A. Valdez, K.E. Sickafus, Volume swelling of amorphous SiC during ion-beam irradiation, Phys. Rev. B 72 (2005) 024116. https://doi.org/10.1103/PhysRevB.72.024116.

[131] C. Adelhelm, M. Balden, M. Rinke, M. Stueber, Influence of doping (Ti, V, Zr, W) and annealing on the sp2 carbon structure of amorphous carbon films, Journal of Applied Physics 105 (2009) 033522. https://doi.org/10.1063/1.3075843.

[132] Z. Zhou, W.M. Rainforth, M.H. Gass, A. Bleloch, A.P. Ehiassarian, P.Eh. Hovsepian, C/CrC nanocomposite coating deposited by magnetron sputtering at high ion irradiation conditions, Journal of Applied Physics 110 (2011) 073301. https://doi.org/10.1063/1.3642996.
[133] L. Yang, C. Liu, M. Wen, X. Dai, Y. Zhang, X. Chen, K. Zhang, Small atoms as reinforced agent for both hardness and toughness of Group-VIB transition metal films, Journal of Alloys and Compounds 735 (2018) 1105–1110. https://doi.org/10.1016/j.jallcom.2017.11.208.
[134] M. Magnuson, M. Andersson, J. Lu, L. Hultman, U. Jansson, Electronic structure and chemical bonding of amorphous chromium carbide thin films, J. Phys.: Condens. Matter 24 (2012) 225004. https://doi.org/10.1088/0953-8984/24/22/225004.
[135] A. Weck, C.W. Sinclair, C.P. Scott, C. Maunder, Supersaturated α-iron in vapour-deposited Fe–C thin films, J Mater Sci 47 (2012) 6939–6947. https://doi.org/10.1007/s10853-012-6641-6.
[136] S. Fritze, M. Chen, L. Riekehr, B. Osinger, M.A. Sortica, A. Srinath, A.S. Menon, E. Lewin, D. Primetzhofer, J.M. Wheeler, U. Jansson, Magnetron sputtering of carbon supersaturated tungsten films – A chemical approach to increase strength, Materials & Design 208 (2021) 109874. https://doi.org/10.1016/j.matdes.2021.109874.
[137] J. Du, Y. Huang, J. Liu, Y. Liu, Z. Wang, Irradiation damage alloying for immiscible alloy systems and its thermodynamic origin, Materials & Design 170 (2019) 107699. https://doi.org/10.1016/j.matdes.2019.107699.
[138] J.A. Santiago, I. Fernández-Martínez, A. Wennberg, J.M. Molina-Aldareguia, M. Castillo-Rodríguez, T.C. Rojas, J.C. Sánchez-López, M.U. González, J.M. García-Martín, H. Li, V. Bellido-González, M.A. Monclús, R. González-Arrabal, Adhesion enhancement of DLC hard coatings by HiPIMS metal ion etching pretreatment, Surface and Coatings Technology 349 (2018) 787–796. https://doi.org/10.1016/j.surfcoat.2018.04.090.
[139] E. Broitman, Zs. Czigány, G. Greczynski, J. Böhlmark, R. Cremer, L. Hultman, Industrial-scale deposition of highly adherent CNx films on steel substrates, Surface and Coatings Technology 204 (2010) 3349–3357. https://doi.org/10.1016/j.surfcoat.2010.03.038.
[140] F. de la Peña, E. Prestat, V.T. Fauske, P. Burdet, J. Lähnemann, P. Jokubauskas, T. Furnival, M. Nord, T. Ostasevicius, K.E. MacArthur, D.N. Johnstone, M. Sarahan, J. Taillon, T. Aarholt, pquinn-dls, V. Migunov, A. Eljarrat, J. Caron, C. Francis, T. Nemoto, T. Poon, S. Mazzucco, actions-user, N. Tappy, N. Cautaerts, S. Somnath, T. Slater, M. Walls, F. Winkler, H.W. Ånes, hyperspy/hyperspy: v2.0, (2023). https://doi.org/10.5281/zenodo.10412190.
[141] W.H. Kirchhoff, LOGISTIC FUNCTION PROFILE FIT: A least-squares program for fitting interface profiles to an extended logistic functiona), Journal of Vacuum Science & Technology A 30 (2012) 051101. https://doi.org/10.1116/1.4736865.
[142] S.A. Wight, C.J. Powell, Evaluation of the shapes of Auger- and secondary-electron line scans across interfaces with the logistic function, Journal of Vacuum Science & Technology A 24 (2006) 1024–1030. https://doi.org/10.1116/1.2209651.
[143] A. Chabanon, A. Michau, M.L. Schlegel, D.C. Gündüz, B. Puga, F. Miserque, F. Schuster, H. Maskrot, C. Pareige, E. Cadel, G. Beainy, V. Cloute-Cazalaa, S. Narasimalu, B. Yao, Z. Dong, F. Balbaud-Célérier, Surface Modification of 304L Stainless Steel and Interface Engineering by HiPIMS Pre-Treatment, Coatings 12 (2022) 727. https://doi.org/10.3390/coatings12060727.
[144] A.P. Ehiasarian, High power pulsed magnetron sputtered CrNx films, Surface and Coatings Technology (2003) 6.

[145] C28 Committee, Test Method for Adhesion Strength and Mechanical Failure Modes of Ceramic Coatings by Quantitative Single Point Scratch Testing, ASTM International, 2022. https://doi.org/10.1520/C1624-22.
[146] S.J. Bull, E.G. Berasetegui, An overview of the potential of quantitative coating adhesion measurement by scratch testing, Tribology International 39 (2006) 99–114. https://doi.org/10.1016/j.triboint.2005.04.013.
[147] R. Saha, W.D. Nix, Effects of the substrate on the determination of thin film mechanical properties by nanoindentation, Acta Materialia 50 (2002) 23–38. https://doi.org/10.1016/S1359-6454(01)00328-7.
[148] X. Zhou, Z. Jiang, H. Wang, R. Yu, Investigation on methods for dealing with pile-up errors in evaluating the mechanical properties of thin metal films at sub-micron scale on hard substrates by nanoindentation technique, Materials Science and Engineering: A 488 (2008) 318–332. https://doi.org/10.1016/j.msea.2008.01.020.
[149] K.W. McElhaney, J.J. Vlassak, W.D. Nix, Determination of indenter tip geometry and indentation contact area for depth-sensing indentation experiments, J. Mater. Res. 13 (1998) 1300–1306. https://doi.org/10.1557/JMR.1998.0185.
[150] A. Bolshakov, G.M. Pharr, Influences of pileup on the measurement of mechanical properties by load and depth sensing indentation techniques, J. Mater. Res. 13 (1998) 1049–1058. https://doi.org/10.1557/JMR.1998.0146.
[151] W.C. Oliver, G.M. Pharr, Measurement of hardness and elastic modulus by instrumented indentation: Advances in understanding and refinements to methodology, Journal of Materials Research 19 (2004) 3–20. https://doi.org/10.1557/jmr.2004.19.1.3.
[152] H. Baker, Properties of Metals, in: J.R. Davis (Ed.), Metals Handbook Desk Edition, ASM International, 1998: pp. 114–121. https://doi.org/10.31399/asm.hb.mhde2.a0003086.
[153] J. Lin, J.J. Moore, W.D. Sproul, B. Mishra, Z. Wu, Modulated pulse power sputtered chromium coatings, Thin Solid Films 518 (2009) 1566–1570. https://doi.org/10.1016/j.tsf.2009.09.118.
[154] G. Greczynski, J. Jensen, L. Hultman, CrNx Films Prepared by DC Magnetron Sputtering and High-Power Pulsed Magnetron Sputtering: A Comparative Study, IEEE Trans. Plasma Sci. 38 (2010) 3046–3056. https://doi.org/10.1109/TPS.2010.2071885.
[155] A.A. Elmustafa, Pile-up/sink-in of rate-sensitive nanoindentation creeping solids, Modelling Simul. Mater. Sci. Eng. 15 (2007) 823–834. https://doi.org/10.1088/0965-0393/15/7/008.
[156] A.C. Fischer-Cripps, Nanoindentation, Springer New York, New York, NY, 2011. https://doi.org/10.1007/978-1-4419-9872-9.
[157] Y.-T. Cheng, C.-M. Cheng, Relationships between hardness, elastic modulus, and the work of indentation, Appl. Phys. Lett. 73 (1998) 614–616. https://doi.org/10.1063/1.121873.
[158] R. Sujith, R. Kumar, Experimental investigation on the indentation hardness of precursor derived Si–B–C–N ceramics, Journal of the European Ceramic Society 33 (2013) 2399–2405. https://doi.org/10.1016/j.jeurceramsoc.2013.04.025.
[159] B.N. Lucas, W.C. Oliver, Indentation power-law creep of high-purity indium, Metall Mater Trans A 30 (1999) 601–610. https://doi.org/10.1007/s11661-999-0051-7.
[160] Z. Huang, A. Harris, S.A. Maloy, P. Hosemann, Nanoindentation creep study on an ion beam irradiated oxide dispersion strengthened alloy, Journal of Nuclear Materials 451 (2014) 162–167. https://doi.org/10.1016/j.jnucmat.2014.03.036.

[161] J. Zhao, P. Huang, K.W. Xu, F. Wang, T.J. Lu, Indentation size and loading strain rate dependent creep deformation of nanocrystalline Mo, Thin Solid Films 653 (2018) 365–370. https://doi.org/10.1016/j.tsf.2018.03.068.

[162] M.E. Kassner, Chapter 2 - Five-Power-Law Creep, in: M.E. Kassner (Ed.), Fundamentals of Creep in Metals and Alloys (Third Edition), Butterworth-Heinemann, Boston, 2015: pp. 7–102. https://doi.org/10.1016/B978-0-08-099427-7.00002-5.

[163] M. Bartosik, R. Pitonak, J. Keckes, In Situ High Temperature X-Ray Diffraction Reveals Residual Stress Depth-Profiles in Blasted TiN Hard Coatings, Advanced Engineering Materials 13 (2011) 705–711. https://doi.org/10.1002/adem.201000299.

[164] X.-C. Chen, J.-P. Zhou, H.-Y. Wang, P.-S. Xu, G.-Q. Pan, *In situ* high temperature X-ray diffraction studies of ZnO thin film, Chinese Phys. B 20 (2011) 096102. https://doi.org/10.1088/1674-1056/20/9/096102.

[165] V. Dolique, A.-L. Thomann, P. Brault, Y. Tessier, P. Gillon, Thermal stability of AlCoCrCuFeNi high entropy alloy thin films studied by in-situ XRD analysis, Surface and Coatings Technology 204 (2010) 1989–1992. https://doi.org/10.1016/j.surfcoat.2009.12.006.

[166] C. Kirchlechner, K.J. Martinschitz, R. Daniel, M. Klaus, C. Genzel, C. Mitterer, J. Keckes, Residual stresses and thermal fatigue in CrN hard coatings characterized by high-temperature synchrotron X-ray diffraction, Thin Solid Films 518 (2010) 2090–2096. https://doi.org/10.1016/j.tsf.2009.08.011.

[167] D.S. Rickerby, S.J. Bull, A.M. Jones, F.L. Cullen, B.A. Bellamy, High-temperature x-ray diffraction studies on physical vapour deposited TiN, Surface and Coatings Technology 39–40 (1989) 397–408. https://doi.org/10.1016/0257-8972(89)90072-8.

[168] W. Zhang, F. Ma, T. Zhang, K. Xu, Stress and microstructure evolution in Al-induced crystallization of amorphous Ge thin films, Thin Solid Films 520 (2011) 708–711. https://doi.org/10.1016/j.tsf.2011.01.398.

[169] A. Kostka, D. Naujoks, T. Oellers, S. Salomon, C. Somsen, E. Öztürk, A. Savan, A. Ludwig, G. Eggeler, Linear growth of reaction layer during in-situ TEM annealing of thin film Al/Ni diffusion couples, Journal of Alloys and Compounds 922 (2022) 165926. https://doi.org/10.1016/j.jallcom.2022.165926.

[170] M.S. Syrtanov, E.B. Kashkarov, A.V. Abdulmenova, D.V. Sidelev, High-temperature oxidation of Zr1Nb zirconium alloy with protective Cr/Mo coating, Surface and Coatings Technology 439 (2022) 128459. https://doi.org/10.1016/j.surfcoat.2022.128459.

[171] K. Bhanumurthy, R. Schmid-Fetzer, Solid-state reaction bonding of silicon carbide (HIPSiC) below 1000°C, Materials Science and Engineering: A 220 (1996) 35–40. https://doi.org/10.1016/S0921-5093(96)10452-4.

[172] K. Bhanumurthy, R. Schmid-Fetzer, Interface reactions between silicon carbide and metals (Ni, Cr, Pd, Zr), Composites Part A: Applied Science and Manufacturing 32 (2001) 569–574. https://doi.org/10.1016/S1359-835X(00)00049-X.

[173] J.S. Park, K. Landry, J.H. Perepezko, Kinetic control of silicon carbide/metal reactions, Materials Science and Engineering: A 259 (1999) 279–286. https://doi.org/10.1016/S0921-5093(98)00899-5.

[174] J.S. Park, J. Cho, S. Yi, J.H. Perepezko, Practical application of diffusion pathway analysis for SiC-metal reactions, Metals and Materials International 12 (2006) 231–238. https://doi.org/10.1007/BF03027536.

[175] Y. Du, J.C. Schuster, L. Perring, Experimental Investigation and Thermodynamic Description of the Constitution of the Ternary System Cr-Si-C, Journal of the American Ceramic Society 83 (2000) 2067–2073. https://doi.org/10.1111/j.1151-2916.2000.tb01513.x.
[176] C. Kunka, B.L. Boyce, S.M. Foiles, R. Dingreville, Revealing inconsistencies in X-ray width methods for nanomaterials, Nanoscale 11 (2019) 22456–22466. https://doi.org/10.1039/C9NR08268A.
[177] Y. Meng, S. Zeng, Z. Teng, X. Han, H. Zhang, Control of the preferential orientation Cr coatings deposited on zircaloy substrates and study of their oxidation behavior, Thin Solid Films 730 (2021) 138699. https://doi.org/10.1016/j.tsf.2021.138699.
[178] K. Quillin, H. Yeom, T. Dabney, M. McFarland, K. Sridharan, Experimental evaluation of direct current magnetron sputtered and high-power impulse magnetron sputtered Cr coatings on SiC for light water reactor applications, Thin Solid Films 716 (2020) 138431. https://doi.org/10.1016/j.tsf.2020.138431.
[179] D.W. Hoffman, J.A. Thornton, Internal stresses in sputtered chromium, Thin Solid Films 40 (1977) 355–363. https://doi.org/10.1016/0040-6090(77)90137-7.
[180] R. Ishibashi, Y. Hayashi, H. Bo, T. Kondo, T. Hinoki, Radiation Effect in Ti-Cr Multilayer-Coated Silicon Carbide under Silicon Ion Irradiation up to 3 dpa, Coatings 12 (2022) 832. https://doi.org/10.3390/coatings12060832.
[181] M. Ohring, Materials science of thin films: deposition and structure, 2nd ed, Academic Press, San Diego, CA, 2002. https://doi.org/10.1016/B978-0-12-524975-1.X5000-9.
[182] J.A. Thornton, D.W. Hoffman, Stress-related effects in thin films, Thin Solid Films 171 (1989) 5–31. https://doi.org/10.1016/0040-6090(89)90030-8.
[183] R. Koch, The intrinsic stress of polycrystalline and epitaxial thin metal films, J. Phys.: Condens. Matter 6 (1994) 9519–9550. https://doi.org/10.1088/0953-8984/6/45/005.
[184] P. Chaudhari, Grain Growth and Stress Relief in Thin Films, Journal of Vacuum Science and Technology 9 (1972) 520–522. https://doi.org/10.1116/1.1316674.
[185] A. Misra, M. Nastasi, Limits of residual stress in Cr films sputter deposited on biased substrates, Appl. Phys. Lett. 75 (1999) 3123–3125. https://doi.org/10.1063/1.125251.
[186] E.J. Herrera-Jimenez, E. Bousser, T. Schmitt, J.E. Klemberg-Sapieha, L. Martinu, Effect of plasma interface treatment on the microstructure, residual stress profile, and mechanical properties of PVD TiN coatings on Ti-6Al-4V substrates, Surface and Coatings Technology 413 (2021) 127058. https://doi.org/10.1016/j.surfcoat.2021.127058.
[187] Ch. Genzel, W. Reimers, Some new aspects in X-ray stress analysis of thin layers, Surface and Coatings Technology 116–119 (1999) 404–409. https://doi.org/10.1016/S0257-8972(99)00235-2.
[188] M. Renzelli, M.Z. Mughal, M. Sebastiani, E. Bemporad, Design, fabrication and characterization of multilayer Cr-CrN thin coatings with tailored residual stress profiles, Materials & Design 112 (2016) 162–171. https://doi.org/10.1016/j.matdes.2016.09.058.
[189] Y. Katoh, T. Koyanagi, J.L. McDuffee, L.L. Snead, K. Yueh, Dimensional stability and anisotropy of SiC and SiC-based composites in transition swelling regime, Journal of Nuclear Materials 499 (2018) 471–479. https://doi.org/10.1016/j.jnucmat.2017.12.009.
[190] Corrosion of zirconium alloys in nuclear power plants, International Atomic Energy Agency, 1993.
[191] G. Sabol, R. Comstock, R. Weiner, P. Larouere, R. Stanutz, In-Reactor Corrosion Performance of ZIRLO™ and Zircaloy-4, in: A. Garde, E. Bradley (Eds.), Zirconium in the Nuclear Industry: Tenth International Symposium, ASTM International, 100 Barr Harbor

Drive, PO Box C700, West Conshohocken, PA 19428-2959, 1994: pp. 724-724–21. https://doi.org/10.1520/STP15217S.

[192] J.-C. Brachet, M. Le Saux, M. Le Flem, S. Urvoy, E. Rouesne, T. Guilbert, C. Cobac, F. Lahogue, J. Rousselot, M. Tupin, P. Billaud, C. Hossepied, F. Schuster, F. Lomello, A. Billard, G. Velisa, E. Monsifrot, J. Bischoff, A. Ambard, ON-GOING STUDIES AT CEA ON CHROMIUM COATED ZIRCONIUM BASED NUCLEAR FUEL CLADDINGS FOR ENHANCED ACCIDENT TOLERANT LWRS FUEL, in: 2015.

[193] J. Bischoff, C. Delafoy, C. Vauglin, P. Barberis, C. Roubeyrie, D. Perche, D. Duthoo, F. Schuster, J.-C. Brachet, E.W. Schweitzer, K. Nimishakavi, AREVA NP's enhanced accident-tolerant fuel developments: Focus on Cr-coated M5 cladding, Nuclear Engineering and Technology 50 (2018) 223–228. https://doi.org/10.1016/j.net.2017.12.004.

[194] D. Kim, H.-G. Lee, J.Y. Park, J.-Y. Park, W.-J. Kim, Effect of dissolved hydrogen on the corrosion behavior of chemically vapor deposited SiC in a simulated pressurized water reactor environment, Corrosion Science 98 (2015) 304–309. https://doi.org/10.1016/j.corsci.2015.05.031.

[195] M. Catti, G. Sandrone, G. Valerio, R. Dovesi, Electronic, magnetic and crystal structure of Cr2O3 by theoretical methods, Journal of Physics and Chemistry of Solids 57 (1996) 1735–1741. https://doi.org/10.1016/0022-3697(96)00034-0.

[196] R. Ishibashi, K. Ishida, T. Kondo, Y. Watanabe, Corrosion-resistant metallic coating on silicon carbide for use in high-temperature water, Journal of Nuclear Materials 557 (2021) 153214. https://doi.org/10.1016/j.jnucmat.2021.153214.

[197] A. Kadari, T. Schemme, D. Kadri, J. Wollschläger, XPS and morphological properties of Cr2O3 thin films grown by thermal evaporation method, Results in Physics 7 (2017) 3124–3129. https://doi.org/10.1016/j.rinp.2017.08.036.

[198] M.C. Biesinger, B.P. Payne, A.P. Grosvenor, L.W.M. Lau, A.R. Gerson, R.St.C. Smart, Resolving surface chemical states in XPS analysis of first row transition metals, oxides and hydroxides: Cr, Mn, Fe, Co and Ni, Applied Surface Science 257 (2011) 2717–2730. https://doi.org/10.1016/j.apsusc.2010.10.051.

[199] B.P. Payne, M.C. Biesinger, N.S. McIntyre, X-ray photoelectron spectroscopy studies of reactions on chromium metal and chromium oxide surfaces, Journal of Electron Spectroscopy and Related Phenomena 184 (2011) 29–37. https://doi.org/10.1016/j.elspec.2010.12.001.

[200] B.V. Crist, The XPS library website: A resource for the XPS community including - The XPS library of information, XPS spectra-base having >70,000 monochromatic XPS spectra, and spectral data processor (SDP) v8.0 software, Journal of Electron Spectroscopy and Related Phenomena 248 (2021) 147046. https://doi.org/10.1016/j.elspec.2021.147046.

[201] M.C. Biesinger, C. Brown, J.R. Mycroft, R.D. Davidson, N.S. McIntyre, X-ray photoelectron spectroscopy studies of chromium compounds, Surface and Interface Analysis 36 (2004) 1550–1563. https://doi.org/10.1002/sia.1983.

[202] V. Maurice, S. Cadot, P. Marcus, Hydroxylation of ultra-thin films of α-Cr2O3(0001) formed on Cr(110), Surface Science 471 (2001) 43–58. https://doi.org/10.1016/S0039-6028(00)00880-3.

[203] A. Machet, A. Galtayries, S. Zanna, L. Klein, V. Maurice, P. Jolivet, M. Foucault, P. Combrade, P. Scott, P. Marcus, XPS and STM study of the growth and structure of passive films in high temperature water on a nickel-base alloy, Electrochimica Acta 49 (2004) 3957–3964. https://doi.org/10.1016/j.electacta.2004.04.032.

[204] M.A. Henderson, S.A. Chambers, HREELS, TPD and XPS study of the interaction of water with the α-Cr2O3(001) surface, Surface Science 449 (2000) 135–150. https://doi.org/10.1016/S0039-6028(99)01246-7.

[205] L. Marchetti, F. Miserque, S. Perrin, M. Pijolat, XPS study of Ni-base alloys oxide films formed in primary conditions of pressurized water reactor, Surface and Interface Analysis 47 (2015) 632–642. https://doi.org/10.1002/sia.5757.

[206] M.C. Biesinger, B.P. Payne, L.W.M. Lau, A. Gerson, R.St.C. Smart, X-ray photoelectron spectroscopic chemical state quantification of mixed nickel metal, oxide and hydroxide systems, Surface and Interface Analysis 41 (2009) 324–332. https://doi.org/10.1002/sia.3026.

[207] Z. Duan, F. Arjmand, L. Zhang, F. Meng, H. Abe, Electrochemical and XPS investigation of the corrosion behavior of Alloy 690 at high-temperature water, J Solid State Electrochem 19 (2015) 2265–2273. https://doi.org/10.1007/s10008-015-2856-1.

[208] W. Mader, H.F. Fischmeister, E. Bergmann, Defect structure of ion-plated titanium nitride coatings, Thin Solid Films 182 (1989) 141–152. https://doi.org/10.1016/0040-6090(89)90251-4.

[209] G. Håkansson, J.-E. Sundgren, D. McIntyre, J.E. Greene, W.-D. Münz, Microstructure and physical properties of polycrystalline metastable Ti0.5Al0.5N alloys grown by d.c. magnetron sputter deposition, Thin Solid Films 153 (1987) 55–65. https://doi.org/10.1016/0040-6090(87)90169-6.

[210] L. Jiang, P. Xiu, Y. Yan, C. Lu, M. Huang, T. Liu, C. Ye, H. Sun, R. Shu, L. Wang, Effects of ion irradiation on chromium coatings of various thicknesses on a zirconium alloy, Journal of Nuclear Materials 526 (2019) 151740. https://doi.org/10.1016/j.jnucmat.2019.151740.

[211] Z. Sun, Y. Li, X. Qiu, D. Sun, P. Du, R. Zhang, Y. Xin, G. Ran, An in-situ TEM investigation of microstructure evolution in Cr-coated zirconium alloy under heavy ion irradiation: Simultaneous evolution of both Cr coating and Zr-4 matrix, Nuclear Instruments and Methods in Physics Research Section B: Beam Interactions with Materials and Atoms 536 (2023) 97–103. https://doi.org/10.1016/j.nimb.2023.01.002.

[212] X. Yi, M.L. Jenkins, M.A. Kirk, Z. Zhou, S.G. Roberts, In-situ TEM studies of 150 keV W+ ion irradiated W and W-alloys: Damage production and microstructural evolution, Acta Materialia 112 (2016) 105–120. https://doi.org/10.1016/j.actamat.2016.03.051.

[213] B. Yao, D.J. Edwards, R.J. Kurtz, TEM characterization of dislocation loops in irradiated bcc Fe-based steels, Journal of Nuclear Materials 434 (2013) 402–410. https://doi.org/10.1016/j.jnucmat.2012.12.002.

[214] J. Gao, K. Yabuuchi, A. Kimura, Characterization of ordered dislocation loop raft in Fe3+ irradiated pure iron at 300 °C, Journal of Nuclear Materials 511 (2018) 304–311. https://doi.org/10.1016/j.jnucmat.2018.09.020.

[215] M.L. Jenkins, Z. Yao, M. Hernández-Mayoral, M.A. Kirk, Dynamic observations of heavy-ion damage in Fe and Fe–Cr alloys, Journal of Nuclear Materials 389 (2009) 197–202. https://doi.org/10.1016/j.jnucmat.2009.02.003.

[216] O. El-Atwani, E. Aydogan, E. Esquivel, M. Efe, Y.Q. Wang, S.A. Maloy, Detailed transmission electron microscopy study on the mechanism of dislocation loop rafting in tungsten, Acta Materialia 147 (2018) 277–283. https://doi.org/10.1016/j.actamat.2018.01.003.

[217] K.A. Smith, A.I. Savva, Y. Wu, D.A. Tenne, D.P. Butt, H. Xiong, J.P. Wharry, Effects of intermediate energy heavy-ion irradiation on the microstructure of rutile TiO_2 single crystal, J Am Ceram Soc 101 (2018) 4357–4366. https://doi.org/10.1111/jace.15576.

[218] X. Zhang, K. Hattar, Y. Chen, L. Shao, J. Li, C. Sun, K. Yu, N. Li, M.L. Taheri, H. Wang, J. Wang, M. Nastasi, Radiation damage in nanostructured materials, Progress in Materials Science 96 (2018) 217–321. https://doi.org/10.1016/j.pmatsci.2018.03.002.

[219] M. Wen, N.M. Ghoniem *, B.N. Singh, Dislocation decoration and raft formation in irradiated materials, Philosophical Magazine 85 (2005) 2561–2580. https://doi.org/10.1080/14786430500154281.

[220] S.L. Dudarev, K. Arakawa, X. Yi, Z. Yao, M.L. Jenkins, M.R. Gilbert, P.M. Derlet, Spatial ordering of nano-dislocation loops in ion-irradiated materials, Journal of Nuclear Materials 455 (2014) 16–20. https://doi.org/10.1016/j.jnucmat.2014.02.032.

[221] A. Gabriel, L. Hawkins, A. French, Y. Li, Z. Hu, L. He, P. Xiu, M. Nastasi, Frank.A. Garner, L. Shao, Effect of dpa rate on the temperature regime of void swelling in ion-irradiated pure chromium, Journal of Nuclear Materials 561 (2022) 153519. https://doi.org/10.1016/j.jnucmat.2022.153519.

[222] K. Quillin, H. Yeom, X. Pu, D. Frazer, K.N. Sasidhar, K. Sridharan, Effects of elevated temperature exposure on the residual stress state and microstructure of PVD Cr coatings on SiC investigated via in situ X-ray diffraction and transmission electron microscopy, Materials Science and Engineering: A 879 (2023) 145273. https://doi.org/10.1016/j.msea.2023.145273.

[223] P.W. Pellegrini, B.C. Giessen, J.M. Feldman, A Survey of the Cr-Rich Area of the Cr-Si-C Phase Diagram, J. Electrochem. Soc. 119 (1972) 535. https://doi.org/10.1149/1.2404246.

[224] Z. Nishiyama, Martensitic Transformation, Academic Press, New York, 1978.

[225] H.I. Aaronson, M. Enomoto, J.K. Lee, Mechanisms of diffusional phase transformations in metals and alloys, CRC Press, Boca Raton, 2010.

[226] G. Kresse, J. Furthmüller, Efficient iterative schemes for ab initio total-energy calculations using a plane-wave basis set, Phys. Rev. B 54 (1996) 11169–11186. https://doi.org/10.1103/PhysRevB.54.11169.

[227] G. Kresse, D. Joubert, From ultrasoft pseudopotentials to the projector augmented-wave method, Phys. Rev. B 59 (1999) 1758–1775. https://doi.org/10.1103/PhysRevB.59.1758.

[228] J.P. Perdew, K. Burke, M. Ernzerhof, Generalized Gradient Approximation Made Simple, Phys. Rev. Lett. 77 (1996) 3865–3868. https://doi.org/10.1103/PhysRevLett.77.3865.

[229] H.J. Monkhorst, J.D. Pack, Special points for Brillouin-zone integrations, Phys. Rev. B 13 (1976) 5188–5192. https://doi.org/10.1103/PhysRevB.13.5188.

[230] D. Shrader, S.M. Khalil, T. Gerczak, T.R. Allen, A.J. Heim, I. Szlufarska, D. Morgan, Ag diffusion in cubic silicon carbide, Journal of Nuclear Materials 408 (2011) 257–271. https://doi.org/10.1016/j.jnucmat.2010.10.088.

[231] F. Gao, W.J. Weber, Empirical potential approach for defect properties in 3C-SiC, Nuclear Instruments and Methods in Physics Research Section B: Beam Interactions with Materials and Atoms 191 (2002) 504–508. https://doi.org/10.1016/S0168-583X(02)00600-6.

[232] D. Nguyen-Manh, A.P. Horsfield, S.L. Dudarev, Self-interstitial atom defects in bcc transition metals: Group-specific trends, Phys. Rev. B 73 (2006) 020101. https://doi.org/10.1103/PhysRevB.73.020101.

[233] X. Wang, H. Zhang, T. Baba, H. Jiang, C. Liu, Y. Guan, O. Elleuch, T. Kuech, D. Morgan, J.-C. Idrobo, P.M. Voyles, I. Szlufarska, Radiation-induced segregation in a ceramic, Nat. Mater. 19 (2020) 992–998. https://doi.org/10.1038/s41563-020-0683-y.

[234] C.A. Hirst, F. Granberg, B. Kombaiah, P. Cao, S. Middlemas, R.S. Kemp, J. Li, K. Nordlund, M.P. Short, Revealing hidden defects through stored energy measurements of

radiation damage, Science Advances 8 (2022) eabn2733. https://doi.org/10.1126/sciadv.abn2733.
[235] I.-T. Lu, M. Bernardi, Using defects to store energy in materials – a computational study, Sci Rep 7 (2017) 3403. https://doi.org/10.1038/s41598-017-01434-8.
[236] L.L. Snead, Y. Katoh, T. Koyanagi, K. Terrani, Stored energy release in neutron irradiated silicon carbide, Journal of Nuclear Materials 514 (2019) 181–188. https://doi.org/10.1016/j.jnucmat.2018.12.005.
[237] J. Du, Y. Huang, J. Liu, Y. Liu, Z. Wang, Irradiation damage alloying for immiscible alloy systems and its thermodynamic origin, Materials & Design 170 (2019) 107699. https://doi.org/10.1016/j.matdes.2019.107699.
[238] M. Palumbo, L. Battezzati, Thermodynamics and kinetics of metallic amorphous phases in the framework of the CALPHAD approach, Calphad 32 (2008) 295–314. https://doi.org/10.1016/j.calphad.2007.12.002.
[239] W.H. Wang, C. Dong, C.H. Shek, Bulk metallic glasses, Materials Science and Engineering: R: Reports 44 (2004) 45–89. https://doi.org/10.1016/j.mser.2004.03.001.
[240] A. Takeuchi, A. Inoue, Classification of Bulk Metallic Glasses by Atomic Size Difference, Heat of Mixing and Period of Constituent Elements and Its Application to Characterization of the Main Alloying Element, Mater. Trans. 46 (2005) 2817–2829. https://doi.org/10.2320/matertrans.46.2817.
[241] X. Yu, A. Gulec, Q. Sherman, K.L. Cwalina, J.R. Scully, J.H. Perepezko, P.W. Voorhees, L.D. Marks, Nonequilibrium Solute Capture in Passivating Oxide Films, Phys. Rev. Lett. 121 (2018) 145701. https://doi.org/10.1103/PhysRevLett.121.145701.
[242] K.N. Sasidhar, X. Zhou, M. Rohwerder, D. Ponge, On the phase transformation pathway during localized grain boundary oxidation in an Fe-10 at% Cr alloy at 200°C, Corrosion Science 214 (2023) 111016. https://doi.org/10.1016/j.corsci.2023.111016.
[243] D.A. Porter, K.E. Easterling, M.Y. Sherif, Phase transformations in metals and alloys, Third edition, CRC Press, Boca Raton, Fla., 2009.
[244] R. Wang, B. Li, P. Li, X. Bai, L. Hu, Q. Huang, J. Xu, F. Huang, F. Ge, Effect of low-dose Xe20+ ion irradiation on the deformation behavior of the magnetron sputtered Cr coatings under nanoindentation, Surface and Coatings Technology 428 (2021) 127907. https://doi.org/10.1016/j.surfcoat.2021.127907.
[245] J. Kabel, T. Koyanagi, Y. Katoh, R. Schoell, D. Kaoumi, C. Ang, P. Hosemann, Interface characterization of candidate dual-purpose barrier coatings for SiC/SiC accident tolerant fuel cladding, in: 2019: pp. 1043–1051. https://www.scopus.com/inward/record.uri?eid=2-s2.0-85080034549&partnerID=40&md5=8c4a6557fcb0ac5fd0ac126117b642c7.
[246] J. Schaufler, C. Schmid, K. Durst, M. Göken, Determination of the interfacial strength and fracture toughness of a-C:H coatings by in-situ microcantilever bending, Thin Solid Films 522 (2012) 480–484. https://doi.org/10.1016/j.tsf.2012.08.031.
[247] A. Riedl, R. Daniel, M. Stefenelli, T. Schöberl, O. Kolednik, C. Mitterer, J. Keckes, A novel approach for determining fracture toughness of hard coatings on the micrometer scale, Scripta Materialia 67 (2012) 708–711. https://doi.org/10.1016/j.scriptamat.2012.06.034.
[248] D. Di Maio, S.G. Roberts, Measuring fracture toughness of coatings using focused-ion-beam-machined microbeams, Journal of Materials Research 20 (2005) 299–302. https://doi.org/10.1557/JMR.2005.0048.

[249] D. Frazer, B. Shaffer, P. Peralta, P. Hosemann, In-Situ Transmission Electron Microscopy Microcantilever and Nanoindentation Testing of UO2, JOM 72 (2020) 3028–3036. https://doi.org/10.1007/s11837-020-04102-x.

[250] Y.Q. Wang, R. Fritz, D. Kiener, J.Y. Zhang, G. Liu, O. Kolednik, R. Pippan, J. Sun, Fracture behavior and deformation mechanisms in nanolaminated crystalline/amorphous micro-cantilevers, Acta Materialia 180 (2019) 73–83. https://doi.org/10.1016/j.actamat.2019.09.002.

[251] J.J. Lewandowski, M. Shazly, A. Shamimi Nouri, Intrinsic and extrinsic toughening of metallic glasses, Scripta Materialia 54 (2006) 337–341. https://doi.org/10.1016/j.scriptamat.2005.10.010.

Appendices

Appendix A: Initial investigations of other coating technologies and materials

During the initial stages of the project, a variety of coating deposition and surface modification technologies were investigated for feasibility. This work is briefly outlined below.

Cold Spray Materials Deposition: Cold spray deposition is a solid-state coating deposition process wherein feedstock powder is accelerated supersonic velocity on to the surface of a substrate where upon impact it deforms at high strain rates to forms a continuous coating. Coating adhesion to the substrate occurs by both mechanical interlocking and metallurgical bonding. The propulsion of the powder occurs by a heated and pressurized carrier gas (typically N_2 or He). The powder particles experience severe plastic deformation upon impact with the substrate and form a coating adhered through mechanical interlocking and metallurgical bonding. The cold spray process enables the properties of the feedstock powder to be maintained in the coating, allows for high deposition rates, limits oxidation during deposition, and can be performed under ambient conditions. A schematic illustration of the cold spray deposition process is shown in Figure A1a.

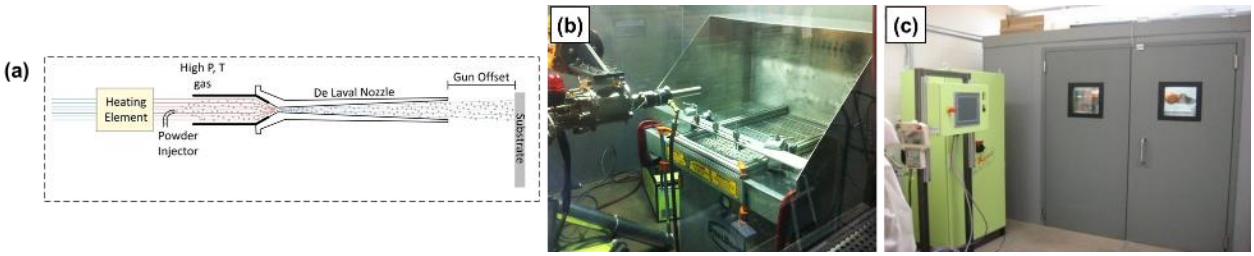

Figure A1: (a) Schematic diagram of the cold spray process; Photographs of the (b) cold spray gun and (c) sound-isolating spray booth located at the University of Wisconsin-Madison.

The University of Wisconsin-Madison is equipped with a commercial-scale Cold Gas Technologies (CGT) Kinetiks 4000/34 cold spray system. The cold spray gun (Figure A1b) is manipulated by a six-axis robotic arm and programming system to deposit coatings on flat and cylindrical samples. The system is housed in a sound-isolating booth, shown in Figure A1c.

Control of many process variables, including the gas temperature, pressure, composition (N_2/He ratio), and gun traverse speed is possible through user inputs in the system interface.

Cold spray deposition of various pure metals and alloys, such as Cr, Nb, FeCrAl, and Al6061 on CVD SiC substrates was performed for corrosion resistance in the earlier phases of this research. Representative SEM images of the sample surface after cold spray deposition are shown in Figure A2. Regardless of coating material, a cohesive coating could not be deposited as a consequence of the high hardness and low deformability of the CVD SiC substrate. After the spray process, the uncoated areas of the SiC exhibited evidence of brittle fracture, indicating damage of the substrate caused by the high-velocity impingement of the particles. Areas can also be seen where it appears that a particle was partially bonded to the substrate and was then knocked off by subsequent particle impacts, as can be seen in Figure A2b.

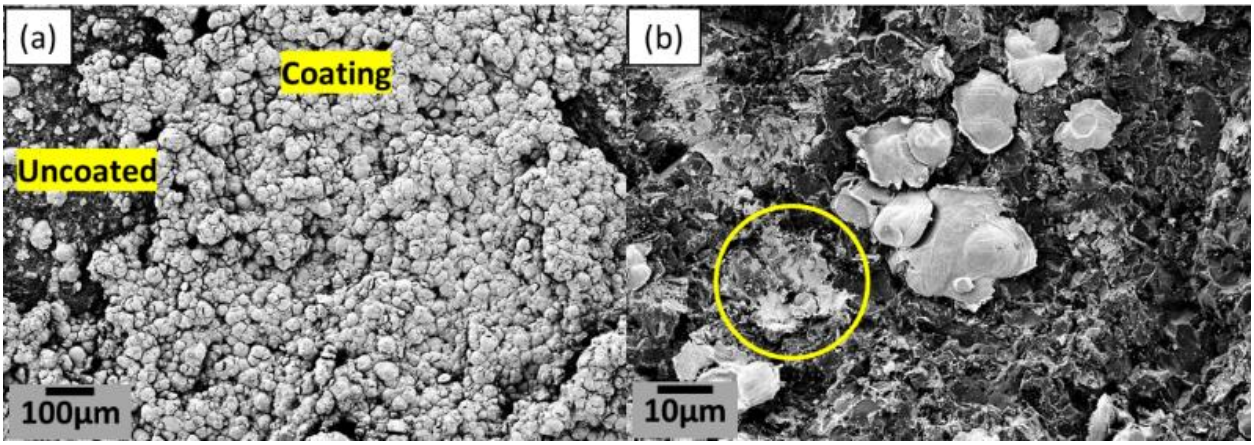

Figure A2: Plan-view SEM images showing (a) surface after cold spray deposition of a FeCrAl alloy and (b) bonded particles and area of particle de-bonding.

*Thermal Diffusion Coating:*_In partnership with a commercial vendor, a chromizing thermal diffusion treatment was performed. The process is analogous to carburizing where a sample is placed in a pack of carbon-bearing precursor material which then diffuses into the surface, but in this treatment investigated, chromium was the diffusing species. The chromizing treatment was

conducted at 950 °C for 12 hours in a pack of Cr powder along with Al_2O_3 and NH_4Cl fillers (process activators).

Figure A3 shows images of a chromized SiC sample. The chromized samples' surfaces were brittle so that the edges were chipped even during handling. SEM of the sample surface revealed that a new layer has formed on the surface of the SiC, which is likely a Cr-carbide formed from the reaction of SiC with the diffusing Cr. XRD results also demonstrated the formation of a Cr-carbide layer in the near-surface region. Because of the low quality of the resulting samples, the chromizing process was not pursued further.

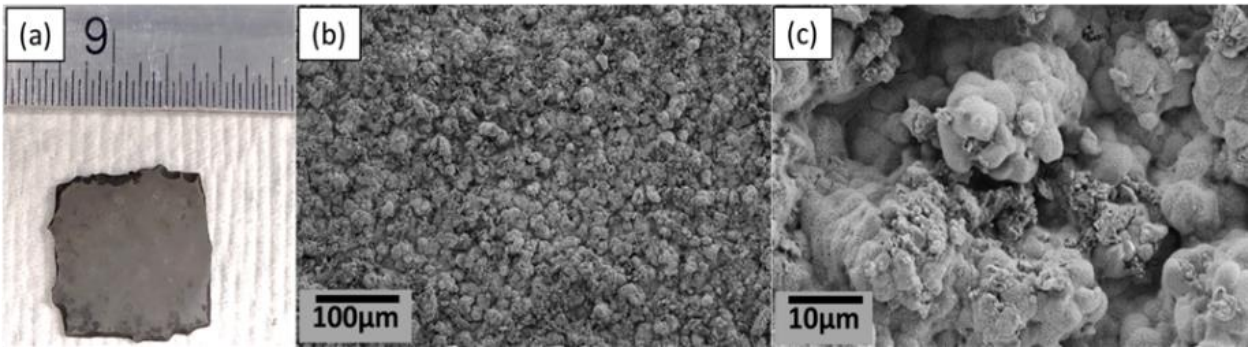

Figure A3: (a) Photograph of a CVD SiC coupon after chromizing treatment; (b) Low magnification and (c) high magnification plan-view SEM images of the chromized CVD SiC.

Cathodic Arc Deposition: Cathodic arc deposition of pure Cr coatings on CVD SiC substrates was performed also in collaboration with a commercial vendor. Cathodic arc deposition is a vacuum-based plasma deposition process within the larger family of physical vapor deposition (PVD) processes. In the cathodic arc process, an electric arc is struck on the metallic target, vaporizing target atoms. Images of the cathodic arc Cr coatings are shown in Figure A4. The coating has a dense, compacted microstructure; however, the coating thickness was only 500 nm. The preferred coating thickness would be around 5 µm to avoid any inhomogeneities or substrate effects. The cathodic arc coating microstructure also contained macroparticles, which are artifacts of the

deposition process that form when localized melting of the target material occurs creating microscale liquid droplets that condense as distinct particles in the coating.

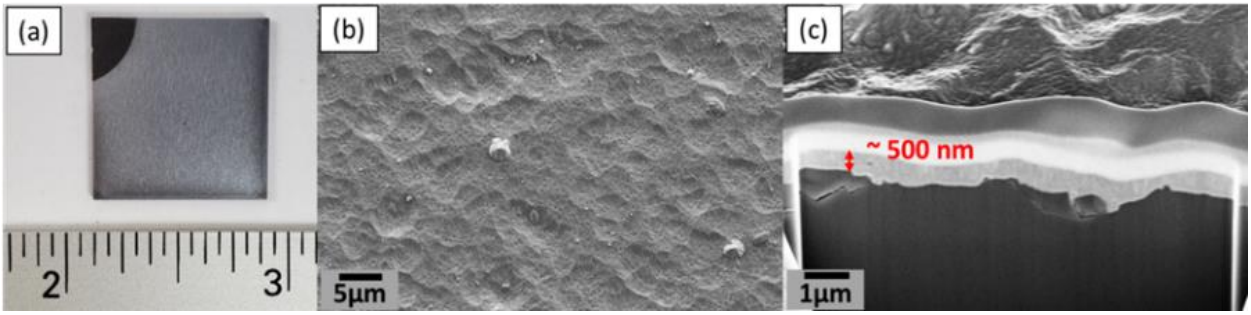

Figure A4: (a) Photograph, (b) plan-view SEM image, and (c) cross-sectional SEM image of the as-deposited cathodic arc Cr coating.

Application of the cathodic arc process to deposit Cr-carbide coatings by flowing methane gas through the vacuum chamber during deposition was also investigated. The coating microstructure appeared dense, and similar to the pure Cr coatings, and macroparticle features were observed on the coating surface, as shown in Figure A5a. Upon cross-sectional observation, an unexpected dual-layer structure was observed, as shown in Figure A5b. After consulting with the supplier, it was determined that a CrN adhesion interlayer layer was deposited on the SiC substrate prior to depositing Cr-carbide, resulting in a dual layered coating. Both the Cr-carbide layer and the CrN adhesion layer were 1.5–2 µm thick.

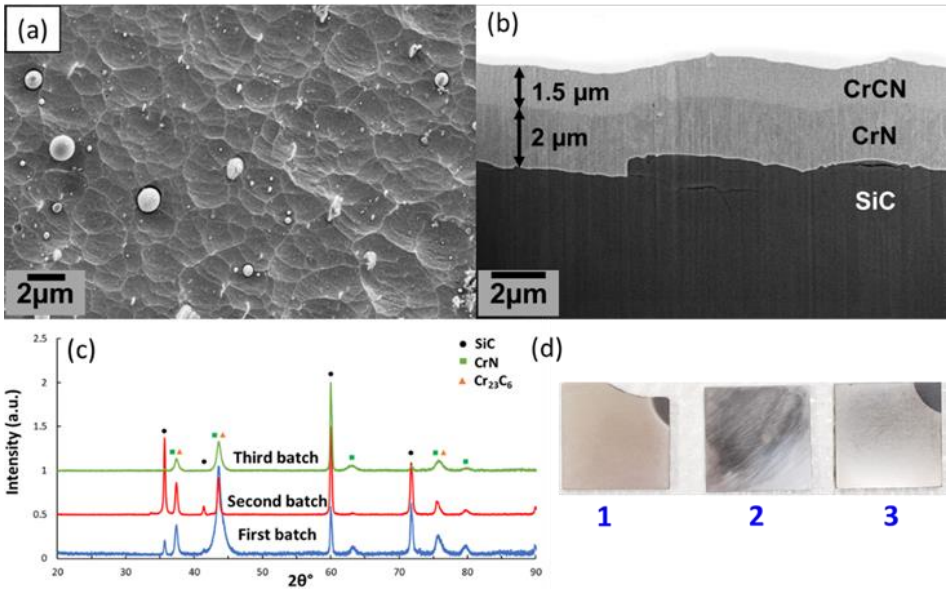

Figure A5: (a) Plan-view SEM image and (b) FIB cross-sectional SEM image for the first batch of PVD Cr-carbonitride coating, (c) XRD pattern of three batches, and (d) as-received samples from the three batches.

Three batches of samples were prepared in collaboration with Vendor III. Some differences were observed between the batches during characterization. For example, cross-sectional imaging indicated different microstructures between the three batches. XPS was used to the composition of the coatings. The first batch of samples was determined to be a Cr-carbonitride compound rather than Cr-carbide. The second batch was essentially a pure CrN coating, and the third batch was again a Cr-carbonitride compound. The compositions of the three batches are shown in Table A1. Clearly, the stoichiometry of the coatings was vastly different. These differences were also manifested in the XRD patterns and in visual inspections, as shown in Figure A5c and d. On account of the good adhesion and seemingly high density, select Cr-carbide coatings were subjected to static water corrosion tests, detailed in Chapter 7.

Table A1: Composition of three batches of Cr-carbide coatings (in atomic percent) deposited in collaboration with Vendor III, as determined by XPS.

	Batch 1	Batch 2	Batch 3
Cr	44.85	48.81	43.76
N	22.47	48.33	33.52
C	32.67	2.87	22.72

Magnetron Sputtering: In the initial stages of the project, coating materials other than pure Cr were deposited in collaboration with Vendor I. The HiPIMS process was used to deposit pure Zr and CrN coatings. As shown in Figure A6, both coatings have the dense microstructure similar to those observed in the HiPIMS Cr coating which was one of the main focus areas of this research. The as-received CrN samples exhibited areas of coating spallation likely due to coefficients of thermal expansion (CTE) mismatch or excessive compressive stress in the coating. Due to this defect, the CrN samples were not subjected to further testing. The Zr coating was dense and fully adhered but performed poorly in corrosion tests.

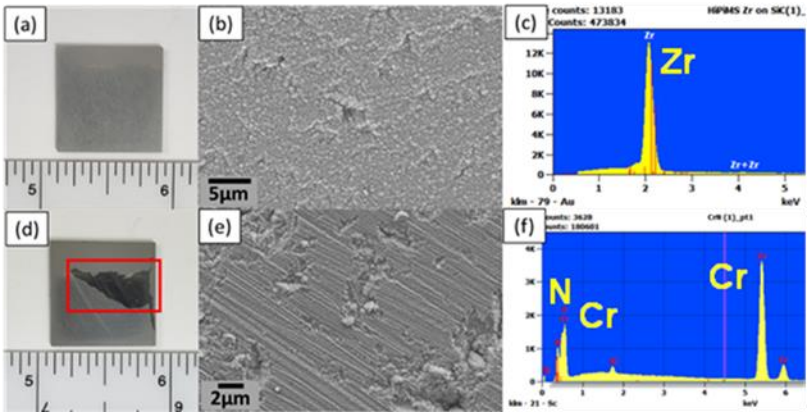

Figure A6: (a) As-received HiPIMS Zr coating, (b) plan-view SEM image, (c) EDS spectrum, (d) As-received HiPIMS CrN coating with spallation area highlighted, (e) plan-view SEM image, (f) EDS spectrum.

The HiPIMS Zr coating was exposed in the static water autoclave (described in Section 7.1). After the first three-day interval of the corrosion test, it was found that the coating had been

completely consumed, as manifested by large weight loss (about 100 times larger than any of the other coatings). There was also a white, powder-like buildup in the autoclave chamber upon completion of the test. In SEM examination, it was determined that the HiPIMS Zr coating completely delaminated from the SiC substrate, as shown in Figure A7. EDS elemental maps showed large areas of exposed SiC and localized areas of ZrO_2. The powder-like buildup was also confirmed to be ZrO_2 via XRD. The corrosion performance of the Zr potentially could be improved by adding alloying elements to form a coating with a composition similar to the Zr-alloys commonly used as LWR fuel cladding. The large mismatch in CTE between Zr and SiC may have also played a role in coating failure.

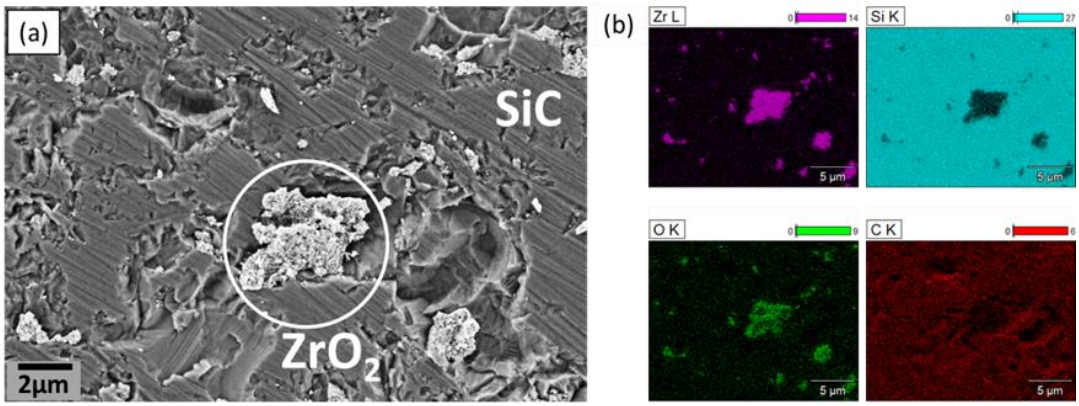

Figure A7: (a) SEM image of HiPIMS Zr surface after 72 hours of autoclave exposure; (b) EDS mapping showing localized presence of ZrO_2.

Hydrothermal Corrosion Tests: The cathodic arc (CA) Cr-carbide and pure Cr coatings were tested in the static water autoclave at 360 °C and 18.6 MPa for 12 days and 15 days, respectively. The weight change data for the CA Cr-carbide and Cr samples is shown in Figure A8 along with those of S-DCMS and HiPIMS Cr coatings. The performance of the PVD Cr-carbide coating was not conclusive based on the large variations between samples of the same batch. One sample consistently lost weight during the autoclave test, while another sample showed essentially no weight change, which is the cause for the large error bars seen in Figure A8. In general, the use of

a ceramic coating material, such as Cr-carbide, does not seem to a be desirable choice due to their limited ductility. The CA Cr coatings performed well in the 15-day autoclave test. There were no indications of loss of adhesion. There was a slight visible color change, similar to that of the HiPIMS Cr coating. However, due to the low thickness of the coating, no further testing on the CA Cr samples was performed.

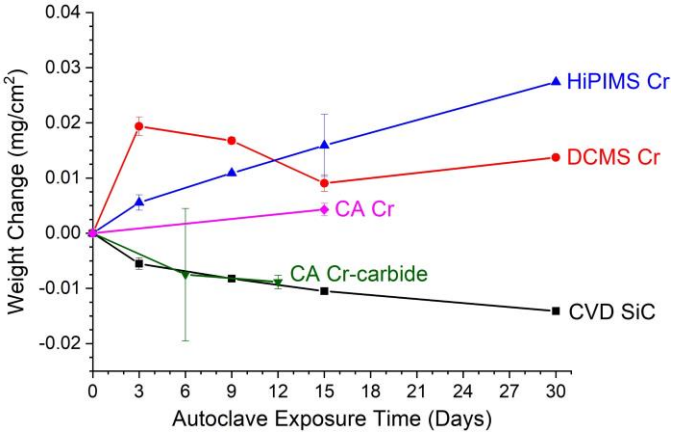

Figure A8: Weight change plot for the S-DCMS Cr, HiPIMS Cr, CA Cr, and CA Cr-carbonitride coatings along with uncoated CVD SiC control samples. The S-DCMS Cr and HiPIMS Cr coatings were tested for 30 days. The CA Cr coating was tested for 15 days in the water autoclave, and the CA Cr-carbide coating was tested for 12 days.

Appendix B: Oxygenated flow loop corrosion experiment

A hydrothermal corrosion experiment was conducted under oxygenated conditions to accelerate corrosion reactions and observe how SiC and Cr-coated samples respond under a different set of conditions than the static autoclave tests. The test was performed for seven days at 360 °C with 2 ppm dissolved oxygen content and with no other chemical additives. The samples included in the flow loop test were uncoated SiC, bulk Cr, as-deposited PI-DCMS Cr, and ion irradiated PI-DCMS Cr (irradiation details provided in Appendix D).

After the seven-day test, the uncoated SiC and all Cr samples exhibited a large weight loss. Upon visual examination of the samples, it was clear that both the as-deposited and ion irradiated Cr coatings had been completely consumed during the test. Nevertheless, SEM characterization of the exposed samples shown in Figure B1 revealed a few interesting and importnat findings. First, significant preferential attack along the grain boundaries was observed in the uncoated SiC samples, which is expected due to the high dissolved oxygen content in the water. The bulk Cr also showed signs of dissolution and material loss rather than passivation. The SEM imaging confirmed that the as-deposited and irradiated Cr coatings had been consumed during the test, leaving behind only the bare SiC substrate. Additionally, Cr_2O_3 particles were observed on the surface of the samples after the test. These particles likely formed on the surface of the samples during cooling of the system when Cr that had dissolved in the coolant precipitated out. The composition of the particles was confirmed using EDS. Other work has also shown that Cr dissolves in highly oxygenated water rather than forming a passivating oxide, a result that is also corroborated by the Pourbaix diagram of Cr [13,196].

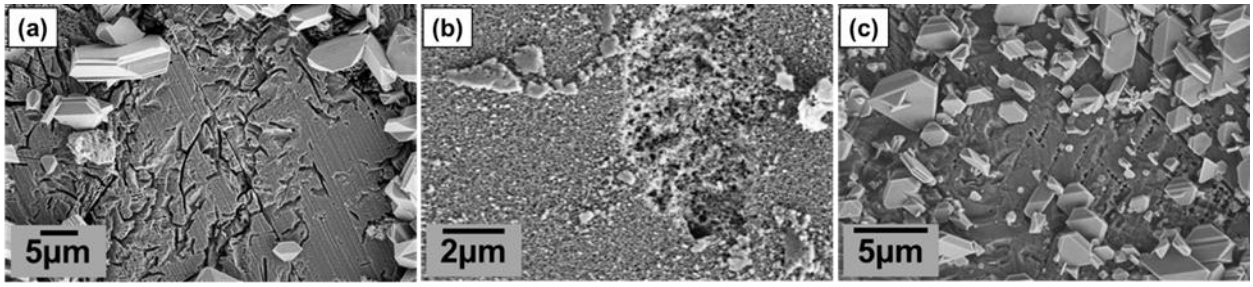

Figure B1: SEM images of (a) uncoated SiC, (b) bulk Cr, and (c) Cr-coated SiC after the seven-day flow loop experiment in oxygenated conditions.

Appendix C: Water radiolysis corrosion experiment

A water radiolysis corrosion experiment was designed through collaboration between the University of Wisconsin-Madison and Argonne National Laboratory (ANL). Water radiolysis in the reactor core can potentially accelerate corrosion reactions through the generation of corrosive species, such as hydrogen peroxide and oxygen radicals. The experiment was designed to employ the Van de Graaff accelerator at the Low Energy Accelerator Facility (LEAF) at ANL to produce the water radiolysis conditions. A custom sample capsule was designed for installation in the Van de Graaff beamline. The effects of water radiolysis on the corrosion kinetics and corrosion product chemistry on uncoated monolithic CVD SiC and Cr-coated SiC samples were planned to be investigated.

Ti-6Al-4V was selected as the sample capsule material based on its passivation characteristics when in contact with high temperature water and good mechanical strength at elevated temperatures. The capsule was a cylinder about 13 mm in diameter and 75 mm in length with a hemispherical cap at one end. The test specimen measuring 8 mm × 10 mm × 1 mm would rest at the bottom of the capsule during the test. The remainder of the test apparatus was fabricated from 316 stainless steel and included space to allow for the recombination of hydrogen gas generated during the experiment. Figure C1 shows the design of the experimental apparatus and its installation in the Van de Graaff beamline at ANL. The electron beam would pass through the capsule and water before impinging on the sample in the center of the capsule. A simulation was conducted to calculate the energy deposition from the electron beam via interaction with the capsule, water, and sample and is shown in Figure C2. Initial testing of the water radiolysis system was completed at ANL to confirm that the operation of the system is satisfactory. A set of corrosion tests was planned to investigate the effect of water radiolysis on the corrosion behavior of uncoated

and Cr-coated CVD SiC. The Cr coating selected for this experiment was the B-HiPIMS coating. Corrosion was to be monitored using a range of post corrosion characterization approaches including SEM, XPS, and profilometry. Unfortunately, the experiment could not be completed due to time constraints.

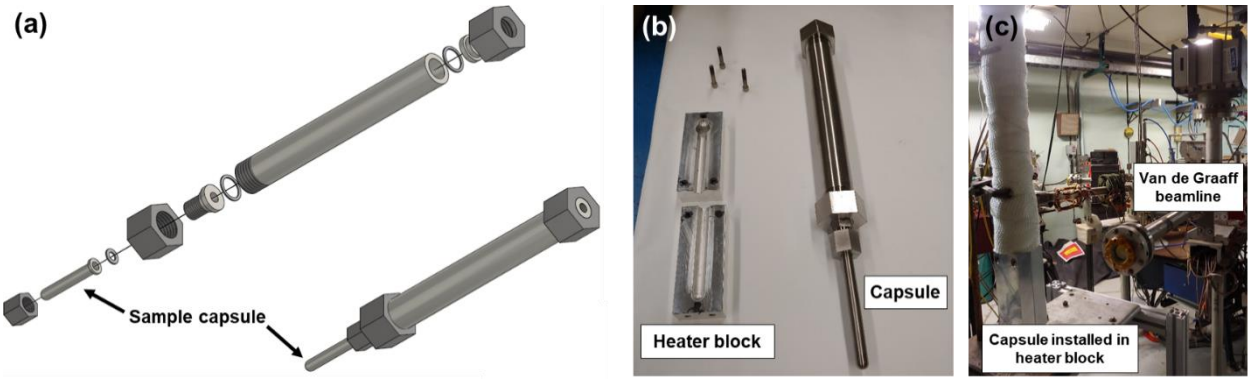

Figure C1: (a) CAD drawing of the test apparatus with sample capsule and overhead pipe allowing space for hydrogen gas recombination; (b) Photograph of the assembled test apparatus and heater block; (c) Test apparatus installed in the heater block at the Van de Graaf beamline at ANL.

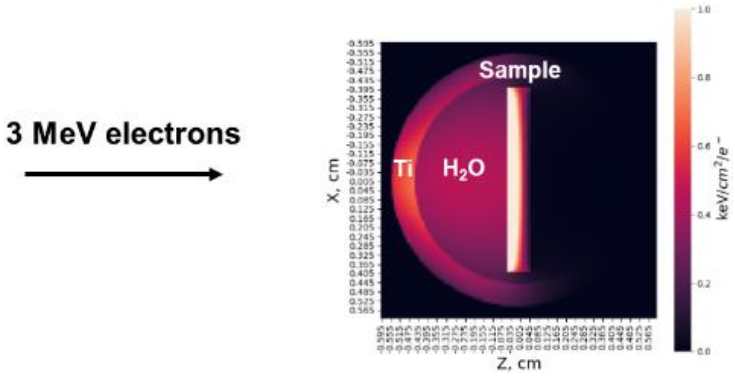

Figure C2: Simulation showing the energy deposition from 3 MeV electron irradiation of the Ti capsule, water, and sample.

Appendix D: Other irradiation experiments

To generate radiation damage in the near-surface region of a Cr coating, heavy ion irradiation was performed at the University of Wisconsin Ion Beam Laboratory. Three PI-DCMS Cr coatings were irradiated at 350 °C with 3.7 MeV Ni ions to a peak dose of 75 dpa. Figure D1a shows the damage profile produced in pure Cr by 3.7 MeV Ni irradiation. Photographs of the PI-DCMS Cr coatings samples before and after irradiation are shown in Figure D1b and c. After irradiation, localized areas on each coating sample were observed to have buckled. The buckling may be a consequence of thermal spikes during irradiation combined with insufficient adhesion strength of the coating. Nevertheless, the ion irradiated coatings were included in a corrosion experiment conducted in a chemistry-controlled flow loop, detailed in Appendix B.

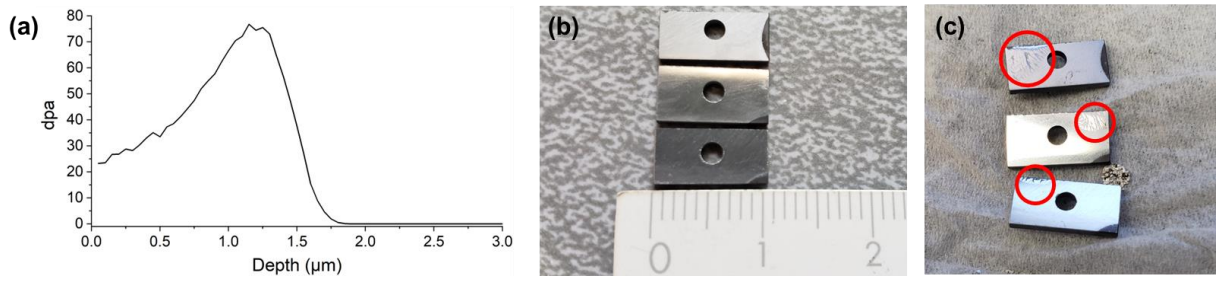

Figure D1: (a) Damage profile of 3.7 MeV Ni ions in Cr calculated using SRIM 2013 for a fluence of 7.5×1016 ions/cm^2; Photographs of PI-DCMS Cr coating samples (b) before and (c) after ion irradiation. Areas of buckling within the coating are circled.

Neutron irradiation of Cr-coated SiC samples was performed in High Flux Isotope Reactor (HFIR) in collaboration with Oak Ridge National Laboratory (ORNL). The PI-DCMS coating was selected for this irradiation based on its highly densest microstructure compared to the coating types that were being investigated at the time of the experiment. An image of the samples sent to ORNL is shown in Figure D2a. Neutron irradiation was conducted at 300 °C to a dose of 2 dpa (in SiC). However, plan-view optical microscopy and cross-sectional SEM images of the irradiated PI-DCMS coating revealed regions of micro-cracking and interfacial debonding, as shown in

Figure D2b and c. Similar to the results of the static water corrosion test, it is likely the debonding occurred due to thermal stresses and poor adhesion strength of the coating. It is anticipated that a coating with very strong adhesion, such as the B-HiPIMS coating, would have demonstrated better performance under neutron irradiation, but these coatings were in their early stages of development to avail of the opportunity for this neutron irradiation campaign.

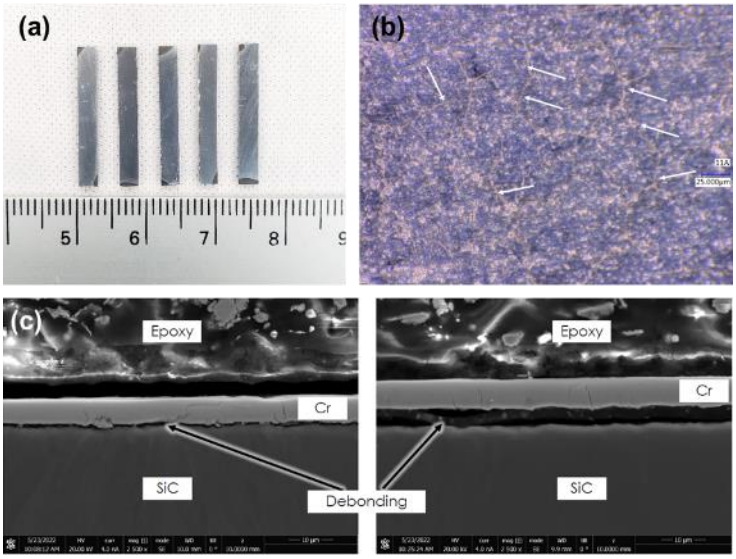

Figure D2: (a) Photograph of PI-DCMS Cr coating samples sent to Oak Ridge National Laboratory for neutron irradiation in the High Flux Isotope Reactor; (b) Plan-view SEM images and (c) cross-sectional SEM images of the PI-DCMS after neutron irradiation. Arrows indicated the presence of micro-cracking or debonding.

Appendix E: Error analysis of residual stress data

The processing and error analysis of the data collected for residual stress measurements using the $\sin^2\psi$ technique is briefly described in this section. Based on the experimental method used in this work, eight XRD scans of the Cr (211) peak at 2θ = 81.7° (nominal peak location at room temperature) performed across a range of ψ-tilts are needed to acquire a single residual stress measurement. An example of the raw data used for the residual stress measurement is shown Figure E1a. To extract peak parameters such as peak location, width, and area, a pseudo-Voigt function was fit to the raw peaks and is shown in Figure E1b. Each fitting parameter has an associated standard error value originating from the numerical fitting algorithm. Using the peak location (the parameter of interest for the residual stress calculation) as an example, the fitting process will output a value for the peak location as follows: 81.30046° ± 0.01886°, which is the fitted 2θ peak location and corresponding uncertainty.

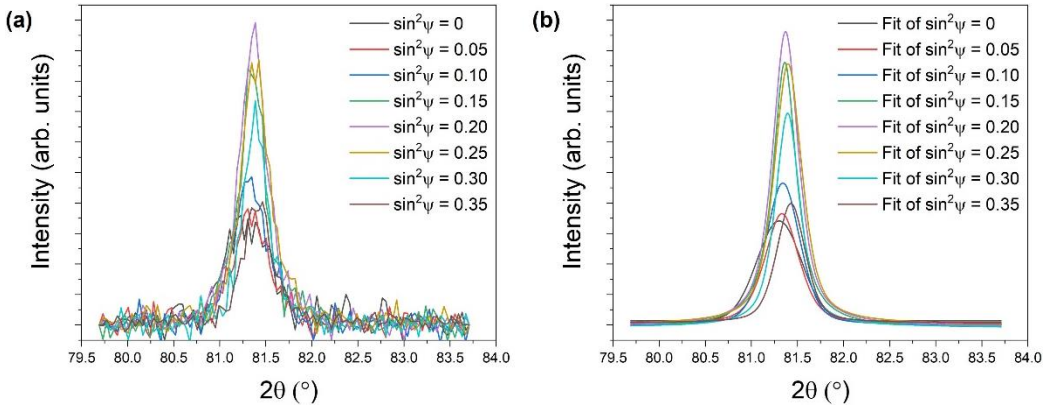

Figure E1: (a) Raw diffraction peaks collected at different ψ-tilts for the residual stress measurement; (b) Pseudo-Voigt fitting of the same peaks shown in (a) to extract peak parameters.

Because the residual stress calculation relies on the relationship between the interplanar d-spacing and $\sin^2\psi$, the peak location values determined from peak fitting are converted to a d-spacing value using Bragg's Law:

$$d = \frac{n\lambda}{2\sin\theta} \qquad \text{(Eq. E1).}$$

In this calculation, only the angle θ has an associated uncertainty value which must be propagated to the d-spacing value. First, the peak location determined from peak fitting (2θ) and its error value must be divided by two to calculate θ. Then, the rules of error propagation are applied to determine the resulting error in d-spacing that is produced by the uncertainty in θ. The generalized rule for error propagation is,

$$\delta z = \sqrt{\left(\frac{\partial z}{\partial x}\delta x\right)^2 + \left(\frac{\partial z}{\partial y}\delta y\right)^2} \quad \text{(Eq. E2)}$$

where z is a function of x and y, δz is the error in z, $\partial z/\partial x$ and $\partial z/\partial y$ are the partial derivatives of z with respect to x and y, and δx and δy are errors associated with x and y. The uncertainty in d-spacing is made simpler by the fact that d-spacing only depends on one variable (θ) and can be calculated as follows:

$$\delta d = \frac{\partial d}{\partial \theta}\delta\theta \quad \text{(Eq. E3)}$$

$$\delta d = \frac{\lambda}{2}\csc\theta\cot\theta\delta\theta \quad \text{(Eq. E4).}$$

The result is that every calculated d-spacing value has an associated uncertainty that is related to the error in fitting of that specific diffraction peak. An example plot of d-spacing vs. $\sin^2\psi$ with error bars is shown in Figure E2. It can be observed that the magnitude of the error bars varies between data points. Ideally, the relationship between d-spacing vs. $\sin^2\psi$ should be linear, and the slope and intercept determined from linear fitting of this data is used in the calculation of the residual stress value. In typical linear fitting, the variance of each data point is assumed to be equal, and the contribution of each point is identical with regards to the fitting process. In the case of this dataset, the uncertainty value varies from point to point. To account for this, a weighted fitting process was used which takes into account the variation of uncertainties between data points. The weight of each data point was proportional to the inverse square of the error value for that point.

Therefore, points with a higher uncertainty value contributed less to the linear fitting than points with a lower uncertainty value.

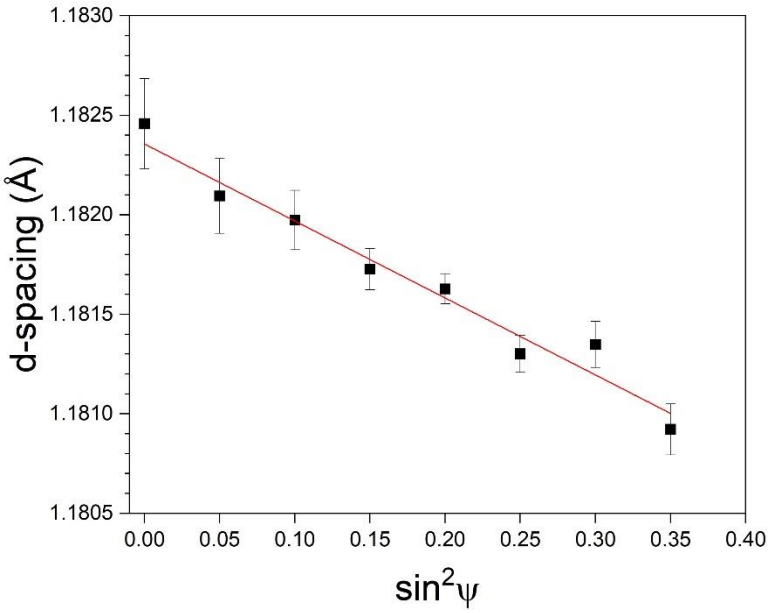

Figure E2: Example plot of d-spacing vs. $\sin^2\psi$ taken from the B-HiPIMS Cr coating at 300 °C with weighted linear fitting that was used for the residual stress calculation.

Representative plots of d-spacing vs. $\sin^2\psi$ for the B-HiPIMS and DCMS coatings at 300 °C and 700 °C are shown in Figure E3. At 300 °C, the linearity of the data was generally very good for both coating types, with R^2 values greater than 0.9. The magnitude of the error in d-spacing was slightly higher for the DCMS coating on account of the lower signal-to-noise ratio of the raw diffraction peak data. In a few instances, data points were found that were clear outliers and did not follow the linear trend. These points were excluded from the linear fitting. At 700 °C, the magnitude of the error bars increased for both coating types, a greater number of points appeared to be outliers, and the degree of linearity decreased. The increase in uncertainty and number of outliers can be attributed to noisier diffraction data at 700 °C. While these factors can certainly contribute to a reduction in linearity of the relationship between d-spacing and $\sin^2\psi$, there are also

physical factors that could contribute to this, such as stress gradients through the thickness of the coating or effects related to texture.

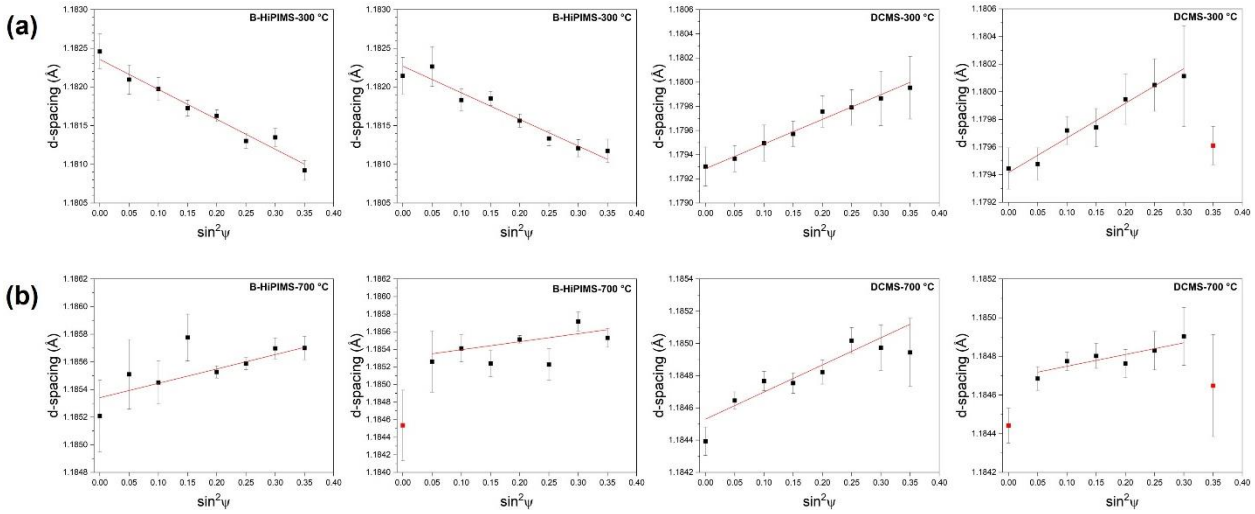

Figure E3: Representative plots of d-spacing vs. $\sin^2\psi$ for the B-HiPIMS and DCMS coatings at (a) 300 °C and (b) 700 °C. Data points in red were excluded from the linear fitting.

The final piece of analysis is the calculation of the residual stress and its associated uncertainty from linear fitting of the d-spacing vs. $\sin^2\psi$ data via the equation (identical to Eq. 3.1),

$$\sigma = \left(\frac{E}{1+\nu}\right)\frac{1}{d_0}\left(\frac{\partial d_\psi}{\partial \sin^2\psi}\right) \qquad \text{(Eq. E5)}$$

where d_0 and $\partial d_\psi/\partial \sin^2\psi$ are the intercept and slope of the linear fit, respectively. Similar to the errors related to peak fitting, both the slope and intercept have a corresponding standard error value. To take one example from the B-HiPIMS dataset at 300°, the values of the intercept and slope determined from linear fitting are 1.18239 Å ± 6.56877×10^{-5} Å (intercept) and -0.00349 Å ± 2.79648×10^{-4} Å (slope). These uncertainty values can be propagated through the residual stress calculation. Because the equation to calculate residual stress is just the simple product of the slope and intercept (multiplied by a constant), the error in the calculated residual stress value can be determined by,

$$\delta\sigma = |\sigma|\sqrt{\left(\frac{\delta d_0}{d_0}\right)^2 + \left(\frac{\delta S}{S}\right)^2} \qquad \text{(Eq. E6)}$$

where δd_0 and δS represent the uncertainties in the intercept and slope and d_0 and S are the values of the intercept and slope. The calculated $\delta\sigma$ value was used for the magnitude of the error bars in all plots of stress vs. time in the Chapter 6.